

Advanced Synthetic Techniques and Emerging Applications of
Porphyrin Paddlewheel Frameworks

by

Brandon J. Burnett

A DISSERTATION

Presented to the Faculty of
The Graduate College at the University of Nebraska
In Partial Fulfillment of Requirements
For the Degree of Doctor of Philosophy

Major: Chemistry

Under the Supervision of Professors Wonyoung Choe and Chin Li Cheung

Lincoln, Nebraska

May, 2013

UMI Number: 3558848

All rights reserved

INFORMATION TO ALL USERS

The quality of this reproduction is dependent upon the quality of the copy submitted.

In the unlikely event that the author did not send a complete manuscript and there are missing pages, these will be noted. Also, if material had to be removed, a note will indicate the deletion.



UMI 3558848

Published by ProQuest LLC (2013). Copyright in the Dissertation held by the Author.

Microform Edition © ProQuest LLC.

All rights reserved. This work is protected against unauthorized copying under Title 17, United States Code



ProQuest LLC.
789 East Eisenhower Parkway
P.O. Box 1346
Ann Arbor, MI 48106 - 1346

Advanced Synthetic Techniques and Emerging Applications of
Porphyrin Paddlewheel Frameworks

Brandon J. Burnett, Ph.D.

University of Nebraska, 2013

Advisors: Wonyoung Choe and Chin Li Cheung

Controlling the assembly of metal–organic frameworks (MOFs) using metalloligands (ligands containing a metal ion within the molecule) has been of particular interest in materials research due to these materials' ability to create porous structures with chemically active metal sites in the internal pores. MOFs are a class of organic–inorganic hybrid materials which are constructed through the coordination of multitopic organic linkers to metal ion nodes. A seemingly endless array of 1, 2, and 3D topologies are possible through judicious selection of the organic linker and metal ion source. Additionally, with the inclusion of metalloligands, a variety of functionality can be included into these MOFs, making them suitable for a variety of applications such as gas storage or catalysis. As a result, the development of advanced synthetic techniques to make these materials and continued search for new applications is very important.

One emerging advanced synthetic approach is a sequential self–assembly (SSA) strategy in which a simple MOF structure is initially synthesized through traditional methods, and used as a template for subsequent self–assembly processes creating new highly pure products. Herein we demonstrate the use of SSA on Porphyrin Paddlewheel Frameworks (PPFs) – a class of MOFs created with a porphyrin metalloligand. In addition, we present emerging applications in catalysis, fluorescence sensing, gas storage, and optical dichroism of these PPFs

ACKNOWLEDGEMENTS

My time at the University of Nebraska-Lincoln (UNL) has been an incredible experience and there are a number of people that have helped me along the way. First, the remarkable faculty at UNL, who have contributed to my academic growth, I thank you. I sincerely thank Professors Barry Cheung and Jason Kautz for taking a special interest in me and making sure I was successful in graduate school.

Secondly, I would like to thank the members (past and present) of the Choe group who have helped me to complete this work. A sincere thanks to Paul Barron, for getting me started down the path of SSA. Additionally, to the undergraduate and high school students who have assisted me, (Victoria Fry, Jacob Johnson, Michael VanBeek, Ryan Wood, Sara Laimans, Isaac Wells, and Tianye Chen): I sincerely thank you. Furthermore, I would like to thank Chunhua “Tony” Hu for helping with all of the X-ray diffraction of our materials. Also, I am extremely grateful to my advisor, Professor Wonyoung Choe, for his constant support, direction, and friendship throughout this work. His creativity and passion are truly awe inspiring. Our enlightening discussions have taught me how to be both a great scientist and individual.

Lastly, I would like to express my love and gratitude towards my family. Without my parents’ constant support and teaching of hard work and sacrifice, this would not be possible. I also thank my siblings, for always being there for me, for making me laugh, and keeping me grounded. I am extremely grateful to you all. Most importantly, I would like to thank my wife, Lyndsi, for her love, sacrifice, and unwavering belief in my abilities that continues to amaze and humble me – I love you so much. This is for you.

TABLE OF CONTENTS

Acknowledgements.....	i
 CHAPTER 1 Introduction to Metal–Organic Frameworks	
1.1 Introduction.....	1
1.2 Metal–Organic Frameworks (MOFs).....	3
1.3 Basic Assembly Principles.....	6
1.4 Applications of MOFs.....	10
1.5 Organization of Dissertation.....	11
1.6 References.....	12
 CHAPTER 2 Porphyrinic Metal–Organic Frameworks	
2.1 Introduction.....	15
2.2 Metalloligand Linkers.....	16
2.3 Brief History of Porphyrin MOFs.....	18
2.4 Synthetic Achievements.....	22
2.5 Properties of Porphyrinic MOFs.....	23
2.6 Porphyrin Paddlewheel Frameworks (PPFs).....	25
2.7 References.....	41
 CHAPTER 3 Sequential Self–Assembly in Porphyrin Paddlewheel Frameworks: Linker Replacement	
3.1 Introduction.....	47
3.2 Experimental Methods.....	52
3.3 Results and Discussion.....	57
3.4 Conclusions.....	82

3.5 References.....	82
---------------------	----

CHAPTER 4 Sequential Self-Assembly in Porphyrin Paddlewheel Frameworks: Linker Insertion

4.1 Introduction.....	87
4.2 Experimental Methods.....	96
4.3 Results and Discussion.....	100
4.4 Conclusions.....	119
4.5 References.....	119

CHAPTER 5 Post-Synthetic Metal Metathesis (PSMM)

5.1 Introduction.....	122
5.2 Experimental Methods.....	126
5.3 PSMM from Zn ₄ O cluster to CuZn ₃ O cluster.....	128
5.4 PSMM from Zn paddlewheel cluster to Cu paddlewheel cluster.....	133
5.5 Conclusions.....	137
5.6 References.....	137

CHAPTER 6 Fluorescence Quenching of Porphyrin Paddlewheel Frameworks for the Detection of Nitro-aromatic Explosive Vapors

6.1 Introduction.....	139
6.2 Experimental Methods.....	142
6.3 Results and Discussion.....	148
6.4 Conclusions.....	174
6.5 References.....	174

CHAPTER 7 Drug Incorporation and Delivery in Porphyrin Paddlewheel Frameworks

7.1 Introduction.....	179
7.2 Experimental Methods.....	183
7.3 Results and Discussion.....	186
7.4 Conclusions.....	198
7.5 References.....	198

CHAPTER 8 Development of Isorecticular Mn(III)–Porphyrin Paddlewheel Framework Series

8.1 Introduction.....	201
8.2 Experimental Methods.....	204
8.3 Results and Discussion.....	208
8.4 Dichroism of PPF–5–Mn/Zn.....	212
8.5 Gas Storage of PPF–31.....	221
8.6 Conclusions.....	225
8.7 References.....	225

CHAPTER 9 Catalytically Active Porphyrin Paddlewheel Framework for Alkene Epoxidation

9.1 Introduction.....	233
9.2 Experimental Methods.....	237
9.3 Results and Discussion.....	240
9.4 Conclusions.....	254
9.5 References.....	254

CHAPTER 10 Porphyrin Paddlewheel Framework Nanosheets Through Exfoliation

10.1 Introduction.....	259
10.2 Experimental Methods.....	263

10.3 Results and Discussion.....	265
10.4 Conclusions.....	276
10.5 References.....	276

CHAPTER 11 Final Thoughts and Future Directions

11.1 Quaternary Structures.....	278
11.2 Multi-fluorophore PPFs.....	281
11.3 ABBA Stacked Fe PPFs through Core–Shell Growth.....	283
11.4 Enzymatic Cascade through Oriented Attachment Growth.....	285
11.5 References.....	287

APPENDIX I Additional Figures and Tables

A1. Chapter 2 Data.....	289
A2. Chapter 3 Data.....	293
A3. Chapter 4 Data.....	296
A4. Chapter 5 Data.....	297
A5. Chapter 7 Data.....	298

CHAPTER 1

INTRODUCTION TO METAL–ORGANIC FRAMEWORKS

1.1 Introduction

It was long thought that there was no connection between the structure and properties of a crystalline substance and the chemical composition, due to changes in a chemical's structure and properties upon crystallization.¹ This was well articulated by Maddox in 1988, “One of the continuing scandals in the physical sciences is that it remains in general impossible to predict the structure of even the simplest crystalline solids from a knowledge of their chemical composition.”¹ This sentiment echoes a dream by Feynman in 1960, “What would the properties of materials be if we could really arrange the atoms the way we want them?”² While this dream has yet to be fully realized, in the past two decades, metal–organic frameworks (MOFs) have made great progress in the ability to predict the structure and properties of crystalline structures based on the selection of materials.

MOFs are a class of often porous materials which are constructed through the self–assembly of organic linkers and metal nodes through coordination bonding (Figure 1.1).³ Through judicious selection of the organic linker and metal ion source, a seemingly endless number of 1, 2, and 3D structures are available.³ Additionally, many of these materials are porous, creating a class of materials with properties that can rival other porous materials such as zeolites for sustainable materials chemistry applications such as gas storage and catalysis.⁴⁻⁶

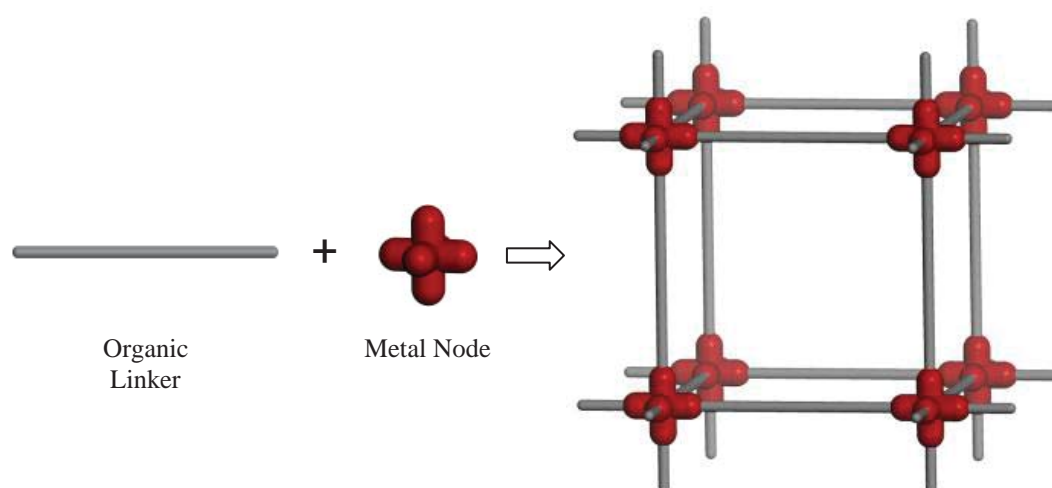


Figure 1.1. Schematic illustration of a metal–organic framework, assembled from organic linkers and metal nodes.

This dissertation discusses a new advanced synthetic technique used to obtain highly pure MOF structures, some of which have not been accessed through traditional synthetic routes. Additionally, new applications of Porphyrin Paddlewheel Frameworks (PPFs) – a class of MOFs which contain the metalloligand porphyrin – are reported.

1.2 Metal–Organic Frameworks (MOFs)

While the first synthetic polymeric coordination compound was that of Prussian Blue which is composed of iron metal centers linked together by cyanide ligands,⁷ it is generally accepted that the first designed coordination polymer was reported by Hoskins and Robson in 1990.⁸ They reported the coordination of 4,4',4'',4'''-tetracyanotetraphenylmethane to copper ions. Since both the organic linker and the metal ion adopt a tetrahedral geometry, the resulting assembly produced a diamond network (Figure 1.2a). This report introduced the idea of using multitopic organic molecular building blocks (ligands) to connect metal ions, resulting in a “potentially extensive class of solid state polymeric materials” symbolizing a new chapter in the design of crystalline materials and the beginning of MOFs. The next great milestone in the history of MOFs came nearly a decade later when Yaghi *et al.* reported on the assembly of a simple cubic structure from the linear 1,4-benzenedicarboxylate (BDC) organic ligand and the octahedral Zn_4O metal node which they named MOF-5 (Figure 1.2b).⁹ This report introduced the idea of predicting the structure of a solid substance by starting with well-defined linkers and metal ion clusters with a known geometry. The ability to logically target a network ‘blueprint’ and identifying the required building blocks for its assembly was later coined by Yaghi as reticular chemistry.^{3b} Additionally, the report of MOF-5 compared MOFs to traditional porous materials such as zeolites, effectively providing a

market to the new class of materials.⁹ Because of these claims, this paper is arguably the most important MOF publication. Shortly after this, another MOF, MIL-101, was reported which was highly stable.¹⁰ MIL-101 is constructed from BDC and a trigonal prismatic Cr_3O metal cluster (Figure 1.2c). This report provided evidence that MOFs could indeed compete in applications that are dominated by other porous materials. Since then, there has been a great surge in research into these materials, largely due to the vast selection of organic linkers and metal sources, allowing for great structural and functional tunability.

1.3 Basic Assembly Principles

MOFs are assembled through the coordination of multitopic linkers to metal ion nodes. The metal nodes can either be a single metal ion or a metal cluster created from multiple metal ions. The assembly of MOFs using metal clusters or secondary building units (SBUs) has become more popular over a single metal ion for multiple reasons. First, metal clusters often form geometrically predictable, highly symmetrical nodes over metal ions that can vary greatly even with the same metal ion source.³ Additionally, SBUs often are more chemically/thermally robust than single metal ions, resulting in MOFs more suitable for gas sorption or catalysis applications.³ Organic linkers also vary in their connection to metal nodes. The most common linkers are carboxylate based because the chelating property of carboxylates create multiple coordination bonds and add strength to the structure.³ Figure 1.3 shows three common SBUs and three common organic linkers along with a representation of their respective preferred geometry.³

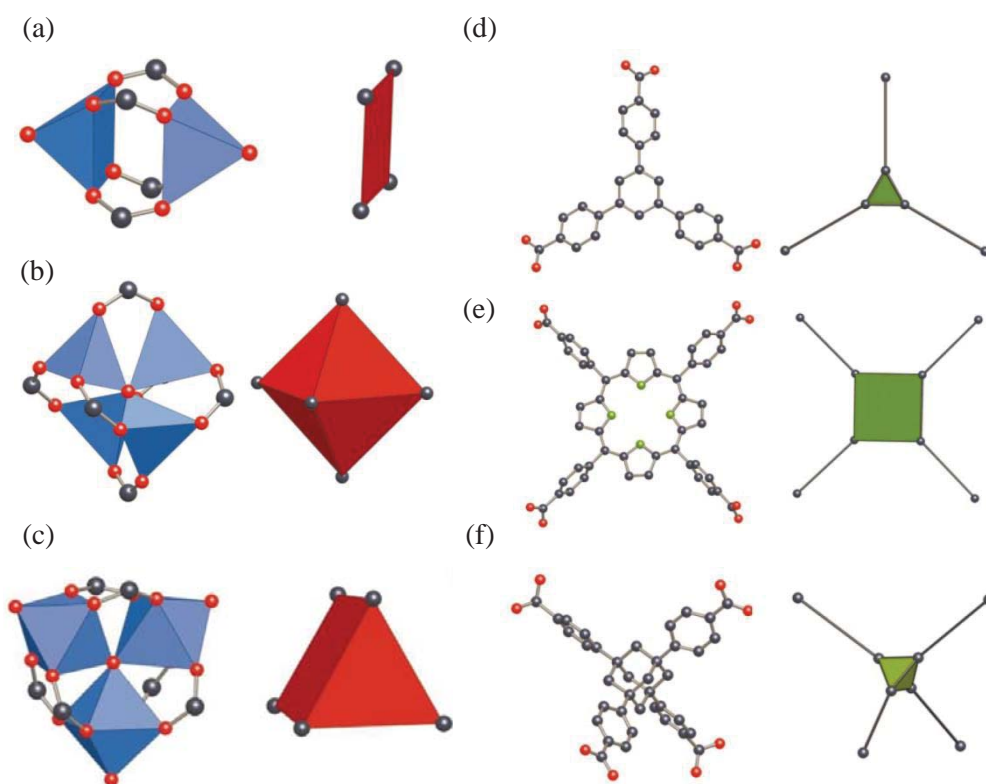


Figure 1.3. Some common building units for the construction of MOFs.^{3b} (a) Paddlewheel, (b) Zn_4O , and (c) trigonal prismatic SBUs. The metal oxygen polyhedral are blue, and the polygon defined by carboxylate carbon atoms are red. (d) Benzenetribenzoate, (e) Tetracarboxyphenylporphyrin, and (f) Adamantana-tetrabenzoate. The structures are simplified as geometric green polygons.

The combination of these two building units creates an infinite 1, 2, or 3D MOFs in which the topology is directly dependent on the preferred geometry of both the organic linker and SBU. For example, choosing a linear organic linker with a square planar SBU will result in a 2D square grid pattern (Figure 1.4a). Keeping the same organic linker, but changing the SBU to a trigonal planar geometry will result in a 2D honeycomb topology (Figure 1.4b). Finally, combining the original organic linker with an octahedral SBU will result in a simple cubic 3D structure (Figure 1.4c). The combination of many different SBUs with various types of organic linkers creates a large amount of possible framework topologies.³

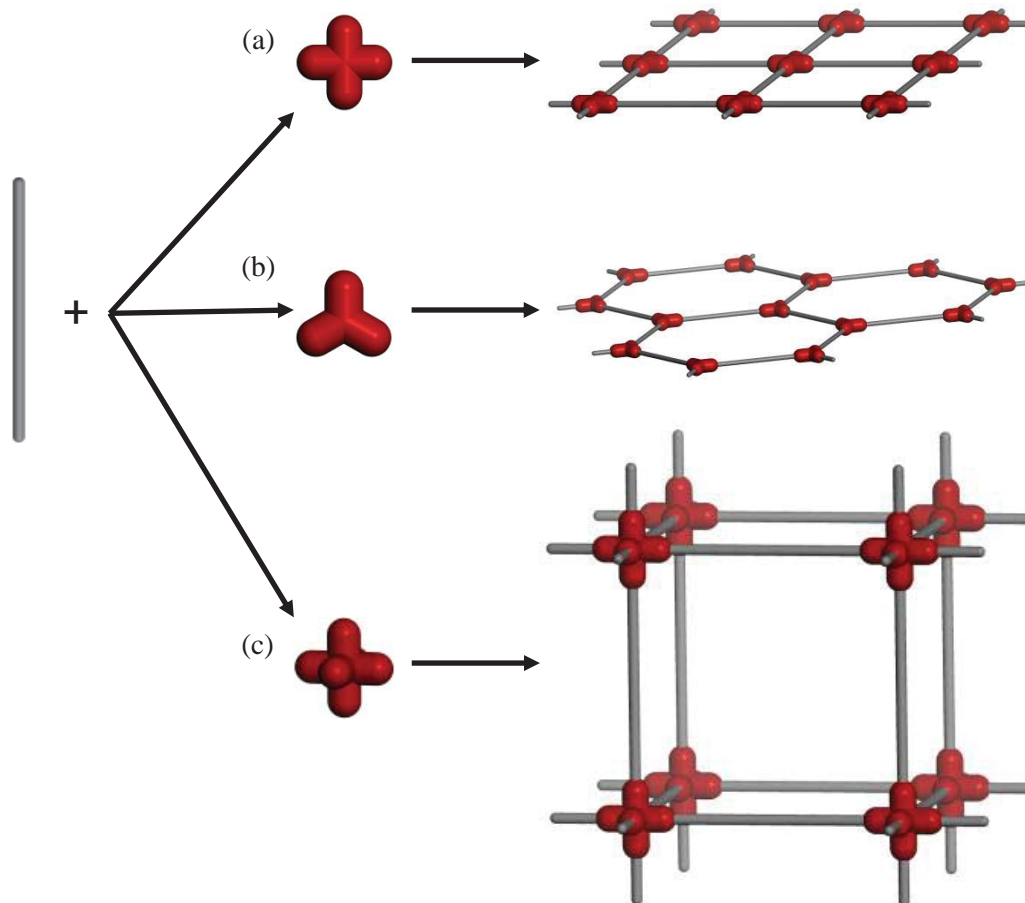


Figure 1.4. Basic network connectivity with a linear linker (grey) and (a) square planar SBU resulting in a 2D square grid pattern, (b) trigonal planar SBU resulting in a 2D honeycomb pattern, and (c) octahedral SBU resulting in a 3D simple cubic structure.

1.4 Applications of MOFs

Since both the structure and the functionality of MOFs is highly tunable based on the large choice in organic linkers and metal nodes, this class of materials has been found to excel in many different applications. A major sought after application for MOFs has been gas storage. Gases bind to surfaces by weak dispersive interactions (physisorption) or through stronger chemical associations (chemisorption). Physisorption correlates with surface area, with greater gas uptake favored by higher surface areas. Many MOFs are highly porous and have the highest surface area of any materials.⁵ The MOF compound NU-110 from Hupp *et al.* currently displays the highest experimental surface area of any material at 7140 m²/g.¹¹ This corresponds to a desktop of surface per crystal the size of a grain of salt.

Along with high surface areas, the functionality of MOFs can be tuned in order to obtain better chemisorption of gasses. The addition of an amine functional group has been shown to increase the interaction between CO₂ gas and the pore surface of MOFs, allowing for not only more gas to fill the pores, but also the possibility of gas separation.¹²

Gas separation and purification is another application in which MOFs have excelled.¹³ By tailoring the pore size of the MOF, size exclusion separation is possible, which is important for the separation of gasses with a large disparity in sizes. For samples which are similar in size, the functionality can be tuned within the pores to get chemically selective separation and purification. Additionally, a group of flexible MOFs have recently been used in order to get a specific response to different gas sorbents, allowing for very specific separations.¹⁴

MOFs have also found utility in a number of applications beyond gas adsorption and separation such as catalysis and drug delivery. Because of the large pores and tunable functionality, there have been a number of examples of MOFs used as heterogeneous catalysts for both gas phase and solution reactions.⁶ Reactants are able to diffuse into the pores of the MOF and interact with the numerous catalytic sites (either on the organic ligand or at the metal node) in the interior surface. The large pores in MOFs have also been shown to store large molecules such as drugs.¹⁵ The MOF thus acts as a drug carrier and delivery material allowing for targeted and controlled release.

These examples are just a few of reported applications for MOFs. Additionally, new applications are being investigated every year. A continued effort to understand the design and assembly of these materials will only serve to further expand the possible applications for these materials.

1.5 Organization of Dissertation

Chapter 1 provides a brief introduction into MOFs and the terminology used throughout the dissertation. Chapter 2 focusses on porphyrinic MOFs including an introduction to PPFs published by the Choe group. This data was originally published in the journal *Crystal Engineering Communications*.¹⁶ Chapter 3 focuses on the sequential self-assembly of PPFs through a linker replacement reaction. This data was originally published in *Journal of American Chemical Society*.¹⁷ Chapter 4 focuses on the sequential self-assembly of PPFs through a linker insertion reaction. This data was originally published in *Dalton Transactions*¹⁸ and *Crystal Engineering Communications*.¹⁹ Chapter 5 details work on post-synthetic metal metathesis in two MOF systems. Chapter 6 details the use of fluorescent PPFs as nitro-aromatic explosives

sensor materials. Chapter 7 focuses on the development of new bio-PPFs for drug delivery applications. Chapter 8 details a new isoreticular PPF series containing Mn(III)porphyrin and includes the optical and gas storage properties of two of these structures. Chapter 9 shows the catalytic activity of a nonporous Mn(III)porphyrin based PPF structure. Chapter 10 focuses on the preparation of PPF-nanosheets from a top-down exfoliation method. Chapter 11 discusses future directions for PPFs and other MOFs. The Appendix contains additional tables and figures to support the data in these chapters. Most of the single crystal data were determined by Dr. Chunhua “Tony” Hu at New York University.

1.6 References

- (1) Maddox, J. *Nature* **1988**, 335, 201.
- (2) Feynman, R. *Eng. Sci.* **1960**, 22.
- (3) (a) Tranchemontagne, D. J.; Mendoza-Cortés, J. L.; O’Keeffe, M.; Yaghi, O. M. *Chem. Soc. Rev.* **2009**, 38, 1257. (b) Yaghi, O. M.; O’Keeffe, M.; Ockwig, N. W.; Chae, H. K.; Eddaoudi, M.; Kim, J. *Nature* **2003**, 423, 705. (c) Moulton, B.; Zaworotko, M. J. *Chem. Rev.* **2001**, 101, 1629. (d) O’Keeffe, M.; Yaghi, O. M. *Chem. Rev.* **2012**, 112, 675.
- (4) (a) Das, M. C.; Xiang, S.; Zhang, Z.; Chen, B. *Angew. Chem. Int. Ed.* **2011**, 50, 10510. (b) Garibay, S. J.; Stork, J. R.; Cohen, S. M. *Prog. Inorg. Chem.* **2009**, 56, 336.
- (5) (a) Murray, L. J.; Dincă, M.; Long, J. R. *Chem. Soc. Rev.* **2009**, 38, 1294. (b) Collins, D. j.; Zhou, H. –C. *J. Mater. Chem.* **2007**, 17, 3154. (c) Farha, O. K.; Oezguer, Y. A.; Eryazici, I.; Malliakas, C. D.; Hauser, B. G.; Kanatzidis, m. G.; Nguyen, S. T.; Snurr, R. Z.; Hupp, J. T. *Nat. Chem.* **2010**, 2, 944. (d) Czaja, A. U.; Trukhan, N.; Müller, U. *Chem. Soc. Rev.* **2009**, 38, 1284. (e) Herm, Z. R.; Swisher, J. A.; Smit, B.; Krishna, R.; Long, J.

- R. *J. Am. Chem. Soc.* **2011**, *133*, 5664. (f) Wang, X. -S.; Megn, L.; Cheng, Q.; Kim, C.; Wojtas, L.; Chrzanowski, M.; Chen, Y. -S.; Zhang, X. P.; Ma, S. *J. Am. Chem. Soc.* **2011**, *133*, 16322.
- (6) (a) Ma, L.; Abney, C.; Lin, W. *Chem. Soc. Rev.* **2009**, *38*, 1248. (b) Lee, J.; Farha, O. K.; Roberts, J.; Scheidt, K. A.; Nguyen, S. T.; Hupp, J. T. *Chem. Soc. Rev.* **2009**, *38*, 1450. (c) Seo, J. S.; Whang, D.; Lee, H.; Jun, S. I.; Oh, J.; Jeon, Y. J.; Kim, K. *Nature* **2000**, *404*, 982. (d) Liqing, M.; Falkowski, J. M.; Abney, C.; Lin, W. *Nat. Chem.* **2010**, *2*, 838. (e) Farha, O. K.; Shultz, A. M.; Sarjeant, A. A.; Nguyen, S. T.; Hupp, J. T. *J. Am. Chem. Soc.* **2011**, *133*, 5652. (f) Yoon, M.; Srirambalaji, R.; Kim, K. *Chem. Rev.* **2012**, *112*, 1196. (g) Uemura, T.; Yanai, N.; Kitagawa, S. *Chem. Soc. Rev.* **2009**, *38*, 1228.
- (7) Batten, S. R.; Turner, D. R.; Neville, S. M. *Coordination Polymers: Design, Analysis, and Application*, 1st ed.; RSC Publishing, Cambridge, 2009; pp 322-323.
- (8) Hoskins, B. F.; Robson, R. *J. Am. Chem. Soc.* **1990**, *112*, 1546.
- (9) Li, H.; Eddaoudi, M.; O'Keeffe, M.; Yaghi, O. M. *Nature* **1999**, *402*, 276.
- (10) Férey, G.; Mellot-Draznieks, C.; Serre, C.; Millange, F.; Dutour, J.; Surble, S.; Margiolaki, I. *Science* **2005**, *309*, 2040.
- (11) Farha, O. K.; Eryazici, I.; Jeong, N. C.; Hauser, B. G.; Wilmer, C. E.; Sarjeant, A. A.; Snurr, R. Q.; Nguyen S. T.; Yazaydin, A. Ö.; Hupp, J. T. *J. Am. Chem. Soc.* **2012**, *134*, 15016.
- (12) McDonald, T. M.; Lee, W. R.; Mason, J. A.; Wiers, B. M.; Hong, C. S.; Long, J. R. *J. Am. Chem. Soc.* **2012**, *134*, 7056.
- (13) Li, J. -R.; Sculley, J.; Zhou, H. -C. *Chem. Rev.* **2012**, *112*, 869.
- (14) Horike, S.; Shimomura, S.; Kitagawa, S. *Nat. Chem.* **2009**, *1*, 695.

- (15) Horcajada, P.; Gref, R.; Baati, T.; Allan, P. K.; Maurin, G.; Couvreur, P.; Férey, G.; Morris, R.; Serre, C. *Chem. Rev.* **2012**, *112*, 1232.
- (16) Burnett, B. J.; Barron, P. M.; Choe, W. *CrystEngComm.* **2012**, *14*, 3839.
- (17) Burnett, B. J.; Barron, P. M.; Hu, C.; Choe, W. *J. Am. Chem. Soc.* **2011**, *133*, 9984.
- (18) Burnett, B. J.; Choe, W. *Dalton Trans.* **2012**, *41*, 3889.
- (19) Burnett, B. J.; Choe, W. *CrystEngComm.* **2012**, *14*, 6129.

CHAPTER 2

PORPHYRINIC METAL–ORGANIC FRAMEWORKS

2.1 Introduction

As stated in Chapter 1, metal–organic frameworks (MOFs) have become increasingly important materials in sustainable materials chemistry during the past two decades. Although the structures and properties of MOFs have been extensively studied, the surface modification of pores is an underexplored research area in MOFs. A key synthetic challenge in the area of MOFs has been to incorporate (or immobilize) coordinatively unsaturated metal centers onto the pore walls of MOFs. Such metal centers can interact with guest molecules in the channel, and can play a significant role in various applications, such as gas adsorption,¹ catalysis,² chromic properties,³ and molecular recognition.⁴ Despite such advantages, rational synthesis of MOFs with accessible metal centers has been a difficult challenge, because metal nodes are often saturated by organic linkers, leaving no accessible metal centers.⁵ Thus, there is an urgent need to identify new, reliable synthetic routes and rational design principles to achieve framework structures with accessible metal centers.

New synthetic strategies and fundamental understanding of the interaction between these metal centers and guest molecules will greatly enhance the performance of MOF materials, and further provide superior tunability in adsorption, catalytic, and optical properties. It is highly desirable to develop multifunctional porous MOFs with tunable pore characteristics and topologies, which can be optimized depending on the

target applications. Such combined efforts, pore surface engineering and control of framework topology, will promote tailor-made multifunctional porous solids in energy, materials, and green chemistry.

2.2 Metalloligand Linkers

Many research groups have focused on creating accessible metal centers on the structural metal nodes of MOFs.⁶ Another approach involves incorporating accessible metal centers in the *organic* linkers. To incorporate accessible metal centers, metalloligands are used in MOF synthesis (Figure 2.1). In this “metalloligand” approach, the metal node does not have to play dual roles, i.e. structure building joint and functional metal center.⁵ Separating these two roles in MOF synthesis is a crucial part of our synthetic strategy, discouraging the degradation of the MOF structure upon interaction with guest molecules. Indeed if a catalytically active metal ion center acts purely as a functional metal center, but not a structural center, the change of oxidation states will not affect the overall structural topology. The inclusion of metalloligands into the construction of MOFs introduces further advantages including additional coordination sites in order to achieve more complex topologies that are difficult with traditional organic linkers. Also, the construction of heterometallic MOFs (MOFs composed of more than one type of metal element) becomes more possible.^{5,7} To date, MOFs have been synthesized from various metalloligands, including pyridine-2-carboxylates,^{7,8} acetylacetonates,⁹ dipyrins,¹⁰ Schiff bases,¹¹ bipyridines,¹² 3,5-pyridinedicarboxylic acid dimers,¹³ ferrocenes,¹⁴ porphyrins,^{1,2,15-34} and other ligands.³⁶

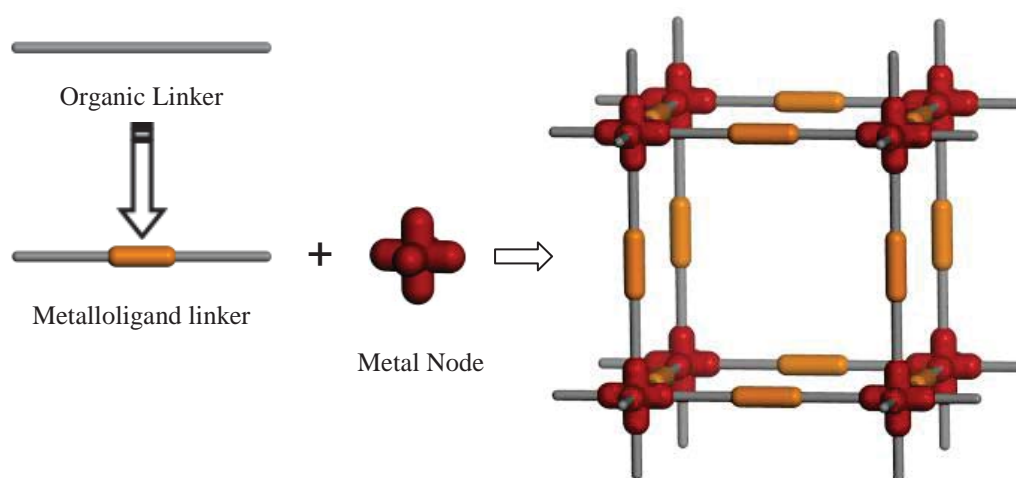


Figure 2.1. Schematic illustration of a MOF assembled from metal nodes and metalloligands.

2.3 Brief History of Porphyrin MOFs

Among the metalloligands, we are particularly interested in porphyrin linkers because these macrocycles can accommodate various elements in the periodic table, ranging from transition metals to main group elements (Figure 2.2).³⁷ Such flexibility in the choice of metals is not feasible when metal nodes are used for functional metal centers. Additionally, many different functional groups can be attached to the exterior of the porphyrin allowing for further flexibility in linker choice for the construction of MOFs (Figure 2.3). Although porphyrin-based frameworks have been reported by Robson,^{16,17} Godlberg,^{18,19} Suslick,²⁰⁻²² Li,²³ Choe,²⁴⁻³¹ Hupp,^{2,4,32,33} Ma,¹ and others,^{34,35} the use of porphyrinic MOFs in materials chemistry is still in its infancy.

H																			He
Li	Be											B	C	N	O	F			Ne
Na	Mg											Al	Si	P	S	Cl			Ar
K	Ca	Sc	Ti	V	Cr	Mn	Fe	Co	Ni	Cu	Zn	Ga	Ge	As	Se	Br			Kr
Rb	Sr	Y	Zr	Nb	Mo	Tc	Ru	Rh	Pd	Ag	Cd	In	Sn	Sb	Te	I			Xe
Cs	Ba		Hf	Ta	W	Re	Os	Ir	Pt	Au	Hg	Tl	Pb	Bi	Po	At			Rn
Fr	Ra		Rf	Db	Sg	Bh	Hs	Mt	Uun	Uuu	Uub								
			La	Ce	Pr	Nd	Pm	Sm	Eu	Gd	Tb	Dy	Ho	Er	Tm	Tb			Lu
			Ac	Th	Pa	U	Np	Pu	Am	Cm	Bk	Cf	Es	Fm	Md	No			Lr

Figure 2.2. Elements known to be incorporated in the core of porphyrin metalloligands.³⁷

The first porphyrinic coordination polymer was reported by Robson *et al.* in 1991.¹⁶ In this report, tetrapyrridyl–palladium porphyrin was connected together into an infinite 3D structure through the coordination to cadmium ion metal nodes. Because the metal source within the porphyrin and the metal source in the metal node are different, this also is the first example of a heterometallic MOF. Additionally in this report, Robson foresaw the utility of using porphyrins in MOF construction, “The stability and rigidity of metalloporphyrins, together with their potential for symmetrical 4–connection to other units, makes them especially attractive as slab–like components for the construction of new infinite structures.”¹⁶ Even from an early time, porphyrins were identified as useful metalloligands for MOF materials.

Robson *et al.* followed up this report in 1994 with another structure in which a tetrapyrridyl–copper porphyrin coordinates with a copper metal ion node to create a 3D **pts** structure.¹⁷ In that report Robson alluded to future applications of porphyrinic MOFs, “With regard to future studies, porphyrins and phthalocyanins are particularly alluring as building blocks for networks with potential applications as microporous heterogeneous catalysts because (1) their relative rigidity and large size, in the correct circumstances, could be used to generate correspondingly large channels and cavities, (2) they show a high degree of thermal stability and could therefore be put to use at elevated temperatures, (3) they readily incorporate a wide range of metal centres, and (4) as discrete molecular species, they are known to catalyse and promote diverse processes.”¹⁷

At the same time as Robson’s 1994 publication, Goldberg *et al.* published two structures constructed by the self-coordination of tetrapyrridyl–zinc porphyrins. In these

structures, the zinc ion in the core of the porphyrin is used as a structural coordination site for the exterior pyridyl functional groups creating 3D structures.¹⁸

Since then, there has been a large growth in the number of porphyrin MOF structures reported in the literature. In fact, the amount of structures reported is growing steadily every year (Figure 2.4). In total, there have been 159 porphyrinic MOF structures reported in the literature as of February 2013 (for a full list of frameworks see Table A1.1 in the Appendix).

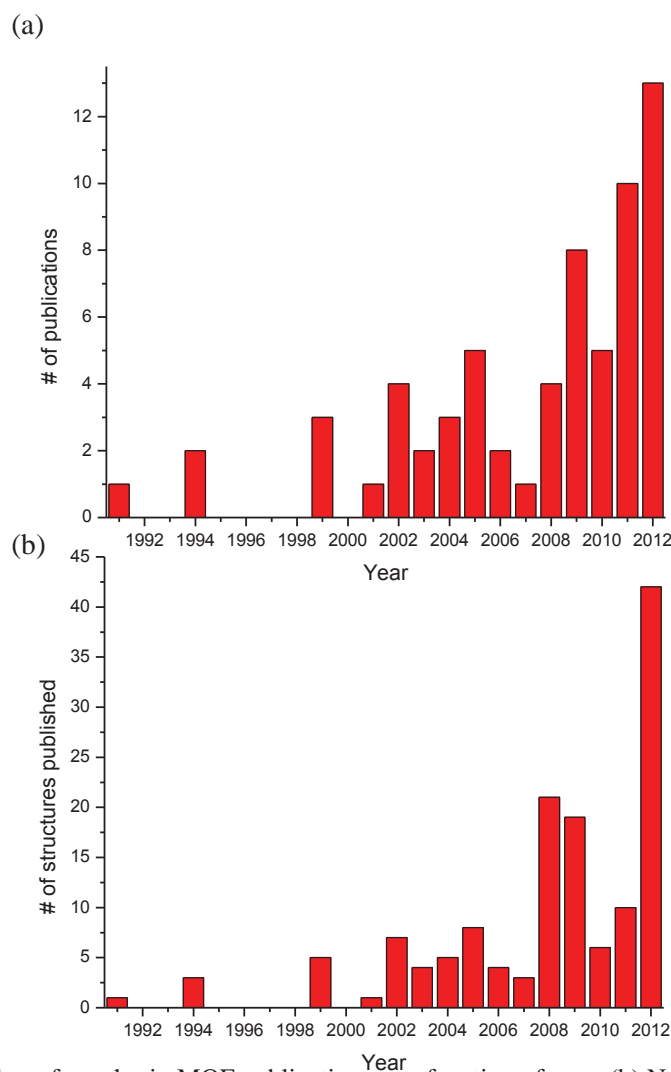


Figure 2.4. (a) Number of porphyrin MOF publications as a function of year. (b) Number of porphyrin MOF structures published as a function of year.

2.4 Synthetic Achievements

Early porphyrinic MOF structures reported by Robson, Goldberg, and others focused on the coordination of tetrapyrrolyl porphyrins to single metal ions.¹⁶⁻¹⁹ Because of this, these structures were not chemically or structurally robust, indeed they did not survive the removal of guest molecules. As discussed in Chapter 1, by changing from a single metal ion node to a metal cluster increases the structural strength of the MOF. Additionally, by changing the functional group on the organic ligand from a single coordinating group to a chelating group will also add structural strength. In 2002, Suslick *et al.* published a new porphyrinic MOF assembled from tetra-(carboxyphenyl) porphyrin (TCPP) and a trinuclear cobalt metal cluster SBU. This MOF exhibits a 3D porous structure which is capable of adsorbing and desorbing different liquid sorbates while retaining porosity.²⁰ The change in synthetic design allowed for increased structural strength making it possible for gas molecules to exchange freely in the pores.

In 2009, Choe *et al.* published the first porphyrinic MOF structure based on TCPP and the symmetrically identical $M_2(COO)_4$ paddlewheel SBU generating a 2D square grid pattern which was shown to be porous by H_2 sorption experiments.²⁴ Choe *et al.* followed this work by connecting these 2D sheets using dipyrrolyl pillars and showed control of the overall topology through (1) preferred coordination geometry of porphyrin metal,²⁵ (2) stoichiometric amount of reactants,²⁶ and (3) the chemical structure of the pillar.²⁷ Additionally, they successfully synthesized the first heterometallic series in porphyrin MOFs.²⁸

In 2011, Ma *et al.* published the first porphyrin MOF based on a polyhedral cage design which eliminates the need for a pillar in order to achieve a porous 3D structure.¹

Instead of designing the porphyrin with only one carboxylic acid per exterior group of the porphyrin, their synthesis included a dicarboxyphenyl functional group on the porphyrin. The assembly of these porphyrins to paddlewheel SBUs creates a polyhedral cage in which the porphyrins make up the walls of the cage. This design yields highly robust frameworks suitable for gas storage or catalysis.

2.5 Properties of Porphyrinic MOFs

While porphyrin MOF materials have been recognized as highly functional since the first report by Robson in 1991,¹⁶ it took until 2002 for Suslick *et al.* to show the first properties.²⁰ This has been because of a lack of structural stability often plagued early porphyrin MOFs. In the report by Suslick, PIZA-1 shows size, shape and functional group selectivity in the sorption of liquid sorbates.

While PIZA-1 was successful in incorporating liquid sorbates into the pores, it wasn't until 2006 when a single crystalline porphyrin MOF structure was used for gas sorption. Tatsumi *et al.* reported the gas sorption properties of their structure assembled from tetra-pyridyl porphyrin and a copper paddlewheel metal node.³⁴ Upon activation the compound retained crystallinity and the adsorption of N₂ showed a BET surface area of 812.08 m² g⁻¹ and a micropore volume of 0.4737 cm³ g⁻¹.

In 2005, Suslick reported a new structure, PIZA-3, which contained catalytically active manganese porphyrin.²² Indeed PIZA-3 was used to catalyze the oxidation and epoxidation of many alkanes and alkenes while retaining its structure. It was found however that the catalysis only occurred on the exterior surface of the crystals instead of inside the pores.

While PIZA-3 was successful as a heterogeneous catalytic system, a MOF which contains open pores with accessible internal catalytic centers is more desirable. Hupp *et al.* reported a zinc–porphyrin based MOF, ZnPO-MOF, which was permanently microporous and catalytically active for the acyl–transfer reaction.³¹ Additionally the internal pores were shown to be involved in the catalytic process.

The Hupp group has also created a 3D structure based on the 2D square grid porphyrin paddlewheel motif for light harvesting.³² BOP MOF is constructed with Zn–TCPP, Zn₂(COO)₄ paddlewheel SBU, and boron dipyrromethane (bodipy) pillaring linker. Upon illumination with 543 nm light, the bodipy linker absorbs the energy and transfers it to Zn–TCPP through a Förster resonance energy transfer mechanism. The Zn–TCPP then relaxes through fluorescence.

Recently, the Ma group synthesized a polyhedral cage porphyrinic MOF which shows selective adsorption of H₂ and O₂ over N₂ and CO₂ over CH₄.^{1a} Ma followed this report with another polyhedral based MOF with the highest surface area of any porphyrin MOF (2037 m² g⁻¹).^{1b}

As shown, the properties of porphyrin MOFs are excellent for applications in gas storage, catalysis, and light harvesting. The examples provided are just a few of the possible properties exhibited by such materials. In this dissertation, new properties such as fluorescence sensing and polychromatism are discussed. The continual effort to construct new porphyrin MOFs will open up more opportunities to study novel properties for sustainable energy research.

2.6 Porphyrin Paddlewheel Frameworks (PPFs)

To build extended porphyrin frameworks, our group uses well-established $M_2(\text{COO})_4$ metal paddlewheel clusters where $M = \text{Co}$ and Zn . These clusters are used as *joints* to bind the porphyrin linkers together. The linkers used are tetra-(4-carboxyphenyl)porphyrin (TCPP) (**L1**), *cis*-di-(4-carboxyphenyl)porphyrin (*cis*-DCPP) (**L2**), and *trans*-di-(4-carboxyphenyl)porphyrin (*trans*-DCPP) (**L3**) (see Figure 2.5). A third component can be introduced through dipyriddy pillar molecules: 4,4'-bipyridine (BPY) (**P1**), 3,6-di-4-pyridyl-1,2,4,5-tetrazine (DPT) (**P2**), and *N,N'*-di-(4-pyridyl)-1,4,5,8-naphthalenetetracarboxydiimide (DPNI) (**P3**) (see Figure 2.5). The combination of these three building units (porphyrin, paddlewheel, and pillaring linker) has resulted in the synthesis of 25 PPFs (PPF stands for *Porphyrin Paddlewheel Framework*) to date (Table 2.1). **L1** ligand and paddlewheel cluster form a 2D square grid (Figure 2.6). Then, the pillar molecules connect the grids together through the coordination of their pyridyl nitrogen to the axial sites of the porphyrin and paddlewheel, creating a 3D framework topology. In most cases, 3D paddlewheel frameworks do not possess accessible metal centers because the paddlewheel clusters are fully coordinated by axial dipyriddy pillars and equatorial carboxylate linkers. In the porphyrin frameworks, however, it is possible to create accessible metal centers inside the framework because of the ability to insert diverse metal ions into the porphyrin macrocycle. Using these three structural variables (*e.g.* porphyrin, paddlewheel, and pillar), topology and pore surface can be systematically controlled.

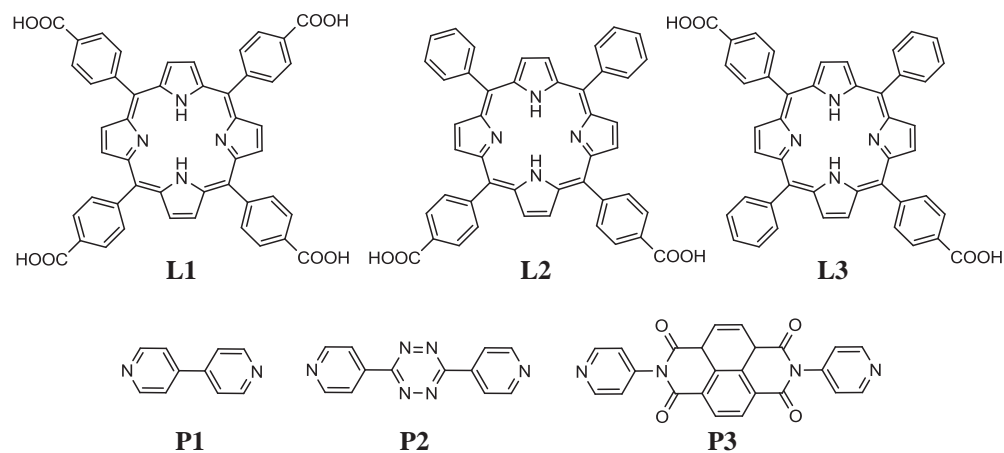


Figure 2.5. Porphyrins (**L1–3**) and pillars (**P1–3**) used in porphyrin paddlewheel frameworks.

Table 2.1. Reported porphyrin paddlewheel frameworks.

Name	Structure pattern	Ref.
PPF-1-Zn/Zn	sql	24
PPF-1-Co/Co	sql	24
PPF-3-Co/Co	pcu-b	25
PPF-3-Mn/Zn	pcu-b	28
PPF-3-Mn/Co	pcu-b	28
PPF-3-Fe/Zn	pcu-b	28
PPF-3-Fe/Co	pcu-b	28
PPF-4	fsx	25
PPF-5-Pd/Co	fsc	25
PPF-5-Pt/Co	fsc	28
PPF-5-Ni/Zn	fsc	28
PPF-5-V=O/Zn	fsc	28
PPF-6-Co/Zn	kgd	29
PPF-6-Zn/Zn	kgd	29
PPF-11-Zn/Zn	fsc	27
PPF-11-Co/Co	fsc	27
PPF-11-Mn/Zn	fsc	27
PPF-11-Fe/Zn	fsc	27
PPF-18	Bilayer	26
PPF-19	fsc	26
PPF-20	fsx	26
PPF-21	Bilayer	26
PPF-22	fsx	26
PPF-25	ant	30
PPF-27	Bilayer	31

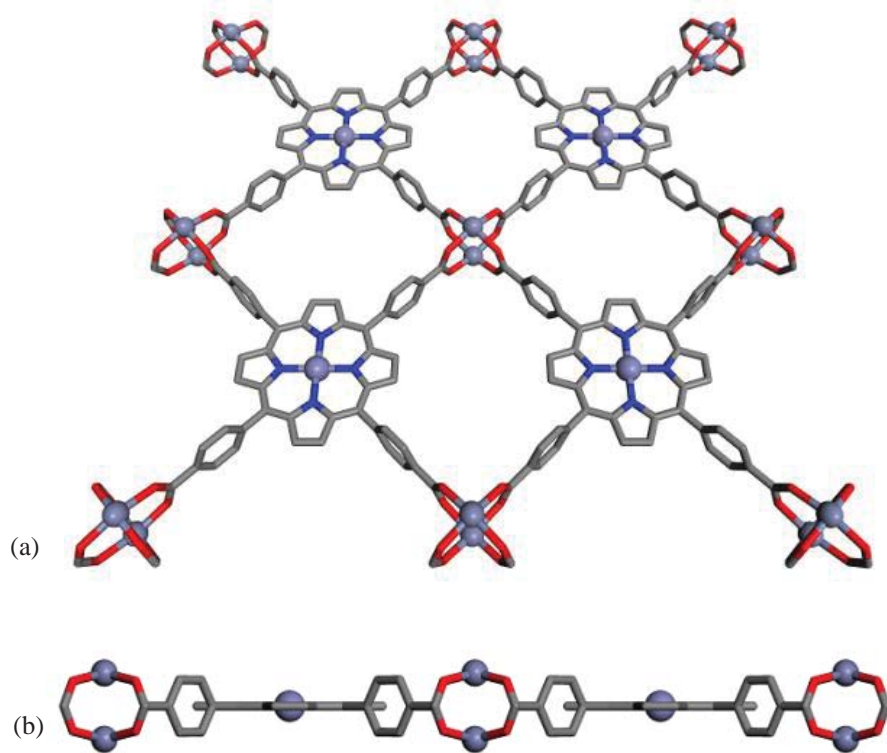


Figure 2.6. M-L1 metalloligands and paddlewheel SBUs combine to assemble a basic 2D PPF grid (sql). (a) A perspective view and (b) an edge view of the layer.²⁴

The first PPF synthesized from our group was a 2D-based MOF, PPF-1.²⁴ PPF-1 is assembled from ZnTCPP (Zn-L1, hereafter) and Zn paddlewheel *via* a solvothermal reaction. The structural building blocks, Zn-L1 and Zn₂(COO)₄ paddlewheel cluster, from 2D **sql** topology, stacked in an AB fashion (Fig. 2.6).²⁴ The interlayer distance was found to be directly dependent on the temperature, showing expansion from 17.49 Å to 18.58 Å in the temperature range of 120 K to 296 K.²⁴ Thermogravimetric analyses of PPF-1 and temperature dependent X-ray powder diffraction (PXRD) patterns show that the framework is stable up to at least 300 °C in air.²⁴ Upon removal of solvent molecules at high temperature, the framework contains exposed Zn metal centers. The nitrogen adsorption-desorption isotherm for PPF-1 shows a Langmuir surface area of 622 m²g⁻¹, demonstrating permanent porosity, and the H₂ adsorption isotherm shows a reversible H₂ uptake of 2.0 wt% at 20 bar and 77 K.²⁴ As mentioned in the introduction, a notable structural feature of PPFs is their superior tunability to accommodate various metals in both the porphyrin linker and paddlewheel cluster, thereby decorating pore surfaces with many possible metal centers, a highly sought-after feature in functional MOFs. This was demonstrated in the isorecticular PPF-1-Co/Co (in this naming scheme, the first metal represents the metal within the porphyrin ring, and the second metal represents the metal in the paddlewheel SBU).²⁴

By introducing a dipyriddy pillaring linker as a third component into the synthesis, the 2D porphyrinic layers can be connected together to yield 3D frameworks. Since there are two different metal centers available for axial bonding (porphyrin metal center and paddlewheel metal center), there are three possible pillaring schemes (Figure 2.7). There is a heterogeneous AB (porphyrin-to-paddlewheel) connection, along with two

homogeneous pillaring connections: an AA (paddlewheel-to-paddlewheel) connection and an A'A' (porphyrin-to-porphyrin) connection. Interestingly, the coordination geometry of the metal centers in porphyrins can be used to govern the stacking sequence of 2D porphyrinic layers.²⁵ This synthetic strategy allows us to control the 3D stacking sequence by the introduction of metallated tetratopic metalloporphyrin linkers. Figure 2.8 shows three tetratopic metalloporphyrin linkers (M-L1; M = Co, Zn, and Pd) used in this study, each representing 6-, 5-, and 4-connected metal coordination respectively.²⁵ These metalloporphyrin linkers and M₂(COO)₄ clusters (M = Zn or Co) form the same 2D pattern as seen in 2D PPF-1. The 2D layers are further pillared by **P1** (see Figure 2.5). The stacking patterns vary from AB (PPF-3) to ABBA (PPF-4), and further to AA (PPF-5), depending on the coordination environment of the metal center in the porphyrin linker.²⁵ *These are the first examples of metal-organic frameworks, in which 3D stacking sequences are systematically controlled by metalloligand coordination.* In this series, the ABBA stacking pattern creates an **fsx** topology and represents an intergrowth of the AA and AB patterns. To further observe the control of topology through the porphyrin metal choice, two heterometallic isorecticular series were synthesized: the AB stacked PPF-3 series (Figure 2.9) which includes PPF-3-Mn/Zn, PPF-3-Mn/Co, PPF-3-Fe/Zn, and PPF-3-Fe/Co, and also the AA stacked PPF-5 series (Figure 2.10) including PPF-5-Pt/Co, PPF-5-Ni/Zn, and PPF-5-V=O/Zn.²⁸ In these series, PPF-3 adopts a **pcu-b** topology and the PPF-5 adopts and **fsc** topology.²⁸ These series impressively show the independent control of two metal centers which is still a challenge in MOF synthesis.

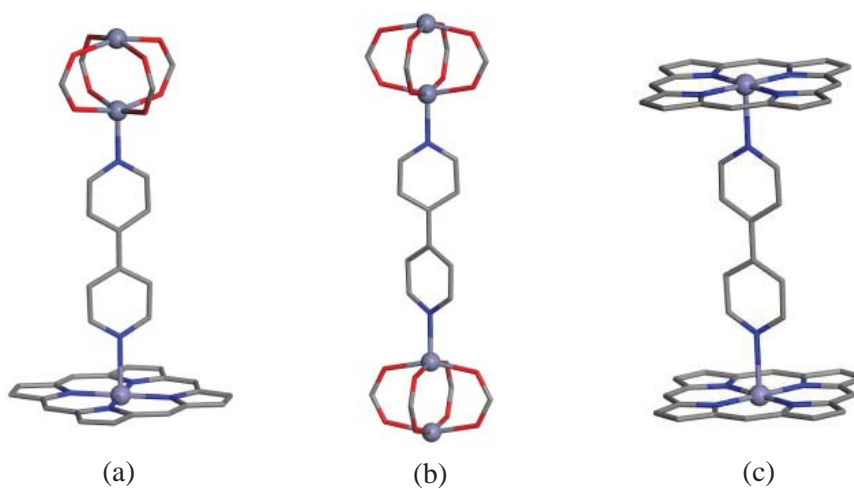


Figure 2.7. Three types of possible pillaring present in porphyrin paddlewheel frameworks using a 4,4'-bipyridine ligand. (a) Heterogeneous AB, (b) homogeneous AA, and (c) homogeneous A'A' connections.

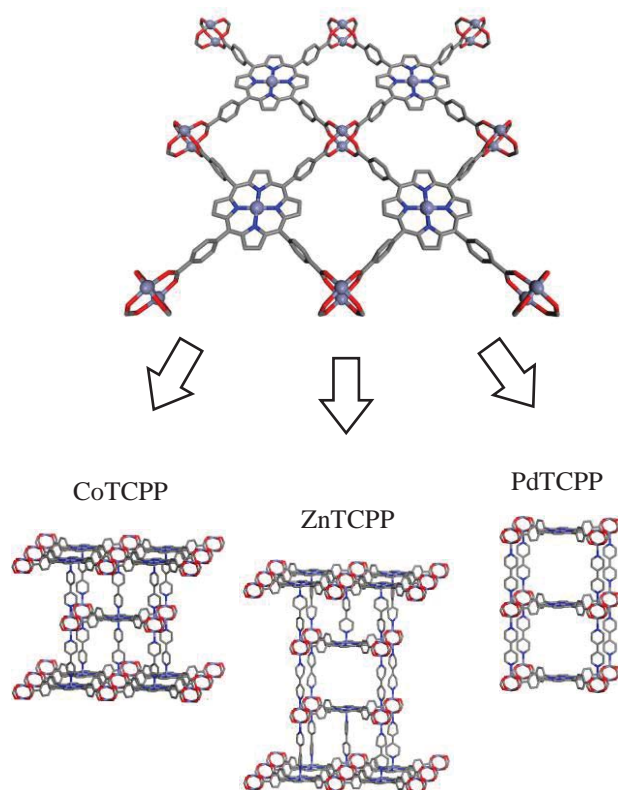


Figure 2.8. Stacking control of porphyrin framework series, PPF-3 (left), PPF-4 (middle), and PPF-5 (right) through M-L1 metal choice.²⁵

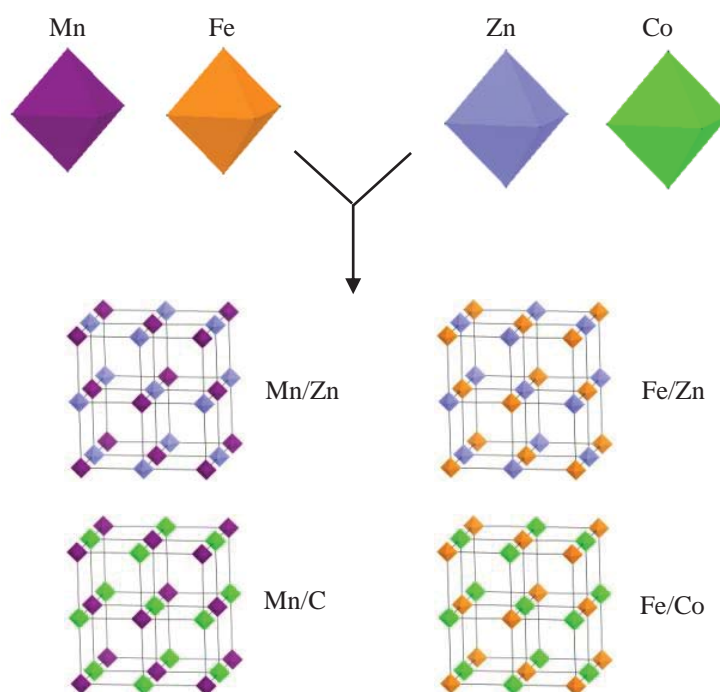


Figure 2.9. The **pcu-b** topology observed in the PPF-3 series: PPF-3-Mn/Zn, PPF-3-Mn/Co, PPF-3-Fe/Zn, and PPF-3-Fe/Co. This approach allows for the synthesis of topologically identical frameworks with various combinations of metals.²⁸

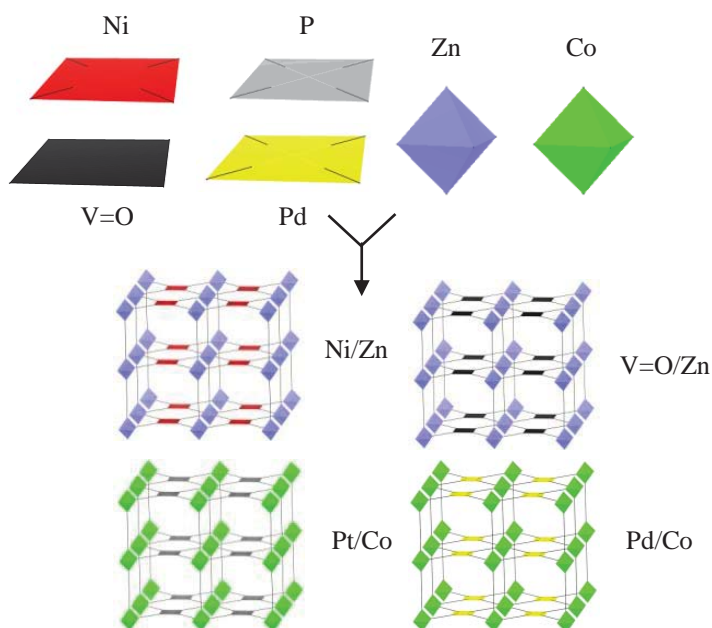


Figure 2.10. The **fsc** topology observed in the PPF-5 series: PPF-5-Ni/Zn, PPF-5-V=O/Zn, PPF-5-Pt/Co, and PPF-5-Pd/Co. The synthetic approach allows for the synthesis of topologically identical frameworks with various combinations of metal centers.²⁸

Although the control of 3D stacking pattern is demonstrated by the preferred coordination geometry of the porphyrin, as shown in the previous series of PPFs (PPF-3, -4, -5), the available metal centers are fully saturated by pillar molecules, leaving no accessible metal centers. One of the main goals in integrating porphyrins into MOFs is to incorporate coordinatively unsaturated, chemically active metal centers in the pores. In this respect, the topology needs to be constructed utilizing only the paddlewheel to paddlewheel connection (AA stacking), effectively “turning off” the governing effect of the coordination geometry of the porphyrin metal center. To achieve this topology with multiple porphyrin metals, our group chose a sterically hindered pillar.²⁷ When a methyl-substituted BPY pillar is used (Figure 2.11), probably due to the steric hindrance, the association constant of the pyridyl group to the metal center inside the porphyrin is drastically lowered. Thus the pillar preferentially coordinates to paddlewheel metal centers creating paddlewheel-to-paddlewheel connection solely.²⁷ The resulting framework, PPF-11, is topologically similar to the 3D AA pattern previously observed in PPF-5 series, being an **fsc** topology. The new isostructural members of the PPF-11 series include homometallic (*e.g.* PPF-11-Zn/Zn and PPF-11-Co/Co) and heterobimetallic (*e.g.* PPF-11-Mn/Zn and PPF-11-Fe/Zn) structures.²⁷ Especially the latter two PPFs contain potentially redox-active, accessible metal centers in MOFs. This approach is noteworthy because the pillar used in this PPF-11 series differentiates the two different metal centers and can be compared with site recognition found in biological systems such as restriction enzymes.^{27,38}

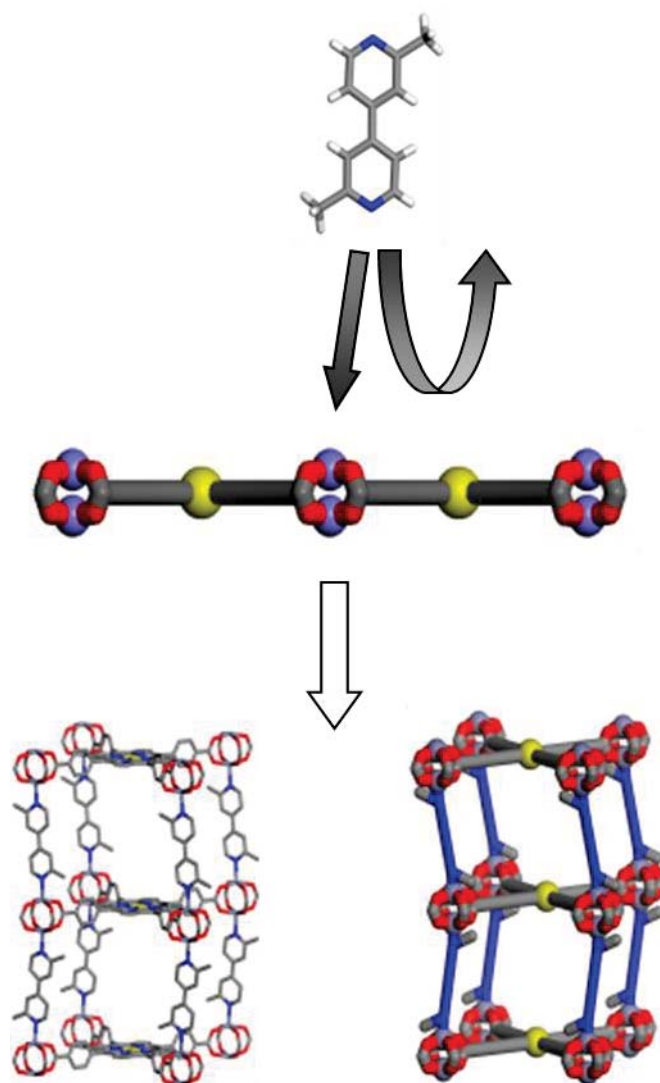


Figure 2.11. Formation of bioinspired MOFs, PPF-11 series. Sterically hindered linker 2,2'-dimethyl bipyridine recognizes metal centers in PPF-11 porphyrin framework series, yielding frameworks with accessible metal centers.²⁷

Further synthetic attempts to control not only the stacking arrangement but also the pore size have been explored using longer organic pillars (see **P2** and **P3**, Figure 2.5). By including these two pillars in the synthesis with Zn–**L1** and the Zn paddlewheel SBU two 3D ABBA structures, PPF-20 and PPF-22, were synthesized.²⁶ PPF-20 and PPF-22 have **fsx** topology and are isostructural with the previously discussed PPF-4, however, differ in the crystallographic *c* parameter (87.680(6) Å for PPF-20, 71.0521(18) Å for PPF-22 and 54.2436(14) Å for PPF-4) because of the longer pillars used in synthesis, creating larger pores within the structure (see Figure 2.12).²⁶

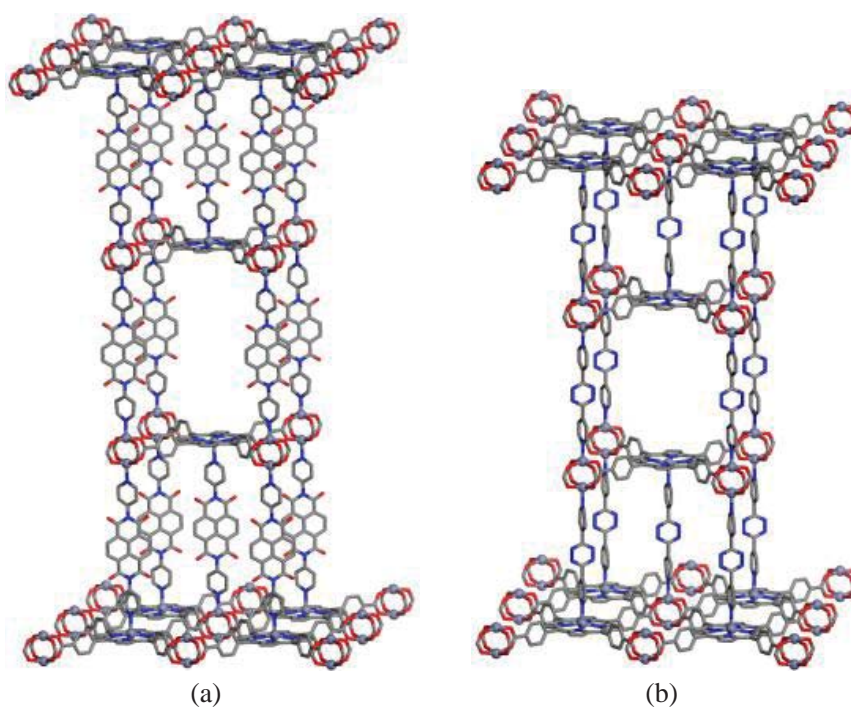


Figure 2.12. Single crystal structure of (a) PPF-20 and (b) PPF-22.²⁶

Two 2D–bilayer structures were also synthesized using a reduced amount of the longer pillars **P2** and **P3**.²⁶ The bilayer structures, PPF-18 and PPF-21, are isostructural and differ only in the intra–layer distance between the 2D porphyrinic sheets within the bilayers created by the different pillars (**P3** and **P2**, respectively) (Figure 2.13). This can be observed in the crystallographic *c* parameters (30.8966(6) Å for PPF-18 and 26.869(9) Å for PPF-21).²⁶ These structures are assembled by pillaring the Zn–**L1** to the axial site of the Zn paddlewheel in an AB fashion, fully saturating the Zn–**L1**. The remaining axial position of the paddlewheel is occupied by solvent, water. A fifth, AA interpenetrated structure, PPF-19, was also synthesized by incorporating **P3** in the synthesis.²⁶ This structure is of note, as it is the first example within PPFs of the stacking sequence being determined by interlayer distance and not by the preferred metal coordination geometry.²⁶

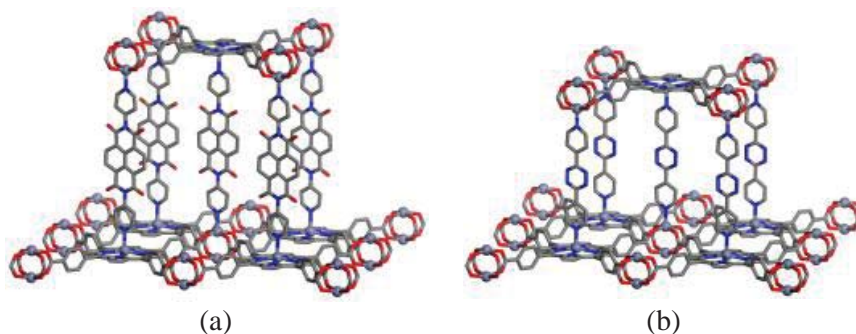


Figure 2.13. Single crystal structure of (a) PPF-18 and (b) PPF-21 bilayer structures.²⁶

In total, by using the metallated **L1** porphyrin linker, paddlewheel cluster, and dipyrindyl linkers, five different structure types have been successfully synthesized: 2D layer,²⁴ 2D bilayer,^{26,31} 3D AA,^{25,27,28} 3D ABBA,^{25,26} and 3D AB types.^{25,28} These five structure types are a part of a larger anticipated group of stacking sequences. By combining the four hypothetical layer interactions (porphyrin–porphyrin, porphyrin–paddlewheel, paddlewheel–paddlewheel, and non–pillared), a total of ten sequences are possible (Figure 2.14). We are currently investigating the synthesis of the additional five structure types.³⁹

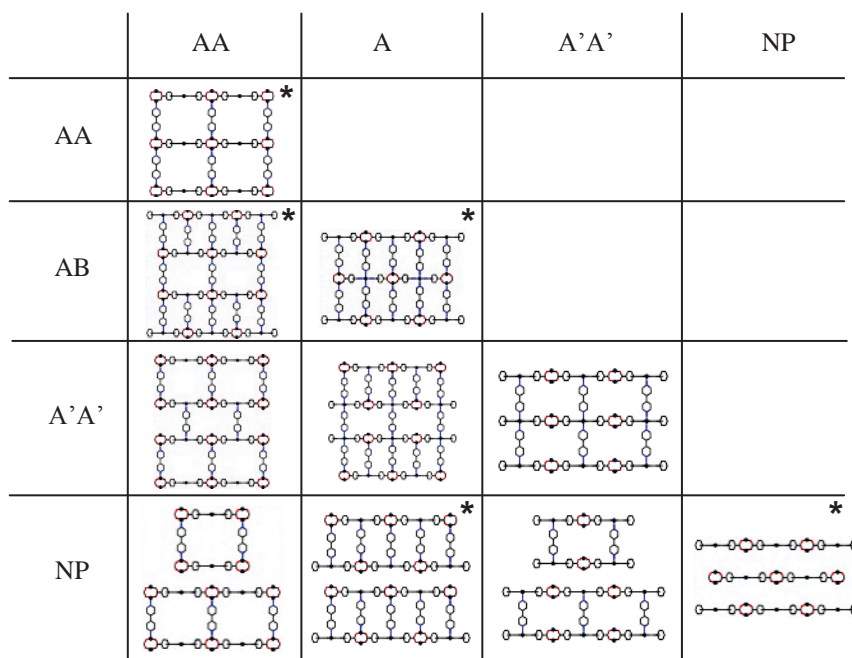


Figure 2.14. The ten possible stacking sequences from the combination of four separate layer to layer interactions: AA (paddlewheel–to–paddlewheel), AB (paddlewheel–to–porphyrin), A'A' (porphyrin–to–porphyrin), and NP (non–pillared). The patterns with * represent stackings in which single crystal structures have been obtained.

MOFs based on low-symmetry porphyrins have also been investigated. The low symmetry is induced by reducing the number of carboxylate groups around the porphyrin ring to two. The first porphyrin investigated was **L2** (See Figure 2.5) which adopts C_{2v} symmetry, compared to the D_{4h} found in **L1**. This change in symmetry leads to a new framework topology even when the same general assembly principles governing the assembly of **P1** are applied. PPF-6-Zn/Co was synthesized by a solvothermal reaction between Zn-**L2**, Co paddlewheel SBU, and **P1**.²⁹ PPF-6-Zn/Co adopts a CdI_2 -type **kgd** 2D topology (Figure 2.15).²⁹ This 2D layer is created by 1D porphyrin-paddlewheel tapes which are pillared heterogeneously (porphyrin-paddlewheel connection) by **P1**.²⁹ The **kgd** topology is relatively rare for MOF structures due to the unusual geometry of the three connected organic node with 90° angles.²⁹

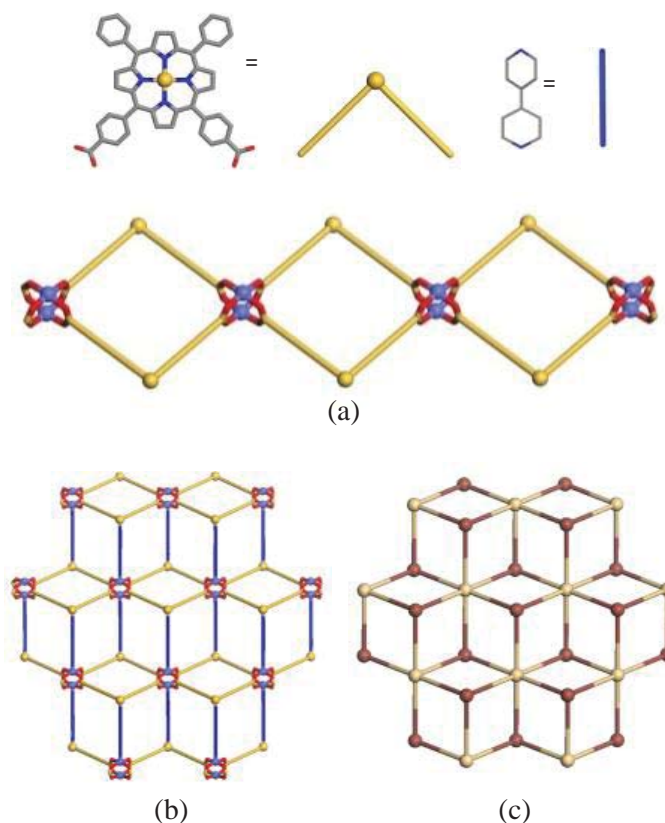


Figure 2.15. (a) 1D tape formed from *cis*-DCPP and paddlewheel SBU. The 2D layers found in (b) PPF-6 and (c) CdI_2 .²⁹

The second dicarboxy porphyrin, **L3**, adopts D_{2h} symmetry (see Figure 2.5). The assembly of Zn-**L3** and Zn paddlewheel SBU creates a 2D grid similar to that of PPF-1, however, half of the paddlewheel sites are missing due to the lack of carboxylate groups. The resulting 2D pattern is observed as a “defective” paddlewheel 2D layer.³⁰ The full assembly with **P1** pillar creates the structure PPF-25 which adopts an interesting (3,6) net with **ant** topology (Figure 2.16).³⁰ **P1** bonds heterogeneously between the porphyrin and paddlewheel of adjacent layers. Thus the paddlewheel SBU acts as a six-connecting octahedral node while the Zn-**L3** adopts a three-connecting T-shaped geometry linker when bonded to **P1**.³⁰ This T-shaped geometry is seldom seen in MOF structures, unlike the more frequently used Y-shaped linker. The difference in bonding geometry is crucial to obtain the **ant** topology over the similar (3,6) net **rtl** topology.³⁰ The **rtl** topology cannot accommodate a T-shaped linker, while the **ant** topology can be obtained through either T- or Y- shaped linkers.³⁰

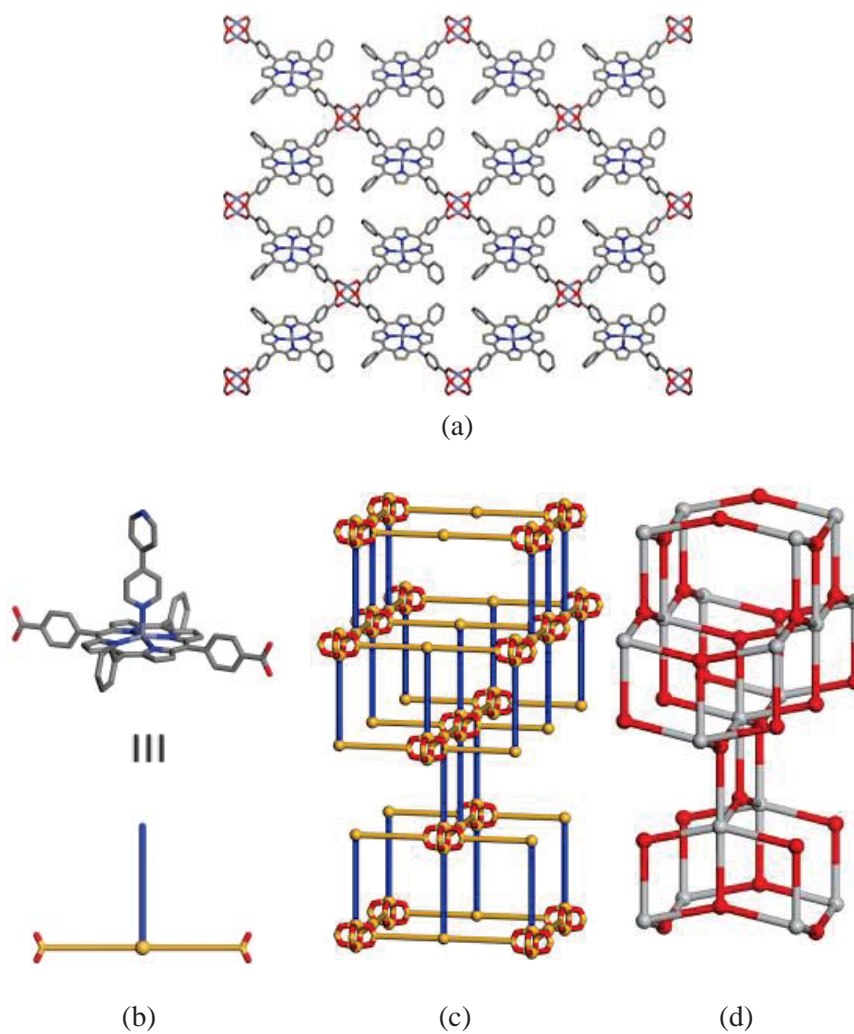


Figure 2.16. (a) Two-dimensional porphyrin paddlewheel grid assembled from Zn-L3 and Zn paddlewheel SBU. (b) T-shaped node formed by Zn-L3 and P1. (c) Crystal structure of PPF-25. (d) The parent anatase structure.³⁰

In total, we were able to build frameworks with five separate coordination geometries around the porphyrin (Figure 2.17). Many of these geometries are very rare for ligands used in MOFs. For example, the octahedral node found in the PPF-3 series (Figure 2.17a) is very difficult to achieve (but has also been observed by Robson using hexaimidazole species).⁴⁰ The square pyramidal geometry (Figure 2.17b) observed in the bilayer structures and the ABBA stacked 3D structures can be found in many Zn–porphyrin frameworks.⁴¹ The T-shaped connectivity (Figure 2.17d) found in PPF-25 by using **L3** is less popular than a Y-shaped ligand. This has recently been observed by Thuéry, Yao, and others.⁴² The three-legged piano stool geometry with angles of 90° (as seen in **L2**) (Figure 2.17e) is quite rare. This geometry is also achievable by using the C_3 –tri-(4-carboxyphenyl)–tri-methoxycyclo-benzylene ligand, as recently observed by the Zheng group.⁴³ All of these geometries are available by using the porphyrin metalloligand in our synthetic design.

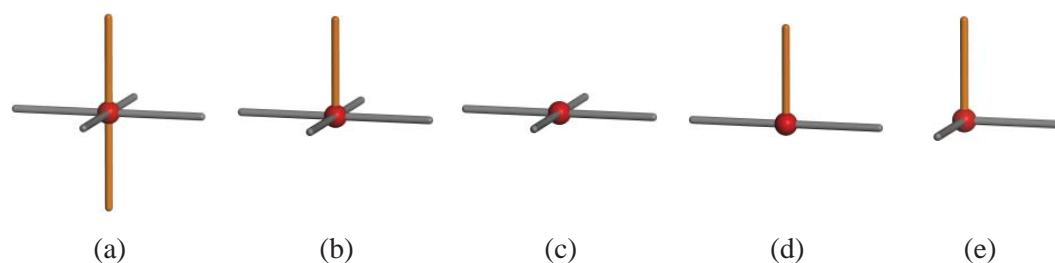


Figure 2.17. Various coordination geometries found in a porphyrin linker during mixed linker PPF assembly. (a) Octahedral (found in PPF-3), (b) square pyramidal (found in PPF-4), (c) square planar (found in PPF-5), (d) T-shaped (found in PPF-25), and (e) three legged, “piano stool” (found in PPF-6) geometries. Orange connection represents a connection to a pillaring ligand.

Pore surface engineering using the porphyrin building blocks provides new insights into framework topology and MOF applications. Through systematic pore surface engineering, a series of porphyrinic MOFs have been synthesized with surfaces decorated with various metal centers and different pore sizes/shapes. Using porphyrin metalloligands in MOFs creates many new and exciting possible applications in MOF chemistry. We expect that this bioinspired material platform will serve as a central component for energy, sensory, and green applications.

2.7 References

- (1) (a) Wang, X. -S.; Meng, L.; Cheng, Q.; Kim, C.; Wojtas, L.; Chrzanowski, M.; Chen, Y. -S.; Zhang, X. P.; Ma, S. *J. Am. Chem. Soc.* **2011**, *133*, 16322. (b) Wang, X. -S.; Chrzanowski, M.; Kim, C.; Gao, W. -Y.; Wojtas, L.; Chen, Y. -S.; Zhang, X. P.; Ma, S. *Chem. Commun.* **2012**, *48*, 7173.
- (2) Farha, O. K.; Shultz, A. M.; Sarjeant, A. A.; Nguyen, S. T.; Hupp, J. T. *J. Am. Chem. Soc.* **2011**, *133*, 5652.
- (3) Suslick, K. S.; Bhyrappa, P.; Chou, J. -H.; Kosel, m. E.; Nakagaki, S.; Smithenry, D. W.; Wilson, S. R. *Acc. Chem. Res.* **2005**, *38*, 283.
- (4) Lee, S. J.; Hupp, J. T. *Coord. Chem. Rev.* **2006**, *250*, 1710.
- (5) Kitagawa, S.; Noro, S.; Nakamura, T. *Chem. Commun.* **2006**, *42*,701.
- (6) (a) Ma, S.; Zhou, H. -C. *J. Am. Chem. Soc.* **2006**, *128*, 11734. (b) Chen, B.; Xiang, S.; Qian, G. *Acc. Chem. Res.* **2010**, *43*, 1115. (c) Seo, j. S.; Whang, D.; Lee, H.; Jun, S. I.; Oh, J.; Jeon, Y. J.; Kim, K. *Nature* **2000**, *404*, 982. (d) Tonigold, M.; Lu, Y.; Bredenkötter, B.; Rieger, B.; Bahnmüller, S.; Hitzbleck, J.; Langstein, G.; Volkmer, D. *Angew. Chem. Int. Ed.* **2009**, *48*, 7546. (e) Jiang, D.; Urakawa, A.; Yulikov, M.; Mallat,

- T.; Jeschke, G.; Baiker, A. *Chem. Eur. J.* **2009**, *15*, 12255. (f) Hong, S. J.; Ryu, J. Y.; Lee, J. Y.; Kim, C.; Kim, S. -J.; Kim, Y. *Dalton Trans.* **2004**, 2697.
- (7) (a) Noro, S. -I.; Miyasaka, H.; Kitagawa, S.; Wada, T.; Okubo, T.; Yamashita, M.; Mitani, T. *Inorg. Chem.* **2005**, *44*, 133. (b) Kitagawa, S.; Kitaura, R.; Noro, S. -I. *Angew. Chem. Int. Ed.* **2004**, *43*, 2334. (c) Garibay, S. J.; Stork, J. R.; Cohen, S. M. *Prog. Inorg. Chem.* **2009**, *56*, 335.
- (8) (a) Noro, S. -I.; Kitagawa, S.; Yamashita, M.; Wada, T. *Chem. Commun.* **2002**, 38, 222. (b) Noro, S. -I.; Kitagawa, S.; Yamashita, M.; Wada, T. *CrystEngComm* **2002**, *4*, 162. (c) Chen, C. -L.; Goforth, A. M.; Smith, M. D.; Su, C. -Y.; zur Loye, H. -C. *Angew. Chem. Int. Ed.* **2005**, *44*, 6673. (d) Ciurtin, D. M.; Smith, M. D.; zur Loye, H. -C. *Dalton Trans.* **2003**, 32, 1245. (e) Chapman, C. T.; Ciurtin, D. M.; Smith, M. D.; zur Loye, H. -C. *Solid State Sci.* **2002**, *4*, 1187. (f) Ciurtin, D. M.; Smith, M. D.; zur Loye, H. -C. *Chem. Commun.* **2002**, 38, 74. (g) Ciurtin, D. M.; Smith, M. D.; zur Loye, H. -C. *Solid State Sci.* **2002**, *4*, 461. (h) Dong, Y. -B.; Smith, M. D.; zur Loye, H. -C. *Angew. Chem. Int. Ed.* **2000**, *39*, 4271. (i) Dong, Y. -B.; Smith, M. D.; zur Loye, H. -C. *J. Solid State Chem.* **2000**, *2*, 335. (j) Dong, Y. -B.; Smith, M. D.; zur Loye, H. -C. *Inorg. Chem.* **2000**, *39*, 1943. (k) Biswas, C.; Mukherjee, P.; Drew, M. G. B.; Gómez-García C. J.; Clemente-Juan, J. M.; Ghosh, A. *Inorg. Chem.* **2007**, *46*, 10771.
- (9) (a) Zhang, Y.; Chen, B.; Fronczek, F. R.; Maverick, A. W. *Inorg. Chem.* **2008**, *47*, 4433. (b) Chen, B.; Fronczek, F. R.; Maverick, A. W. *Inorg. Chem.* **2004**, *43*, 8209. (c) Vreshch, V. D.; Lysenko, A. B.; Chernega, A. N.; Howard, J. A. K.; Sieler, J.; Domasevitch, K. V. *Dalton Trans.* **2003**, 32, 1707.

- (10) (a) Stork, J. R.; Thoi, V. S.; Cohen, S. M. *Inorg. Chem.* **2007**, *46*, 11213. (b) Garibay, S. j.; Stork, J. R.; Wang, Z.; Cohen, S. M.; Telfer, S. G. *Chem. Commun.* **2007**, *43*, 4881. (c) Halper, S. R.; Do, L.; Stork, J. R.; Cohen, S. M. *J. Am. Chem. Soc.* **2006**, *128*, 15255. (d) Halper, S. R.; Cohen, S. M. *Inorg. Chem.* **2005**, *44*, 486. (e) Murphy, D. L.; Malachowski, M. R.; Campana, C. F.; Cohen, S. M. *Chem. Commun.* **2005**, *41*, 5506.
- (11) (a) Cho, S. -H.; Ma, B.; Nguyen, S. T.; Hupp, J. T.; Albrecht-Schmitt, T. E. *Chem. Commun.* **2006**, *42*, 2563. (b) Chen, B.; Zhao, X.; Putkham, A.; Hong, K.; Lobkovsky, E. B.; Hurtado, E. J.; Fletcher, A. J.; Thomas, K. M. *J. Am. Chem. Soc.* **2008**, *130*, 6411. (c) Kitaura, R.; Onoyama, G.; Sakamoto, H.; Matsuda, R.; Noro, S. -I.; Kitagawa, S. *Angew. Chem. Int. Ed.* **2004**, *43*, 2684. (d) Clérac, R.; Miyasaka, H.; Yamashita, M.; Coulon, C. *J. Am. Chem. Soc.* **2002**, *124*, 12837.
- (12) (a) Szeto, K. C.; Kongshuag, K. O.; Jakobsen, S.; Tilset, M.; Lillerud, K. P. *Dalton Trans.* **2008**, 2054. (b) Szeto, K. C.; Prestipino, C.; Lamberti, C.; Zecchina, A.; Bordiga, S.; Bjørgen, m.; Tilset, M.; Lillerud, K. P. *Chem. Mater.* **2007**, *19*, 211. (c) Szeto, K. C.; Lillerud, K. P.; Tilset, M.; Bjørgen, M.; Prestipino, C.; Zecchina, A.; Lamberti, C.; Bordiga, S. *J. Phys. Chem. B* **2006**, *110*, 21509.
- (13) (a) Burrows, A. D.; Mahon, M. F.; Wong, C. T. F. *CrystEngComm* **2008**, *10*, 487. (b) Hafizovic, J.; Krivokapic, A.; Szeto, K. C.; Jakobsen, S.; Lillerud, K. P.; Olsbye, U.; Tilset, M. *Cryst. Growth Des.* **2007**, *7*, 2302.
- (14) (a) Horikoshi, R.; Mochida, T.; Moriyama, H. *Inorg. Chem.* **2002**, *41*, 3017. (b) Dong, G.; Bing-guang, Z.; Chun-ying, D.; Zin, C.; Qing-jin, M. *Dalton Trans.* **2003**, *32*, 282.

- (15) For porphyrin framework reviews, see: (a) Smitherly, D. W.; Suslick, K. S. *J. Porphyrins Phthalocyanines* **2004**, *8*, 182. (b) Goldberg, I. *CrystEngComm* **2008**, *10*, 637. (c) DeVries, L. D.; Choe, W. *J. Chem. Crystallogr.* **2009**, *39*, 299.
- (16) Abrahams, B. F.; Hoskins, B. F.; Robson, R. *J. Am. Chem. Soc.* **1991**, *113*, 3606.
- (17) Abrahams, B. F.; Hoskins, B. F.; Michail, D. M.; Robson, R. *Nature* **1994**, *369*, 727.
- (18) Krupitsky, H.; Stein, Z.; Goldberg, I.; Strouse, C. E. *J. Incl. Phenom. Mol. Rec. Chem.* **1994**, *18*, 177.
- (19) (a) Shmilovits, M.; Vinodu, M.; Goldberg, *Cryst. Growth Des.* **2004**, *4*, 633. (b) Shmilovits, M.; Diskin-Posner, Y.; Vinodu, M.; Goldberg, I. *Cryst. Growth Des.* **2003**, *3*, 855. (c) Diskin-Posner, Y.; Dahal, S.; Goldberg, I. *Angew. Chem. Int. Ed.* **2000**, *39*, 1288.
- (20) Kosal, M. E.; Chou, J. -H.; Wilson, S. R.; Suslick, K. S. *Nat. Mater.* **2002**, *1*, 118.
- (21) Smitherly, D. W.; Wilson, S. R.; Suslick, K. S. *Inorg. Chem.* **2003**, *42*, 7719.
- (22) Suslick, K. S.; Bhyrappa, P.; Chou, J. -H.; Kosal, M. E.; Nakagaki, S.; Smitherly, D. W.; Wilson, S. R. *Acc. Chem. Res.* **2005**, *38*, 283.
- (23) Pan, I.; Kelly, S.; Huang, X.; Li, J. *Chem. Commun.* **2002**, *38*, 2334.
- (24) Choi, E. -Y.; Wray, C. A.; Hu, C.; Choe, W. *CrystEngComm* **2009**, *11*, 553.
- (25) Choi, E. -Y.; Barron, P. M.; Novotny, R. W.; Son, H. -T.; Hu, C.; Choe, W. *Inorg. Chem.* **2009**, *48*, 426.
- (26) Chung, H.; Barron, P. M.; Novotny, R. W.; Son, H. -T.; Hu, C.; Choe, W. *Cryst. Growth Des.* **2009**, *9*, 3327.
- (27) Barron, P. M.; Wray, C. A.; Hu, C.; Guo, Z.; Choe, W. *Inorg. Chem.* **2010**, *49*, 10217.

- (28) Barron, P. M.; Son, H. -T.; Hu, C.; Choe, W. *Cryst. Growth Des.* **2009**, *9*, 1960.
- (29) Choi, E. -Y.; Barron, P. M.; Novotny, R. W.; Hu, C.; Kwon, Y. -U.; Choe, W. *CrystEngComm* **2008**, *10*, 824.
- (30) Verduzco, J. M.; Chung, H.; Hu, C.; Choe, W. *Inorg. Chem.* **2009**, *48*, 9060.
- (31) Burnett, B. J.; Barron, P. M.; Hu, C.; Choe, W. *J. Am. Chem. Soc.* **2011**, *133*, 9984.
- (32) Shultz, A. M.; Farha, O. K.; Hupp, J. T.; Nguyen, S. T. *J. Am. Chem. Soc.* **2009**, *131*, 4204.
- (33) Lee, C. Y.; Farha, O. K.; Hong, B. J.; Sarjeant, A. A.; Nguyen, S. T.; Hupp, J. T. *J. Am. Chem. Soc.* **2011**, *133*, 15858.
- (34) Ohmura, T.; Usuki, A.; Fukumori, K.; Ohta, T.; Ito, M.; Tatsumi, K. *Inorg. Chem.* **2006**, *45*, 7988.
- (35)(a) Fateeva, A.; Devautour-Vinot, S.; Heymans, N.; Devic, T.; Grenèche, J. -M.; Wuttke, S.; Miller, S.; Lago, A.; Serre, C.; De Weireld, G.; Maurin, G.; Vimont, A.; Férey, G. *Chem. Mater.* **2011**, *23*, 4641. (b) Kempe, R. *Z. Anorg. Allg. Chem.* **2005**, *631*, 1038. (c) Hagrman, D.; Hagrman, P. J.; Zubieta, J. *Angew. Chem. Int. Ed.* **1999**, *38*, 3165. (d) Carlucci, L.; Ciani, G.; Proserpio, D. M.; Porta, F. *CrystEngComm* **2005**, *7*, 78. (e) Krishnamohan Sharma, C. V.; Broker, G. A.; Huddleston, J. G.; Baldwin, J. w.; Metzger, R. M.; Rogers, R. D. *J. Am. Chem. Soc.* **1999**, *121*, 1137.
- (36) Li, K.; Huang, G.; Xu, Z.; Zhang, M.; Zeller, M.; Hunter, A. D.; Chui, S. S. -Y.; Che, C. -M.; Wong, W. -Y. *Inorg. Chem.* **2007**, *46*, 4844.
- (37) Sanders, J. K. M. *et al.*; in *The Porphyrin Handbook*; Kadish, k. M.; Smith, K. M.; Guillard, R.; Eds.; Academic Press, San Diego, CA, **2000**, Vol.3, pp. 1-48.

(38) (a) Nelson, M.; Raschke, E.; McClelland, M.; *Nucleic Acids Res.* **1993**, *21*, 3139. (b) Wilson, G. G.; Murray, N. E. *Annu. Rev. Gener.* **1991**, *25*, 585. (c) Kobayashi, I. *Nucleic Acids Res.* **2001**, *29*, 3742. (d) Tock, M. R.; Dryden, D. T. F. *Curr. Opin. Microbiol.* **2005**, *8*, 466.

(39) While we have not been able to achieve the A'A' connection, this connection has been observed previously by Goldberg and coworkers. See ref.19.

(40) Robson, R. *Dalton Trans.* **2000**, 3735.

(41) (a) Fletcher, A. J.; Cussen, E. J.; Bradshaw, D.; Rosseinsky, M. J.; *J. Am. Chem. Soc.* **2004**, *126*, 9750. (b) Zheng, N. F.; Bu, X. H.; Feng, P. Y. *J. Am. Chem. Soc.* **2002**, *124*, 9688. (c) Choe, W.; Kiang, Y. -H.; Xu, Z.; Lee, S. *Chem. Mater.* **1999**, *11*, 1776. (d) Carlucci, L.; Ciani, G.; Prosperpio, D. M.; Porta, F. *CrystEngComm* **2005**, *7*, 78. (e) Lee, S. J.; Hupp, J. T. *Coord. Chem. Rev.* **2006**, *250*, 1710.

(42) (a) Thuéry, P.; Masci, B.; *CrystEngComm*, **2012**, *14*, 131. (b) Zhang, X.; Yang, J. -X.; Zhang, J.; Cheng, J. -K.; Sun, M. -L.; Yao, Y. -G. *Inorg. Chem. Commun.* **2011**, *14*, 986. (c) Li, Z. -X.; Chu, X.; Cui, G. -H.; Liu, Y.; Li, L.; Xue, G. -L. *CrystEngComm* **2011**, *13*, 1984. (d) Chen, S. -M.; Lian, T. -T. *Inorg. Chem. Commun.* **2010**, *13*, 1380.

(43) Yu, J. -T.; Sun, J.; Huang, Z. -T.; Zheng, Q. -Y. *CrystEngComm* **2012**, *14*, 112.

CHAPTER 3

SEQUENTIAL SELF-ASSEMBLY IN PORPHYRIN PADDLEWHEEL FRAMEWORKS: LINKER REPLACEMENT

3.1 Introduction

Coordination-driven self-assembly has become an indispensable synthetic approach for inorganic materials chemists to produce compounds with topologies and functions that were only imaginable a few decades ago.¹ Recent notable examples of the coordination-driven self-assembled systems include inorganic-organic hybrid materials called metal-organic frameworks (MOFs) or porous coordination polymers.^{2,3} A conventional “one-pot” self-assembly strategy *via* solvothermal reactions has been remarkably successful, creating many rationally synthesized MOFs through careful selection of organic linkers and SBUs.³⁻⁵

As a continuing effort to further improve the synthesis of MOFs to obtain highly functionalized and topologically interesting structures, we and others are exploring new methods for modifying MOFs post-crystallization. One such approach involves altering the functional group in the organic linker after the initial reaction while keeping the same framework topology. This post-synthetic modification (PSM) approach, later coined by Cohen,⁶ was first conceived by Hoskins and Robson⁷ and demonstrated a decade later by Lee and co-workers,⁸ who treated an alcohol functional group with the linker trifluoroacetic anhydride to form an ester. Recently, the groups of Cohen, Yaghi, and

many others have decorated the pore surfaces of MOFs for applications including catalysis and superhydrophobicity.⁹

An interesting new approach is a sequential self-assembly (SSA) method. SSA is a multi-step synthetic process, first synthesizing a self-assembled system, and then using it as a starting template for the subsequent *self-assembly* steps.^{10,11} Analogous multistep syntheses in discrete molecular systems have been routinely utilized in organic chemistry, as exemplified by the total synthesis of natural products to create highly complex biomolecules from simple starting materials.¹² In contrast, SSA demonstrated in multi-dimensional organizations (*i.e.* 2D and 3D MOFs) is exceptionally rare.¹³⁻¹⁷ This chapter focusses on the specific use of SSA for the replacement of organic linkers in MOFs.

The concept of linker replacement has been widely used in discrete organometallic species, but is still new to MOF synthesis. In this process, one structural multi-topic linker is replaced by a dissimilar structural multi-topic linker, retaining the dimensionality of the structure, but changing either the pore size or structure (Figure 3.1). Previously, it was assumed that organic linkers cannot be altered in insoluble, extended solids like MOFs.¹⁸ However, examples provided herein are rather surprising by showing that a replacement is indeed possible even in insoluble crystalline MOFs. The M-L coordination bond, while being strong enough for structural stability, is weak enough that they can be broken under the correct conditions facilitating this transformation.¹⁵

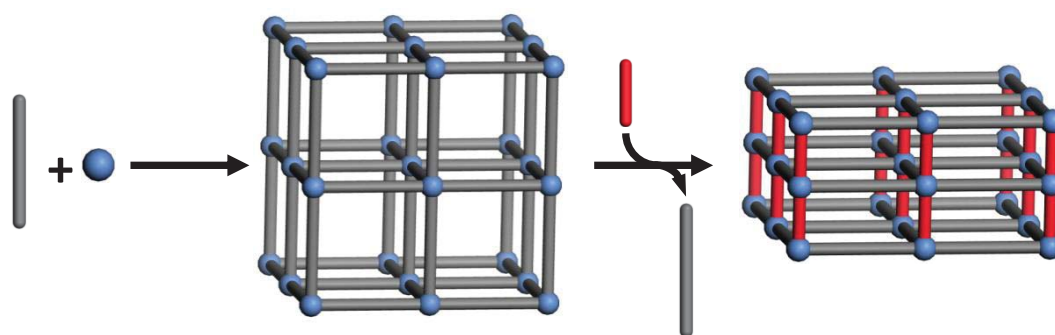


Figure 3.1. Schematic illustration of the replacement of structural organic linkers in SSA.

Examples in the literature of linker replacement include a report from Cohen *et al.* which detailed a replacement in a 3D MOF using dicarboxylate linkers coordinated with a Zr (IV) based metal node.¹⁵ This transformation is quite surprising because of the strong Zr–O coordination bond. The combination of BDC with zirconium chloride created the porous structure UiO-66. Incubating UiO-66 in a solution containing N₃–, OH–, or 2,5–(OH)₂– functionalized BDC linkers resulted in the partial transformation to UiO-66-N₃, UiO-66-OH, and UiO-66-2,5-(OH)₂, respectively. Multilinker structures were also obtained by combining 2–bromo–1,4–dicarboxylate constructed UiO-66-Br with BDC. The temperature at which this replacement took place directly affected the percentage of transformation.

Hupp *et al.* recently reported using this SSA approach to replace Zn–metalloporphyrin–based pillars in the pillared paddlewheel structure ZnZn-RPM (RPM stands for Robust Porphyrinic Material) with a series of other porphyrin based pillars including unmetallated porphyrin, Al–metalloporphyrin, and Sn–metalloporphyrin with retention of crystallinity.¹⁶ They found however, that the replacement did not go to completion, leaving a mixed pillared compound. Only 43-51% replacement was confirmed by ¹H NMR and inductively coupled plasma–optical emission spectroscopy experiments. While the replacement didn't go to completion, the new RPMs were used to examine the catalytic activity for an epoxide ring–opening reaction. The catalytic activity was shown to depend strongly on the identity of the metal ion present in the metalloporphyrin-based pillar. The Al-metalloporphyrin showed 60% conversion, while the other metals ranged from <1– 6% conversion.

Zhou and coworkers reported the replacement of linkers within metal–organic polyhedra (MOPs) to create an isorecticular series of soluble, paddlewheel based MOPs with various pore sizes, shapes, and functionalities.¹⁷ In this series, the copper paddlewheel–dicarboxylate bond is broken and a new bond is formed with the replacing linker. Both partial and full conversion from MOP structure to MOP structure was possible.

In this chapter, we report two examples of replacement reactions of structure-building linkers in 2D and 3D MOF systems that result in single–crystal to single–crystal transformations. To our knowledge, these are the first examples of linker–replacement reactions in multidimensional MOFs. Additionally, we report a 2D to 3D transformation that occurs via a linker–insertion mechanism upon the introduction of excess linkers.

3.2 Experimental Methods

PPF-18 A mixture of 5,10,15,20-tetrakis(4-carboxyphenyl)-21*H*,23*H*-porphyrin (TCPP)(7.9 mg, 0.01 mmol), zinc nitrate hexahydrate (8.9 mg, 0.03), *N,N'*-di-(4-pyridyl)-1,4,5,8-naphthalenetetracarboxydiimide (DPNI) (4.2 mg, 0.01 mmol), and 1.0 M nitric acid in ethanol (50 μ L, 0.05 mmol) were added to a mixture of *N,N*-diethyl formamide (DEF) (1.5 mL) and ethanol (0.5 mL) in a capped vial and heated to 80 °C for 24 hrs, followed by slow-cooling to room temperature over 9 hrs. Yield: 12.1 mg (79% based on porphyrin). Anal. Calcd. for [C₇₂H₃₆N₈O₁₂Zn₃] 3.6 DEF · 0.5 H₂O · 3.0 ethanol: C, 59.0; H, 4.9; N, 9.0%. Found: C, 59.0; H, 4.9; N, 9.0%.

PPF-19 A mixture of TCPP (7.9 mg, 0.01 mmol), zinc nitrate hexahydrate (8.9 mg, 0.03), DPNI (8.4 mg, 0.02 mmol), and 1.0 M nitric acid in ethanol (30 μ L, 0.03 mmol) were added to a mixture of *N,N*-dimethyl formamide (DMF) (0.8 mL) and ethanol (1.2 mL) in a capped vial and heated to 80 °C for 24 hrs, followed by slow-cooling to room temperature over 9 hrs.

PPF-20 A mixture of TCPP (7.9 mg, 0.01 mmol), zinc nitrate hexahydrate (8.9 mg, 0.03), DPNI (16.8 mg, 0.04 mmol), and 1.0 M nitric acid in ethanol (30 μ L, 0.03 mmol) were added to a mixture of DMF (1.5 mL) and ethanol (0.5 mL) in a capped vial and heated to 80 °C for 24 hrs, followed by slow-cooling to room temperature over 9 hrs. Yield: 15.1 mg (76% based on porphyrin). Anal. Calcd. for [C₈₄H₄₂N₁₀O₁₄Zn₃] 3.0 DMF · 2.0 H₂O · ethanol: C, 60.7; H, 4.3; N, 9.1%. Found: C, 61.1; H, 4.4; N, 9.2%.

PPF-27 from PPF-18 A mixture of filtered crystals of PPF-18* (20.0 mg, 0.01 mmol) and 4,4'-bipyridine (BPY) (3.2 mg, 0.02 mmol) were added to a mixture of DEF (1.5 mL) and ethanol (0.5 mL) in a capped vial, swirled by hand to mix, and left to react at

room temperature typically for ~3hrs. Yield: 14.0 mg (93% based on porphyrin). Anal. Calcd. for $[\text{C}_{58}\text{H}_{32}\text{N}_6\text{O}_8\text{Zn}_3] \cdot 2.5 \text{ DEF} \cdot 2 \text{ H}_2\text{O} \cdot 0.5 \text{ ethanol} \cdot 0.5 \text{ BPY}$: C, 59.3; H, 4.6; N, 9.5% Found: C, 59.3; H, 4.5; N, 9.5%.

PPF-4 from PPF-18 A mixture of filtered crystals of PPF-18* (20.0 mg, 0.01 mmol) and BPY (8.0 mg, 0.05 mmol) were added to a mixture of DEF (1.5 mL) and ethanol (0.5 mL) in a capped vial, swirled by hand to mix, and left to react at room temperature typically for ~3hrs.

PPF-4 from PPF-20 A mixture of filtered crystals of PPF-20* (19.9 mg, 0.01 mmol) and BPY (6.4 mg, 0.04 mmol) were added to a mixture of DEF (1.5 mL) and ethanol (0.5 mL) in a capped vial, swirled by hand to mix, and left to react at room temperature typically for ~3hrs. Yield: 13.7 mg (97% based on porphyrin). Anal. Calcd. for $[\text{C}_{63}\text{H}_{36}\text{N}_7\text{O}_8\text{Zn}_3] \cdot 2 \text{ DEF} \cdot 2 \text{ H}_2\text{O} \cdot 0.5 \text{ ethanol}$: C, 60.2; H, 4.4; N, 8.5% Found: C, 60.1; H, 4.6; N, 8.4%

* During the pillar replacement reactions, crystals of the synthesized parent structure were filtered and washed with DEF before introducing them into the BPY solution to promote pillar replacement and hinder epitaxial growth.

Single crystal structure determination:

Plate-shaped crystals of PPF-27 (120 μm x 120 μm) were sealed in a capillary for XRD measurement. Geometry and intensity data were obtained at room temperature with a Bruker SMART Apex CCD area detector diffractometer. Preliminary lattice parameters and orientation matrices were obtained from three sets of frames. Data were collected using graphite-monochromated and MonoCap-collimated Mo-K α radiation ($\lambda = 0.71073$ Å) with ω scan method.¹⁹ Data was processed with the SAINT+ program²⁰ for reduction

and cell refinement. Multi-scan absorption corrections were applied to the data set using the SADABS program for area detector.²¹ The structure was solved by direct method and refined using SHELXTL.²² Disordered, independent solvent molecules inside the frameworks were eliminated in the refinement by PLATON/SQUEEZE.²³ All atoms were refined with anisotropic displacement parameters.

X-ray powder diffraction (PXRD):

Because the PPF crystals have platelet morphology, the PXRD spectra show significant preferred orientation when mounted onto a traditional flat stage. The relative intensities in the diffraction peaks thus deviate significantly to the simulated PXRD spectra which assume perfectly random orientations of the crystals. To overcome these deviations in intensity, we followed a method developed by Farha in which crystals are mounted in a sealed capillary tube, and PXRD was performed while the tube was spinning to remove the preferential orientation.²⁴ Both traditional flat stage and spinning capillary spectra are included. Traditional flat stage X-ray diffraction data were taken with a Rigaku D/Max-B X-ray diffractometer with Bragg-Brentano parafocusing geometry, a diffracted beam monochromator, and a conventional copper target X-ray tube set to 40 KV and 30 mA. Spinning capillary X-ray diffraction data were taken with a Bruker AXS DA X-ray diffractometer with a GADDS area detector and a conventional copper target X-ray tube set to 40 KV and 40 mA. Crystals were mounted in a 0.5 mm quartz capillary tube with a drop of mother liquor and sealed with epoxy. The X-ray diffraction data were collected with an area detector exposed for 10 minutes as rotation frames over 360° in ϕ , a χ angle of 54.74° , and at 2θ values of 21° and 25° . The resulting experimental PXRD patterns were treated for amorphous background scatter and

collected into a single pattern, then compared to simulated patterns obtained from the single crystal structures using Mercury software.²⁵ The program Unit Cell was used to generate the cell parameters of the experimental data.²⁶

Thermogravimetric analysis:

Performed on a Perkin Elmer STA 6000 thermogravimetric analyzer, heated from 25 °C to 800 °C at a rate of 10 °C/minute under N₂ atmosphere.

Elemental analysis:

Data was performed by MidwestMicro Labs LLC.

UV/Vis analysis:

Data was recorded on a Shimadzu UV-2401PC spectrophotometer.

¹H NMR analysis:

Performed on a Bruker FT-NMR spectrometer (400 MHz).

Conolly surface models:

Calculated using Materials Studio software.²⁷

Single-crystal to single-crystal study:

To confirm the solid to solid mechanism proposed, a series of single-crystal to single-crystal experiments were performed following the established method reported by Suh.²⁸ Single crystals of PPF-18 and PPF-20 were mounted inside of a 0.3 mm capillary tube with a drop of mother liquor. After photographs of single crystal PPF-18 and PPF-20 crystals were taken and the unit cell parameters measured, the mother liquor was drawn out of the capillary tube and a BPY solution was introduced into the capillary tube containing the single crystal samples and allowed to react overnight. Photographs and the unit cell parameters of the resulting single crystal structures were then obtained.

Reaction kinetics study:

To observe the reaction proceed, multiple UV/Vis spectra were taken of the reaction solution at different times during the reaction showing DPNI molecules coming out from the framework into solution. Fresh crystals of PPF-20 (7.0 mg, 0.0035 mmol) were introduced into 2 mL 3:1 DEF/ethanol mixture containing BPY (1.56 mg, 0.01 mmol) and stirred constantly by a nutator for various periods of time. After the designated time period, the solution was quickly separated from the crystals to stop any extra reaction from happening. The solution was then diluted for UV/Vis spectroscopy. Blank samples were prepared identically with no BPY in solution to induce the transformation. The UV/Vis spectra of blank sample were subtracted from the sample spectra to give the reported spectra. Absorbance spectra were obtained from standard solutions of DPNI and used to make calibration curves at 360 nm and 380 nm. Absorbance spectra were obtained from standard solutions of ZnTCPP and used to make a calibration curve at 427 nm.

Acid Digestion Study:

In order to observe if there was any residual DPNI linker left inside of the pores of the daughter structures, samples of the daughter structures were digested in acid according the method reported by Cohen.²⁹ Approximately 5 mg of sample was filtered and washed ≥ 3 times with DMF and dried under vacuum at 90 °C overnight and digested with sonication in 500 μL of $\text{DMSO-}d_6$ and 100 μL of dilute DCI (10 μL of 35% DCI in D_2O diluted with 500 μL of $\text{DMSO-}d_6$). ^1H NMR and UV/Vis spectra were obtained from the resulting solution.

3.3 Results and Discussion

In this initial investigation into linker replacement transformation, pillared paddlewheel frameworks were speculated to be suitable candidates because the axial metal–nitrogen bonds are relatively weaker than the metal–oxygen bonds in this class of frameworks.³⁰ Thus, selective replacement of the bipyridyl pillars could be achieved without the destruction of the 2D porphyrin paddlewheel layers. To demonstrate the linker replacement, two PPF structures, 2D PPF-18 and 3D PPF-20, were synthesized as ‘parent’ structures.

PPF-18 and PPF-20 were synthesized via a solvothermal reaction following the published method³¹ and confirmed by PXRD (Figures 3.2 and 3.3). Solvothermal synthesis was selected because it is faster and easily reproducible compared to other crystallization techniques, such as diffusion or evaporation. PPF-18 is a 2D bilayer structure in which the porphyrin paddlewheel layers are stacked in an AB fashion, creating $P4/nmm$ symmetry (Figure 3.2).³¹ The zinc atoms in the porphyrin cores are pentacoordinated, whereas the $Zn_2(COO)_4$ paddlewheels are axially coordinated by solvent molecules between the bilayers. PPF-20 is a 3D structure in which the porphyrin paddlewheel layers are stacked in an ABBA fashion, creating $I4/mmm$ symmetry (Figure 3.3).³¹

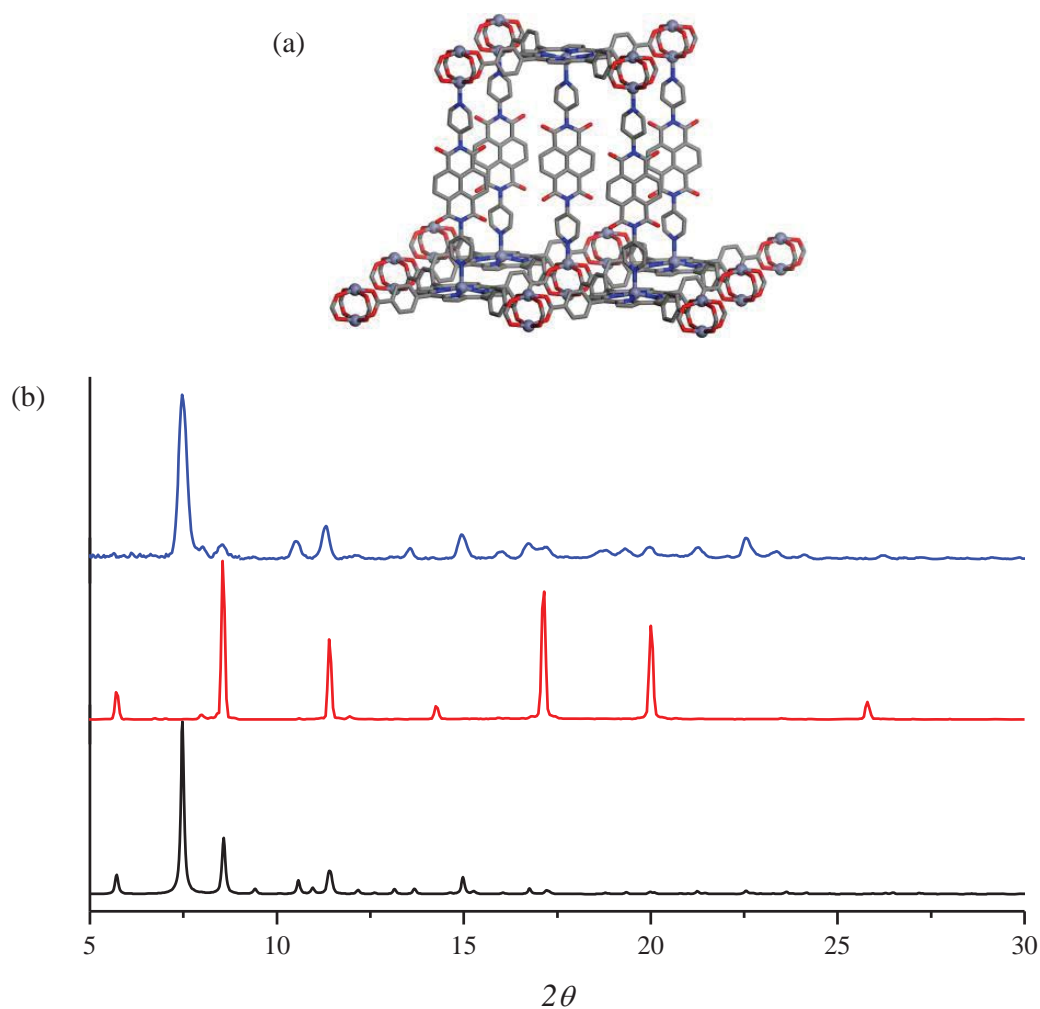


Figure 3.2. (a) Representation of single crystal structure of PPF-18. (b) Theoretical (bottom) and experimental (top and middle) PXRD patterns of PPF-18. The middle PXRD pattern was obtained on a flat mount showing high preferred orientation about the (001) plane. The top PXRD pattern was obtained using the spinning capillary method. The experimental patterns match well with the theoretical PXRD. The experimental unit cell parameters for PPF-18 ($a = 16.70(1) \text{ \AA}$, $c = 31.02(3) \text{ \AA}$) match well with the single crystal unit cell parameter of $a = 16.7134(2) \text{ \AA}$, $c = 30.8966(6) \text{ \AA}$.

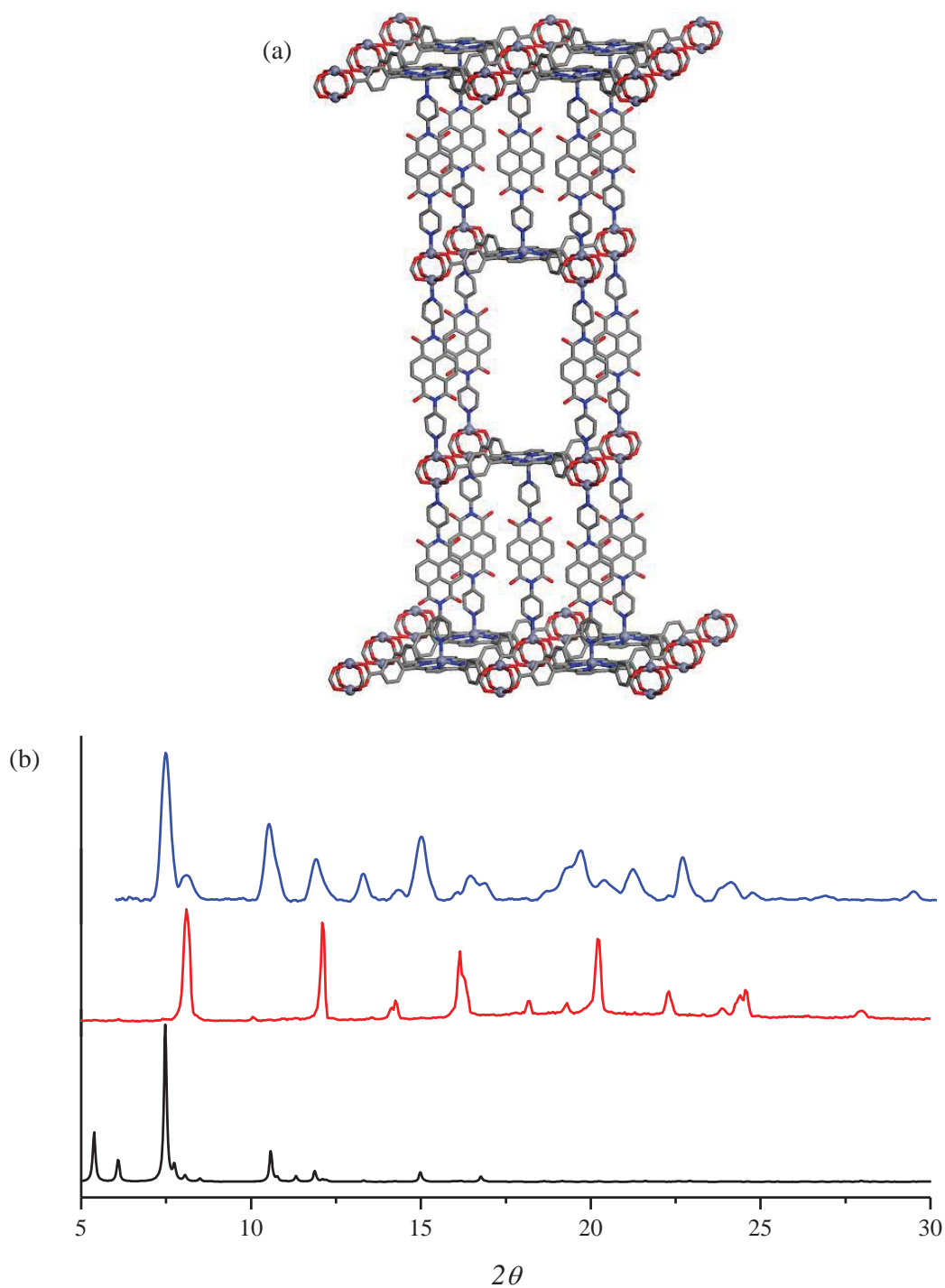


Figure 3.3. (a) Representation of single crystal structure of PPF-20. (b) Theoretical (bottom) and experimental (top and middle) PXRD patterns of PPF-20. The middle PXRD pattern was obtained on a flat mount showing high preferred orientation about the (001) plane. The PXRD pattern was obtained using the spinning capillary method. The experimental patterns match well with the theoretical PXRD pattern. The experimental unit cell parameters for PPF-20 ($a = 16.72(1) \text{ \AA}$, $c = 87.71(3) \text{ \AA}$) match well with the single crystal unit cell parameter of $a = 16.7065(6) \text{ \AA}$, $c = 87.680(6) \text{ \AA}$.

For the replacement reaction, crystals of PPF-18 were filtered and washed in DEF and then introduced into DEF/EtOH solution containing BPY as the replacement linker and left to exchange for 2 hrs at room temperature. During this time, BPY entered into the pores of PPF-18 and replaced the DPNI linkers. As shown in Figure 3.4, a new phase, PPF-27, was obtained and confirmed by PXRD. Single-crystal X-ray diffraction data were obtained for PPF-27 (Table 3.1). PPF-27 is a BPY pillared 2D bilayer structure which retains the AB stacking and $P4/nmm$ symmetry of PPF-18, but the distance between layers in the bilayer is reduced to 21.2 to 12.8 Å. The unit cell volume is also reduced from 8630 to 5793 Å³. Interestingly, the BPY-linked bilayer structure has not been reported to date in PPFs because of difficulties in synthesis.³¹ With the traditional “one-pot” solvothermal synthesis, the bilayer was only a secondary phase together with major-phase PPF-4 structure. To obtain PPF-27 as a single phase, this sequential self-assembly via linker replacement is advantageous. When excess amounts of BPY (>2 equiv) were added to the reaction mixture, a second phase was observed by PXRD. Additional BPY linkers coordinate to the open paddlewheels between the bilayers, resulting in the formation of the further coordinated ABBA-stacked 3D PPF-4 phase, a MOF previously reported by our group.³² Single-phase PPF-4 was obtained when the amount of BPY was increased to 4 equivalents, as confirmed by PXRD (Figure 3.5).

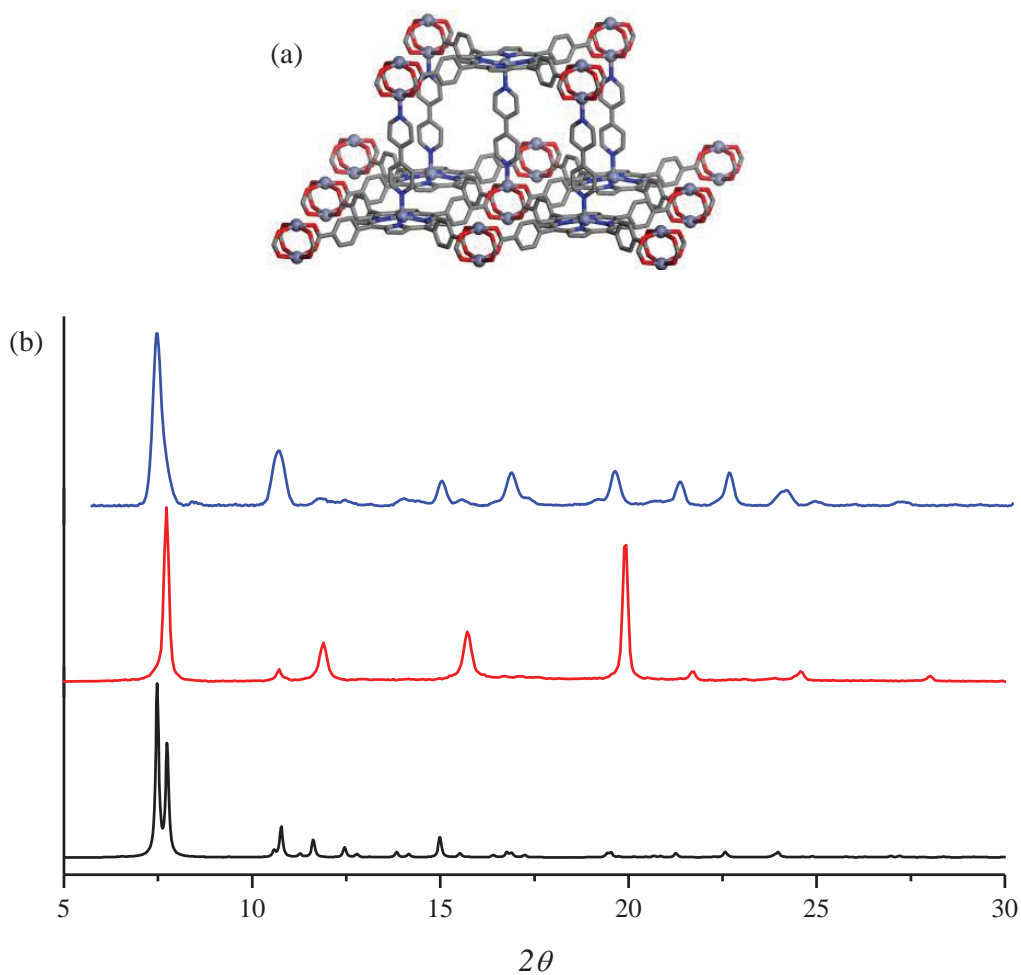


Figure 3.4. (a) Representation of the single crystal structure of PPF-27. (b) Theoretical (bottom) and experimental (top and middle) PXRD patterns of PPF-27. The middle PXRD pattern was obtained on a flat mount showing high preferred orientation about the (001) plane. The top PXRD pattern was obtained using the spinning capillary method. The experimental patterns match well with the theoretical PXRD pattern. The experimental unit cell parameters for PPF-20 ($a = 16.69(2)$ Å, $c = 21.54(3)$ Å) match well with the single crystal unit cell parameter of $a = 16.7036(9)$ Å, $c = 20.765(2)$ Å.

Table 3.1. Crystal data for PPF-27

Complex	PPF-27
chemical formula*	C ₅₈ H ₃₄ N ₆ O ₉ Zn ₃
formula weight*	1155.08
crystal system	tetragonal
space group	<i>P4/nmm</i>
<i>a</i> (Å)	16.7036(9)
<i>b</i> (Å)	16.7036(9)
<i>c</i> (Å)	20.765(2)
<i>V</i> (Å ³)	5793.6(7)
<i>Z</i>	2
ρ _{calc} (g/cm ³)*	0.662
μ (mm ⁻¹)*	0.645
R ₁ , I>2σ(I)	0.0654
wR ₂ , I>2σ(I)	0.1700

*Based on the formula without uncoordinated solvent molecules.

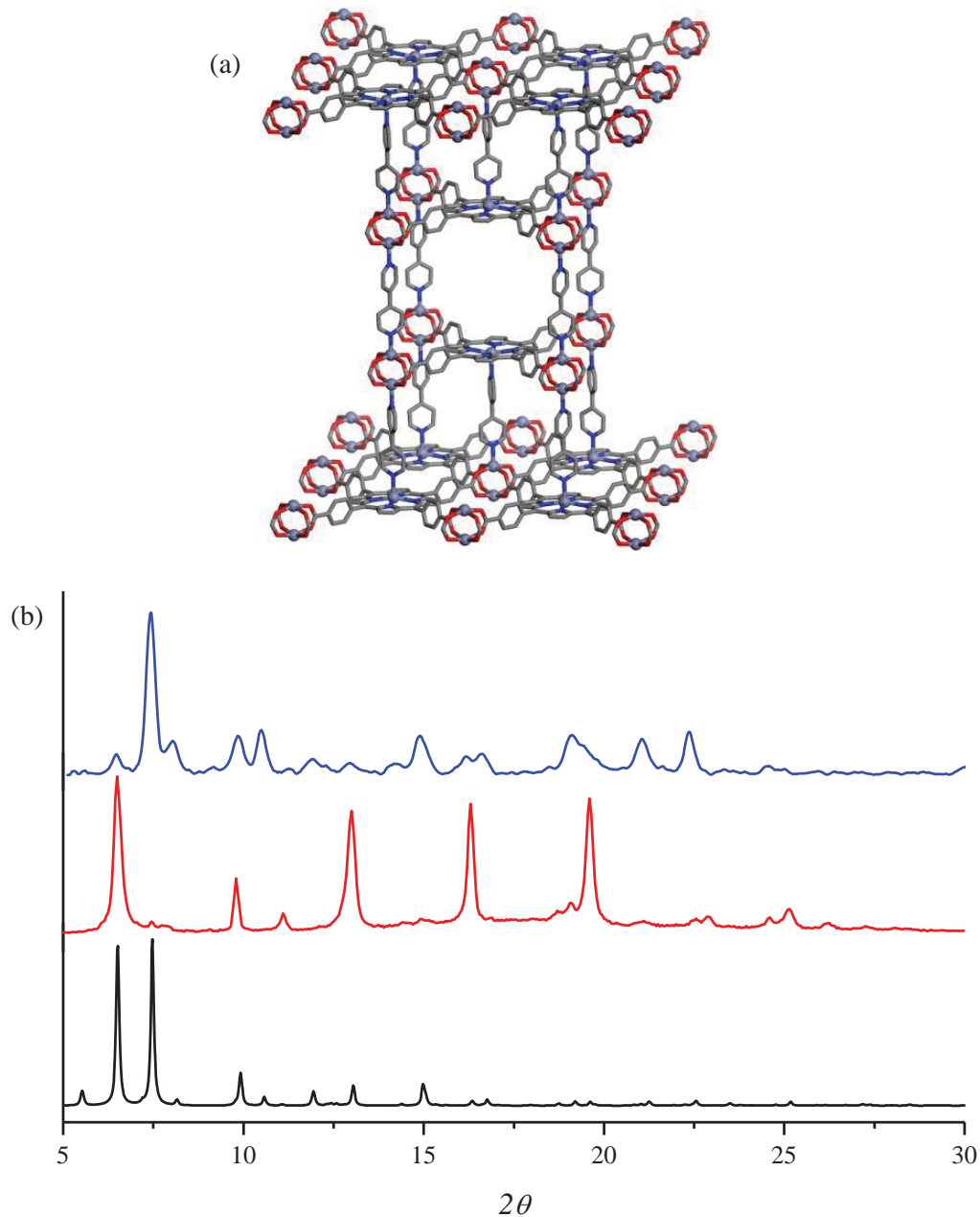


Figure 3.5. (a) Representation of single crystal structure of PPF-4. (b) Theoretical (bottom) and experimental (top and middle) PXRD patterns for PPF-4 transformed by bridging linker replacement and linker insertion from PPF-18. The middle PXRD pattern was obtained on a flat mount showing high preferred orientation about the (001) plane. The top PXRD pattern was obtained using the spinning capillary method. The experimental patterns match well with the theoretical PXRD pattern. The experimental unit cell parameters for PPF-20 ($a = 16.719(9) \text{ \AA}$, $c = 54.29(4) \text{ \AA}$) match well with the single crystal unit cell parameter of $a = 16.7122(2) \text{ \AA}$, $c = 54.2436(14) \text{ \AA}$.

To further demonstrate the utility of this transformation on 3D systems, crystals of PPF-20 were introduced into a DEF/EtOH solution containing excess BPY ligands and left to exchange for 2hrs at room temperature, similar to the case for PPF-18. Single phase PPF-4 was obtained, as confirmed by PXRD (Figure 3.6). The c parameters in PPF-20 and PPF-4 are 87.68 and 54.24 Å, respectively, showing the contraction in the c parameter upon replacement of the bridging linker.

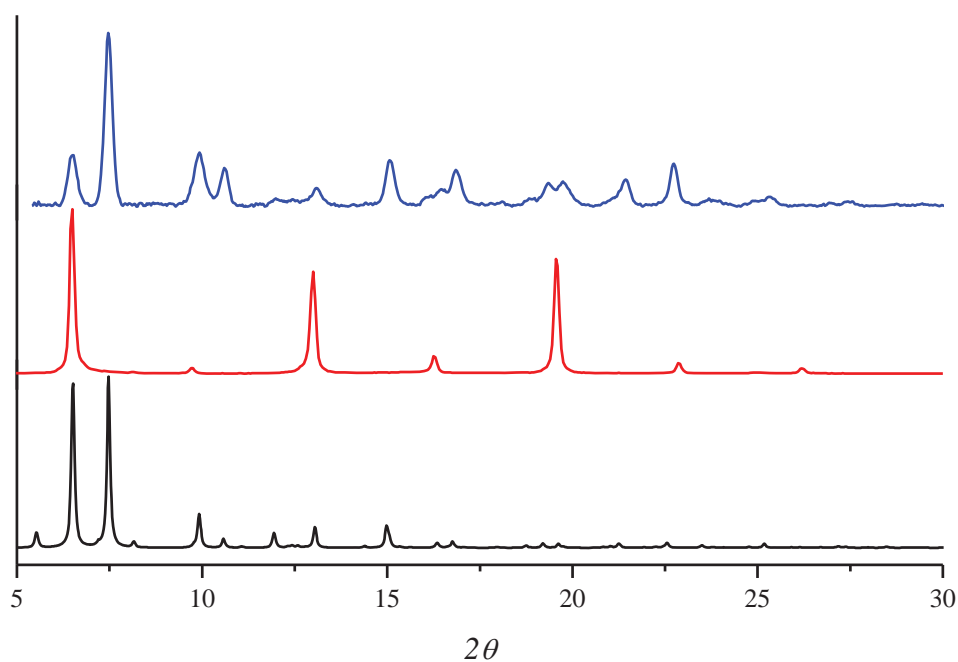


Figure 3.6. Theoretical (bottom) and experimental (top and middle) PXRD patterns for PPF-4 transformed by bridging linker replacement from PPF-20. The middle PXRD pattern was obtained on a flat mount showing high preferred orientation about the (001) plane. The top PXRD pattern was obtained using the spinning capillary method. The experimental patterns match well with the theoretical PXRD pattern. The experimental unit cell parameters for PPF-20 ($a = 16.73(2)$ Å, $c = 54.21(3)$ Å) match well with the single crystal unit cell parameter of $a = 16.7122(2)$ Å, $c = 54.2436(14)$ Å.

This process was monitored by a series of UV/Vis spectra of the solution as the replacement proceeded. The DPNI bridging linker, like many naphthalenediimides, shows absorption bands at 360 nm and 380 nm,³³ and an increasing signal due to DPNI was observed as a function of time (Figure 3.7a). This signal was then converted to concentration of DPNI linker and used to estimate the percent transformation versus time (Figure 3.7b). On the bases of this estimation, the transformation was 97% accomplished after 2hrs.

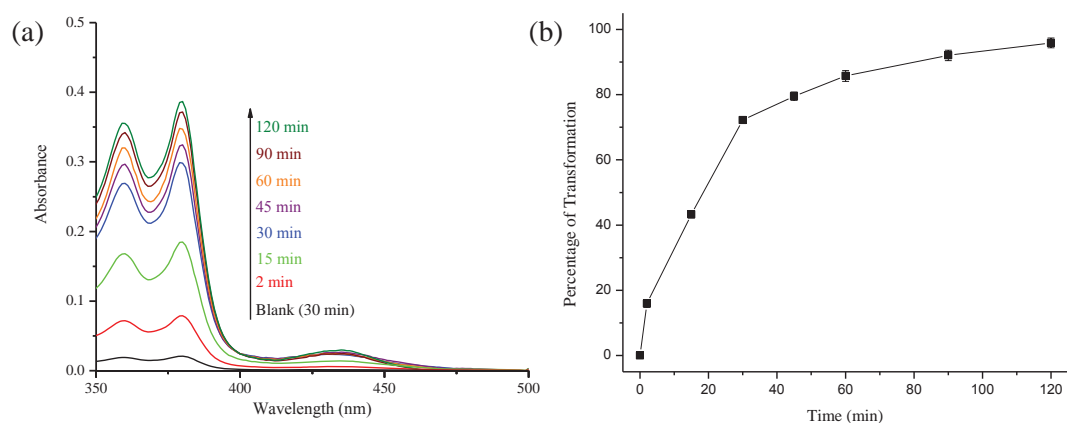


Figure 3.7. (a) UV/vis absorption spectra of DPNI bridging linker as replacement reaction proceeds from PPF-20 to PPF-4. A blank sample run for 30 minutes is included for comparison purposes. (b) Kinetic profile of the transformation of PPF-20 to PPF-4 as calculated from DPNI linker coming out into solution during the transformation.

Single-crystal to single-crystal experiments were performed for both the 2D and 3D systems, following the method reported by Suh,²⁸ confirming a solid to solid mechanism and excluding the possibility of a dissolution/recrystallization mechanism. Single crystals of PPF-18 and PPF-20 were selected and inserted into a 0.3 mm capillary tube. Photographs were taken before the transformation (Figure 3.8), and the unit cell parameters were measured and compared to the unit cell parameters obtained from the solved single-crystal structures (Tables 3.2, 3.3, and 3.4). The single crystals were then introduced to a BPY solution and left to react overnight. The resulting single crystals were photographed to show the overall shape retention during the transformation (Figure 3.8). The unit cell parameters were measured to compare to those of the daughter structure obtained from single-crystal data (Tables 3.2, 3.3, and 3.4). The presence of DPNI linkers stuck in the pores after each transformation was probed by solution ¹H NMR and UV/Vis spectroscopy of acid-digested samples following the method reported by Cohen.²⁹ For each of the systems, no residual DPNI linkers were observed in either the ¹H NMR or UV/Vis spectra (Figures 3.9 – 3.14). The reverse replacement reactions were attempted for both the 2D and 3D systems, but no transformations were observed by PXRD, indicating that the coordination equilibrium favors coordination to BPY over DPNI.³⁴ This could be due to differences in the pK_a of the two pillars. Long *et al.* showed that, from a thermodynamic standpoint, MOF stability can be related to the basicity (pK_a) of the ligand.^{35,36} Since MOFs are derived from Lewis acid–base coordination complexes between metal ions and ligands, the pK_a of the isolated ligand can be used to predict the thermodynamic strength of the resulting metal–ligand bond. This work was further supported by Low *et al.*, who also found that the strength of the bond between metal

oxide cluster and the bridging linker is important in defining the hydrothermal stability of various MOFs.^{37,38} According to this argument, BPY, being the more basic of the two pillars (see Table 3.5), will form a stronger coordination bond with the zinc paddlewheel SBU, making the replacement energetically favorable.

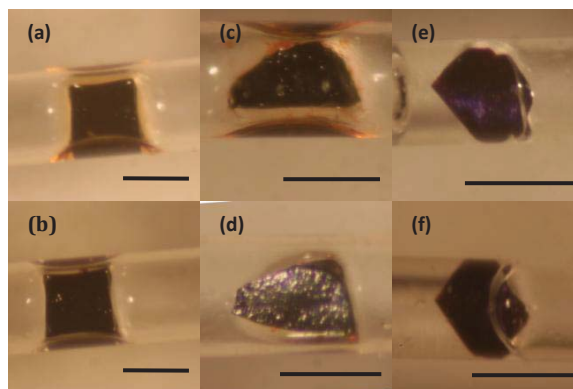


Figure 3.8. Photographs of PPF crystals in single-crystal to single-crystal transformation. (a) PPF-18 crystal before transformation. (b) After immersion in BPY solution overnight to afford PPF-27. (c) PPF-18 crystal before transformation. (d) After immersion in BPY solution overnight to afford PPF-4. (e) PPF-20 crystal before transformation. (f) After immersion in BPY solution overnight to afford PPF-4. The scale bar in the figures represents 300 μm .

Table 3.2. Tetragonal unit cell parameters of PPF-18 to PPF-27, exhibiting single-crystal to single-crystal transformation

Compound	a , Å	b , Å	c , Å	V , Å ³
Before	16.718(8)	16.718(8)	31.36(5)	8764(21)
After	16.704(2)	16.704(2)	20.86(4)	5818(16)
PPF-18*	16.7134(2)	16.7134(2)	30.8966(6)	8630.6(2)
PPF-27*	16.7036(9)	16.7036(9)	20.765(2)	5793.6(7)

* Unit cell parameters from .CIF files of respective structures.

Table 3.3. Tetragonal unit cell parameters of PPF-18 to PPF-4, exhibiting single-crystal to single-crystal transformation

Compound	<i>a</i> , Å	<i>b</i> , Å	<i>c</i> , Å	<i>V</i> , Å ³
Before	16.709(9)	16.709(9)	31.21(6)	8713(18)
After	16.722(6)	16.722(6)	54.38(4)	15206 (15)
PPF-18*	16.7134(2)	16.7134(2)	30.8966(6)	8630.6(2)
PPF-4*	16.7122(9)	16.7122(9)	54.2436(14)	15150.1(5)

* Unit cell parameters from .CIF files of respective structures.

Table 3.4. Tetragonal unit cell parameters of PPF-20 to PPF-4, exhibiting single-crystal to single-crystal transformation

Compound	<i>a</i> , Å	<i>b</i> , Å	<i>c</i> , Å	<i>V</i> , Å ³
Before	16.727(2)	16.727(2)	87.59(5)	24507(50)
After	16.706(6)	16.706(6)	54.89(3)	15319(24)
PPF-20*	16.7065(6)	16.7065(6)	87.680(6)	24472.1(2)
PPF-4*	16.7122(9)	16.7122(9)	54.2436(14)	15150.1(5)

* Unit cell parameters from .CIF files of respective structures.

Table 3.5. Comparison of the pK_a values of pillaring linkers used in replacement reactions.

Pillar	pK _a	
	Literature	Calculated ^a
BPY	4.82 ⁴⁹	4.93
DPNI	not available	3.98

^aCalculated values of pK_a was obtained using the ACD/I-Lab Web Service³⁹

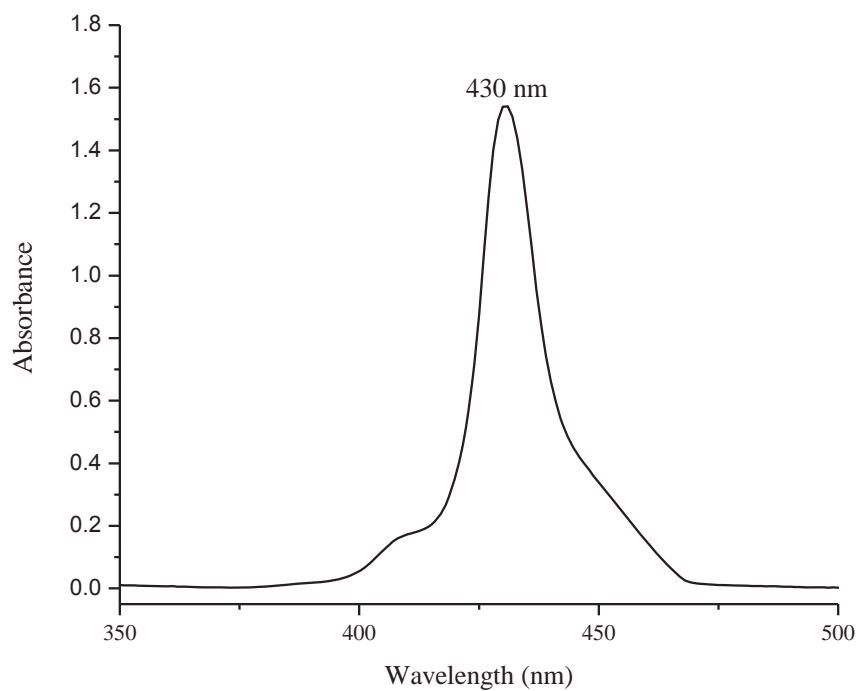


Figure 3.9. UV/vis absorption spectra of digested PPF-27 synthesized from PPF-18. Main absorption is centered at 430 nm which corresponds to the Soret band of ZnTCPP. There is no visible absorption at either 360 nm or 380 nm implying that there is no DPNI linker in the digested sample.

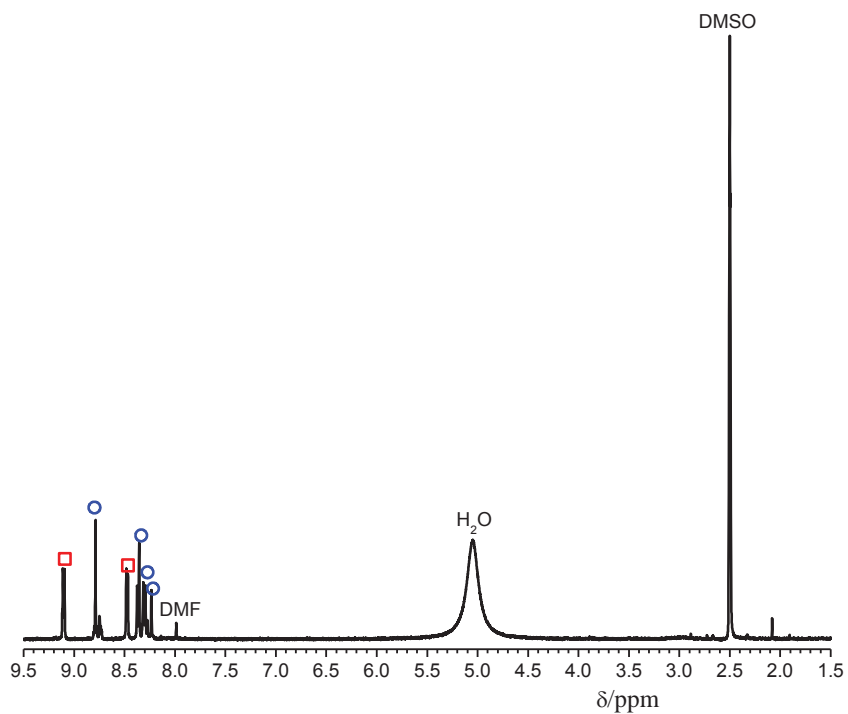


Figure 3.10. ^1H NMR spectra of digested PPF-27 synthesized from PPF-18. Red squares and blue circles represent signals of BPY linker and ZnTCPP respectively.

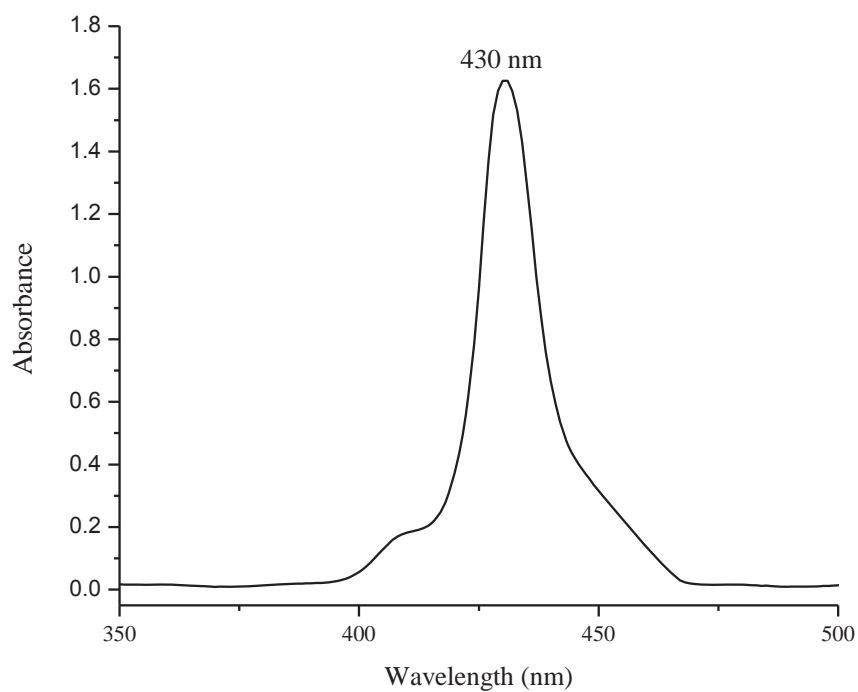


Figure 3.11. UV/vis absorption spectra of digested PPF-4 synthesized from PPF-18. Main absorption is centered at 430 nm which corresponds to the Soret band of ZnTCPP. There is no visible absorption at either 360 nm or 380 nm implying that there is no DPNI linker in the digested sample.

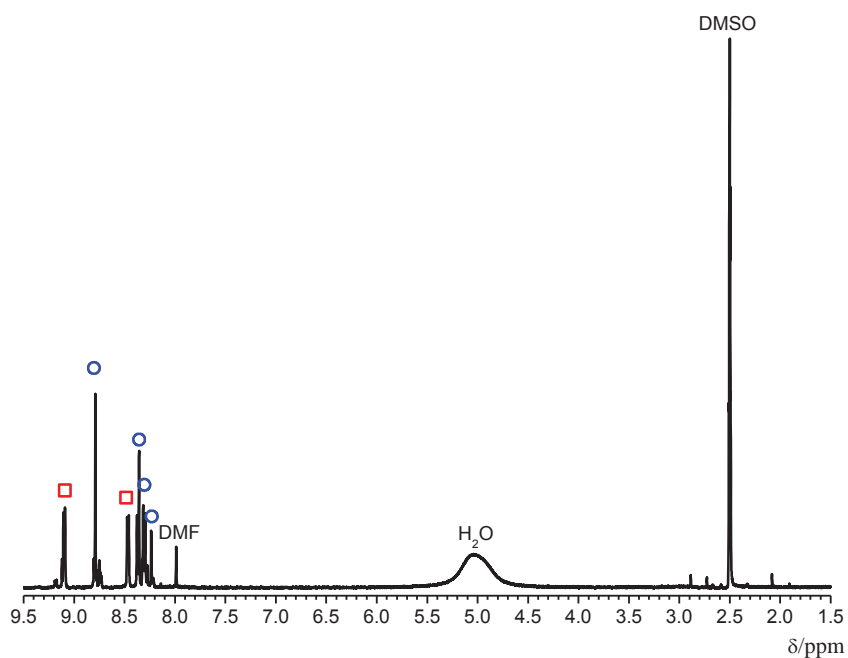


Figure 3.12. ^1H NMR spectra of digested PPF-4 synthesized from PPF-18. Red squares and blue circles represent signals of BPY linker and ZnTCPP respectively.

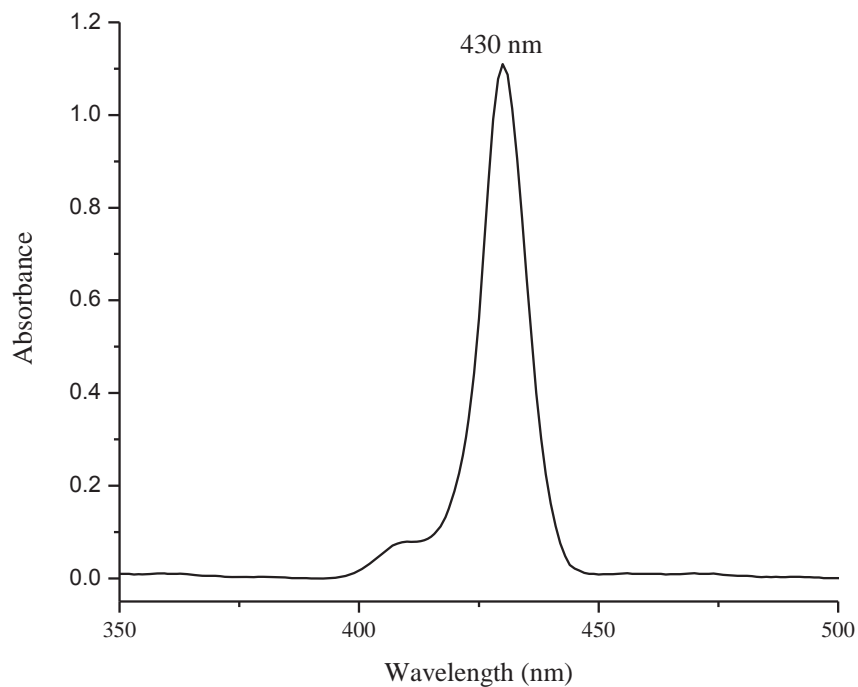


Figure 3.13. UV/vis absorption spectra of digested PPF-4 synthesized from PPF-20. Main absorption is centered at 430 nm which corresponds to the Soret band of ZnTCPP. There is no visible absorption at either 360 nm or 380 nm implying that there is no DPNI linker in the digested sample.

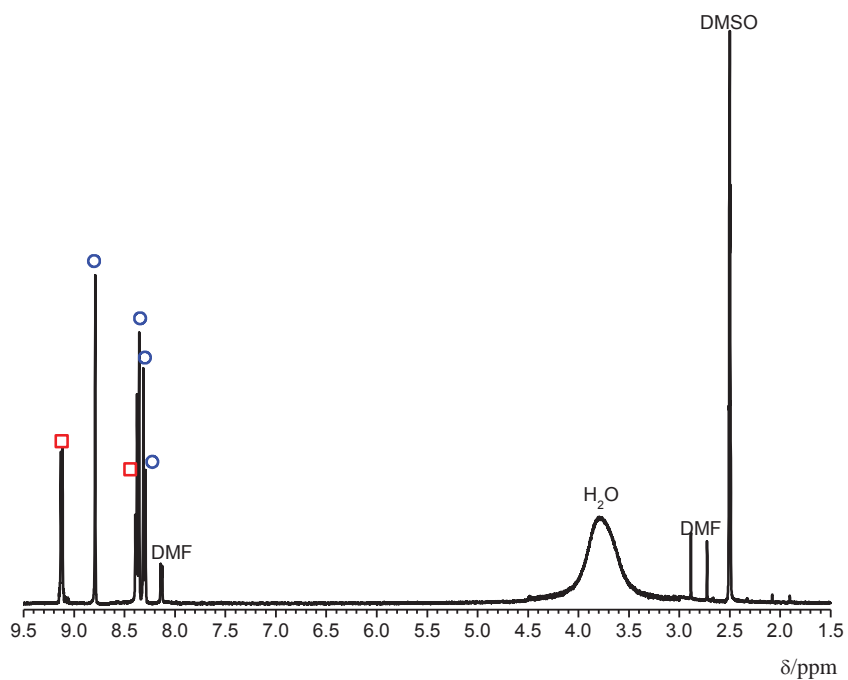


Figure 3.14. ^1H NMR spectra of digested PPF-4 synthesized from PPF-20. Red squares and blue circles represent signals of BPY linker and ZnTCPP respectively.

An interesting templating effect was also observed in both the 2D and 3D systems during this linker–replacement transformation (Figure 3.15). There was no lateral shift in the 2D porphyrin paddlewheel layers during the replacement, allowing retention of the parent stacking sequence in the daughter structure, as exemplified by the PPF-18 → PPF-27 transformation when there was limited amount of BPY in solution. When the parent structure (PPF-18) was stacked in an AB fashion, the daughter (PPF-27) retained this stacking sequence. We also noticed a similar trend in the PPF-20 → PPF-4 transformation, where the ABBA stacking pattern of the parent was conserved in the daughter (Figure 3.15). One can imagine that the ABBA PPF-4 structure can be synthesized from the PPF-27 bilayer structure through lateral movement. When excess BPY linkers were *inserted*, the AB bilayer system shifted laterally, similar to the other known cases for 2D paddlewheel MOFs.¹³ The paddlewheel metal nodes coordinated further to create the ABBA structure.⁴⁰

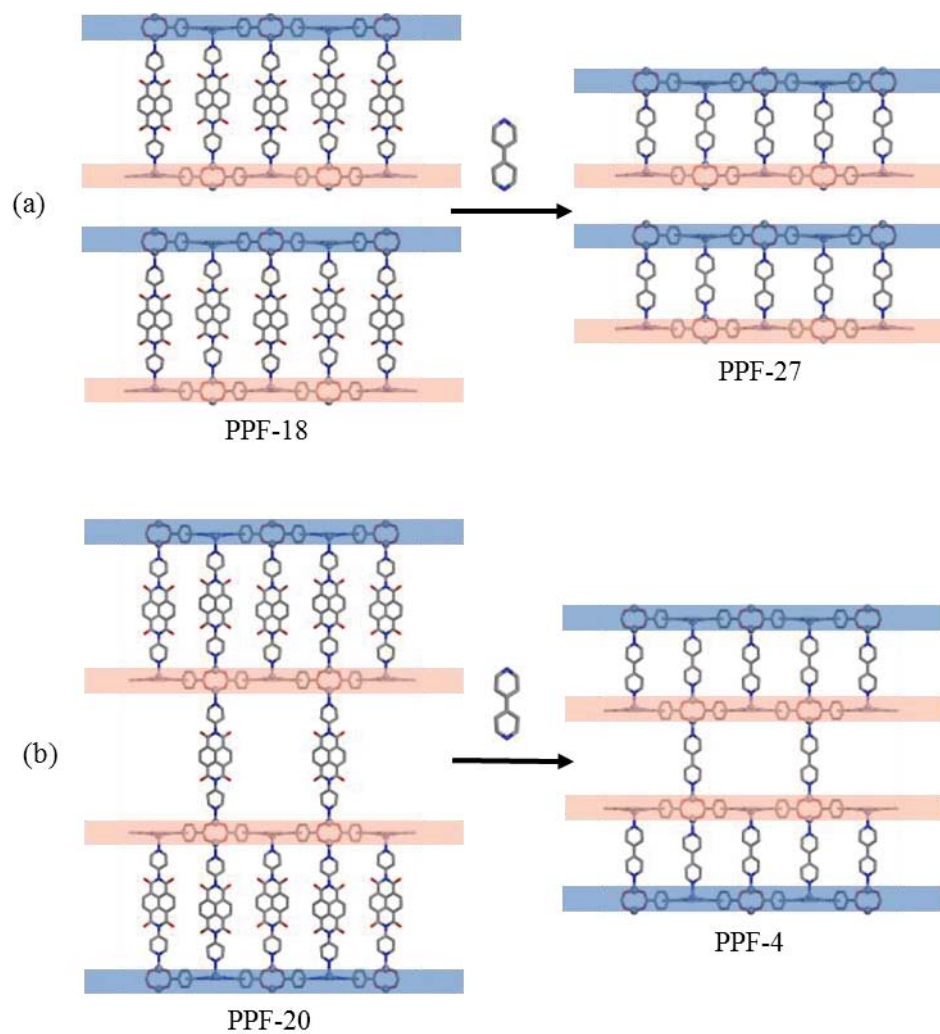


Figure 3.15. Introduction of the bridging linker BPY to crystals of (a) PPF-18 and (b) PPF-20, transforming them to PPF-27 and PPF-4, respectively. Blue and pink bands represent “A” and “B” layers, respectively. The AB and ABBA topologies in PPF-18 and PPF-20 are retained in PPF-27 and PPF-4, respectively, showing a templating effect.

In both the 2D and 3D replacement transformations, the porous nature of these MOFs facilitates the transformation.⁴¹ Dipyriddy bridging linkers have the ability to diffuse into the interior of these MOFs. Indeed, Connolly surface models indicate that the pillar dimensions are small enough to diffuse into the pores (Figures 3.16 – 3.21). There the replacing linkers can access the internal metal centers and replace the existing linkers even when those linkers are structurally integral to these MOFs. The linkers from the parent structure then can diffuse out of the structure, as seen in the UV/Vis experiment (Figure 3.7) and modeled by Connolly surface models. This linker replacement in multidimensional MOFs demonstrates the dynamic nature of the internal compartment of MOFs in the solid state. Such a phenomenon is rather remarkable. A common assumption has been that extended solids cannot be used as starting materials for sequential self-assembly because these solids are insoluble in solution. However, these two systems, PPF-18 and PPF-20, show that a replacement synthesis can indeed be accomplished even with crystalline solid intermediates, as evidenced by the single-crystal to single-crystal experiments and supported by the UV/Vis experiment. The peak centered around 430 nm in the UV/Vis spectra (Figure 3.7) corresponds to the Soret band of ZnTCPP (427 nm) indicating that there is a maximum of 2.26×10^{-8} mol of ZnTCPP breaking off of PPF-20 (0.65% of the framework) into solution during the transformation, confirming that the overall 2D porphyrin paddlewheel structure stays intact.

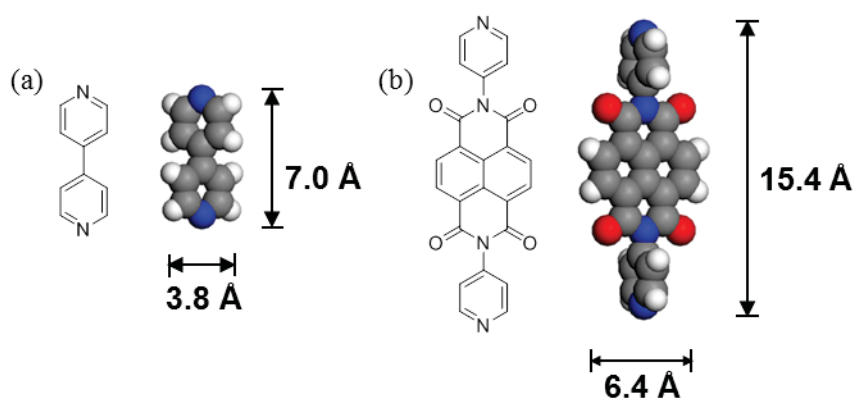


Figure 3.16. Molecule structure and estimated dimensions of (a) BPY and (b) DPNI pillars.

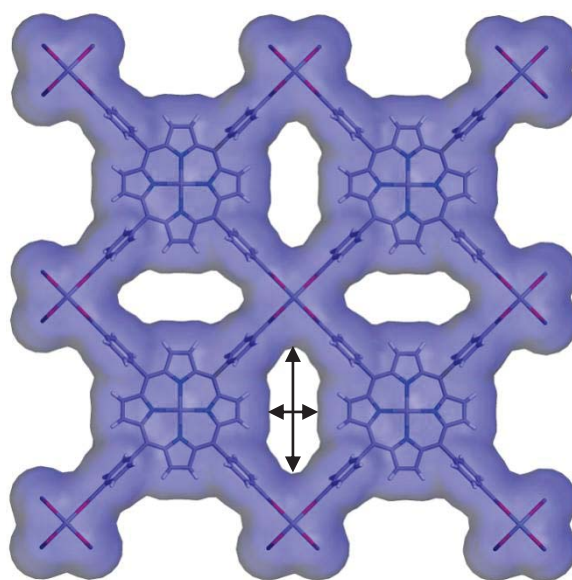


Figure 3.17. Connolly surface of PPF 2D layer ((001) face) showing 1D channel (9.3 Å X 3.7 Å) calculated with 1.4 Å VDW scale factor.

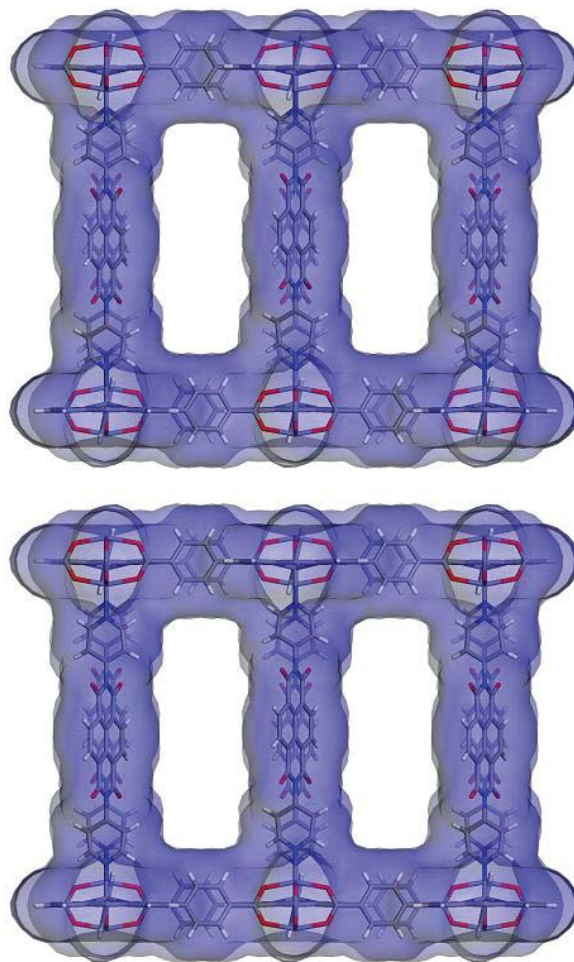


Figure 3.18. Connolly surface of PPF-18 along the (110) direction showing 1D channel (14.5 Å X 5.1 Å) calculated with 1.4 Å VDW.

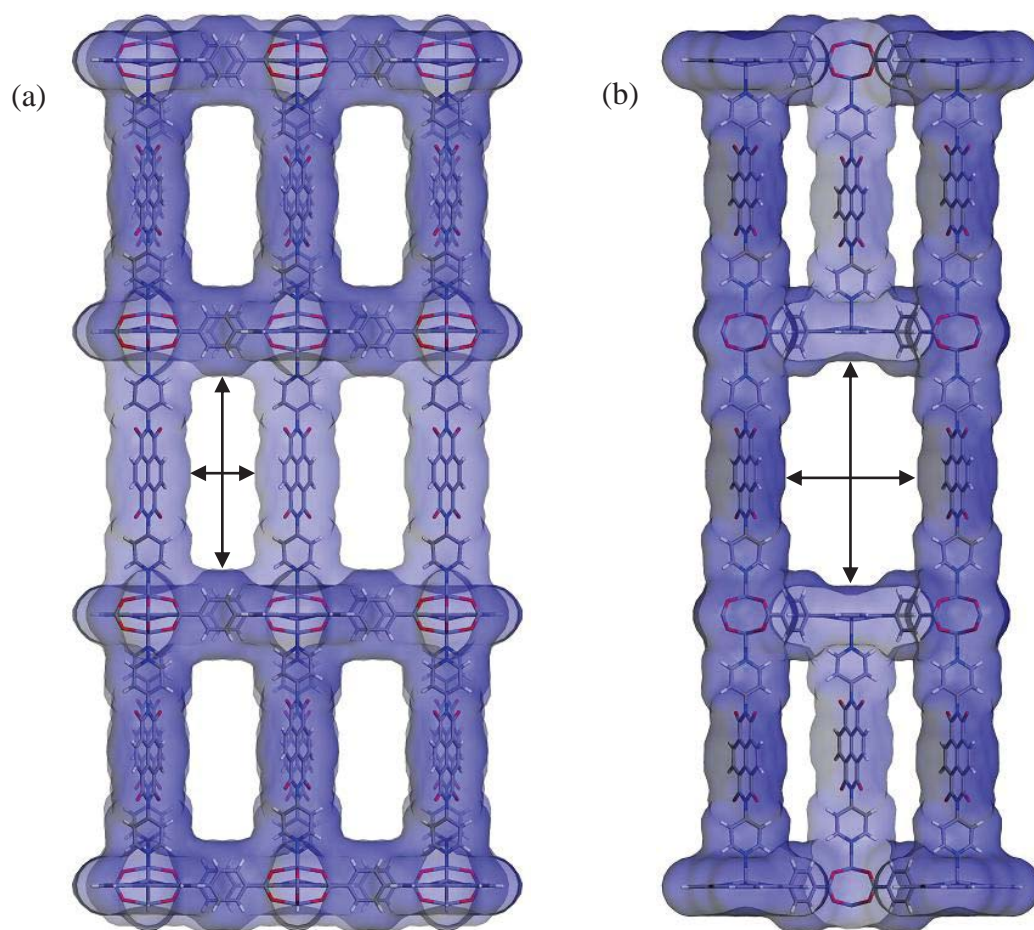


Figure 3.19. Connolly surface of PPF-20 (a) along the (110) direction and (b) along the (100) direction, showing 1D channel ((14.5 Å X 5.1 Å) and (17.3 Å X 10.3 Å) respectively) calculated with 1.4 Å VDW.

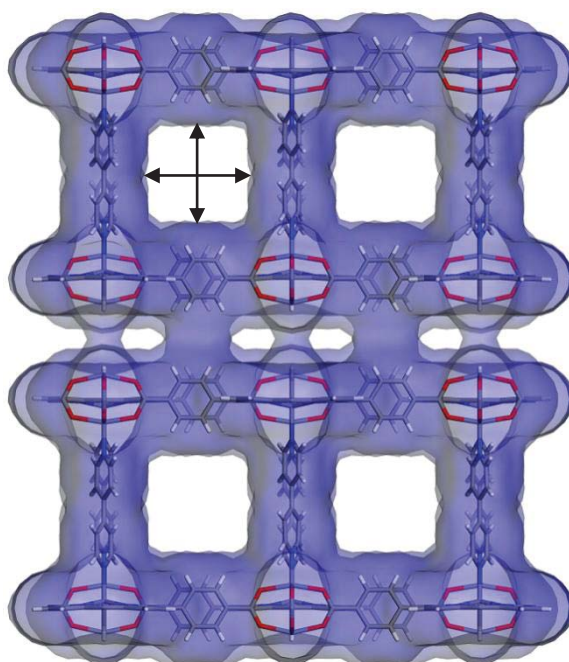


Figure 3.20. Connolly surface of PPF-27 along the (110) direction showing 1D channel (7.1 Å X 7.3 Å) (8.3 Å diagonal) calculated with 1.4 Å VDW.

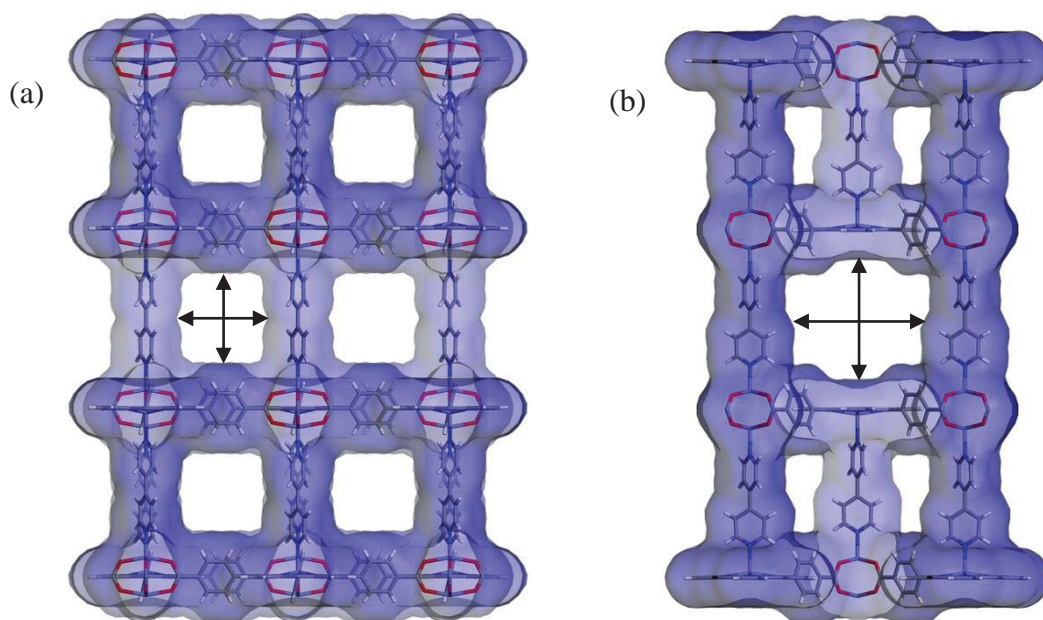


Figure 3.21. Connolly surface of PPF-4 (a) along the (110) direction and (b) along the (100) direction, showing 1D channels ($7.2 \text{ \AA} \times 7.3 \text{ \AA}$) and ($8.9 \text{ \AA} \times 10.3 \text{ \AA}$) respectively) calculated with 1.4 \AA VDW.

This work was extended to observe the effect of interpenetration on the ability to replace the structural linkers. PPF-19 was synthesized via a solvothermal following the published method³¹ and confirmed by PXRD (Figure 3.22). PPF-19 is a structural isomer of PPF-18 – both having the same stoichiometry of 1ZnTCPP: 1paddlewheel SBU: 1DPNI pillar. PPF-19 however is a monoclinic AA–interpenetrated structure with $C2/m$ symmetry. The PPF layers within PPF-19 are connected together by DPNI pillars which coordinate exclusively to the axial paddlewheel coordination sites. The zinc ion within the core of porphyrin are further coordinated with solvent molecules. Because of the interpenetrated nature of PPF-19, the DPNI pillars are locked into place between two porphyrins of the alternating PPF-layer (see Figure 3.22c) possibly impeding the replacing BPY and making it more difficult for the DPNI to diffuse out of the crystal. Indeed upon immersing crystals of PPF-19 in a solution of BPY for an extended amount of time (~ 1 week), no replacement reaction is observed by PXRD. The replacement is either not possible because of the interpenetration, or the kinetics of this process are much slower than that of the non–interpenetrated structures PPF-18 and PPF-20.

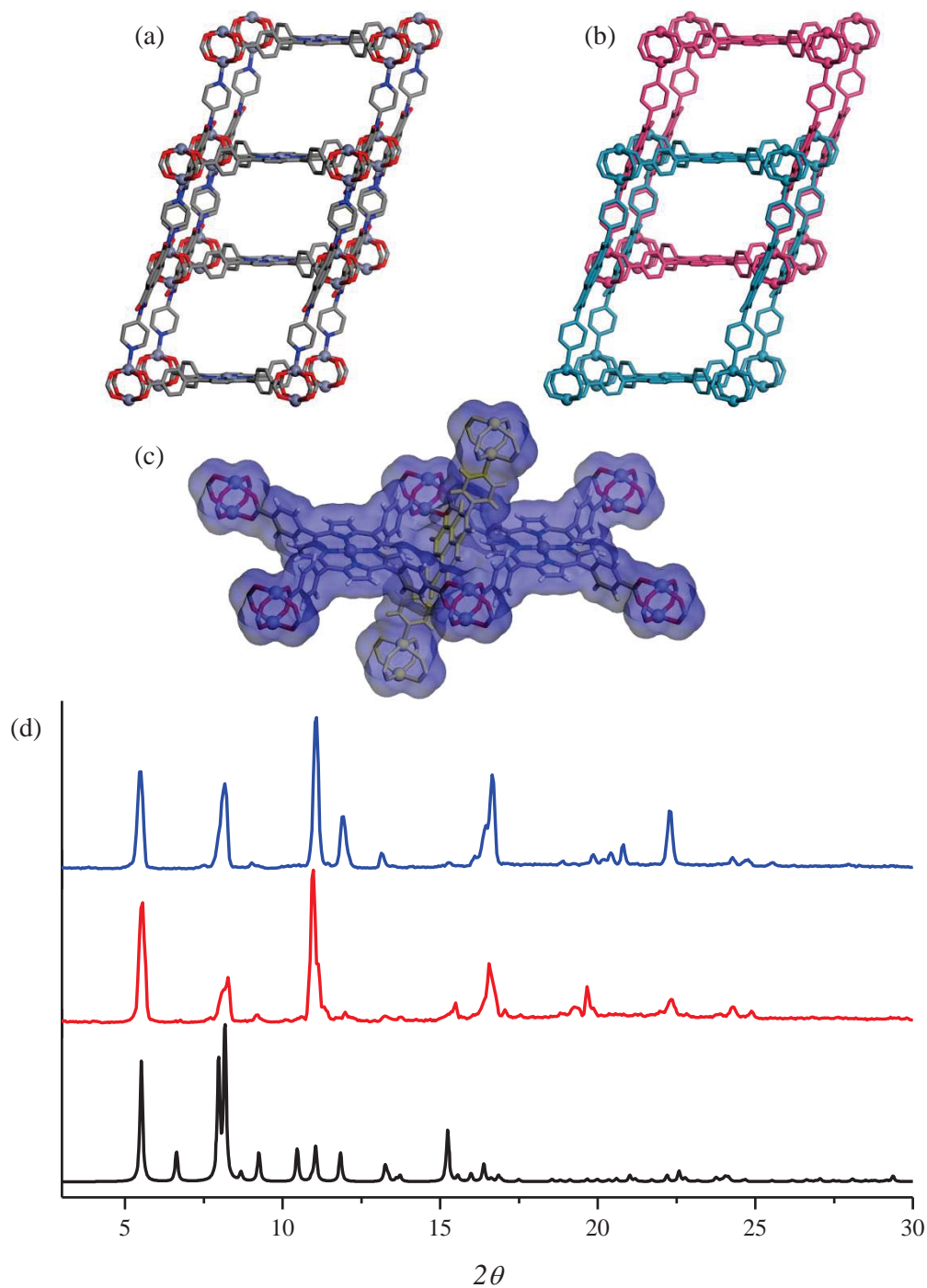


Figure 3.22. (a) Representation of PPF-19. (b) Blue and Pink colored interpenetrated AA stacked nets. (c) Connolly surface model of a DPNI pillar between two porphyrins of the alternating PPF layer calculated with 1.4 Å VDW. (d) Theoretical (bottom), as synthesized (middle), and after immersion in BPY solution (top) PXRD patterns of PPF-19. As can be seen by the peak positions after immersion, PPF-19 is the only phase observed.

3.4 Conclusion

We have demonstrated how linker replacement can be applied to two cases of 2D and 3D MOFs. Because of the porous nature of these MOFs, dipyriddy linkers can diffuse into the interiors of the MOFs and replace the existing structure dipyriddy linkers. The stacking patterns of the parent structures are well maintained throughout the transformations, showing a templating effect. Such linker replacement can also be utilized in a sequential self-assembly process, despite the fact that these MOFs are insoluble in solution. The replacement of 'locked' pillars however has yet to be achieved, even though the process is energetically favorable, as was seen in the case of PPF-19. This may be due to the inability for DPNI to escape the pores. The development of replacement reactions in MOFs is not limited to the synthesis of single-phase materials that are otherwise unattainable, as seen with PPF-27 in this study. Rather, the replacement reaction in MOFs, together with other sequential self-assembly processes, can offer a new avenue for manipulating MOFs in the pursuit of constructing complex architectures designed for specific functions.

4.5 References

- (1) (a) Park, Y. K.; Choi, S. B.; Kim, H.; Kim, K.; Won, B. -H.; Choi, K.; Choi, J. -S.; Ahn, W. -S.; Won, N.; Kim, S.; Jung, D. H.; Choi, S. -H.; Kim, G. -H.; Cha, S. -S.; Jhon, Y. H.; Yang, J. K.; Kim, J. *Angew. Chem. Int. Ed.* **2007**, *46*, 8230. (b) Robson, R. *Dalton Trans.* **2008**, *37*, 5113.
- (2) Tranchemontagne, D. J.; Mendoza-Cortés, J. L.; O'Keeffe, M.; Yaghi, O. M. *Chem. Soc. Rev.* **2009**, *38*, 1257.

- (3) Horike, S.; Kitagawa, S. *Metal–Organic Frameworks: Applications from catalysis to Gas Storage*, 1st ed.; Wiley–VCH Verlag GmbH & Co., 2011; pp 1-21.
- (4) (a) Moulton, B.; Zaworotko, M. J. *Chem. Rev.* **2001**, *101*, 1629. (b) O’Keeffe, M.; Yaghi, O. M. *Chem. Rev.* **2012**, *112*, 675.
- (5) Yaghi, O. M.; O’Keeffe, M.; Ockwig, N. W.; Chae, H. K.; Eddaoudi, M.; Kim, J. *Nature* **2003**, *423*, 705.
- (6) For reviews on post-synthetic modification, see: (a) Wang, Z.; Cohen, S. M. *Chem. Soc. Rev.* **2009**, *38*, 1315. (b) Tanabe, K. K.; Cohen, S. M.; *Chem. Soc. Rev.* **2011**, *40*, 498. (c) Cohen, S. M. *Chem. Sci.* **2010**, *1*, 32. (d) Song, Y. –F.; Cronin, L. *Angew. Chem. Int. Ed.* **2008**, *47*, 4635.
- (7) Hoskins, B. F.; Robson, R. *J. Am. Chem. Soc.* **1990**, *112*, 1546.
- (8) Kiang, Y. –H.; Gardner, G. B.; Lee, S.; Xu, Z.; Lobkovsky, E.; *J. Am. Chem. Soc.* **1999**, *121*, 8204.
- (9) (a) Nguyen, J. G.; Cohen, S. M. *J. Am. Chem. Soc.* **2010**, *132*, 4560. (b) Tanabe, K. K.; Cohen, S. M. *Angew. Chem. Int. Ed.* **2009**, *48*, 7424. (c) Oisaki, K.; Li, Z.; Furukawa, H.; Czaja, A. U.; Yaghi, O. M. *J. Am. Chem. Soc.* **2010**, *132*, 9262.
- (10) For examples of SSA in discrete molecular systems see: (a) Mal, P.; Nitschke, J. R. *Chem. Commun.* **2010**, *46*, 2417. (b) Newton, G. N.; Onuki, T.; Shiga, T.; Noguchi, M.; Matsumoto, T.; Mathieson, J. S.; Nihei, M.; Nakano, M.; Cronin, L.; Oshio, H. *Angew. Chem. Int. Ed.* **2011**, *50*, 4844.
- (11) A major difference between SSA and PSM is that SSA is focused on the self assembly of structural linkers in a multi–step synthesis, whereas PSM is focused on the functionalization of structural linkers. See reference 6.

- (12) (a) Rivkin, A.; Chou, T. –C.; Danishefsky, S. J. *Angew. Chem. Int. Ed.* **2005**, *44*, 2838. (b) Downer–Riley, N. K.; Jackson, Y. A. *Annu. Rep. Prog. Chem., Sect. B* **2011**, *107*, 157.
- (13) Kitaura, T.; Iwahori, F.; Matsuda, R.; Kitagawa, S.; Kubota, Y.; Takata, M.; Kobayashi, T. C. *Inorg. Chem.* **2004**, *43*, 6522.
- (14) Burnett, B. J.; Barron, P. M.; Hu, C.; Choe, W. *J. Am. Chem. Soc.* **2011**, *133*, 9984.
- (15) Kim, M.; Cahill, J. F.; Su, Y.; Prather, K. A.; Cohen, S. M. *Chem. Sci.* **2012**, *3*, 126.
- (16) Takaishi, S.; DeMarco, E. J.; Pellin, M. J.; Farha, O. K.; Hupp, J. T. *Chem. Sci.* **2013**, *4*, 1509.
- (17) Li, J. –R.; Zhou, H. –C. *Nat. Chem.* **2010**, *2*, 893.
- (18) Li, J. –R.; Timmons, D. J.; Zhou, H. –C. *J. Am. Chem. Soc.* **2009**, *131*, 6368.
- (19) SMART (version 6.532). *Program for Bruker CCD X–ray Diffractometer Control*, Bruker AXS Inc., Madison, WI, **2005**.
- (20) SAINT+ (version 6.45). *Program for Reduction of Data Collected on Bruker CCD Area Detector Diffractometer*, Bruker AXS Inc., Madison, WI, **2003**.
- (21) Sheldrick, G. M. SADABS, version 2.10, *Program for Empirical Absorption correction of Area Detector Data*, University of Göttingen, **2007**.
- (22) Sheldrick, G. M. SHELXTL, version 6.15, *Program Package for Structure Solution and Refinement*, Bruker Analytical X–ray Systems, Inc., Madison, WI, **2008**.
- (23) Speck, A. . *J. App. Cryst.* **2003**, *36*, 7.
- (24) Farha, O. K.; Sultz, A. M.; Sarjeant, A. A.; Nguyen, S. T.; Hupp, J. T. *J. Am. Chem. Soc.* **2011**, *133*, 5652.
- (25) <http://www.ccdc.cam.ac.uk/products/mercury>

- (26) <http://www.ccp14.ac.uk/ccp/web-mirrors/crush/astaff/Holland/UnitCell.html>
- (27) *Material Studio* (version 4.3): Program for Molecular Modeling and Analysis; Accelrys Software Inc.
- (28) Choi, H. J.; Suh, M. P. *J. Am. Chem. Soc.* **2004**, *126*, 15844.
- (29) Wang, Z.; Tanabe, K. K.; Cohen, S. M. *Inorg. Chem.* **2009**, *48*, 296.
- (30) The binding energies for Zn-N and Zn-O were estimated to be 150 and 360 kJ/mol, respectively. See reference 2.
- (31) Chung, H.; Barron, P. M.; Novotny, R. W.; Son, H. -T.; Hu, C.; Choe, W. *Cryst. Growth Des.* **2009**, *9*, 3327.
- (32) (a) Choi, E. -Y.; Wray, C. A.; Hu, C.; Choe, W. *CrystEngComm* **2009**, *11*, 553.
(b) Choi, E. -Y.; Barron, P. M.; Novotny, R. W.; Son, H. -T.; Hu, C.; Choe, W. *Inorg. Chem.* **2009**, *48*, 426.
- (33) (a) Ozser, M. E.; Uzun, D.; Elci, I.; Icil, H.; Demuth, M. *Photochem. Photobiol. Sci.* **2003**, *2*, 218. (b) Erten, Ş.; Posokhov, Y.; Alp, S.; İçli, S. *Dyes and Pigments* **2005**, *64*, 171.
- (34) Kondo, M.; Furukawa, S.; Hirai, K.; Kitagawa, S. *Angew. Chem. Int. Ed.* **2010**, *49*, 5327.
- (35) Colombo, V.; Galli, S.; Choi, H. J.; Han, G. D.; Maspero, A.; Palmisano, G.; Masciocchi, N.; Long, J. R. *Chem. Sci.* **2011**, *2*, 1311.
- (36) Choi, H. J.; Dincă, M.; Dailly, A.; Long, J. R. *Energy Environ. Sci.* **2010**, *3*, 117.
- (37) Low, J. J.; Benin, A. I.; Jakubczak, P.; Abrahamian, J. F.; Faheem, S. A.; Willis, R. *J. Am. Chem. Soc.* **2009**, *131*, 15834.
- (38) Jasuja, H.; Burch, N. C.; Huang, Y.; Cai, Y.; Walton, K. S. *Langmuir* **2013**, *29*, 633.

(39) Advanced Chemistry Development, Inc.: Toronto, Canada, 1996-2005.

<http://www.acdlabs.com>.

(40) This phenomena is also seen in intercalation chemistry of Layered Double Hydroxide (LDH) compounds. O'Hare reported a similar transformation in the Zn_2Cr LDH system. Upon introduction of excess adipate anions, first the succinate and tartrate anions would be replaced. After this replacement, adipate further replaced the Cl^- anions in the remaining layers. See: Feng, Y. J.; Williams, G. R.; Lerous, F.; Taviot-Gueho, C.; O'Hare, D *Chem. Mater.* **2006**, *18*, 4312. This report, however, provides only powder X-ray diffraction data to support their discussion. By using MOFs, we are able to report single crystal information on this phenomenon. We report transformations replacing a large linker with a smaller linker, showing a contraction between layers. Interestingly O'Hare's report indicates that a similar transformation could happen from smaller linker to larger linker, as seen from the longer adipate anion replacing the smaller succinate and tartrate anions. We believe that this concept could be adopted into MOF synthesis.

(41) Porosity is conventionally defined by two parameters: demonstration of permeability, and retention of structure upon guest removal/exchange. See: Barbour, L. J. *Chem. Commun.* **2006**, *42*, 1163. The observation of pillar molecules into solution during the transformation indicates the permeability of the structure, similar to reports of proving porosity by inclusion of dye molecules into the crystal demonstrated by Lin. See: Ma, L.; Lin, W. *J. Am. Chem. Soc.* **2008**, *130*, 13834. The 2D square-grid layers retain their structure during the transformation as exemplified by the templating effect. Had the structure fully dissolved and recrystallized, contamination by either 2D or 3D species would be evident in the X-ray powder diffraction pattern.

CHAPTER 4

SEQUENTIAL SELF-ASSEMBLY IN PORPHYRIN PADDLEWHEEL FRAMEWORKS: LINKER INSERTION

4.1 Introduction

For the past two decades, metal–organic frameworks (MOFs) have been extensively studied as a unique platform for crystal engineering as well as materials for applications in sustainable materials chemistry.^{1–3} Conventional one–pot, coordination–driven self–assembly has been phenomenally successful in creating many interesting 2D and 3D topologies in MOFs through careful selection of the organic linkers and metal secondary building units (SBUs).⁴ However, the complexity of synthesized structures is still limited through this one–step synthetic route. Furthermore, this simple synthetic approach occasionally produces a mixture of framework isomers.⁵

Recently to gain more control over synthesis, a sequential self–assembly (SSA) strategy has been explored.⁶ One way that this SSA can be accomplished is through a linker replacement reaction (see chapter 3).⁷ An alternate approach is to *insert* linkers into MOF material to increase dimensionality. This insertion transformation has been well demonstrated in the field of layered material such as layered double hydroxides (LDHs) to control interlayer spacing and to add functionality (*e.g.* optical absorption and hydrophobicity) to the materials.^{8–10}

In MOF material, this form of transformation is best applied in systems in which the SBUs are coordinated to both the organic linker and to a labile solvent or capping

ligands. The most popular SBU for this type of transformation is the paddlewheel SBU. In 2D MOFs, the equatorial position of the paddlewheel is coordinated to the structural organic linker, but is axially coordinated to labile solvent.^{11,12} As a second structural ditopic linker is introduced, it coordinates to the metal site previously occupied by the solvent, effectively inserting into the structure, increasing the dimensionality of the material or changing the pore characteristics.

Linker insertion is possible with soluble MOPs as the initial template. In this strategy, a discrete MOP is first synthesized by assembling an angular dicarboxylate linker with a paddlewheel SBU. The MOP is then used as a supramolecular unit connected together in a subsequent step through ditopic linkers to make a 3D MOF.¹³⁻¹⁵ The molecular geometry of the MOP dictates the resulting topology of the MOF. By using the MOP as a structural building unit, the topology can be better predicted than using traditional metal ion nodes. Also, by using this strategy, structural building units with a higher coordination number can be achieved, creating more complex MOF topologies. Additionally, the resulting MOF contains two distinctive cavities, that of the retained cavity inside the MOP and the “inter MOP” cavity.

Zhou *et al.* reported the combination of the 90° angular dicarboxylate, 9*H*-carbazole-3,6-dicarboxylate, and the copper paddlewheel creating the molecular octahedron in which the copper paddlewheel clusters occupy the six corners of the octahedron.¹³ The exterior axial positions of the paddlewheel copper ions are coordinated to weakly bound solvent or capping pyridine molecules. Introducing the structural linker 4,4-bipyridine (BPY) to MOP crystals affords an interpenetrated 3D MOF by coordinating to the exterior paddlewheel, replacing the coordinated solvent or pyridine

molecules (Figure 4.1). In this synthetic strategy, the MOP is a six-connected node linked together to make a **pcu-a** topology. Even with interpenetration, the framework still preserves a 76% solvent-accessible area. Adding these components sequentially can lead to new MOFs that it may be difficult or impossible to assemble *via* the traditional one-step method.¹⁴

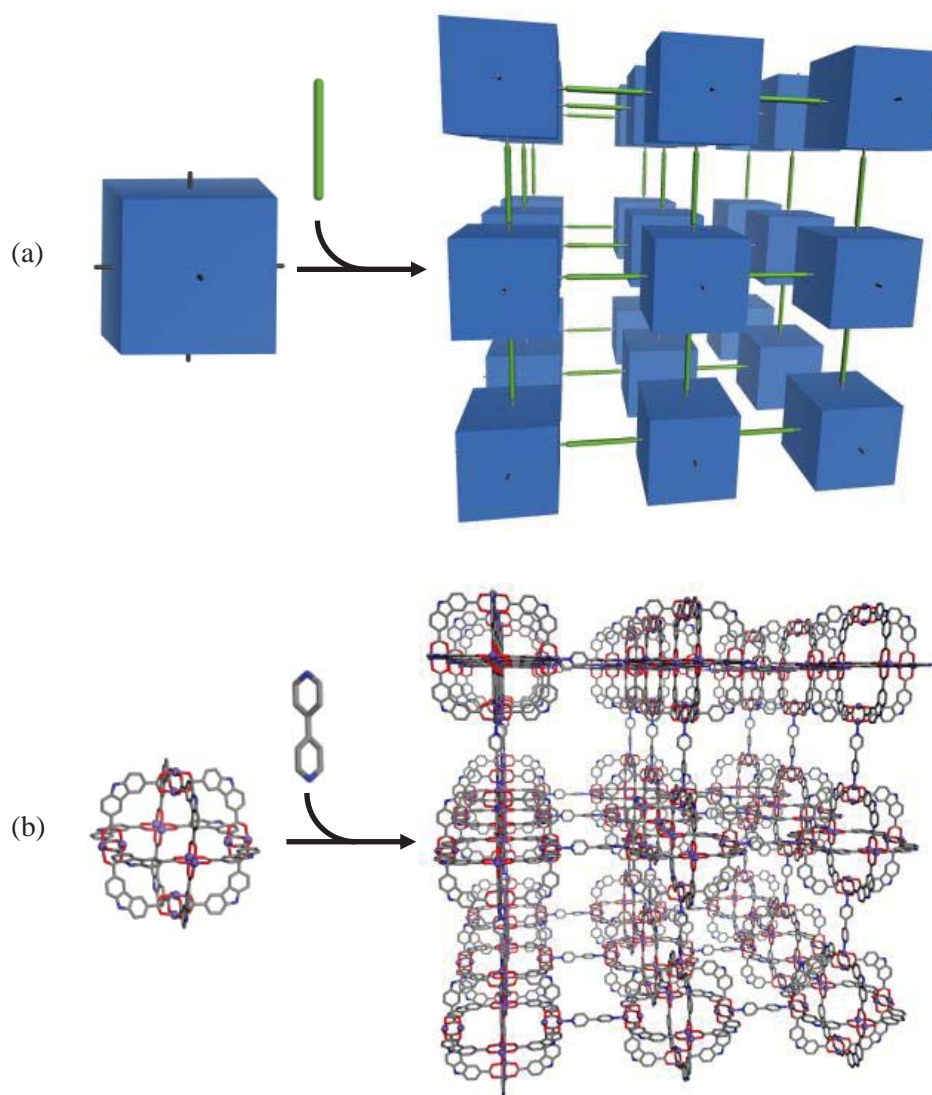


Figure 4.1. (a) Representation of the conversion from discrete MOPs (blue) to 3D MOFs by the insertion of ditopic linkers (green). (b) Octahedral MOP used as a supramolecular unit to create a **pcu-a** topology when assembled with BPY (the other interpenetrated net is not shown).¹³

Su *et al.* reported a similar design in which the cubohemioctahedral MOP-15 is synthesized by the combination of the 120° angular 5-NH₂-1,3-benzenedicarboxylate and the copper paddlewheel.¹⁵ The 12 exterior paddlewheel sites in MOP-15 are axially coordinated to labile H₂O molecules. A 3D MOF is obtained by the self-assembly of MOP-15 and BPY (Figure 4.2). In the extended MOF, the MOPs act as a 12 connecting node attached together to achieve a complex **fcu** net with two types of cavities, a microporous cavity and a mesoporous cavity in a hierarchical system. The first MOP cavity retains the cubohemioctahedra cage (16 Å X 16 Å inter diameter). The second inter MOP cavity is larger (23.18 Å X 32.63Å inter diameter) and exhibits a truncated octahedral shape. The incorporation of both cavities produces 80% void space within the MOF.

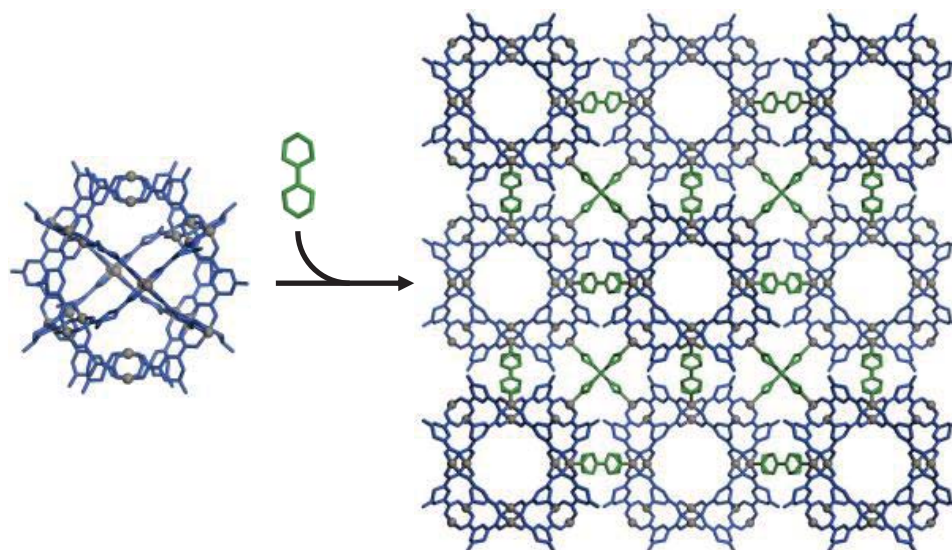


Figure 4.2. Cubohemioctahedral cage MOP-15 connected together with BPY to create a **fcu** net topology.¹⁵

Kitagawa *et al.* reported the sequential self-assembly of the 3D porous pillared paddlewheel framework from a 2D layered structure through linker-insertion transformation in 2004 (Figure 4.3).¹¹ The initial 2D copper paddlewheel structure was synthesized *via* a solvothermal reaction of tetrafluorobenzene-1,4-dicarboxylate and copper (II) formate. The 2D layers were stacked in an AB fashion, in which the copper paddlewheel in layer A lies directly over the void in layer B. Adding 1,4-diazabicyclo[2.2.2]octane (DABCO) to the 2D paddlewheel layers produces the 3D pillared framework, confirmed by X-ray powder diffraction (PXRD). Even though the channels within the original 2D structure are too small to incorporate DABCO (3.8 Å X 3.1 Å), the transformation proceeds even at room temperature, increasing the channel size to 6.3 Å X 6.3 Å and 3.5 Å X 4.7 Å. Because of the AB stacking pattern, upon the introduction of the DABCO pillar, a lateral shift movement between the layers occurs, aligning them into an AA stacking arrangement. This shift movement occurs with only slight degradation of the crystal. This ability to shift laterally was facilitated by the repulsion of the F atoms on the dicarboxylates between layers. In a similar system, Chen and coworkers reported a 2D paddlewheel structure assembled with benzene dicarboxylate (BDC) and zinc paddlewheel, transforming to a 3D pillared paddlewheel structure upon the addition of DABCO at 110 °C for 48 hrs.¹² This process was reported to be reversible; upon leaving the 3D structure in air for 72 hrs, the DABCO was removed from the structure and the 2D structure was obtained again.

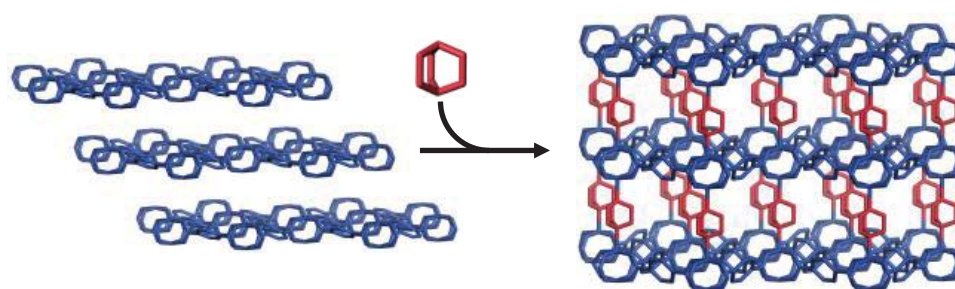


Figure 4.3. Representation of the insertion of the DABCO linker (pink) between the sheets of the 2D paddlewheel framework (blue), creating a 3D porous framework.¹¹

While the previous examples of 2D to 3D transformations were constructed with three different building units (dicarboxylate organic linker, metal node, and dipyridyl pillaring linker), Zhao and coworkers observed that this transformation could also be achieved with a homoligand linker insertion.¹⁶ In their report, a 2D structure is first synthesized by a modified liquid–liquid diffusion of BDC and zinc nitrate hexahydrate in the presence of triethylamine (TEA) to make a Zn_3 SBU that is coordinated equatorially to six BDC linkers. The axial positions of the Zn_3 SBU are coordinated by labile H_2O molecules. Upon introducing these crystals to excess BDC a 3D pillared compound is produced (Figure 4.4). In this structure BDC acts as the lateral linking unit and also the pillaring linker between the 2D sheets. The secondary BDC coordinates vertically to the Zn_3 SBU creating large intersecting channels. This transformation was observed to have the best yields in the presence of TEA and acetic acid (using a different organic amine in the transformation does not produce substantial yields). This suggests that TEA is not only acting as a base to deprotonate the BDC linker, but also as a structure directing agent during the coordination of BDC linkers to the axial Zn_3 position. Additionally, the transformation is dependent on the presence of the initial 2D framework; the direct combination of zinc nitrate hexahydrate with BDC will not produce the desired 3D MOF, showing the importance of having a simple template structure precursor in the assembly of the more complex 3D porous structure.

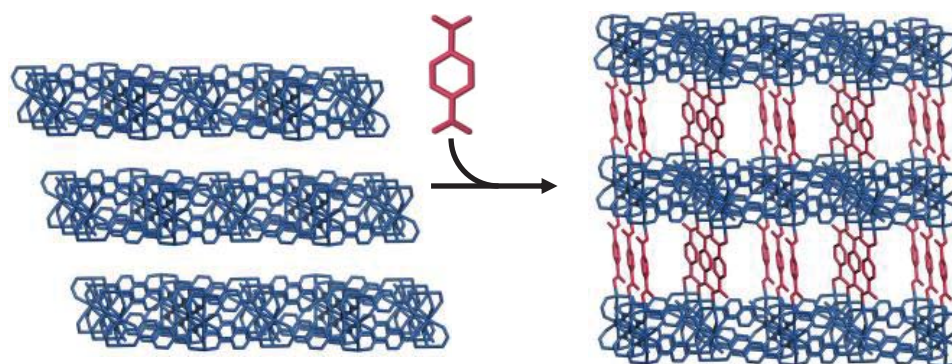


Figure 4.4. Representation of the homoligand insertion of BDC linker (pink) between the sheets of the 2D paddlewheel framework assembled from BDC and the Zn_3SBU creating a 3D porous framework.¹⁶

While linker insertion transformations have mainly been instrumental in increasing the dimensionality of the MOF, this mechanism can also be implemented to induce a change in the pore size and shape without changing the dimensionality of the structure. Suh and coworkers reported the insertion of di(4-pyridyl)-1,2,4,5-tetrazine (DPT) into a 3D *N,N,N',N'*-tetrakis(4-carboxyphenyl)biphenyl-4,4'-diamine and zinc paddlewheel structure SNU-30, transforming it in a single-crystal to single-crystal transformation to another 3D structure, SNU-31.¹⁷ While there is no change in dimensionality of the structure, the pore size is decreased and the shape is changed, which changes the gas adsorption properties. SNU-30 adsorbs N₂, O₂, H₂, CO₂, and CH₄, while SNU-31 selectively adsorbs CO₂ over N₂, O₂, H₂, and CH₄. Also, because DPT is a highly colored linker, the optical properties were changed upon insertion. SNU-31 is a red color, changed from yellow SNU-30.

The work presented herein describes the construction of three isorecticular bilayer MOFs by inserting pillaring linkers within the layers of a 2D paddlewheel MOF. Additionally, the first example of the insertion of a dipyridyl linker in *two sequential steps* to transform a 2D layered MOF to a 2D bilayer, and finally to a 3D MOF is reported.

4.2 Experimental Methods

PPF-1 A mixture of 5,10,15,20-tetrakis(4-carboxyphenyl)-21*H*,23*H*-porphyrin (TCPP) (55.3 mg, 0.07 mmol), zinc nitrate hexahydrate (62.3 mg, 0.21 mmol), and pyrazine (11.2 mg, 0.14 mmol) were added to a mixture of *N,N*-diethyl formamide (DEF) (10.5 mL) and ethanol (3.5 mL) in a capped pressure vessel and heated to 80 °C for 24hrs, followed by slow cooling to room temperature over 9hrs. Yield: 73.3 mg (71% based on porphyrin). Anal. Calcd. for [C₄₈H₂₄N₄O₈Zn₃] 3.3 DEF · 1.5 H₂O · ethanol · 0.4 pyrazine: C, 57.7; H, 5.0; N, 8.9%. Found: C, 57.8; H, 5.0; N, 9.0%.

PPF-27 from PPF-1 A mixture of filtered crystals of PPF-1* (44.1 mg, 0.03 mmol) and 4,4'-bipyridine (BPY) (9.6 mg, 0.06 mmol) were added to a mixture of DEF (4.5 mL) and ethanol (1.5 mL) in a capped vial, swirled by hand to mix, and left to react at room temperature typically for ~ 2hrs. Yield: 45.1 mg (95%). Anal. Calcd. for [C₅₈H₃₂N₆O₈Zn₃] 3DEF · 2 H₂O · ethanol · 0.2 BPY: C, 59.5; H, 5.0; N, 9.0%. Found: C 59.4; H, 5.0; N, 9.0%.

PPF-18 from PPF-1 A mixture of filtered crystals of PPF-1* (14.7 mg, 0.01 mmol) and *N,N'*-di-(4-pyridyl)-1,4,5,8-naphthalenetetracarboxydiimide (DPNI) (8.5 mg, 0.02 mmol) were added to a mixture of DEF (1.5 mL) and ethanol (0.5 mL) in a capped vial, swirled by hand to mix, and left to react at room temperature typically ~ 2hrs. Yield: 21.2 mg (86%). Anal. Calcd. for [C₇₂H₃₆N₈O₁₂Zn₃] 3.6 DEF · 0.5 H₂O · 3.0 ethanol · 0.2 pyrazine: C, 59.0; H, 4.9; N, 9.0%. Found: C, 59.0; H, 4.9; N, 9.0%.

PPF-21 from PPF-1 A mixture of filtered crystals of PPF-1* (14.7 mg, 0.01 mmol) and 3,6-di-(4-pyridyl)-1,2,4,5-tetrazine (DPT) (4.6 mg, 0.02 mmol) were added to a mixture of DEF (1.5 mL) and ethanol (0.5 mL) in a capped vial, swirled by hand to mix, and left

to react at room temperature typically ~ 2hrs. Yield: 16.8 mg (89%). Anal. Calcd. for $[\text{C}_{60}\text{H}_{32}\text{N}_{10}\text{O}_8\text{Zn}_3]$ 1.7 DEF · 2.8 ethanol: C, 58.6; H, 4.49; N, 10.8%. Found C, 58.8; H, 4.52; N, 10.7%.

PPF-4 from PPF-27 A mixture of filtered crystals of PPF-27* (15.8 mg, 0.01 mmol) and BPY (8.0 mg, 0.05 mmol) were added to a mixture of DEF (1.5 mL) and ethanol (0.5 mL) in a capped vial, swirled by hand to mix, and left to react at room temperature typically ~ 2hrs. Yield: 15.0 mg (92%). Anal. Calcd. for $[\text{C}_{63}\text{H}_{36}\text{N}_7\text{O}_8\text{Zn}_3]$ 3.3 DEF · 1.5 H_2O · ethanol: C, 60.3; H, 5.1; N, 8.9%. Found: C, 61.0; H, 5.4; N, 8.9%.

PPF-4 from PPF-1 A mixture of filtered crystals of PPF-1* (14.7 mg, 0.01 mmol) and BPY (3.2 mg, 0.02 mmol) were added to a mixture of DEF (1.5 mL) and ethanol (0.5 mL) in a capped vial, swirled by hand to mix, and left to react at room temperature typically ~ 2hrs. Purity of PPF-27 was confirmed by PXRD.

PPF-27 from PPF-18 A mixture of filtered crystals of PPF-18* (24.5 mg, 0.01 mmol) and BPY (3.2 mg, 0.02 mmol) were added to a mixture of DEF (1.5 mL) and ethanol (0.5 mL) in a capped vial, swirled by hand to mix, and left to react at room temperature typically ~ 2hrs. Purity of PPF-27 was confirmed by PXRD.

PPF-27 from PPF-21 A mixture of filtered crystals of PPF-21* (18.9 mg, 0.01 mmol) and BPY (3.2 mg, 0.02 mmol) were added to a mixture of DEF (1.5 mL) and ethanol (0.5 mL) in a capped vial, swirled by hand to mix, and left to react at room temperature for ~ 2hrs. Purity of PPF-27 was confirmed by PXRD.

*During the pillar insertion reactions, crystals of the synthesized parent structure were filtered and washed with DEF before introducing them into the BPY solution to promote pillar replacement and hinder epitaxial growth.

X-ray powder diffraction (PXRD):

Because the PPF crystals have platelet morphology, the PXRD spectra show significant preferred orientation when mounted onto a traditional flat stage. The relative intensities in the diffraction peaks thus deviate significantly to the simulated PXRD spectra which assume perfectly random orientations of the crystals. To overcome these deviations in intensity, we followed a method developed by Farha *et al.* in which crystals are mounted in a sealed capillary tube, and PXRD was performed while the tube was spinning to remove the preferential orientation.¹⁸ Spinning capillary X-ray diffraction data were taken with a Bruker AXS DA X-ray diffractometer with a GADDS area detector and a conventional copper target X-ray tube set to 40 KV and 40 mA. Crystals were mounted in a 0.5 mm quartz capillary tube with a drop of mother liquor and sealed with epoxy. The PXRD data were collected with an area detector exposed for 10 minutes as rotation frames over 360° in ϕ , a χ angle of 54.74°, and at 2θ values of 21° and 25°. The resulting experimental PXRD patterns were treated for amorphous background scatter and collected into a single pattern, then compared to simulated patterns obtained from the single crystal structures using Mercury software.¹⁹ The program Unit Cell was used to generate the cell parameters of the experimental data.²⁰

Thermogravimetric analysis:

Performed on a Perkin Elmer STA 6000 thermogravimetric analyzer, heated from 25 °C to 800 °C at a rate of 10 °C/minute under N₂ atmosphere.

Elemental analysis:

Data was performed by MidwestMicro Labs LLC.

¹H NMR analysis:

Performed on a Bruker FT-NMR spectrometer (400 MHz).

Acid Digestion Study:

In order to observe the amount of inserting linker inside the daughter structures, samples of the daughter structures were digested in acid according to the method reported by Cohen.²¹ Approximately 5 mg of sample was filtered and washed ≥ 3 times with DMF and dried under vacuum at 90 °C overnight and digested with sonication in 500 μ L of DMSO-*d*₆ and 100 μ L of dilute DCl (10 μ L of 35% DCl in D₂O diluted with 500 μ L of DMSO-*d*₆). ¹H NMR spectra were obtained from the resulting solution.

4.3 Results and Discussion

In this investigation into linker insertion in PPF systems, the 2D layered structure PPF-1 was chosen as a parent MOF because it has multiple axial coordination sites (*e.g.* paddlewheel and porphyrin core sites) available for connection by dipyrindyl linkers (Figure 4.5).²² PPF-1 is synthesized following the published method using pyrazine as a directing agent, aiding in the AB stacking pattern observed by powder and single crystal X-ray diffraction spectra (Figure 4.5).²² Without pyrazine in the experimental procedure, a different phase is observed in the PXRD pattern. Thus, it is believed that pyrazine is needed for the construction of the AB stacked PPF-1 structure. Pyrazine, however was not observed in the single crystal structure and elemental analysis indicates only 0.4 pyrazine molecules per unit cell indicating that it acts as a guest molecule instead of a coordinated linker. To quantify how much pyrazine was in PPF-1 structure, we digested samples of PPF-1 in acid and obtained a ¹H NMR spectrum of the resulting solution (Figure 4.6). Analysis of the integration of porphyrin signals to pyrazine signals indicate a porphyrin to pyrazine ratio of 1:0.3 which supports the conclusion that pyrazine is a guest and not a coordinated linker which would yield a porphyrin to pyrazine ratio of 1:1. The layers of PPF-1 are stacked in an AB fashion creating *I4/mmm* space group symmetry.²² On the one hand, the zinc ion within the porphyrin prefers a square pyramidal coordination geometry and is coordinated once axially by a solvent molecule. On the other hand, the zinc paddlewheel SBU prefers an octahedral coordination geometry and is coordinated twice axially by two solvent molecules.²²

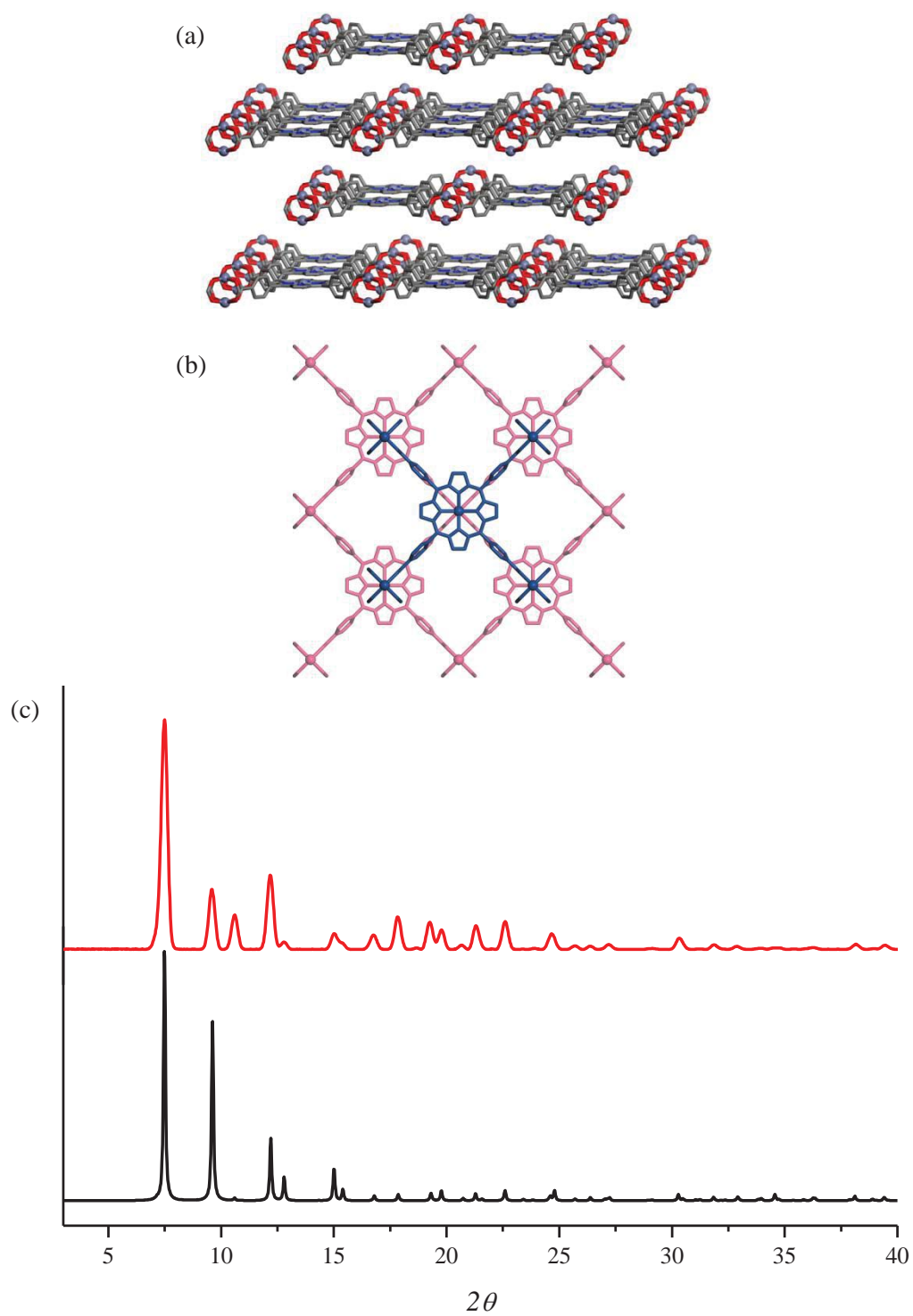


Figure 4.5. (a) Representation of single crystal structure of PPF-1. (b) Alternative representation of PPF-1 highlighting the AB stacking arrangement. (c) Simulated (bottom) and experimental (top) PXRD patterns for PPF-1.

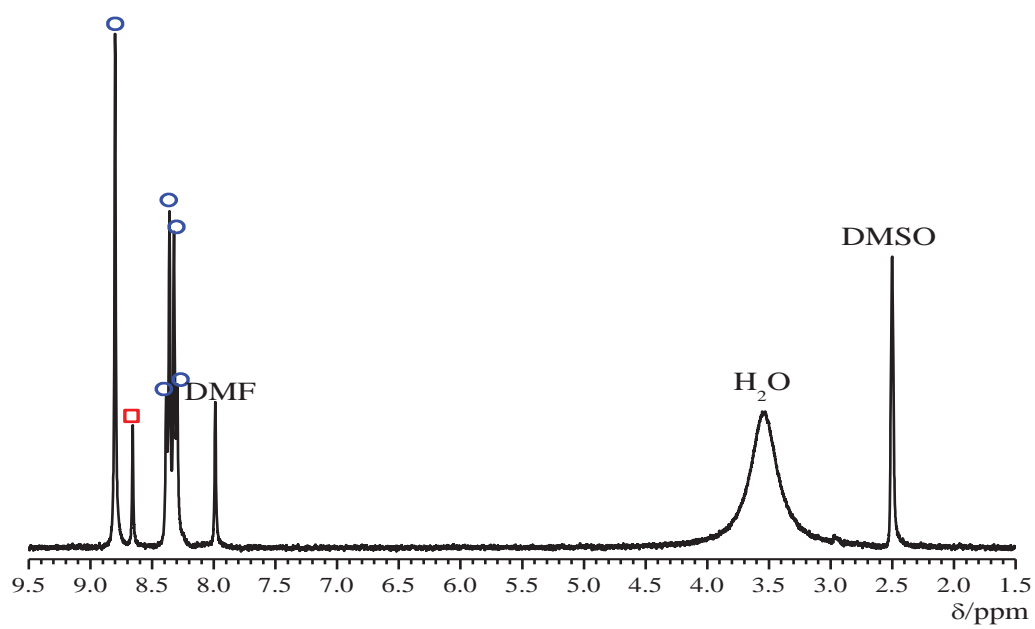


Figure 4.6. ^1H NMR spectra of digested PPF-1. Red squares and blue circles represent signals of pyrazine and ZnTCPP respectively.

For the initial insertion reaction, crystals of PPF-1 were introduced to a solution containing BPY, as the inserting linker and left for 2 hrs at room temperature. During this time, BPY pillaring linkers were able to penetrate into the 2D layers of PPF-1. As shown from Figure 4.7, the single-phase structure, PPF-27, was obtained and confirmed by PXRD. PPF-27 retains the AB stacking of PPF-1 creating $P4/nmm$ symmetry. This demonstrates that during this transformation a templating effect occurs in which it is possible to insert linkers without the lateral shear movement of the PPF sheets. In PPF-27 the zinc ion within the porphyrin core is coordinated once axially by BPY to the paddlewheel of the next subsequent PPF layer. The Zn paddlewheel SBU is coordinated once axially by BPY and once by a solvent molecule. To quantify the occupation of the BPY linker in PPF-27, crystals were digested in acid following the same method described above and analyzed by ^1H NMR (Figure 4.8). Analysis of the ^1H NMR spectra shows 93% occupation of BPY linker in PPF-27. It should be noted that PPF-27 is not accessible via the traditional one-pot synthetic route. This linker insertion route is a second SSA approach to achieve this structure (See chapter 3 for the linker replacement route).^{7,23}

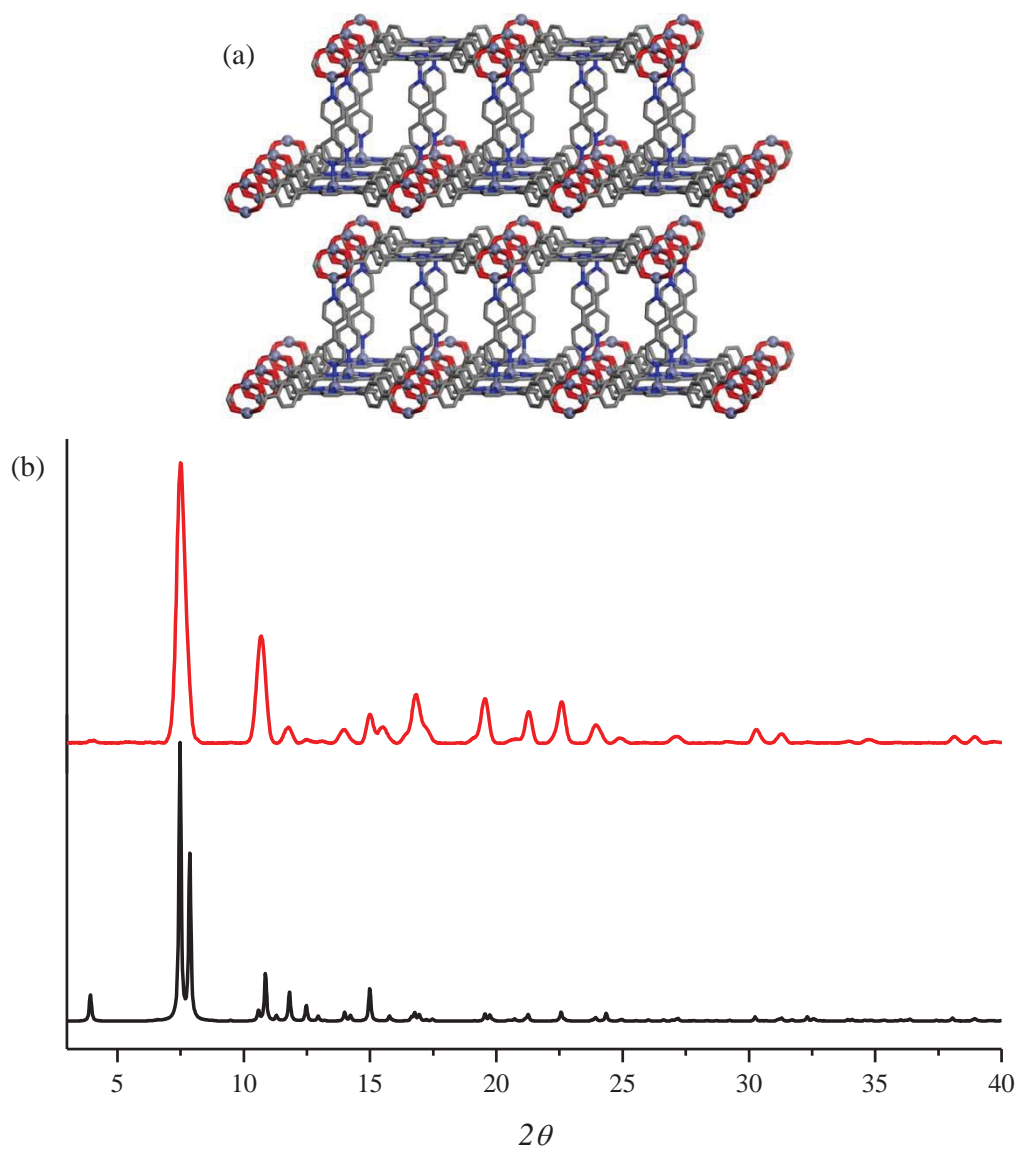


Figure 4.7. (a) Representation of single crystal structure of PPF-27. (b) Simulated (bottom) and experimental (top) PXRD patterns of PPF-27.

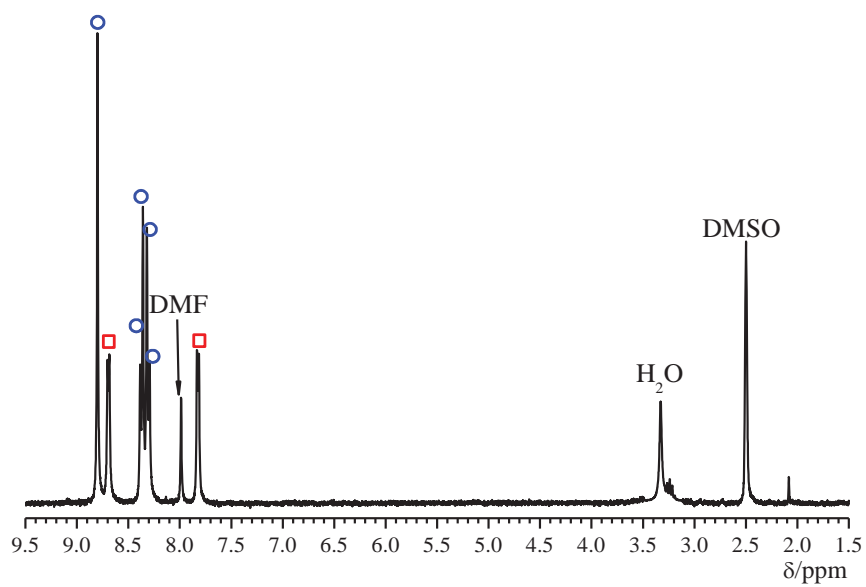


Figure 4.8. ^1H NMR spectra of digested PPF-27. Red squares and blue circles represent signals of BPY and ZnTCPP respectively.

The linker insertion mechanism was also investigated using longer dipyridyl linkers: DPT and DPNI. Similar syntheses were performed with these linkers to afford single-phase of the 2D bilayer structures PPF-21 and PPF-18 respectively as confirmed by PXRD (Figures 4.9 and 4.10 respectively). The crystal structures of these two phases were previously reported.^{7,23} The templating effect of PPF-1 is also observed in PPF-21 and PPF-18. Both PPF-21 and PPF-18 are AB stacked creating $P4/nmm$ symmetry. To quantify the occupation of DPT and DPNI in PPF-21 and PPF-18 respectively, crystals were digested in acid and analyzed similar to that of PPF-27 (Figures 4.11 and 4.12 respectively). Analysis of the ^1H NMR spectra shows 87 and 89% occupation of DPT and DPNI linker in PPF-21 and PPF-18 respectively. It is noteworthy that single phases of PPF-21 and PPF-18 are only obtained through this two-step SSA. Using the traditional one-step method, these phases are contaminated by other secondary phases, *e.g.* framework isomer PPF-19.²³ This linker insertion method thus represents a unique synthetic route to access single-phase isorecticular bilayer MOFs.

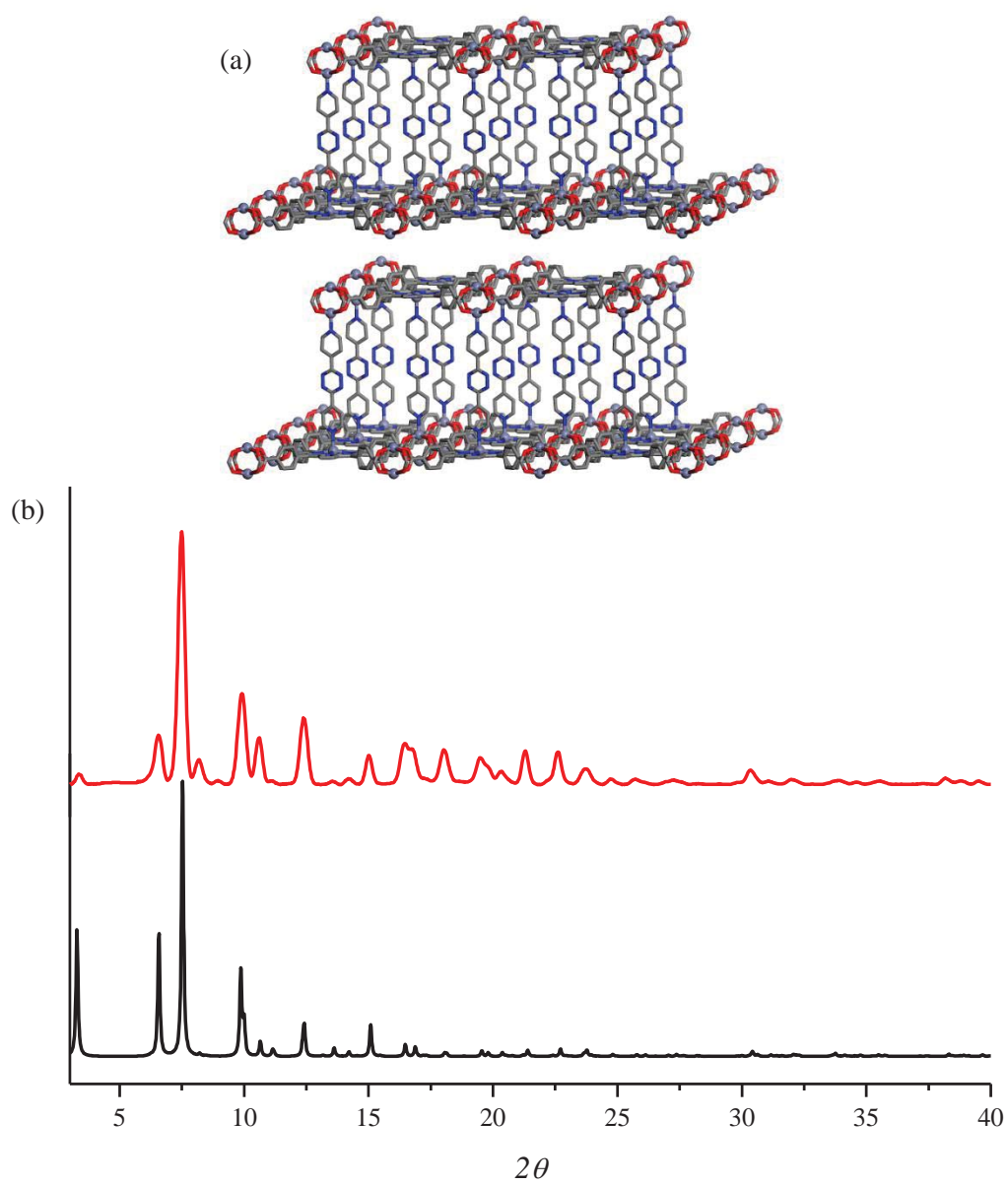


Figure 4.9. (a) Representation of single crystal structure of PPF-21. (b) Simulated (bottom) and experimental (top) PXRD patterns of PPF-21.

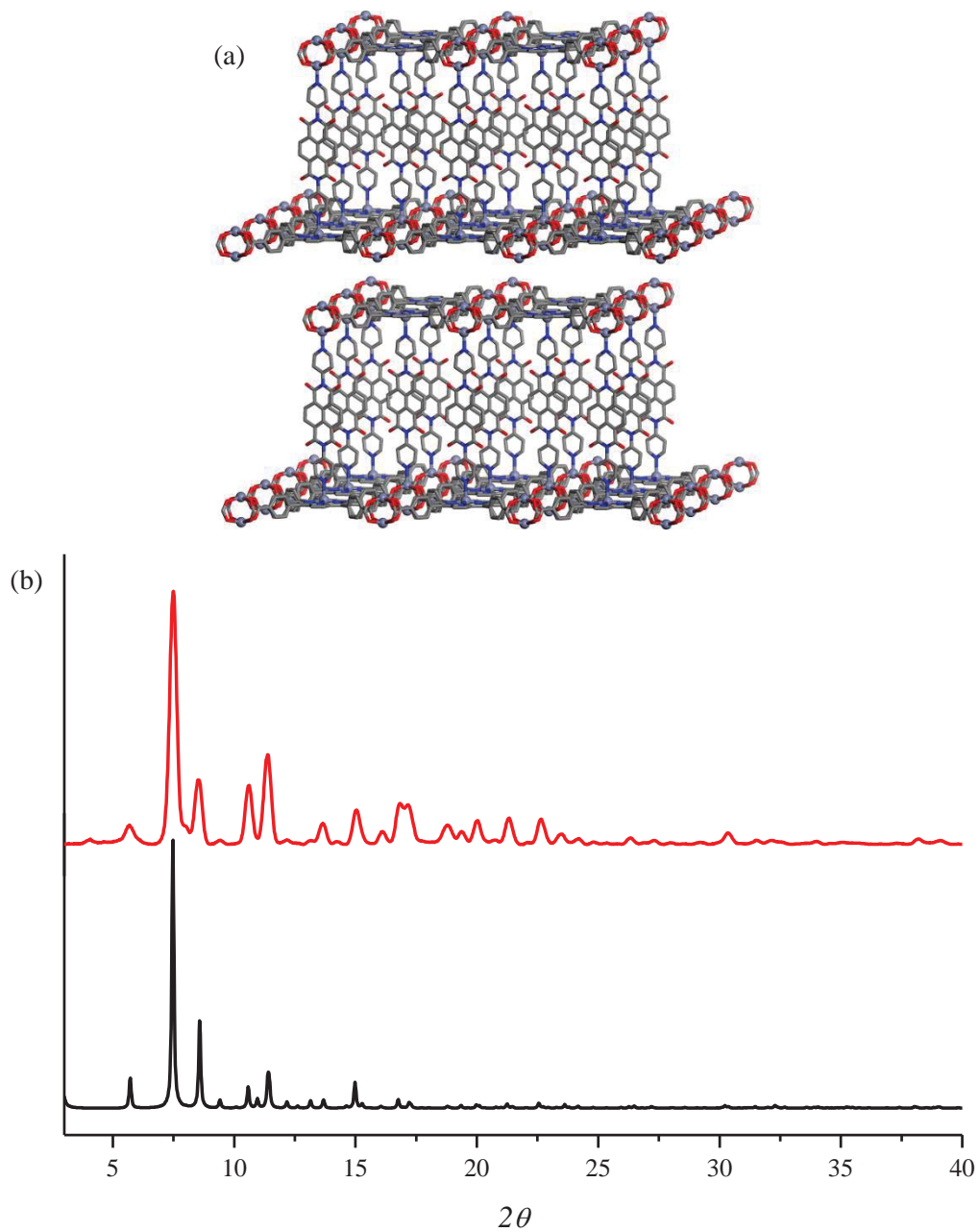


Figure 4.10. (a) Representation of single crystal structure of PPF-18. (b) Simulated (bottom) and experimental (top) PXRD patterns of PPF-18.

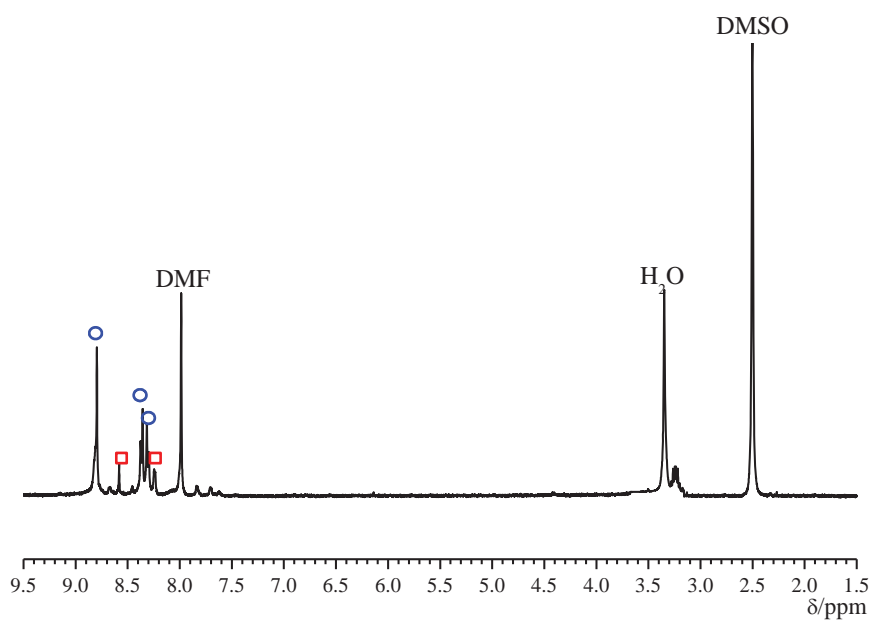


Figure 4.11. ¹H NMR spectra of digested PPF-21. Red squares and blue circles represent signals of DPT and ZnTCPP respectively.

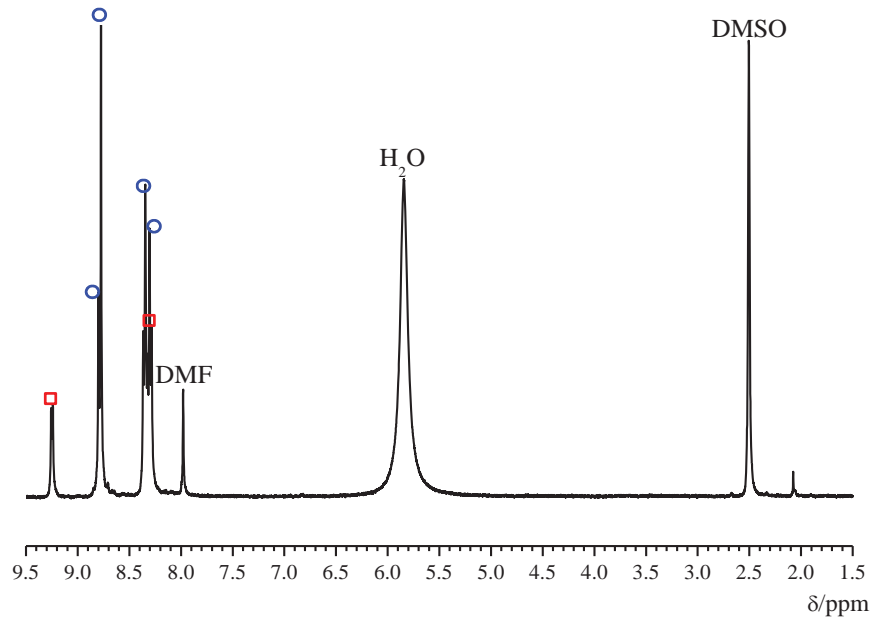


Figure 4.12. ¹H NMR spectra of digested PPF-18. Red squares and blue circles represent signals of DPNI and ZnTCPP respectively.

Following the construction of the bilayer MOFs, we envisioned that an additional linker insertion into these bilayer MOFs might be possible because there are remaining metal nodes for further coordination. Although additional coordination to the zinc ion within the porphyrin core is not possible within the bilayer structure, the paddlewheel SBUs still have one axial position available for further connection by replacing solvent molecules with BPY pillars.²⁴ If the bilayers were to shear laterally to connect adjacent paddlewheel SBUs, the fully coordinated ABBA stacked PPF-4 can be obtained.²⁵ To test this hypothesis, crystals of the BPY pillared bilayer PPF-27 were washed with DEF and then introduced into a DEF/ethanol solution containing excess amounts (over 5 equivalents) of BPY and left to react for another 2hrs at room temperature. The result was the formation of single phase 3D ABBA stacked PPF-4 as confirmed by PXRD (Figure 4.13). The occupancy of BPY in PPF-4 was analyzed similar to before showing 95% occupation (Figure 4.14). Although a significant lateral shear movement of *ca.* 11.7 Å is required for this transformation,^{7,24} by providing a large excess of pillaring linkers, we observe the further coordinated ABBA stacked PPF-4. Other groups also observed similar shear movement in MOFs. Kitagawa and co-workers previously noticed a lateral movement of *ca.* 7.7 Å upon the insertion of the dabco pillars between the 2D paddlewheel sheets constructed from 2,3,5,6-tetrafluorobenzene-1,4-dicarboxylate (tfbdc).¹¹ These authors attributed the lateral shear movement to repulsion between the fluorine atoms between adjacent tfbdc molecules. The transformation from 2D PPF-27 to 3D PPF-4 shows that the interaction between the adjacent bilayers is not strong enough to prevent incorporation of BPY pillars, thus allowing lateral shear movement. It should be

noted that PPF-4 can be synthesized directly if excess BPY is added straight to PPF-1 promoting both pillaring steps simultaneously (Figures 4.15 and 4.16).

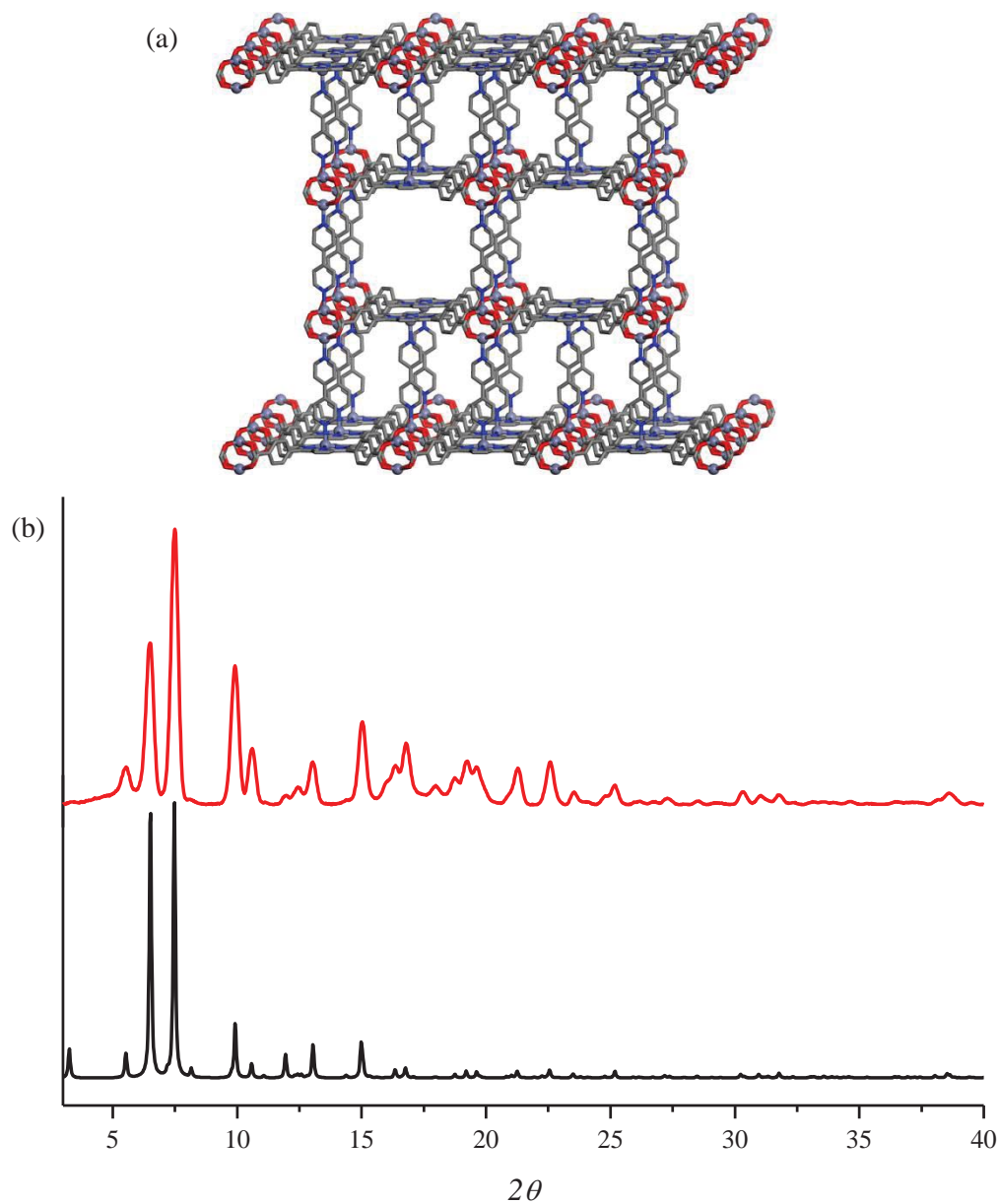


Figure 4.13. (a) Representation of single crystal structure of PPF-4. (b) Simulated (bottom) and experimental (top) PXRD patterns of PPF-4 synthesized from PPF-27.

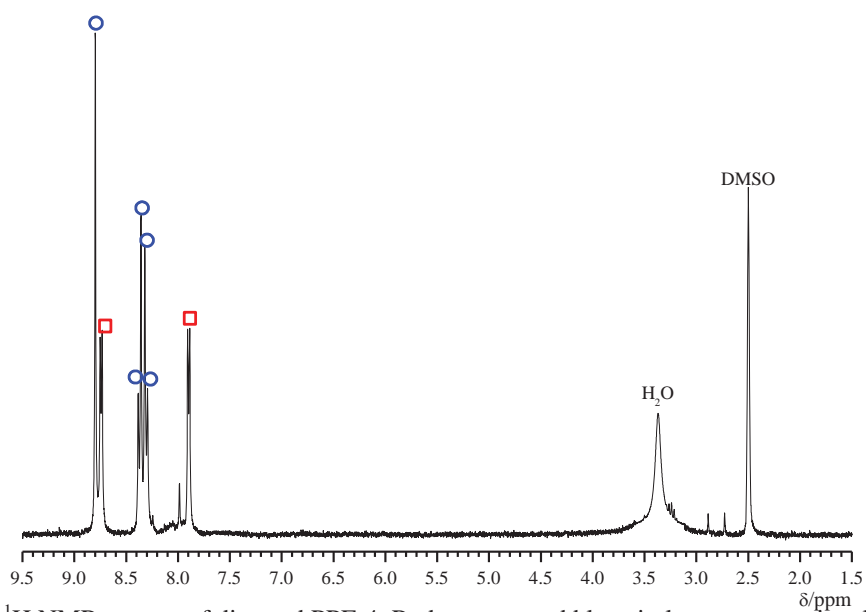


Figure 4.14. ^1H NMR spectra of digested PPF-4. Red squares and blue circles represent signals of BPY and ZnTCPP respectively.

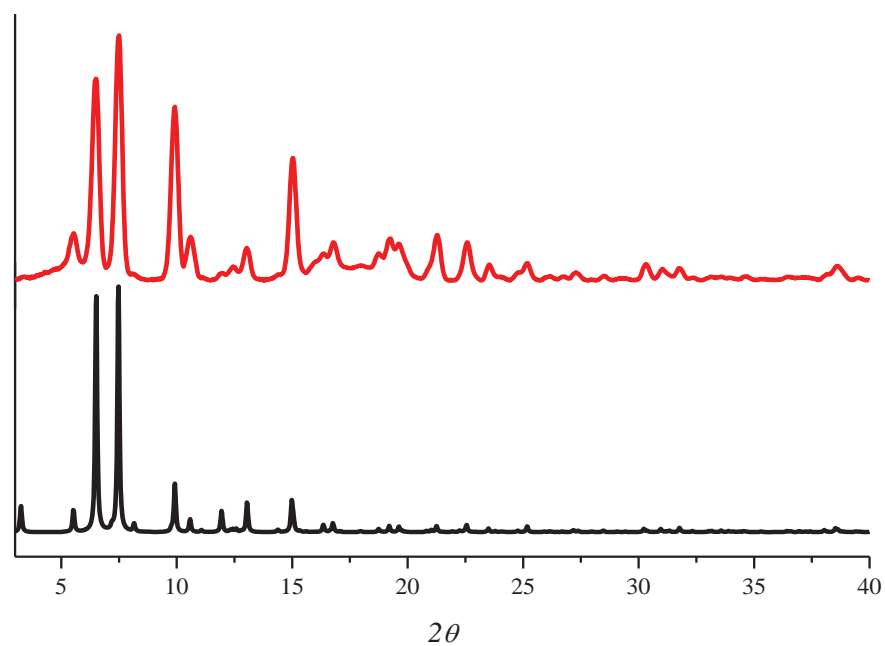


Figure 4.15. Simulated (bottom) and experimental (top) PXRD patterns of PPF-4 synthesized from PPF-1.

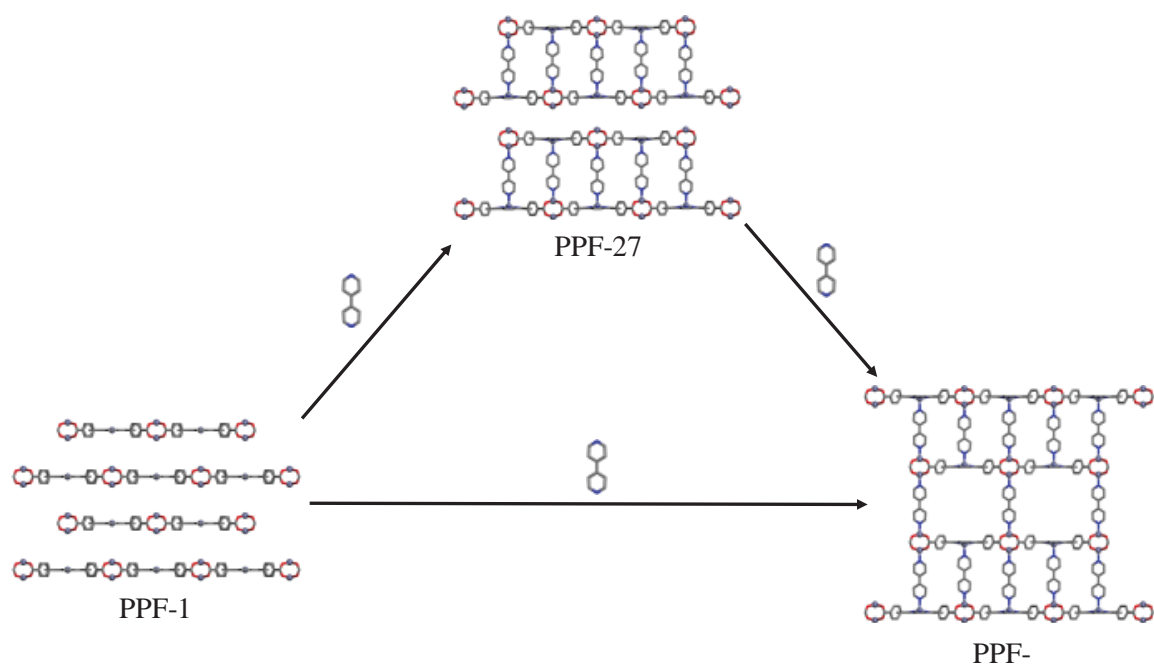


Figure 4.16. Schematic representation of stepwise linker insertion from PPF-1 to PPF-4

This stepwise insertion for the overall construction of PPF-4 *via* the linker insertion method is akin to a phenomenon observed in LDH intercalation chemistry called the “staging” effect.^{8,9} Staging is a phenomenon in which linkers will insert between some layers fully while others stay empty initially, and in a second step, fill the additional layers.⁹ The axial sites of PPF-1 are coordinated to solvent molecules defining it as a 1st stage layered material. After the first insertion, every other layer is coordinated axially by BPY making a 2nd stage layered material. After the second insertion, every available axial site is coordinated with BPY returning it to a 1st stage layered material (Figure 4.17).⁹ This is the first example of the staging effect within MOF material.

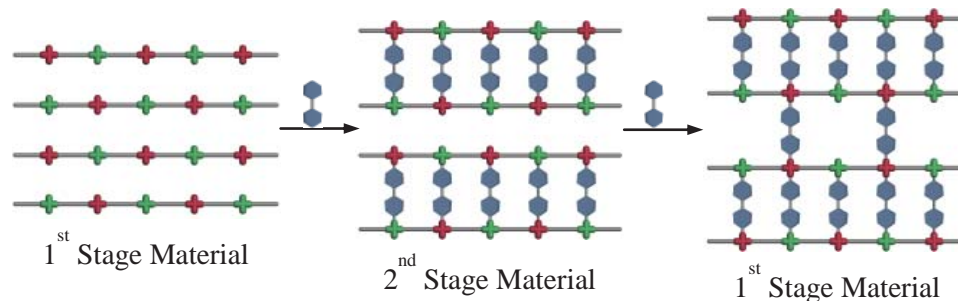


Figure 4.17. Schematic Representation of staging effect exhibited in linker insertion transformation in PPFs. Red crosses represent paddlewheel SBUs, green crosses represent ZnTCPP, and blue dumbbells represent BPY pillars.

The reason for the staging effect being possible in PPF structures is because of the two coordination sites available for coordination in PPF-1 allowing for two separate types of connectivity during linker insertion. During the initial coordination by dipyriddy linkers, the AB connectivity between the layers is fully saturated to create the bilayer structure PPF-27. In order to further coordinate, the lateral shear movement is necessary to align the paddlewheels for an AA connection. A third type of connection, A'A' connection, was not observed in these trials, but is theoretically possible. However, traditional paddlewheel structures, having only one type of coordination site, would be more difficult to separate different coordination events, *i.e.* every connection is a paddlewheel–paddlewheel AA connection (Figure 4.18).



Figure 4.18. The difference in linker insertion connectivity between frameworks with one single metal node and two different metal nodes.

The transformation from bilayer structure to ABBA 3D structure turns out to be a very difficult transformation for the larger pillar systems such as DPT and DPNI.

Although ABBA counterparts for DPT and DPNI can be synthesized *via* a one-pot reaction,²³ in both cases of PPF-21 and PPF-18, regardless of the amount of DPT and DPNI introduced, the resulting phases remained as the initial bilayer structures. This is a rather peculiar phenomenon, considering that 1st stage pillar insertion was not a problem even for the bulkier DPNI pillar. Currently we do not have a clear explanation why the 2nd stage pillar insertion is harder for the longer pillars such as DPT and DPNI. However, upon attempting to insert the shorter BPY pillars between the bilayers of DPT-based PPF-21 or DPNI-based PPF-18, we obtained BPY-based PPF-27, demonstrating replacement (instead of insertion) of pillars (Table 4.1, Figure 4.19).

Table 4.1. Amounts of reactants and resulting structures for the linker insertion investigation of PPFs.

Starting Structure	Pillar	Pillar Amt. (equivalents)	Phase(s) Identified ^a
PPF-1	BPY	0.8	PPF-1 + PPF-27
PPF-1	BPY	1.0	PPF-1 + PPF-27
PPF-1	BPY	2.0	PPF-27
PPF-1	BPY	4.0	PPF-27 + PPF-4
PPF-1	BPY	5.0	PPF-4
PPF-1	DPNI	1.0	PPF-1 + PPF-18
PPF-1	DPNI	2.0	PPF-18
PPF-1	DPNI	5.0	PPF-18
PPF-1	DPT	1.0	PPF-1 + PPF-21
PPF-1	DPT	2.0	PPF-21
PPF-1	DPT	5.0	PPF-21
PPF-27	BPY	1.0	PPF-27
PPF-27	BPY	2.0	PPF-27
PPF-27	BPY	4.0	PPF-27 + PPF-4
PPF-27	BPY	5.0	PPF-4
PPF-18	DPNI	5.0	PPF-18
PPF-21	DPT	5.0	PPF-21
PPF-18	BPY	2.0	PPF-27
PPF-21	BPY	2.0	PPF-27

^a based upon PXRD pattern analysis

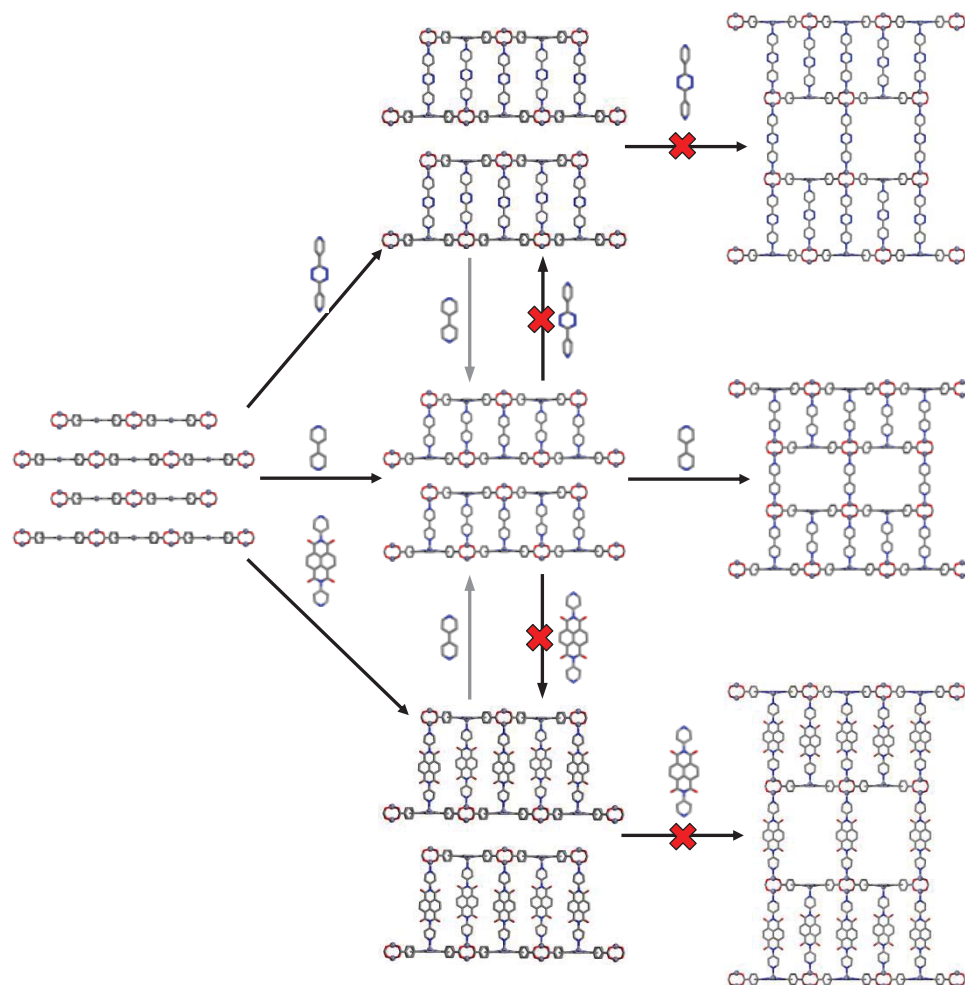


Figure 4.19. Schematic representation of all attempted linker insertion reactions in PPFs. Red crosses denote reactions which were not successful. Grey arrows denote a linker replacement reaction which was previously reported (see Chapter 3).

4.4 Conclusion

We have successfully synthesized an isorecticular series of 2D bilayers through an SSA approach in which pillaring linkers are inserted in between every other layer of the 2D layered structure PPF-1. The first linker insertion of BPY creates single phase PPF-27, which is not accessible *via* a one-pot synthetic strategy. Upon introducing PPF-27 to excess BPY linkers, the 3D ABBA stacked PPF-4 structure is constructed. This is a simple example illustrating great control over the overall construction of the MOF, by separating the assembly into three sequential steps. A staging effect was observed in the sequential steps of PPF-1 to PPF-27 and further to PPF-4, which is commonly observed in other layered material such as LDHs.

4.5 References

- (1) (a) Murray, L. J.; Dincă, M.; Long, J. R. *Chem. Soc. Rev.* **2009**, *38*, 1294. (b) Czaja, A. U.; Trukhan, N.; Müller, U. *Chem. Soc. Rev.* **2009**, *38*, 1284. (c) Herm, Z. R.; Swisher, J. A.; Smit, B.; Krishna, R.; Long, J. R. *J. Am. Chem. Soc.* **2011**, *133*, 5664. (d) Wang, X.-S.; Meng, L.; Cheng, W.; Kim, C.; Wojtas, L.; Chrzanowski M.; Chen, R.-S.; Zhang, X. P.; Ma, S. *J. Am. Chem. Soc.* **2011**, *133*, 16322.
- (2) (a) Farha, O. K.; Shultz, A. M.; Sarjeant, A. A.; Nguyen, S. T.; Hupp, J. T. *J. Am. Chem. Soc.* **2011**, *133*, 5652. (b) Lee, J. Y.; Farha, O. K.; Roberts, J.; Sheidt, K. A.; Nguyen, S. T.; Hupp, J. T. *Chem. Soc. Rev.* **2009**, *38*, 1450. (c) Yoon, M.; Srirambalaji, R.; Kim K. *Chem. Rev.* **2012**, *112*, 1196. (d) Ma, L.; Abney, C.; Lin, W. *Chem. Soc. Rev.* **2009**, *38*, 1248. (e) Uemura, T.; Yanai, N.; Kitagawa, S. *Chem. Soc. Rev.* **2009**, *38*, 1228.
- (3) (a) Kreno, L. E.; Leong, K.; Farha, O. K.; Allendorf, M.; Van Duyne, R. P.; Hupp, J. T. *Chem. Rev.* **2012**, *112*, 1105. (b) Rocha, J.; Carlos, L. D.; Paz, F. A. A.; Ananias, D.

- Chem. Soc. Rev.* **2011**, *40*, 926. (c) Ciu, Y.; Yue, Y.; Qian, G.; Chen, B. *Chem. Rev.* **2012**, *112*, 1126. (d) Lan, A.; Li, K.; Wu, H.; Olson, D. H.; Emge, T. J.; Ki, W.; Hong, M.; Li, J. *Angew. Chem. Int. Ed.* **2009**, *48*, 2334. (e) Pramanik, S.; Zheng, C.; Zhang, X.; Emge, T. J.; Li, J. *J. Am. Chem. Soc.* **2011**, *133*, 4153.
- (4) (a) Moulton, B.; Zaworotko, M. J. *Chem. Rev.* **2001**, *101*, 1629. (b) O’Keeffe, M.; Yaghi, O. M. *Chem. Rev.* **2001**, *112*, 675. (c) Tranchemontagne, D. J.; Mendoza–Cortés, J. L.; O’Keeffe, M.; Yaghi, O. M. *Chem. Soc. Rev.* **2009**, *38*, 1257.
- (5) Makal, T. A.; Yakovenko, A. A.; Zhou, H. –C. *J. Phys. Chem. Lett.* **2011**, *2*, 1682.
- (6) Burnett, B. J.; Choe, W. *Dalton Trans.* **2012**, *41*, 3889.
- (7) Burnett, B. J.; Barron, P. M.; Hu, C.; Choe, W. *J. Am. Chem. Soc.* **2011**, *133*, 9984.
- (8) Williams, G. R.; Khan, A. I.; O’Hare, D. *Struct. Bond* **2006**, *119*, 161.
- (9) (a) Williams, G. R.; O’Hare, D. *J. Mater. Chem.* **2006**, *16*, 3065. (b) Feng, Y. J.; Williams, G. R.; Leroux, F.; Traviot–Guého, C.; O’Hare, D. *Chem. Mater.* **2006**, *18*, 4312. (c) Williams, G. R.; Fogg, A. M.; Sloan, J.; Traviot–Guého, C.; O’Hare, D. *Dalton Trans.* **2007**, *36*, 3499.
- (10) (a) Ragavan, A.; Khan, A. I.; O’Hare, D. *J. Phys. Chem. Solids* **2006**, *67*, 983. (b) Williams, G. R.; Dunbar, T. G.; Beer, A. J.; Fogg, A. M.; O’Hare, D. *J. Mater. Chem.* **2006**, *16*, 1231. (c) Costa, F. R.; Leuteritz, A.; Wagenknecht, U.; Auf der Landwehr, M.; Jehnichen, D.; Haeussler, L.; Heinrich, G. *Appl. Clay Sci.* **2009**, *44*, 7. (d) McIntyre, L. J.; Jackson, L. K.; Fogg, A. M. *J. Phys. Chem. Solids* **2008**, *69*, 1070. (e) Tanaka, T.; Nishimoto, S.; Kameshima, Y.; Matsukawa, J.; Fujita, Y.; Takaguchi, Y.; Matsuda, M.; Miyake, M. *J. Solid State Chem.* **2010**, *183*, 479.

- (11) Kitaura, T.; Iwahori, F.; Matsuda, R.; Kitagawa, S.; Kubota, Y.; Takata, M.; Kobayashi, T. C. *Inorg. Chem.* **2004**, *43*, 6522.
- (12) Chen, Z.; Xiang, S.; Zhao, D.; Chen, B. *Cryst. Growth Des.* **2009**, *9*, 5293.
- (13) Li, J. -R.; Timmons, D. J.; Zhou, H. -C. *J. Am. Chem. Soc.* **2009**, *131*, 6368.
- (14) Zaworotko, M. J. *Nat. Chem.* **2009**, *1*, 267.
- (15) Wang, H. -N.; Meng, X.; Yang, G. -S.; Wang, X. -L.; Shao, K. -Z.; Su, Z. -M.; Wang, C. -G. *Chem. Commun.* **2011**, *47*, 7128.
- (16) Sun, J.; Zhou, Y.; Fang, Q.; Chen, Z.; Weng, L.; Zhu, G.; Qiu, S.; Zhao, D. *Inorg. Chem.* **2006**, *45*, 8677.
- (17) Park, H. J.; Cheon, Y. E.; Suh, M. P. *Chem. Eur. J.* **2010**, *16*, 11662.
- (18) Farha, O. K.; Sultz, A. M.; Sargeant, A. A.; Nguyen, S. T.; Hupp, J. T. *J. Am. Chem. Soc.* **2011**, *133*, 5652.
- (19) <http://www.ccdc.cam.ac.uk/products/mercury/>
- (20) <http://www.ccp14.ac.uk/ccp/web-mirrors/crust/astaff/holland/UnitCell.html>
- (21) Wang, Z.; Tanabe, K. K.; Cohen, S. M. *Inorg. Chem.* **2009**, *48*, 296.
- (22) Choi, E. -Y.; Wray, C. A.; Hu, C.; Choe, W. *CrystEngComm* **2009**, *11*, 553.
- (23) Chung, H.; Barron, P. M.; Novotny, R. W.; Son, H. -T.; Hu, C.; Choe, W. *Cryst. Growth Des.* **2009**, *9*, 3327.
- (24) We have only observed pentacoordinated Zn within the porphyrin core in our PPF structures. See Ref. 6.
- (25) Choi, E. -Y.; Barron, P. M.; Novotny, R. W.; Son, H. -T.; Hu, C.; Choe, W. *Inorg. Chem.* **2009**, *48*, 426.

CHAPTER 5

POST-SYNTHETIC METAL METATHESIS

5.1 Introduction

As discussed in Chapter 1, the structures and internal pore environments in MOF material can be in principle controlled through judicious selection of metal ion nodes and organic linkers. While this has been highly successful in creating thousands of structures over the past decade, the conventional direct synthesis often involves significant trial and error to achieve a particular desired structure. Furthermore, the lack of control during one-pot direct syntheses poses considerable difficulties, often producing materials that do not possess the preferred interior decoration or structure. These drawbacks have led to the consideration of post-synthetic and sequential self-assembly approaches as a viable option for the preparation of new analogues of the porous structures. In chapters 3 and 4, the sequential self-assembly through linker replacement and linker insertion were discussed. In this chapter, the metathesis (or replacement) of metal ions integral to the structure of the MOFs will be discussed. In this post-synthetic metal metathesis (PSMM), the ions used in constructing the secondary building units (SBUs) are replaced without altering the basic structure or topology of the frameworks. Utilizing PSMM can change the chemical and structural properties of the MOF, making them more appropriate for industrial applications.¹⁻⁶ Although this idea seems simple and feasible, PSMM reactions in porous MOFs are still rare. Since this process involves breaking and reforming multiple coordination bonds, this process often results in destroying the single

crystallinity of the material.⁷ There are some notable examples, however, of both partial and full PSMM in MOFs resulting in a single-crystal to single-crystal transformation.

Kim *et al.* was the first to report PSMM in which the initial MOF was created by the solvothermal reaction of cadmium nitrate tetrahydrate and an ethyl substituted truxene tricarboxylic acid organic linker creating a cubic network similar to that of sodalite.¹ The SBU contained in this structure is a square planar Cd_4O which connects to the carboxylate groups of eight surrounding organic ligands. Upon immersing this MOF in an aqueous lead nitrate solution for a week, a complete metathesis of the structural cadmium ions with lead ions was observed by inductively coupled plasma atomic emission spectroscopy (ICP-AES) and subsequently by single-crystal X-ray diffraction. Interestingly, the metal ion metathesis is reversible upon soaking the lead analogue in a cadmium nitrate solution for up to three weeks. Additionally, PSMM was proven possible using dysprosium and neodymium ions as well.

Kim *et al.* followed this work with a later report detailing a new framework (POST-65) being able to undergo single-crystal to single-crystal PSMM.² POST-65 is synthesized by a traditional solvothermal reaction of manganese chloride and hexamethyltruxene tricarboxylic acid organic linker creating a sodalite-like cubic network centered on a Mn_4Cl SBU connected to 8 organic ligands each. Indeed PSMM was achieved with a number of replacing metal ions including Fe(III), Co(II), Ni(II), and Cu(II) as confirmed by ICP-AES and single-crystal X ray diffraction. The hydrogen adsorption properties of POST-65(Fe) show significant improvement in higher hydrogen-uptake and stronger bond enthalpy over the other analogues which is a result of the higher affinity of Fe(III) for H_2 .

The groups of Zhao and Lah both reported that by using PSMM to induce a single-crystal to single-crystal transformation, where the sorption properties of the resulting materials were drastically changed.^{3,4} Zhao reported by changing structural zinc ions in the SBU with copper ions increased the structural integrity of the resulting MOF.³ Thus, the pores were well maintained upon activation, significantly improving the sorption properties. Lah *et al.* expanded on this idea to partially metathesized frameworks.⁴ In their report, core shell structures were achieved if PSMM wasn't allowed to fully react as evidenced by optical microscopy, ICP-AES and XRD. The parent zinc or cobalt structures suffered from pore collapse during activation and show no significant sorption of N₂. Using PSMM to exchange the SBU ions to either copper or nickel drastically increased the structural integrity and the sorption properties. Interestingly, if a core/shell structure was created by stopping the PSMM process before it is finished similarly increased sorption properties were observed. The partial metathesis influenced both the framework stability of the shell region and also the framework stability of the core region of the structure.

Zou *et al.* reported PSMM of a fully coordinated paddlewheel structure in a single-crystal to single-crystal transformation.⁵ Two parent structures, SUMOF-1-Zn and SUMOF-1-Co were synthesized by solvothermal reaction between zinc nitrate hexahydrate or cobalt nitrate hexahydrate respectively, triyl-benzoic acid and pyridine. The resulting crystal structures are isostructural 3D Pt₃O₄ net containing paddlewheel SBUs that are equatorially coordinated to the carboxylates of the triyl-benzoic acid and axially coordinated to the pyridine functional groups of bipyridine. Immersing the parent structure SUMOF-1-Zn in nickel nitrate afforded the partially replaced SUMOF-1-

Ni:2Zn. This replacement was found to be reversible. Similarly SUMOF-1-Zn could be partially replaced when immersed in cobalt nitrate to afford SUMOF-1-Co:2Zn. PSMM of SUMOF-1-Zn and SUMOF-1-Co in copper nitrate trihydrate solution resulted in the full replacement to SUMOF-1-Cu. This process however was not reversible, showing the relative stability of copper based paddlewheels to be greater than that of zinc, cobalt, and nickel.

Finally Dincă *et al.* envisioned using PSMM to deliberately create an unsaturated metal ion with unusual geometry in the SBU of the MOF.⁶ In their report, the iconic MOF-5 was soaked in a nickel nitrate hexahydrate for one year to afford single-crystalline MOF-5 with a stoichiometry of 1:3 Ni:Zn at the SBU. The crystals after this transformation were yellow, indicating that the nickel in the NiZn₃O SBU was in an octahedral geometry. It was found that since nickel, being a d⁸ ion, prefers an octahedral geometry, it was coordinated to two additional solvent molecules along with the four structural coordination bonds. Upon activating the crystals by vacuum, the color quickly turned to orange, and subsequently to a deep blue, indicating the subsequent loss of solvent molecules one at a time to first achieve square pyramidal and then tetrahedral nickel within the SBU. Both geometries are rare in molecular nickel coordination complexes.

In this chapter, two attempts at site specific PSMM are described. The first attempt is to exchange a specific zinc ion within a Zn₄O SBU based on coordination geometry. The second attempt is to exchange the zinc ions in a paddlewheel SBU in a PPF structure while leaving an iron ion within the metalloporphyrin ligand unexchanged.

5.2 Experimental Methods

SUMOF-4 A mixture of benzene-1,4-dicarboxylic acid (BDC) (83 mg, 0.50 mmol), biphenyl-1,4-dicarboxylic acid (BPDC) (61 mg, 0.25 mmol), and zinc nitrate hexahydrate (228 mg, 0.76 mmol) were added to *N,N*-dimethyl formamide (DMF) (10 mL) in a capped vial and heated to 130 °C for 4 hrs. Yield: 120 mg. Purity was confirmed by PXRD.

PPF-5-Fe/Zn A mixture of 5,10,15,20-tetrakis(4-carboxyphenyl)-Mn(III)-porphyrin chloride (FeTCPPCl) (8.9 mg, 0.01 mmol), zinc nitrate hexahydrate (6.0 mg, 0.02 mmol), 4,4'-bipyridine (1.2 mg, 0.008 mmol), and 1.0 M nitric acid in methanol (40.0 μ L, 0.04 mmol) were added to a mixture of DMF (1.5 mL) and methanol (0.5 mL) in a capped vial and heated to 80 °C for 24 hrs, followed by slow-cooling to room temperature over 9 hrs. Yield: 12.7 mg. Purity was confirmed by PXRD.

X-ray powder diffraction (PXRD):

Data was collected on a Rigaku D/Max-B X-ray diffractometer with Bragg-Brentano parafocusing geometry, a diffracted beam monochromator, and a conventional copper target X-ray tube set to 35 KV and 25 mA.

Inductively coupled plasma-optical emission spectroscopy (ICP-OES)

Data was collected on a Thermo Jarell Ash IRIS Advantage Inductively Coupled Plasma Optical Emission Spectrometer (ICP-OES). 200 ppm and 50 ppm standards of Cu^{2+} , Fe^{3+} , and Zn^{2+} were used to calibrate for analysis. Triplicate trials were performed for each sample.

PSMM of SUMOF-4 and PPF-5-Fe/Zn

PSMM of both SUMOF-4 and PPF-5-Fe/Zn was performed according to the literature.⁵ About 10 mg of single crystalline samples were immersed in a DMF solution of copper nitrate trihydrate (0.04 M) for their respective time. After decanting the solution, the Cu²⁺-exchanged crystals were washed thoroughly with DMF and then soaked in fresh DMF.

Setup for ICP-OES analysis of Cu²⁺-exchanged MOFs

For ICP-OES analysis, the crystals were transferred to fresh DMF, kept there for 7 days to remove the excess metal salt within the pores. The crystals were then filtered and washed with DMF until the washing solvent showed no copper concentration as found by UV-vis analysis. The crystals were then dried at 100 °C overnight. They were digested by sonicating in 0.2 M HCl (aq) and diluted until appropriate concentration for analysis.

5.3 PSMM from Zn₄O to CuZn₃O cluster

Single crystals of SUMOF-4 were synthesized according to the reported synthesis.⁸ In this synthesis, two different dicarboxylates, BDC and BPDC, were assembled with a Zn₄O octahedral cluster creating an orthorhombic space group *Pnmm* (Figure 5.1). Each Zn₄O is connected to four BDC linkers to form a two-dimensional square network, which is further linked by BPDC axially to form a three-dimensional framework. The framework of SUMOF-4 adopts a two-fold interpenetration. Even with this interpenetration, the cavities within SUMOF-4 have free diameters of *ca.* 6.0 Å and 7.9 Å.⁸ Interestingly, three of the zinc ions in the Zn₄O cluster are tetrahedrally coordinated while the last zinc ion is octahedrally coordinated. Since Zn(II) has a d¹⁰ configuration, there are no crystal field stabilizations.⁹ Thus, Zn(II) shows similarities with the main-group metal magnesium, favoring 4-coordinate tetrahedral complex over octahedral.⁹ Dincă *et al.* proved that PSMM was possible in the Zn₄O cluster even if all zinc ions were tetrahedrally coordinated.⁶ However the extent of the PSMM was always limited to result in a metal to zinc ratio of 1:3 and there was no control over which zinc ion in the cluster was exchanged.⁶ It is our goal to expand on this work and to target a specific zinc ion within the Zn₄O cluster due to the relative instability of the octahedrally coordinated zinc ion compared to the three tetrahedrally coordinated zinc ions. If this is possible, the copper substituted SUMOF-4 could display interesting new properties. In the SUMOF-4 single crystal structure, the octahedrally coordinated zinc ions of each interpenetrated structure point to each other (see Figure 5.1c). If these ions were replaced with a more chemically active metal ion, like Cu(II), there could be an increased heat of

adsorption by gases due to a tandem effect observed by the gasses interacting with two different SBUs.

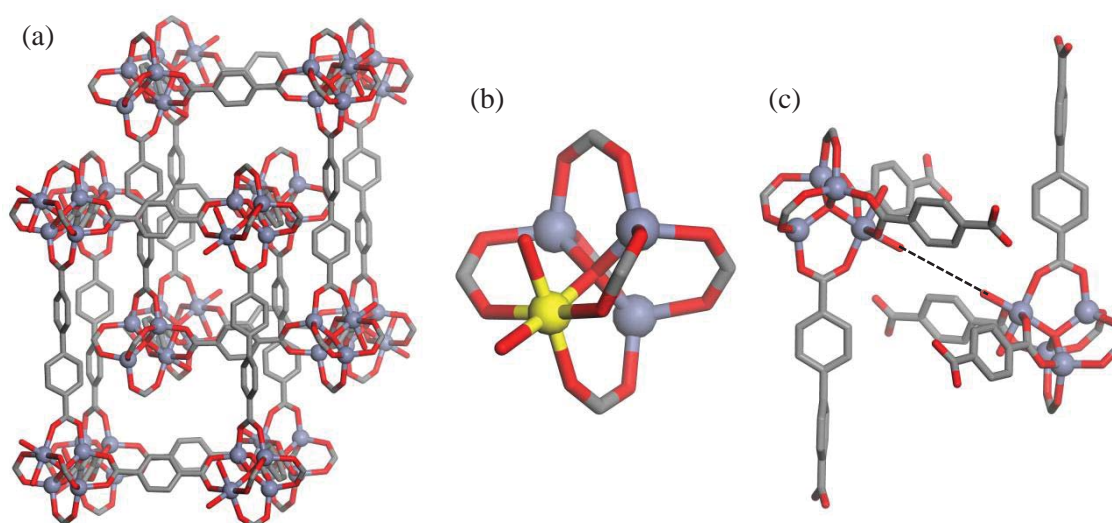


Figure 5.1. (a) Representation of the single crystal structure of SUMOF-4. (b) View of Zn₄O SBU in SUMOF-4 highlighting the octahedrally coordinated zinc ion (yellow). (c) Two interpenetrated nets of SUMOF-4 with the octahedrally coordinated zinc ions directed at each other.

Transparent crystals of SUMOF-4 were synthesized and immersed in a copper nitrate solution according to the literature procedure. After a few minutes, the crystals began changing color to a transparent blue indicating that the copper ions had either begun exchanging within the Zn_4O SBU, or at least diffused into the pores of SUMOF-4 (Figure 5.2). In order to distinguish whether the copper ions were guest ions within the pores or had indeed exchanged in the SBU, the copper nitrate solution was decanted, fresh DMF was introduced into the vial, and the crystal were left to sit for one week in order to remove any guest copper ions from the crystals. After a week, the crystals were still blue in color. The crystals were then filtered and washed with fresh DMF until the washings showed no copper monitored by UV-vis spectroscopy, and even still, the crystals were light blue in color, indicating that the copper ions were indeed incorporated into the structure. ICP-OES analysis shows that the initial rapid incorporation of the copper ions in SUMOF-4 reach the stoichiometric 1:3 ratio of copper to zinc by 36 hours creating a $CuZn_3O$ cluster (Figure 5.3). Even upon immersing the crystals for extended time periods (up to 3 days), the copper to zinc ratio never exceeds 1:3 indicating that once one of the four zinc ions within the SBU is exchanged, the other three zinc ions will not be exchanged. While we have not been able to obtain single crystal X-ray diffraction data for the copper substituted SUMOF-4 structure, PXRD patterns of the bulk copper substituted SUMOF-4 matches well with the as synthesized and simulated patterns indicating that the structure didn't change during this process (Figure 5.4).

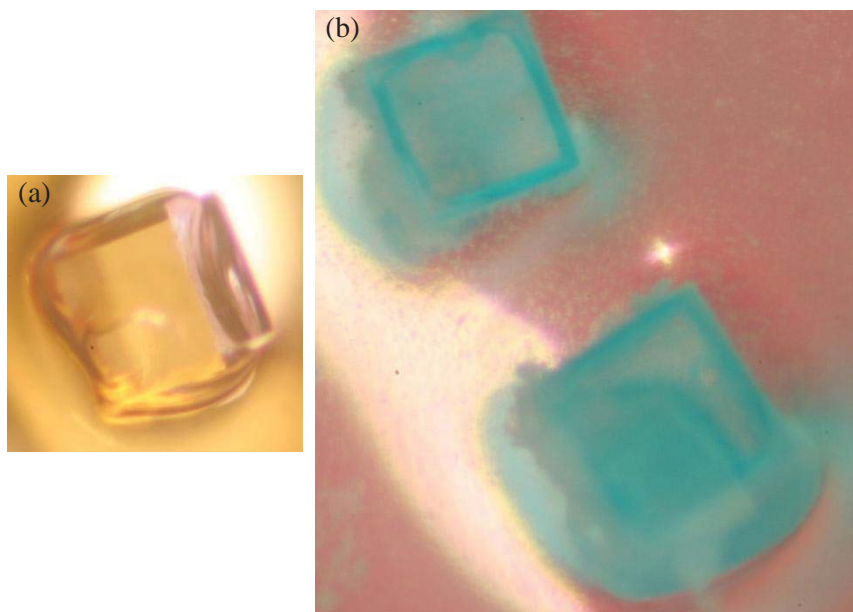


Figure 5.2. Photographs of crystals of SUMOF-4 (a) before and (b) after immersion in copper nitrate solution.

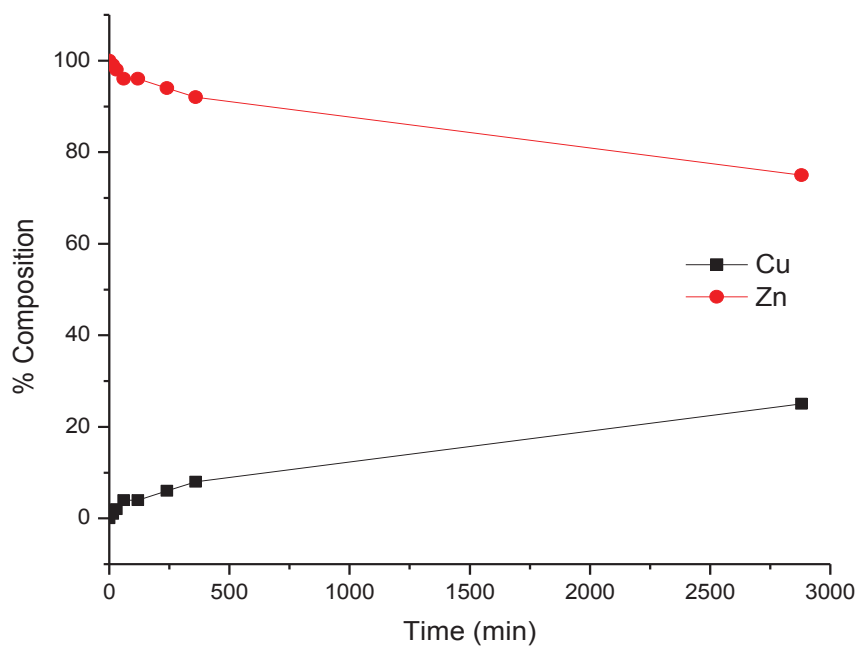


Figure 5.3. Kinetic profile of the PSMM of the Zn₄O SBU in SUMOF-4 into a CuZn₃O SBU.

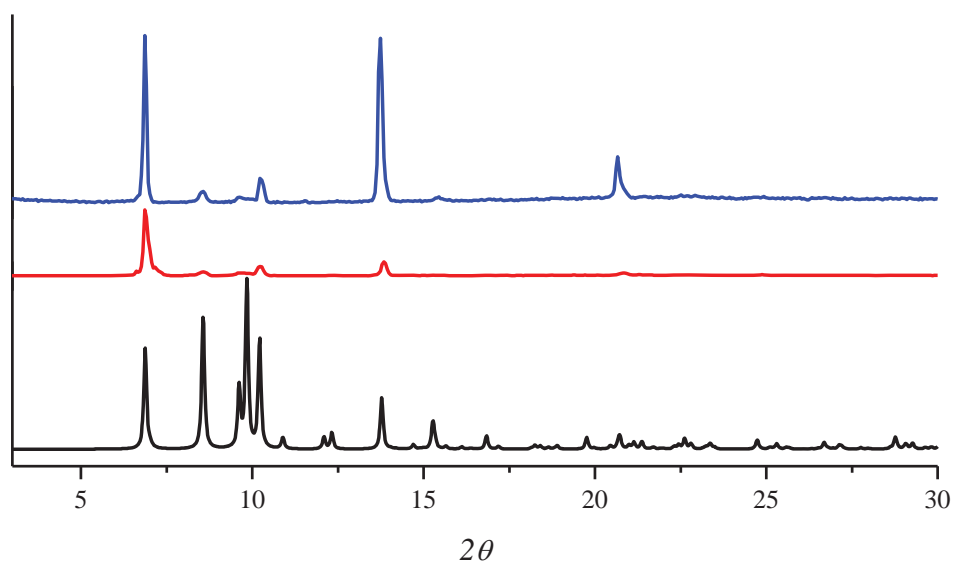


Figure 5.4. Theoretical (bottom), as synthesized (middle) and post copper exchange (top) PXRD patterns for SUMOF-4. All PXRD patterns match well indicating that during the PSMM process, the crystal structure is well maintained.

5.4 PSMM from Zn paddlewheel cluster to Cu paddlewheel cluster

In Chapter 2, we discussed that incorporating metalloligands such as porphyrin in the synthesis of MOFs can increase the subsequent MOFs' chemical properties for applications in catalysis, sensors, gas storage, etc. These properties are dependent upon the functional metals in the porphyrins being coordinatively unsaturated. This is a daunting task for traditional solvothermal syntheses because this process is intrinsically influenced by the preferred coordination geometry of the metal building units.¹⁰ Thus, the metals within the porphyrin core are often fully coordinated by structural linkers. Previously our group has found a way to synthesize porphyrin paddlewheel frameworks that contain coordinatively unsaturated Fe(III) ions in the porphyrin.¹¹ PPF-5-Fe/Zn (in this nomenclature the first metal indicates the ion within the porphyrin core, and the second metal indicates the ion in the paddlewheel SBU) is synthesized via a traditional solvothermal synthesis of FeTCPPCl, zinc nitrate hexahydrate, and BPY in which there is a stoichiometric limiting amount of BPY. The coordination of FeTCPPCl with zinc ions creates 2D porphyrin paddlewheel square grid lattices which are connected together by axial coordination of BPY. By limiting the amount of BPY used in the synthesis, coordination is observed selectively to the paddlewheel SBU, instead of at both the porphyrin and paddlewheel. The resulting crystals are single phase AA stacked containing coordinatively unsaturated Fe(III) ions within the porphyrin core (Figure 5.5). While PPF-5-Fe/Zn represents a significant accomplishment in producing functional PPF material, it suffers from a lack of stability during activation. One of the major contributions to the lack structural strength is the weak coordination bond between the carboxylic acid functional groups and pyridyl functional groups with the zinc ions within

the paddlewheel SBU. Zou *et al.* showed in their report that the zinc paddlewheel was one of the weakest paddlewheel units, and that copper paddlewheels were stronger.⁵ The direct synthesis of PPF-5-Fe/Cu however results in non-crystalline material. Thus a PSMM approach is highly attractive for creating robust PPF-5-Fe/Cu for the use in gas storage or catalysis.

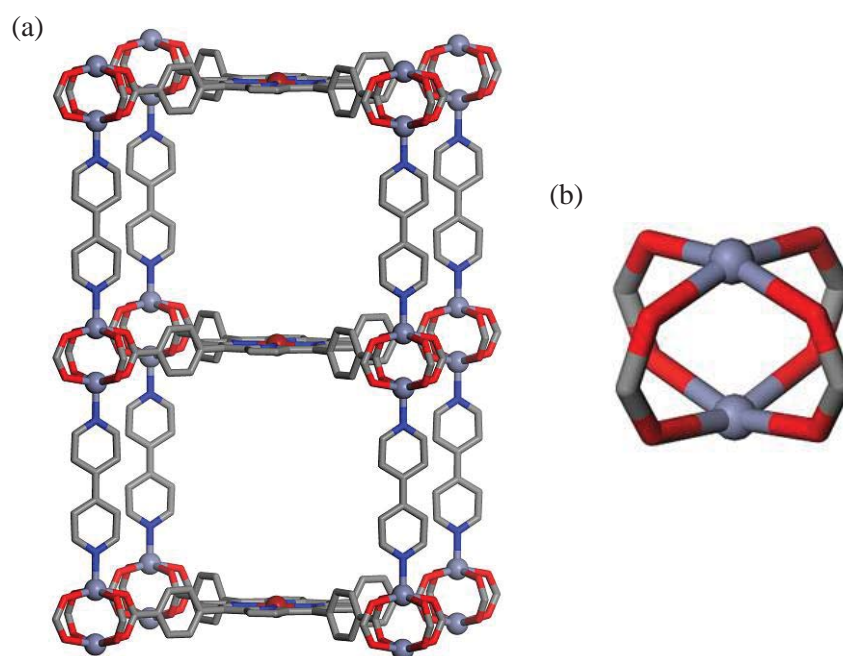


Figure 5.5. (a) Representation of the single crystal structure of PPF-5-Fe/Zn. (b) View of $\text{Zn}_2(\text{COO})_4$ paddlewheel SBU in PPF-5-Fe/Zn.

Single crystals of PPF-5-Fe/Zn were synthesized and immersed in a copper nitrate solution. Because of the large absorptivity of the porphyrin in PPF-5-Fe/Zn, there is no obvious color change of the crystals upon immersion in the copper nitrate solution. After a couple of days, the copper nitrate solution was decanted and replaced with fresh copper nitrate solution in order to complete the PSMM. After one week, the copper solution was decanted, fresh DMF was introduced, and the crystals were left for 1 week to remove any guest copper ions from the pores of PPF-5. The crystals were then filtered and washed with DMF until copper was no longer observed in the washings as monitored by UV-vis. Digested samples of PPF-5-Fe/Cu were investigated by ICP-OES. The ICP-OES data shows that after one week of immersion, almost all of the structure contains structural copper ions instead of zinc ions indicating complete conversion from zinc paddlewheel to copper paddlewheel (Figure 5.6). Additionally, the iron ion concentration was investigated. A control experiment was setup in which crystals of PPF-5-Fe/Zn were placed in DMF for one week instead of a copper nitrate solution. The iron ion concentration of the replaced PPF-5-Fe/Cu (92.8 ppm) compared well to the iron ion concentration of the standard (95.3 ppm) indicating that the iron ion inside the porphyrin core remained unchanged during this process. PXRD patterns of the bulk PPF-5-Fe/Cu matches well with the as synthesized and simulated patterns of PPF-5-Fe/Zn indicating that the structure didn't change during this process (Figure 5.7).

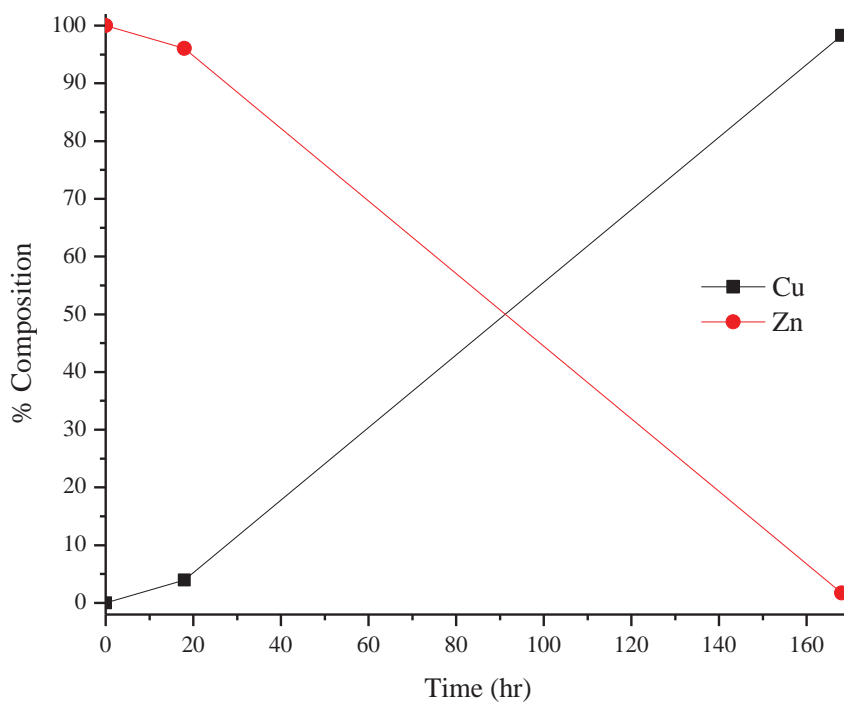


Figure 5.6. Kinetic profile of the PSMM of the $\text{Zn}_2(\text{COO})_4$ paddlewheel SBU in PPF-5-Fe/Zn into a $\text{Cu}_2(\text{COO})_4$ paddlewheel SBU in PPF-5-Fe/Cu.

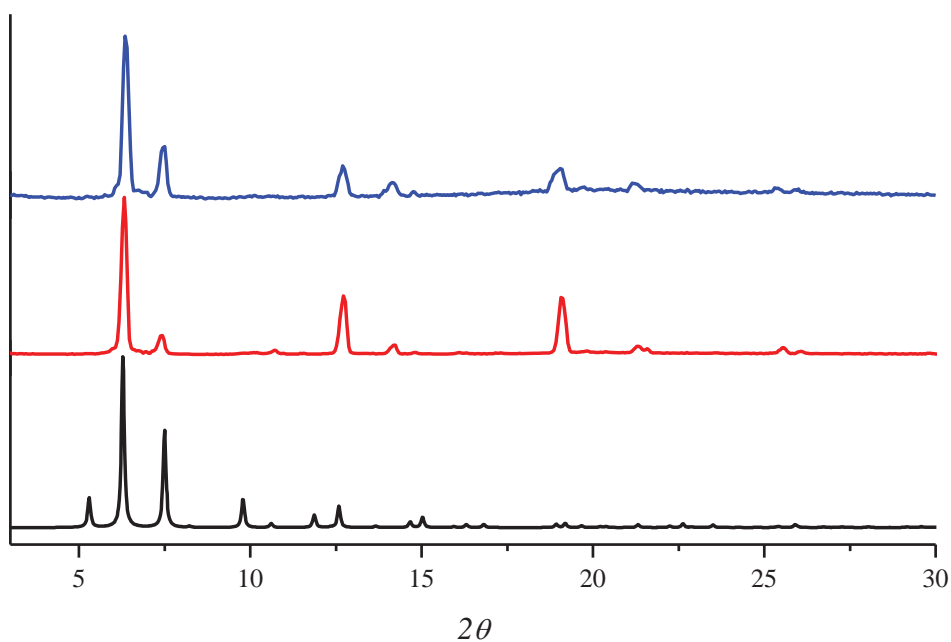


Figure 5.7. Theoretical (bottom), as synthesized PPF-5-Fe/Zn (middle) and post copper exchange PPF-5-Fe/Cu (top) PXRD patterns. All PXRD patterns match well indicating that during the PSMM process, the crystal structure is well maintained.

5.5 Conclusions

We have successfully demonstrated the targeted PSMM based on two different conditions. First, we successfully exchanged a targeted zinc ion within a Zn_4O cluster in SUMOF-4 based on the coordination geometry. Second, we successfully exchanged a targeted zinc ion in the paddlewheel SBU of PPF-5-Fe/Zn while leaving the iron ions in the porphyrin core unexchanged based on the weak coordination bonds of the carboxylic acid functional groups and pyridyl groups to the zinc ions within the paddlewheel SBU. For SUMOF-4, the copper substituted analogue could exhibit increased adsorption properties due to a possible tandem interaction in which a guest molecule interacts with two copper ions from two separate interpenetrated structures. For PPF-5-Fe/Cu, the replacement of zinc ions within the paddlewheel with copper ions could increase its structural stability, making it possible to successfully activate the material for gas storage or catalytic applications.

5.6 References

- (1) Das, S.; Kim, H.; Kim, K. *J. Am. Chem. Soc.* **2009**, *131*, 3814.
- (2) Kim, Y.; Da, S.; Bhattacharya, S.; Hong, S.; Kim, M. G.; Yoon, M.; Natarajan, S.; Kim, K. *Chem. Eur. J.* **2012**, *18*, 16642.
- (3) Wang, X. -J.; Li, P. -Z.; Liu, L.; Zhang, Q.; Borah, P.; Wong, J. D.; Chan, X. X.; Rakesh, G.; Li, Y.; Zhao, Y. *Chem. Commun.* **2012**, *48*, 10286.
- (4) Song, X.; Kim, T. K.; Kim, H.; Kim, D.; Jeong, S.; Moon, H. R.; La, M. S. *Chem. Mater.* **2012**, *24*, 3065.
- (5) Yao, Q.; Sun, J.; Li, K.; Su, J.; Peskov, M. V.; Zou, X. *Dalton Trans.* **2012**, *41*, 3953.
- (6) Brozek, C. K.; Dincă, M. *Chem. Sci.* **2012**, *3*, 2110.

- (7) Pan, F.; Wu, J.; Hou, H.; Fan, Y. *Cryst. Growth Des.* **2010**, *10*, 3835.
- (8) Yao, Q.; Su, J.; Cheung, O.; Liu, Q.; Hedin, N.; Zou, X. *J. Mater. Chem.* **2012**, *22*, 10345.
- (9) Greenwood, N. N.; Earnshaw, A. *Chemistry of the Elements*, 2nd ed.; Butterworth–Heinemann: Oxford, 2001; pp 1205–1210.
- (10) (a) Ockwig, N. W.; Delgado–Friedrichs, O.; O’Keeffe, M.; Yaghi, O. M. *Acc. Chem. Res.* **2005**, *38*, 176. (b) Delgado–Friedrichs, O.; O’Keeffe, M.; Yaghi, O. M. *Phys. Chem. Chem. Phys.* **2007**, *9*, 1034.
- (11) Barron, P. M. Design, Synthesis and Characterization of Porphyrin Paddlewheel Frameworks. Ph. D. Dissertation, University of Nebraska–Lincoln, State College, NE, May 2010.

CHAPTER 6

FLUORESCENCE QUENCHING OF PORPHYRIN PADDLEWHEEL FRAMEWORKS FOR THE DETECTION OF NITRO-AROMATIC EXPLOSIVE VAPORS

6.1 Introduction

Currently, there is much research dedicated to the rapid standoff detection of explosives. There are many different methods for detecting explosives, including mass spectroscopy, infrared spectroscopy, and raman spectroscopy.¹⁻³ While these methods typically can successfully detect explosive molecules, they are inherently expensive, heavy, bulky, need extensive training to operate, and often need extended time for detection. Additionally, some methods cannot distinguish different explosive analytes.¹ In the continued effort to make small, simple, and inexpensive devices for rapid detection and determination of explosive materials, colorimetric and fluorescent sensors have become highly attractive owing to their high sensitivity, easy visualization, and short response time for detection.^{1,4,5}

Fluorescence-based detection has been a very successful approach for detecting nitro-aromatic explosives such as 2,4-dinitrotoluene (DNT) and 2,4,6-trinitrotoluene (TNT).^{1,5-10} The most popular method involves a fluorescence quenching mechanism in which the analyte reduces the intensity of light emitted by the fluorescent indicator through an electron transfer mechanism.^{1,5} Nitro-aromatics are great candidates for this type of sensing because they are electron-deficient molecules typically having a low-

lying LUMO.^{1,5} Thus, once the fluophore is excited, there is an exergonic driving force for an electron transfer to the LUMO of the nitro–aromatic analyte.¹

Among the investigated materials for fluorescence quenching has been materials made with porphyrin. Zn–, Cd–, and unmetallated porphyrin are highly fluorescent in the visible range and the fluorescence quenches in the presence of nitro–aromatics such as nitrobenzene (NB), DNT, and TNT.^{1,7,8} Zn–porphyrin–doped porous silica shows high sensitivity to both DNT and TNT vapors, reaching a quenching maximum of ~50% and 90% respectively within 60 seconds of exposure to the vapors.⁷ While great success has been achieved by loading metalloporphyrins in porous material, this strategy often suffers from poor porphyrin loading, pore blockage, and self–quenching of the porphyrins due to aggregation.^{7,8,11} In an attempt to create improved porphyrinic material for the fast and sensitive sensing of nitro–aromatic explosives, we have investigated metal organic frameworks (MOFs) assembled with fluorescent Zn–porphyrins. MOFs are a class of often porous materials that have shown great potential for applications in gas storage, catalysis, and small molecule sensing.¹² There are currently a number of MOFs that are fluorescent,^{9,10,13} but a surprising few have been investigated for explosives detection by a fluorescence quenching mechanism.^{9,10} While these structures successfully detect many different analytes, many of the structures observe fluorescence quenching in the UV spectrum, making it difficult to visually observe the detection of analytes.⁹ By creating MOF materials using Zn–porphyrin as one of the building units cleverly allows for highly fluorescent crystals in the visible range. Additionally, distinguishing between different nitro–aromatic explosives is possible based on the quenching spectra of the porphyrin.

Herein, we report: (1) a new 2D bilayer porphyrin paddlewheel framework (PPF-23) which is highly fluorescent in the visible range and shows very fast and reversible detection of NB, DNT, and TNT vapors; (2) the ability to distinguish between different nitro–aromatic analytes based on the quenching of two fluorescent bands in PPF-23; (3) our attempt to identify the interaction of the vapors within the pores of PPF-23 and another framework, PPF-27; (4) a new method for quantifying fluorescence quenching using fluorescence microscopy.

6.2 Experimental Methods

***N,N'*-di-(4-pyridyl)-benzenetetracarboxydiimide (DPBI)** Pyromellitic dianhydride (0.218 g, 1.00 mmol) and 4-aminopyridine (0.282 g, 2.00 mmol) were dissolved in *N,N*-dimethylacetamide (DMA, 50 mL) in a 100 mL round-bottom flask. The solution was stirred overnight at 135 °C under Ar atmosphere. After the reaction mixture cooled to room temperature, the solution was poured into diethyl ether (200 mL). The precipitate was filtered and washed with diethyl ether. The product was dried under vacuum to yield 0.280 g (74% yield). ¹H NMR (CF₃COOD): δ/ppm: 8.880 (d, 4H), 8.7779 (d, 4H), 8.712 (s, 2H).

PPF-23 A mixture of 5,10,15,20-tetrakis(4-carboxyphenyl)-2*H*,23*H*-porphyrin (TCPP) (7.9 mg, 0.01 mmol), zinc nitrate hexahydrate (8.9 mg, 0.03), DPBI (7.4 mg, 0.02 mmol), and 1.0 M nitric acid in ethanol (90 μL, 0.09 mmol) were added to a mixture of *N,N*-dimethyl formamide (DMF) (1.5 mL) and ethanol (0.5 mL) in a capped vial and heated to 80 °C for 24 hrs, followed by slow-cooling to room temperature over 9 hrs. Yield: 14.8 mg (88.6% based on porphyrin). Anal. Calcd. for [C₆₈H₃₄N₈O₁₂Zn₃] 2.5 DEF · 5 H₂O: C, 57.1; H, 4.2; N, 8.9% Found: C, 56.9; H, 3.7; N, 9.2%.

PPF-27 PPF-27 was synthesized following a two-step linker insertion method previously reported by us.¹⁴ First, crystals of the 2D layered compound PPF-1 were synthesized according to the procedure previously published by our group.¹⁵ Filtered PPF-1 crystals (14.7 mg, 0.01 mmol) were then introduced to 2mL of a 3:1 *N,N*-diethyl formamide (DEF)/ethanol solution containing 3.2 mg (0.02 mmol) of 4,4'-bipyridine in a capped vial, swirled by hand to mix, and left at room temperature to react for ~ 2hrs to produce single phase PPF-27 as evident by powder X-ray diffraction. Yield: 15.2 mg (92% based

on porphyrin). Anal. Calcd. for $[C_{58}H_{32}N_6O_8Zn_3] \cdot 3 \text{ DEF} \cdot 2 \text{ H}_2\text{O} \cdot \text{ethanol}$: C, 60.5; H, 5.3; N, 8.7% Found: C, 59.4; H, 5.0; N, 9.0%.

X-ray single crystal diffraction:

Plate-shaped crystals of PPF-23 ($170 \mu\text{m} \times 170 \mu\text{m}$) were sealed in a capillary for XRD measurement. Geometry and intensity data were obtained at room temperature with a Bruker SMART Apex CCD area detector diffractometer. Preliminary lattice parameters and orientation matrices were obtained from three sets of frames. Data were collected using graphite-monochromated and MonoCap-collimated Mo- K_α radiation ($\lambda = 0.71073 \text{ \AA}$) with ω scan method.¹⁶ Data was processed with the SAINT+ program¹⁷ for reduction and cell refinement. Multi-scan absorption corrections were applied to the data set using the SADABS program for area detector.¹⁸ The structure was solved by direct method and refined using SHELXTL.¹⁹ Disordered, independent solvent molecules inside the frameworks were eliminated in the refinement by PLATON/SQUEEZE.²⁰ All atoms were refined with anisotropic displacement parameters.

X-ray powder diffraction:

X-ray diffraction data were taken with a Rigaku D/Max-B X-ray diffractometer with Bragg-Brentano parafocusing geometry, a diffracted beam monochromator, and a conventional copper target X-ray tube set to 40 KV and 30 mA. Non-preferred orientation X-ray diffraction data were taken using a spinning capillary method¹⁴ with a Bruker AXS DA X-ray diffractometer with a GADDS area detector and a conventional copper target X-ray tube set to 40 KV and 40 mA. The program Unit Cell was used to generate the cell parameters of the experimental data.²¹

Thermogravimetric analysis:

Performed on a Perkin Elmer STA 6000 thermogravimetric analyzer, heated from 25 °C to 800 °C at a rate of 10 °C/minute under N₂ atmosphere.

Elemental analysis:

Data was performed by MidwestMicro Labs LLC.

UV/Vis analysis:

Suspension data were recorded on a Shimadzu UV–2401PC spectrophotometer.

Fluorescence analysis:

Suspension data were obtained from a Shimadzu RF–5301 PC Fluorimeter using 405 nm as the excitation wavelength.

Fluorescence microscope images for fluorescence spectra were obtained from a Nikon A1 confocal laser scanning microscope using 405 nm laser light for excitation.

Fluorescence microscope images for the quenching experiments were obtained from an Olympus FV500 Confocal Laser Scanning System with IX81 Inverted Fluorescence Microscope using 405 nm laser light for excitation. The fluorescence image intensities were quantified by using Image J software.²²

¹H NMR analysis:

Performed on a Bruker FT–NMR spectrometer (400 MHz).

Conolly surface models:

Calculated using Materials Studio software.²³

Activation:

Samples of PPF-23 and PPF-27 were activated by first wet depositing samples on cleaned glass slide covers, followed by gentle heating on a hot plate to dry off excess

solvent, then placed in a vacuum desiccator and actively pumped ≥ 3 days under mild heating conditions.

Resolvation:

Samples of PPF-23 and PPF-27 were resolvated by heating at 40 °C for 6 hrs in DMF/ethanol and DEF/ethanol solutions respectively.

Suspension UV–vis and Fluorescence Spectra:

Samples of PPF-23 and PPF-27 were sonicated for 30 min in a 3:1 DMF/ethanol and DEF/ethanol solution respectively to form a crystal suspension. Powder X–ray diffraction spectra were measured before and after sonication. UV–vis and fluorescence spectra were obtained for the suspensions. Because the laser used for fluorescence microscopy emits at 405 nm, suspension fluorescence spectra were obtained using the same excitation wavelength. The crystals were then separated from the solution by centrifugation (3000 RPM for 10 min) and UV–vis and fluorescence spectra were obtained of the solution. The suspension emission spectra of Zn–TCPP in 3:1 DMF/ethanol was also taken as a reference. Solid state emission spectra were obtained from fluorescence microscope images and were compared qualitatively to the suspension spectra.

Explosive Detection Experimental Design:

Around 100 mg of DNT and TNT and 3 mL of NB were placed in separate small (20 mL) open glass vials. These vials were placed into capped (500 mL) glass bottle reaction chambers for ≥ 2 weeks following the published procedure²⁴ to ensure that the equilibrated vapor pressure of each analyte was reached ($\sim 1.4 \times 10^{-4}$, 8.0×10^{-6} , and 0.24 Torr respectively at 25 °C).^{2,8}

Triplicate fluorescence images corresponding to emission at 650 ± 30 nm (excitation wavelength = 405 nm) of activated PPF crystals into the bottles containing the analytes. After a specified exposure time, the slide cover was taken out and without any delay was mounted on the microscope and triplicate fluorescence images at the same emission range were recorded. Control experiments were ran in which PPF crystal samples were not introduced to the explosive vapors, but held under the fluorescence microscope for the duration of the timeframe studied.

Recyclability experiments were performed for the activated PPF crystals. After the first quenching using the same procedure described above, the samples was simply heated at 80 °C for 2 minutes to be fully recovered. The sample was then investigated again.

Data Interpretation:

The original triplicate fluorescence images of each sample were collected before placing the particular sample into the reaction chamber containing the analyte under investigation. The average fluorescence intensity from the images was obtained using Image J software.²² By averaging the image intensity obtained from multiple samples, inconsistencies due to focusing or sample thickness are minimized. After the samples are exposed to the explosive vapors, triplicate fluorescence images were again recorded and the average fluorescence intensity is obtained following the same procedure. The quenching % is then calculated by:

$$\%_{quench} = \frac{(I_0 - I)}{I_0} \times 100$$

in which I_0 is the average initial fluorescence intensity and I is the average final fluorescence intensity.

It is important to mention, that fluorescence intensities obtained through the Image J software are based on the entire image, and not on a focused area within the image. This is true for all images except ones in which there is a large absence of PPF crystals in the image, which would falsely lower the average intensity. For such cases, the image intensity is obtained by integrating the areas that are covered with PPF crystals and excluding the areas absent of crystals.

6.3 Results and Discussion

Purple crystals of PPF-23 were grown by the solvothermal reaction of zinc nitrate hexahydrate, TCPP, DPBI, DMF, and ethanol at 80 °C for 24 hrs. The purity of the resulting crystals was confirmed by elemental analysis and powder X-ray diffraction (Figure 6.1). A single crystal suitable for single-crystal X-ray diffraction was obtained for PPF-23 (see Table 6.1). PPF-23 is a new 2D bilayer structure in which the porphyrin paddlewheel layers are stacked in an AB fashion, creating $P4/nmm$ symmetry (Figure 6.2). By incorporating the Zn-porphyrin into the framework of PPF-23, the porphyrin to porphyrin distance between layers within the bilayer is around 25.8 Å inhibiting self-quenching. Indeed crystals of PPF-23 are visibly bright when illuminated by a UV lamp (at 360 nm). UV/Vis and fluorescence spectra were obtained of a colloid suspension of PPF-23 crystals (Figure 6.3). X-ray powder diffraction spectra were taken of the samples before and after sonication showing that upon sonication the structure retained crystallinity (Figure 6.4). The majority of the UV-vis and fluorescence intensity is from the crystalline PPF-23 and not due to monomeric porphyrin in solution, as observed by a 76% reduction in intensity (at the Soret absorption) after the crystals were separated by centrifugation. The position of the bands in the fluorescence emission spectra of PPF-23 compares well to that of monomer Zn-TCPP (Figure 6.5). Fluorescence microscope images were obtained for PPF-23 and used to get a solid state fluorescence spectrum of large crystals of PPF-23 (Figure 6.6). The fluorescence microscope was also used to visibly observe and quantify the fluorescence quenching of PPF-23.

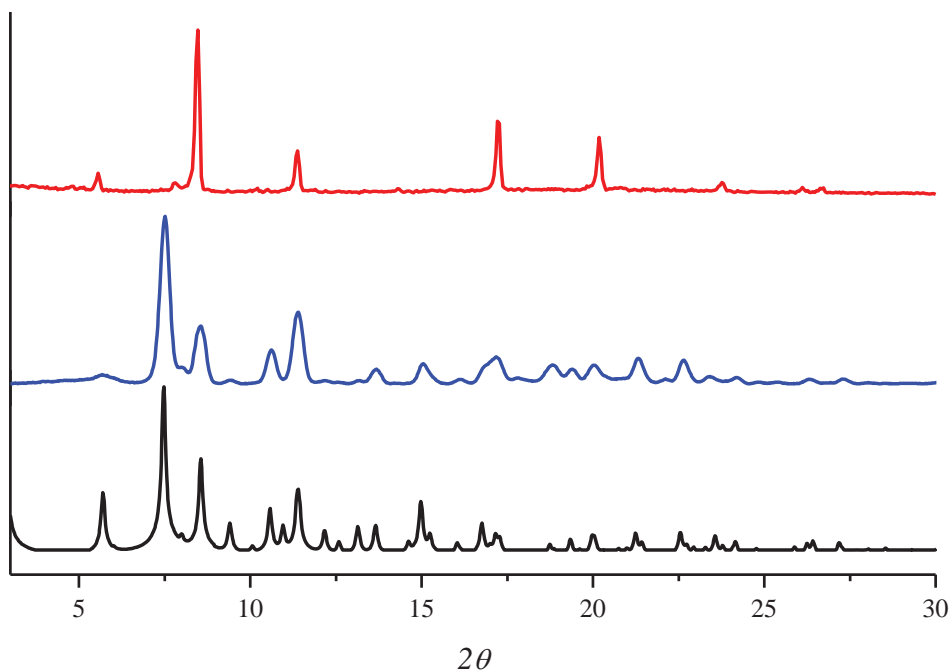


Figure 6.1. Theoretical (bottom) and experimental (top and middle) PXRD patterns for PPF-23. The middle PXRD was obtained on a flat mount showing high preferred orientation about the (001) plane. The top PXRD pattern was obtained using the spinning capillary method described above.

Table 6.1. Crystal data for PPF-23

Complex	PPF-100
chemical formula*	$C_{68}H_{36}N_8O_{13}Zn_3$
formula weight*	1369.16
crystal system	tetragonal
space group	$P4/nmm$
a (Å)	16.714(3)
b (Å)	16.714(3)
c (Å)	30.976(8)
V (Å ³)	8653(3)
Z	2
ρ_{calc} (g/cm ³)*	0.525
μ (mm ⁻¹)*	0.438
$R_1, I > 2\sigma(I)$	0.0573
$wR_2, I > 2\sigma(I)$	0.1587

*Based on the formula without uncoordinated solvent molecules.

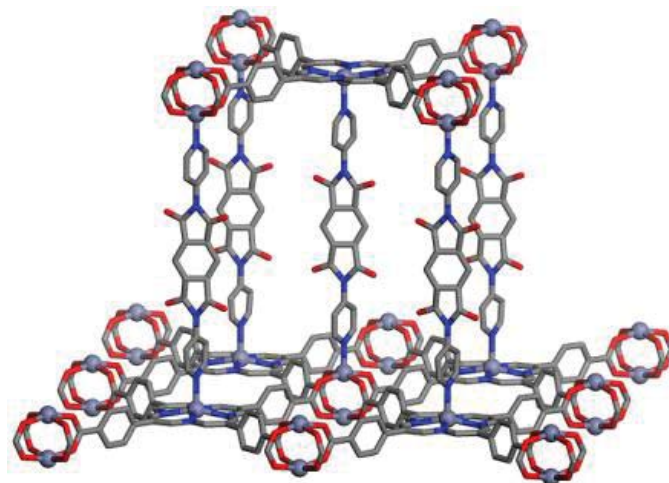


Figure 6.2. Schematic representation of single crystal structure of PPF-23.

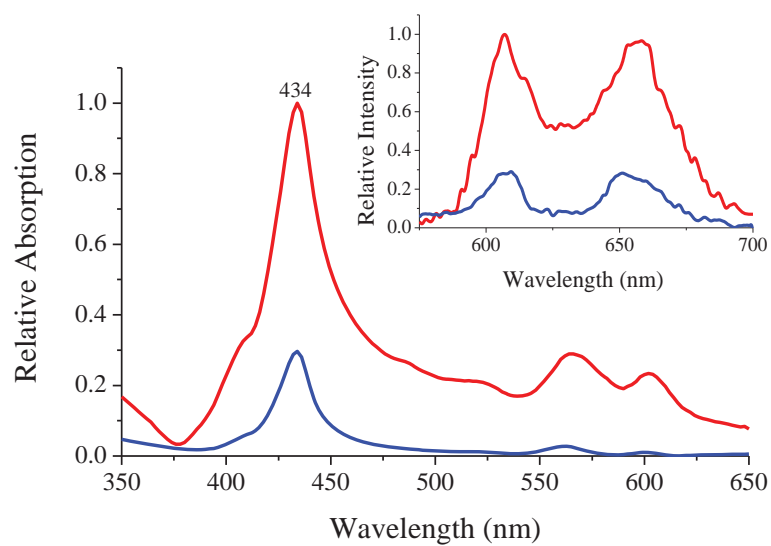


Figure 6.3. UV/Vis absorption and fluorescence emission (inset) spectra of the PPF-23 suspension (red) and solution (blue).

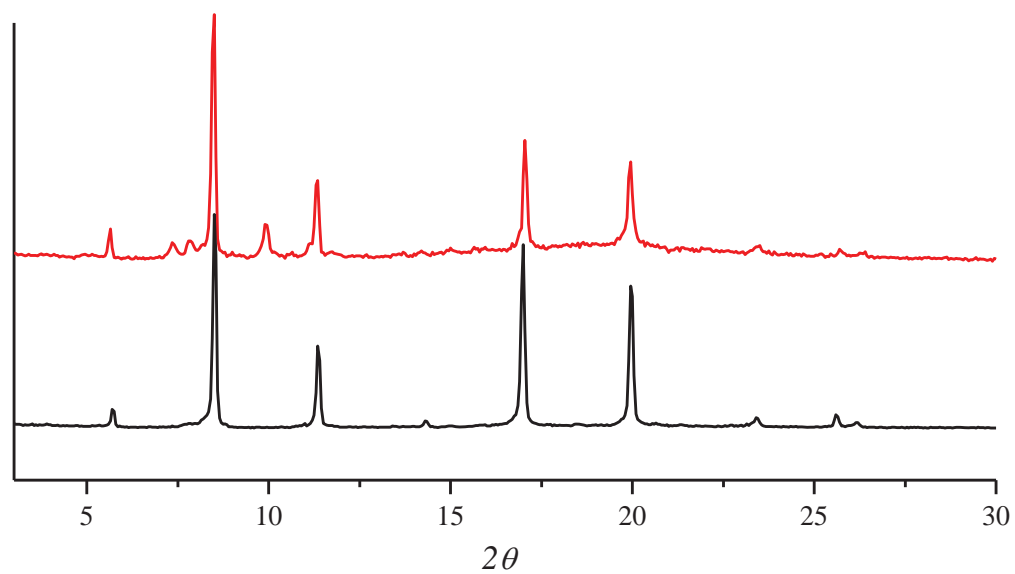


Figure 6.4. PXRD patterns of as synthesized (bottom) and sonicated (top) PPF-23. As seen from the patterns, the structure is retained after this step.

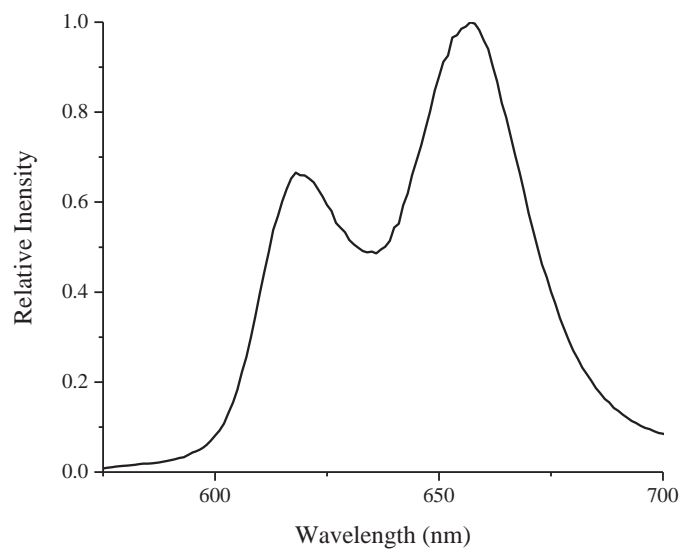


Figure 6.5. Fluorescence emission spectra of Zn-TCPP

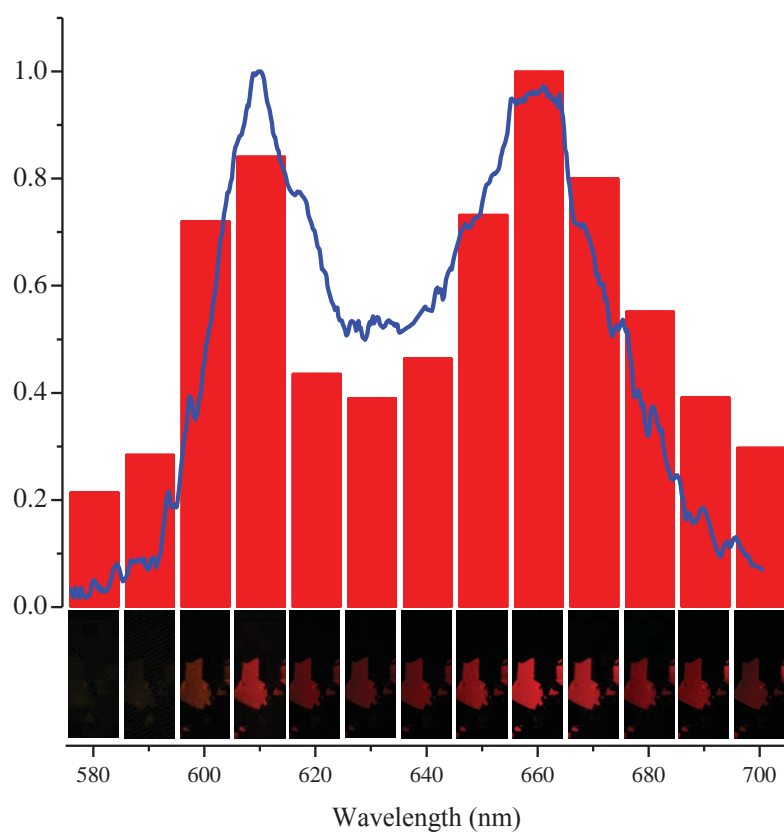


Figure 6.6. Bottom: Fluorescence microscope images of PPF-23 crystals (150 μm in length) above their corresponding emission wavelength. Top: Relative fluorescence emission intensity of each fluorescence image (red columns). Fluorescence emission from suspension (blue line) is added for comparison purposes.

Samples of PPF-23 were mildly activated, and X-ray powder diffraction patterns obtained for as-synthesized, activated, and resolvated samples (Figure 6.7). As indicated by the sharp peaks after activation and resolution, the structure retains crystallinity and framework stability. The experimental unit cell parameters of the as-synthesized, activated, and resolvated PPF-23 were generated and compared to the single crystal unit cell showing, upon activation, retention of the 2D PPF layer, and a slight contraction of the inter-bilayer channel which is reversed upon resolvating (Table 6.2). TGA of the as synthesized and activated PPF-23 shows solvent loss at ~150 °C and the total collapse beginning at ~375 °C (Figure 6.8). The activated TGA graph of PPF-23 shows that 7.2% of the mass due to solvent is removed upon activation which matches well with the 7.1% weight loss calculated by losing a water and DEF molecule upon activation. Fluorescence quenching of activated PPF-23 by DNT vapors was visibly evident from fluorescence microscope images (Figure 6.9). Quantitative analysis of the fluorescence quenching as a function of time shows very fast quenching (37% quenched at 10 seconds and a maximum quenching of 70% by 25 seconds) (Figure 6.10). Control experiments show no significant bleaching of the fluorescence of PPF-23 by either the laser used in the fluorescence microscope or the atmosphere confirming that quenching was due to exposing the samples to DNT vapors.

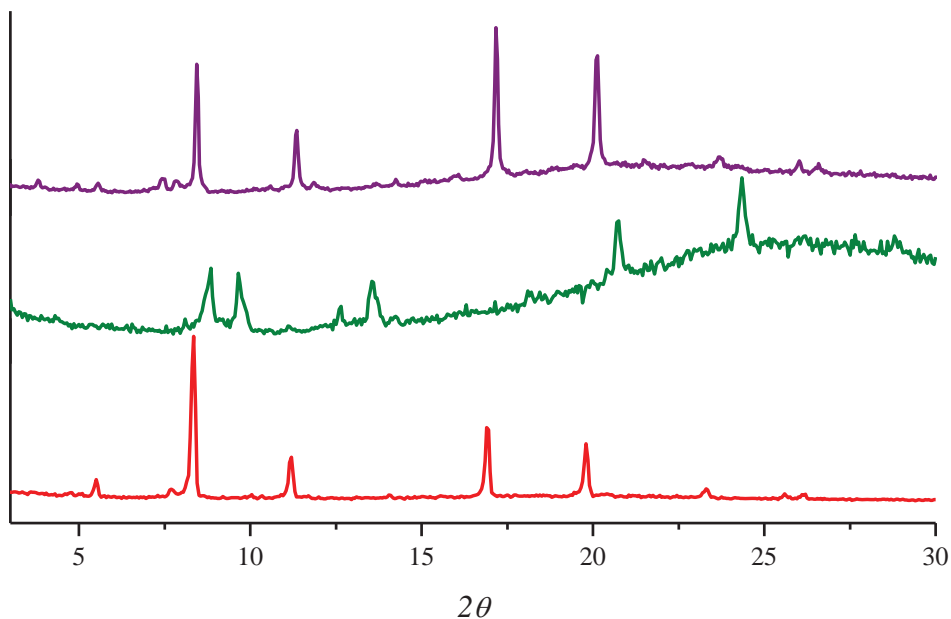


Figure 6.7. PXRD of as synthesized (bottom), activated (middle) and resolvated (top) PPF-23. As seen from the patterns the structure is well maintained, with a slight shift in $(00l)$ peaks upon activation which return upon resolution.

Table 6.2. Tetragonal unit cell parameters of PPF-23.

PPF-23	$a, \text{Å}$	$b, \text{Å}$	$c, \text{Å}$	$V, \text{Å}^3$
Single Crystal*	16.714(3)	16.714(3)	30.976(8)	8653(3)
As Synthesized	16.671(8)	16.671(8)	30.98(2)	8612(10)
Activated	16.72(4)	16.72(4)	29.72(3)	8013(43)
Resolvated	16.680(5)	16.680(5)	30.96(1)	8614(26)

*Obtained from .CIF file

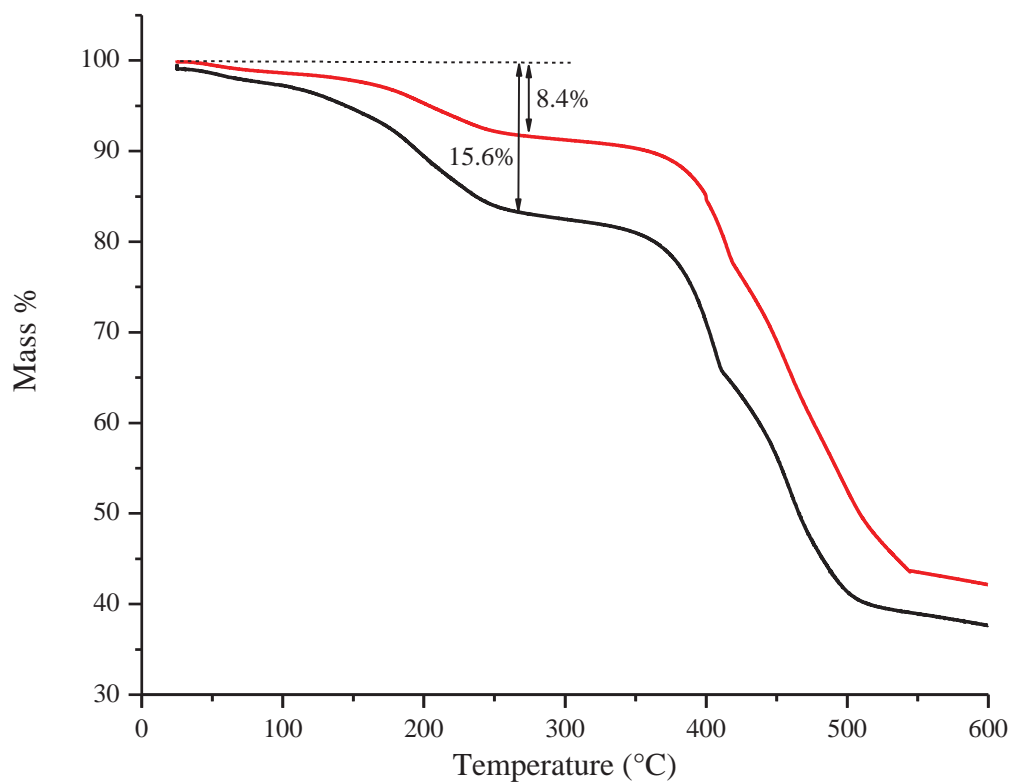


Figure 6.8. TGA data for PPF-23 as synthesized (black) and activated (red).

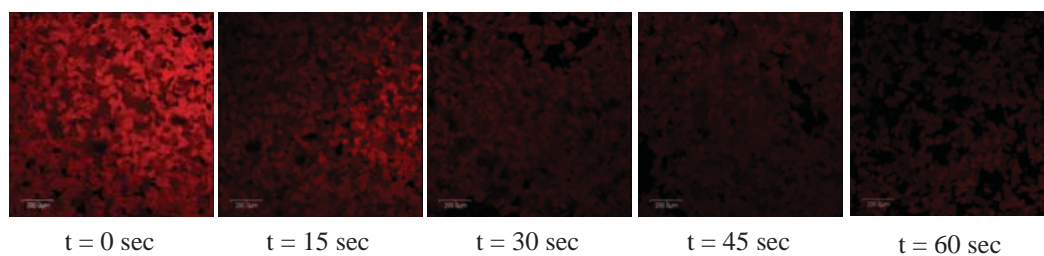


Figure 6.9. Fluorescence microscope images of PPF-23 after exposure to DNT vapors for the corresponding times (emission light is artificially colored red to denote the emission range of 650 ± 30 nm).

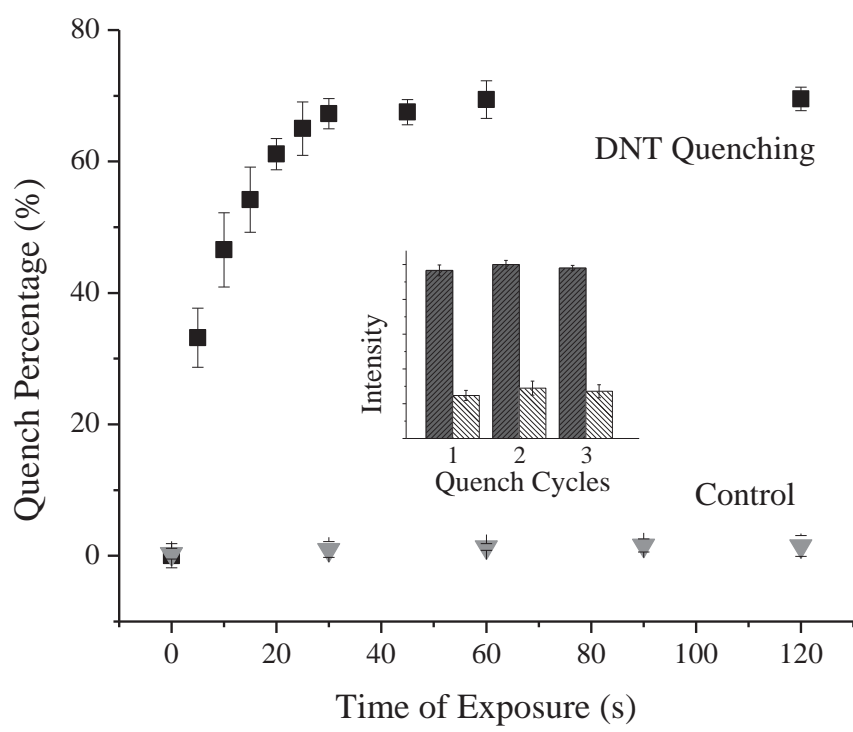


Figure 6.10. Time dependent fluorescence quenching of PPF-23 by DNT. Inset: three consecutive quench/regeneration cycles.

Quenching of PPF-23 by TNT shows more drastic quenching as visibly evident from the fluorescence microscope images (Figure 6.11). Quantitative analysis shows similar quenching times compared to DNT quenching, reaching a quenching maximum at 25 seconds. However, the % quenching is drastically higher for TNT than DNT (85% quenched for TNT) (Figure 6.12), which is consistent with other porphyrinic material.^{7,8}

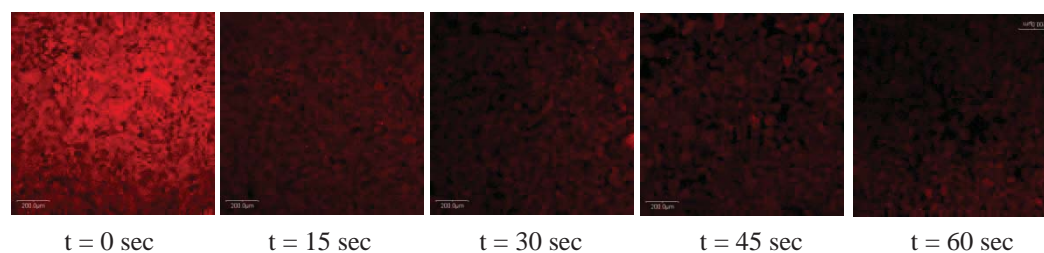


Figure 6.11. Fluorescence microscope images of PPF-23 after exposure to TNT vapors for the corresponding times (emission light is artificially colored red to denote the emission range of 650 ± 30 nm).

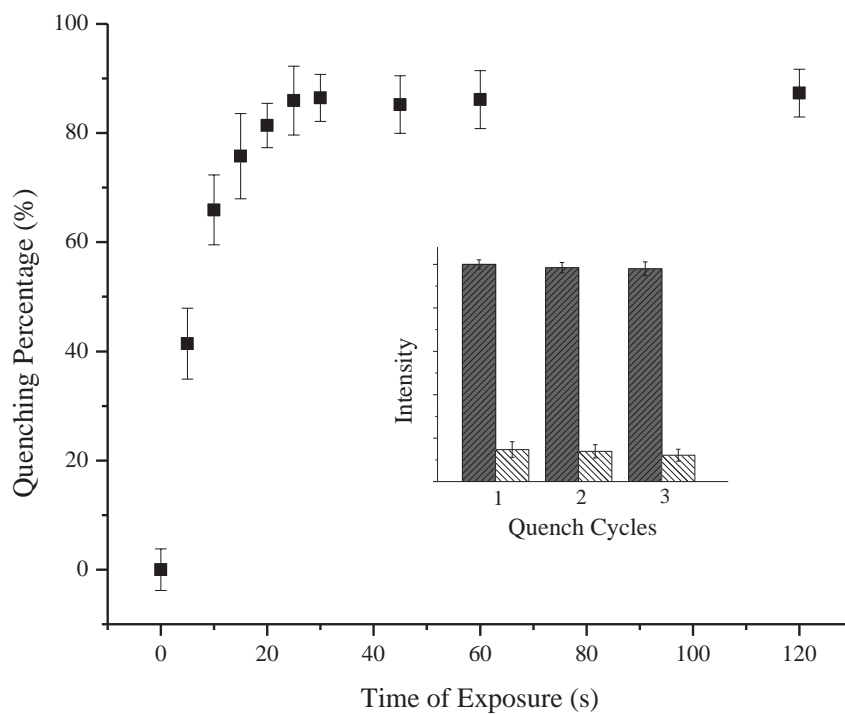


Figure 6.12. Time dependent fluorescence quenching of PPF-23 by TNT. Inset: three consecutive quench/regeneration cycles.

The high sensitivity of the Zn-porphyrin to the nitro-aromatic compounds comes from the high binding constant of the Zn-porphyrin with the nitro-aromatics ($K_b=103 \text{ dm}^{-3} \text{ mol}^{-1}$) and the strong electronic interaction between the Zn-porphyrin and the explosives.^{7,25} Even though the vapor pressure of DNT is 18x higher than TNT, the fluorescence quenching is significantly lower. This is explained by the difference in exergonicity between the electron transfer reactions between the Zn-porphyrin and the different quenchers favoring TNT which has the higher redox potential ($E_{\text{red}} = -0.7 \text{ V}$ vs. -1.0 V for DNT).^{5,7}

We also investigated the quenching due to non-explosive nitro-aromatic analytes such as NB. PPF-23 reaches a quenching maximum of 35% by 30 seconds (Figures 6.13 and 6.14). Additionally, upon heating the fully quenched PPF-23 samples, fluorescence is recovered, and can again be quenched showing excellent recyclability (Figures 6.10, 6.12, and 6.14 insets).

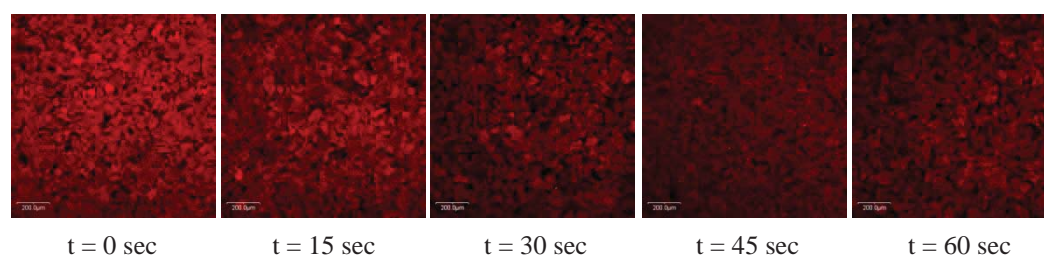


Figure 6.13. Fluorescence microscope images of PPF-23 after exposure to NB vapors for the corresponding times (emission light is artificially colored red to denote the emission range of $650 \pm 30 \text{ nm}$).

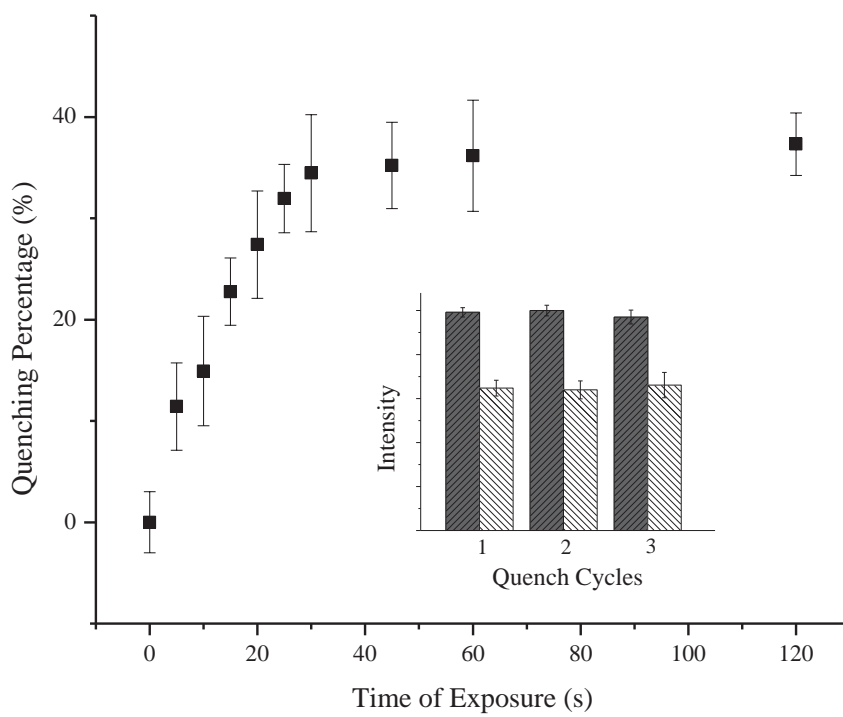


Figure 6.14. Time dependent fluorescence quenching of PPF-23 by NB. Inset: three consecutive quench/regeneration cycles.

In order to better understand the interaction between the MOF and analyte, another porphyrinic MOF (PPF-27) (Figure 6.15) was synthesized following the published procedure and confirmed by X-ray powder diffraction (Figure 6.16).¹⁴ This structure was used to detect NB, DNT, and TNT. PPF-27, like PPF-23, is a highly fluorescent bilayer structure (Figures 6.17, 6.18, and 6.19), but contains 4,4'-bipyridine (BPY) as the pillaring linker instead of DPBI used in PPF-23. Because BPY is much smaller than DPBI, the intra-bilayer channels of PPF-27 are significantly smaller (ca. 7.1 X 7.3 Å compared to 5.4 X 13.0 Å of PPF-23) (Figures 6.20 and 6.21). If the main pathway of the analyte to porphyrin center were through these intra-bilayer channels, we expect to observe a slower quenching of PPF-27 compared with PPF-23. To this end, PPF-27 was activated like PPF-23 and X-ray powder diffraction patterns obtained for as-synthesized, activated, and resolvated samples (Figure 6.22). As indicated by the sharp peaks after activation and resolvation, the structure retains crystallinity and framework stability post-activation. Similar to PPF-23, the experimental unit cell parameters of the as-synthesized, activated, and resolvated PPF-27 were generated and compared to the single crystal unit cell showing, upon activation, retention of the 2D PPF layer, and a slight contraction of the inter-bilayer channel which is reversed upon resolvating (Table 6.3). TGA of the as synthesized and activated PPF-27 shows weight loss due to loss of solvent at ~150 °C and the total collapse beginning at ~375 °C (Figure 6.23). The activated TGA graph of PPF-27 shows that 11.7% of the mass due to solvent is removed upon activation which matches well with the 12.1% weight loss calculated by losing two DEF molecules upon activation. Surprisingly, activated PPF-27 shows almost identical quenching kinetics to PPF-23 (Figures 6.24–6.29), suggesting that the inter-bilayer space

is the main mode of diffusion into the crystal and furthermore, the main interaction of the analyte is to the inter-bilayer face of the porphyrin. This is further supported by a single crystal structure of Zn-porphyrin and DNT reported by Goldberg, in which the DNT is positioned directly over the zinc ion in the porphyrin core (Figure 6.30).²⁶ In the PPF structures, this could only be achievable between bilayers because of the pillar coordinated on the opposite side. Further studies into the diffusion and interaction with the porphyrin are currently being performed.

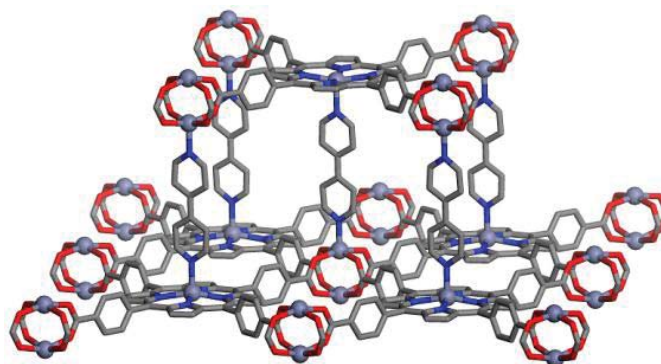


Figure 6.15. Schematic representation of single crystal structure of PPF-27.

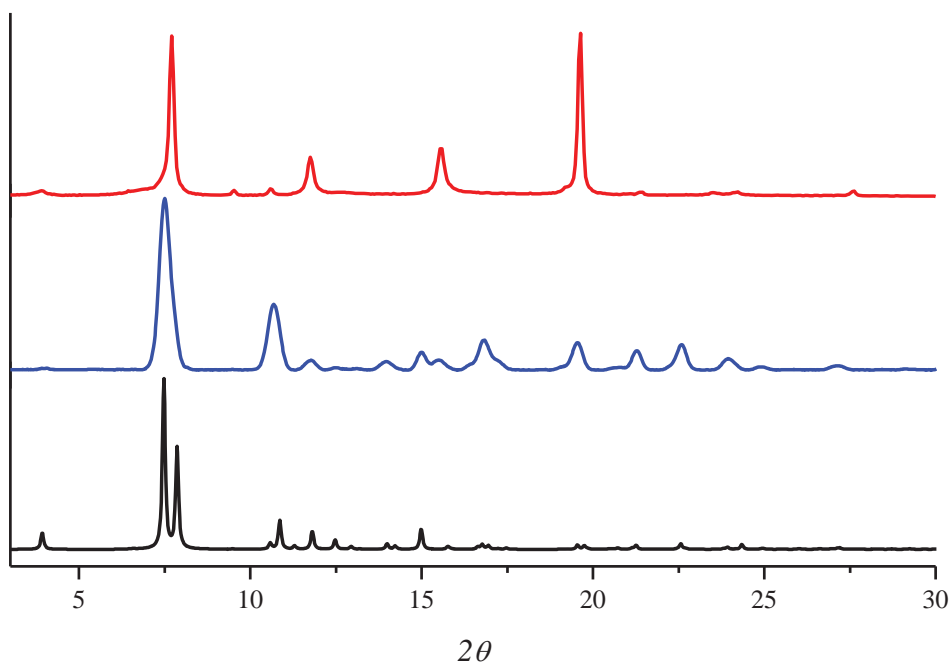


Figure 6.16. Theoretical (bottom) and experimental (top and middle) PXR patterns for PPF-27. The middle PXR was obtained on a flat mount showing high preferred orientation about the $(00l)$ plane. The top PXR pattern was obtained using the spinning capillary method described above.

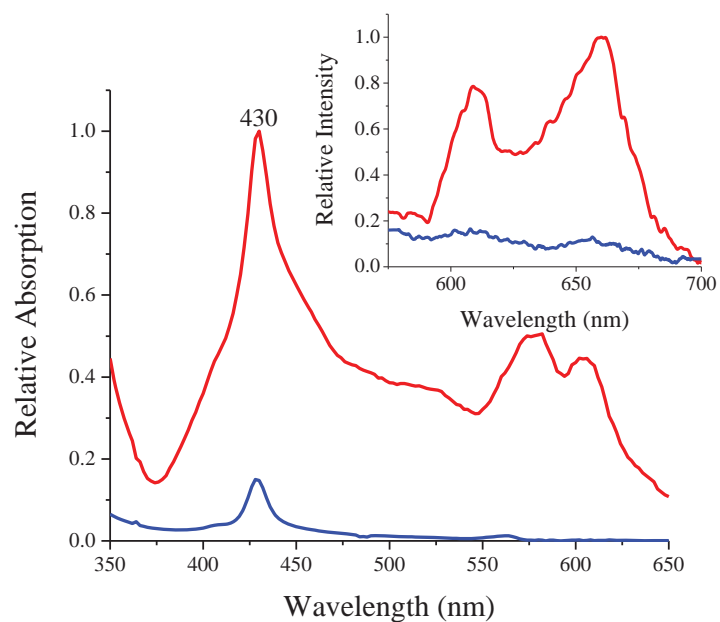


Figure 6.17. UV/Vis absorption and fluorescence emission (inset) spectra of the PPF-27 suspension (red) and solution (blue).

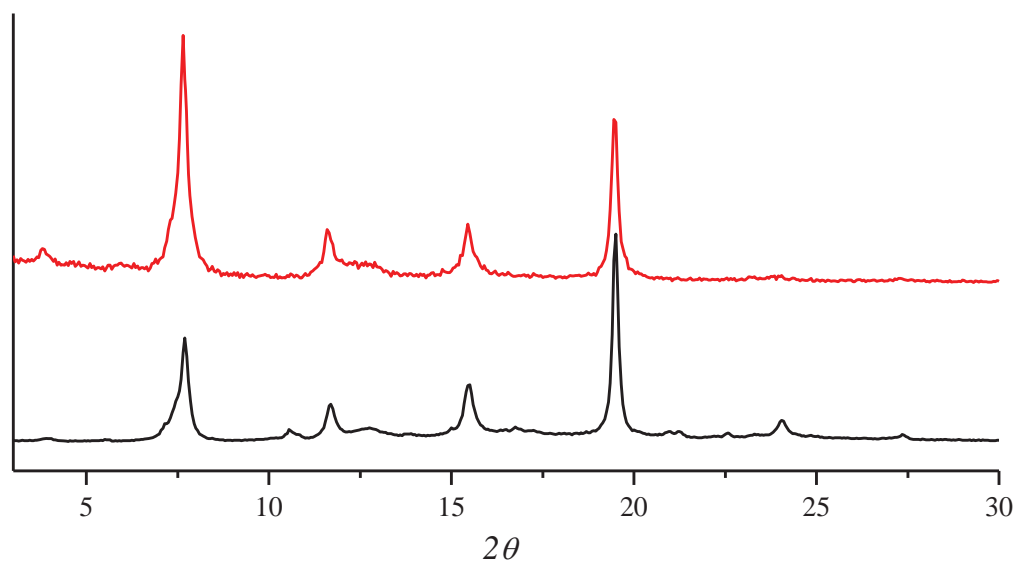


Figure 6.18. PXRD patterns of as synthesized (bottom) and sonicated (top) PPF-27. As seen from the patterns, the structure is retained after this step.

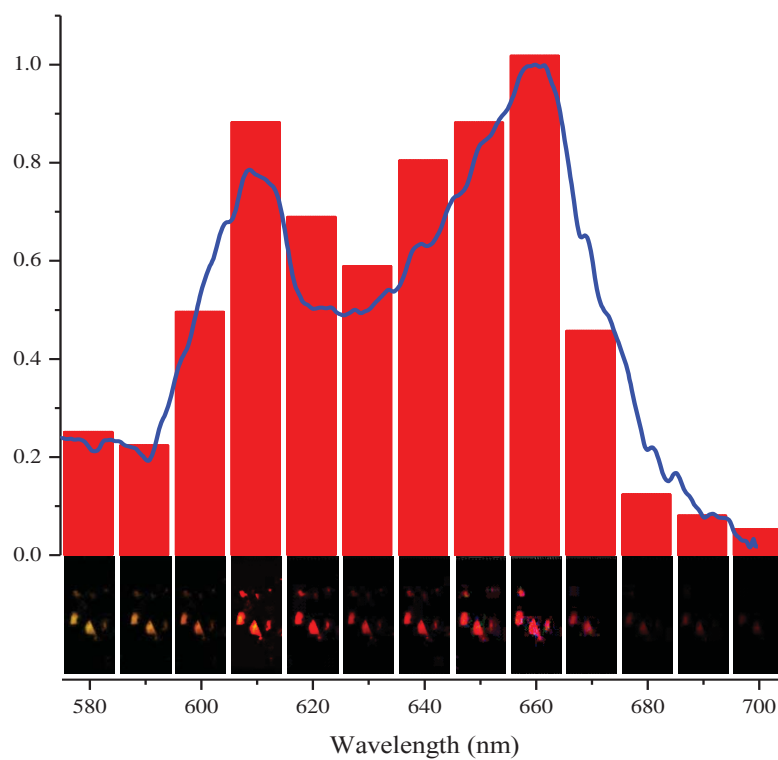


Figure 6.19. Bottom: Fluorescence microscope images of PPF-27 crystals above their corresponding emission wavelength. Top: Relative fluorescence emission intensity of each fluorescence image (red columns). Fluorescence emission from suspension (blue line) is added for comparison purposes.

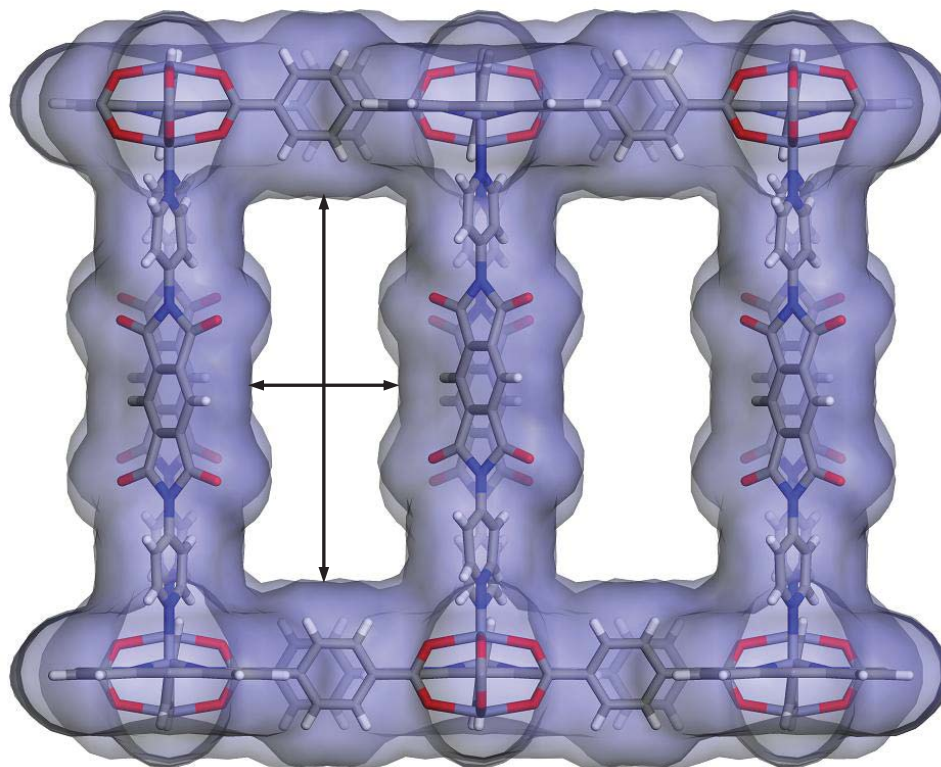


Figure 6.20. Connolly surface of PPF-23 showing 1D channel (5.4 X 13.0 Å) calculated with 1.4 Å VDW scale factor.

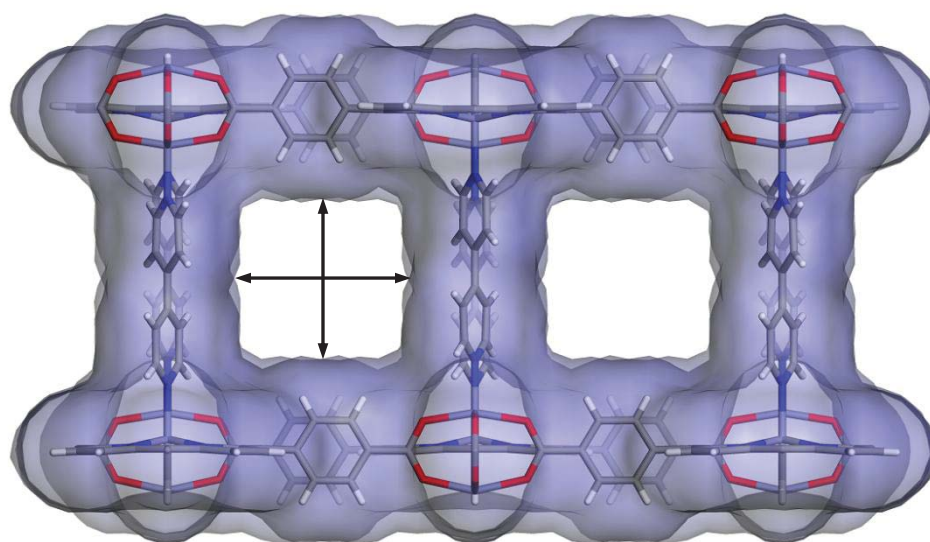


Figure 6.21. Connolly surface of PPF-27 showing 1D channel (7.1 X 7.3 Å) (8.3 Å diagonal) calculated with 1.4 Å VDW scale factor.

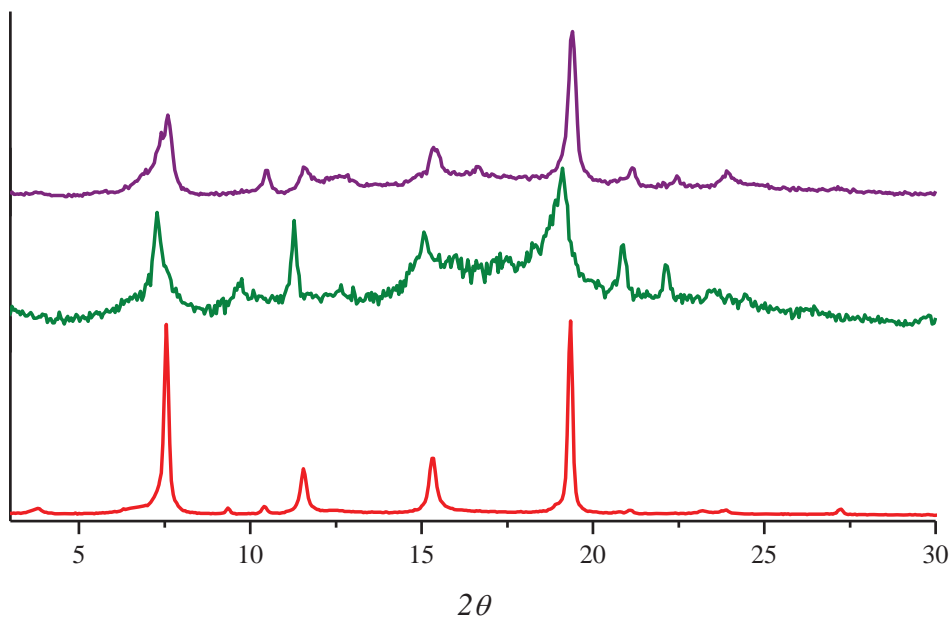


Figure 6.22. PXRD of as synthesized (bottom), activated (middle) and resolvated (top) PPF-27. As seen from the patterns the structure is well maintained, with a slight shift in $(00l)$ peaks upon activation which return upon resolution.

Table 6.3. Tetragonal unit cell parameters of PPF-27.

PPF-27	a , Å	b , Å	c , Å	V , Å ³
Single Crystal*	16.7036(9)	16.7036(9)	22.461(2)	6266.9(7)
As Synthesized	16.688(2)	16.688(2)	22.53(4)	6274(14)
Activated	16.698(2)	16.698(2)	21.36(4)	5955(17)
Resolvated	16.683(5)	16.683(5)	22.59(6)	6314(21)

*Obtained from .CIF file

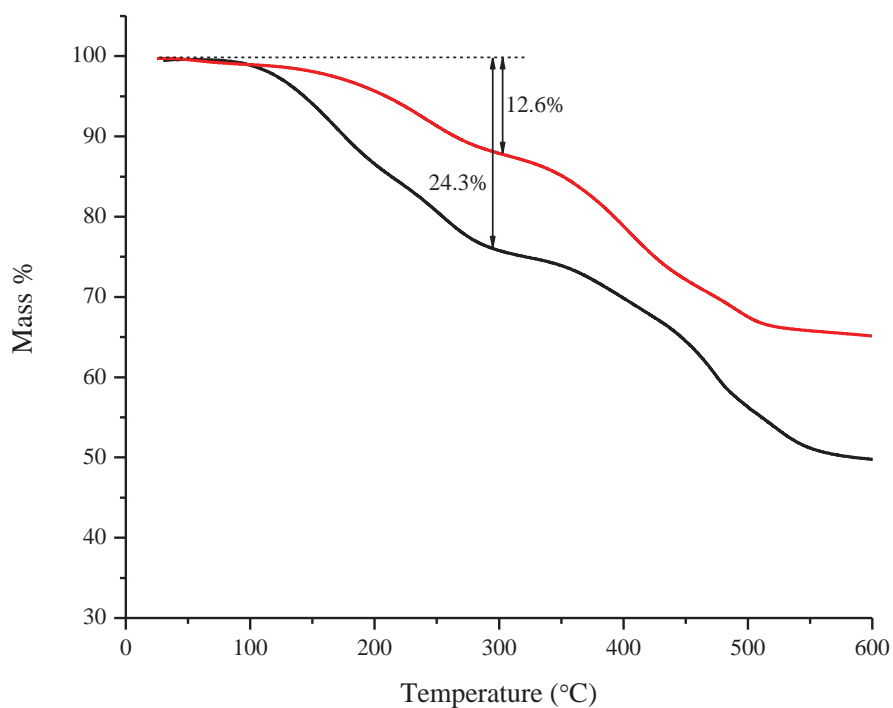


Figure 6.23. TGA data for PPF-27 as synthesized (black) and activated (red).

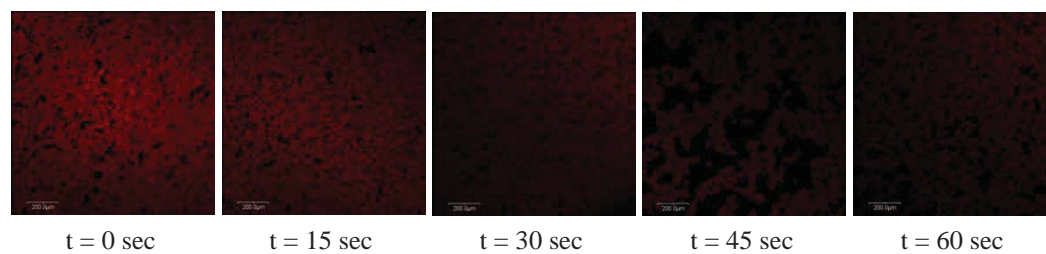


Figure 6.24. Fluorescence microscope images of PPF-27 after exposure to DNT vapors for the corresponding times (emission light is artificially colored red to denote the emission range of 650 ± 30 nm).

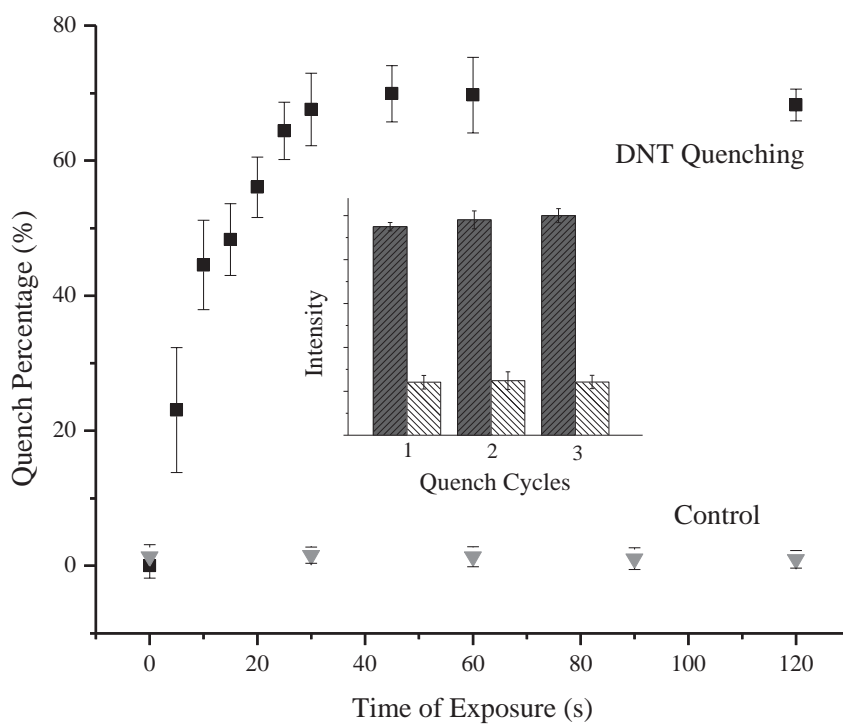


Figure 6.25. Time dependent fluorescence quenching of PPF-27 by DNT. Inset: three consecutive quench/regeneration cycles.

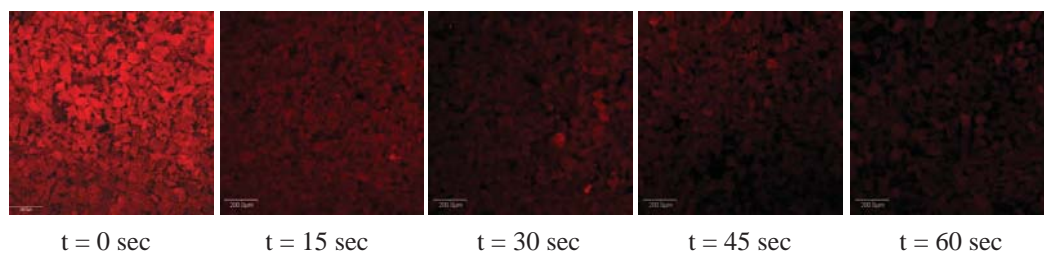


Figure 6.26. Fluorescence microscope images of PPF-27 after exposure to TNT vapors for the corresponding times (emission light is artificially colored red to denote the emission range of 650 ± 30 nm).

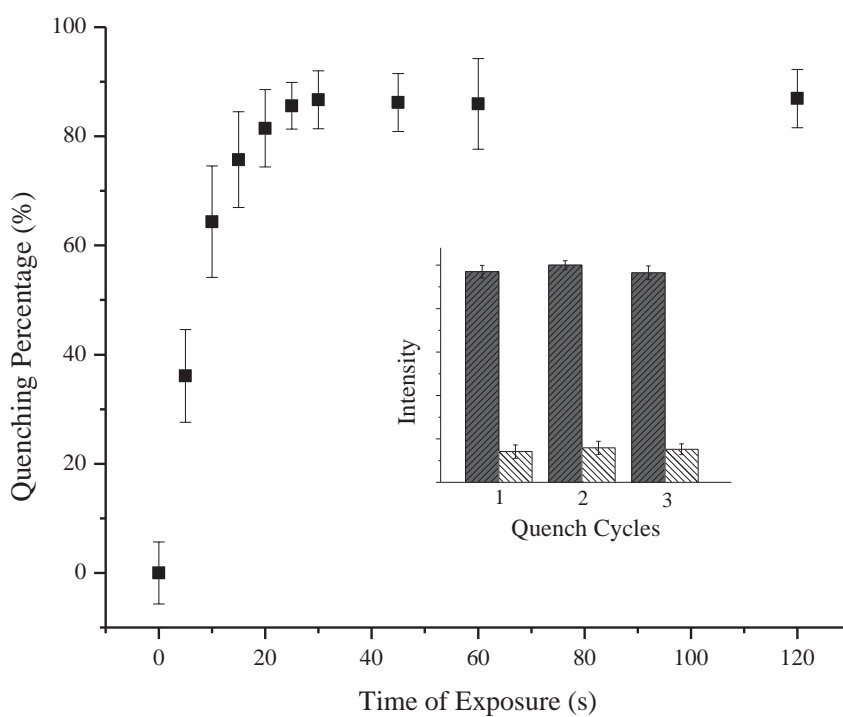


Figure 6.27. Time dependent fluorescence quenching of PPF-27 by DNT. Inset: three consecutive quench/regeneration cycles.

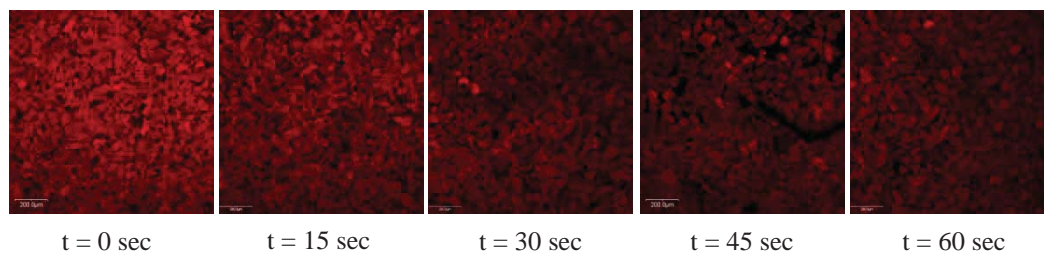


Figure 6.28. Fluorescence microscope images of PPF-27 after exposure to DNT vapors for the corresponding times (emission light is artificially colored red to denote the emission range of 650 ± 30 nm).

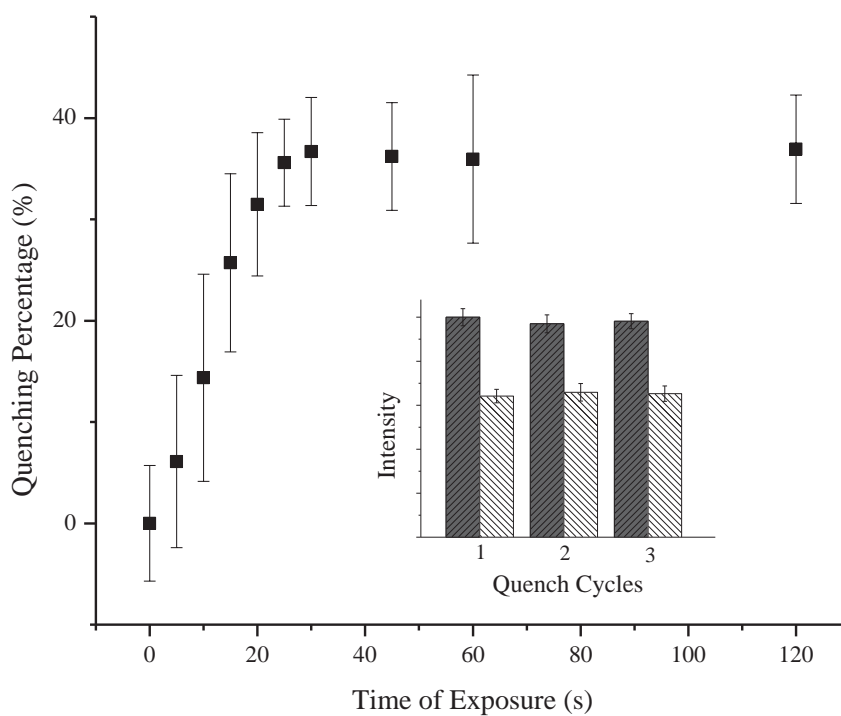


Figure 6.29. Time dependent fluorescence quenching of PPF-27 by NB. Inset: three consecutive quench/regeneration cycles.

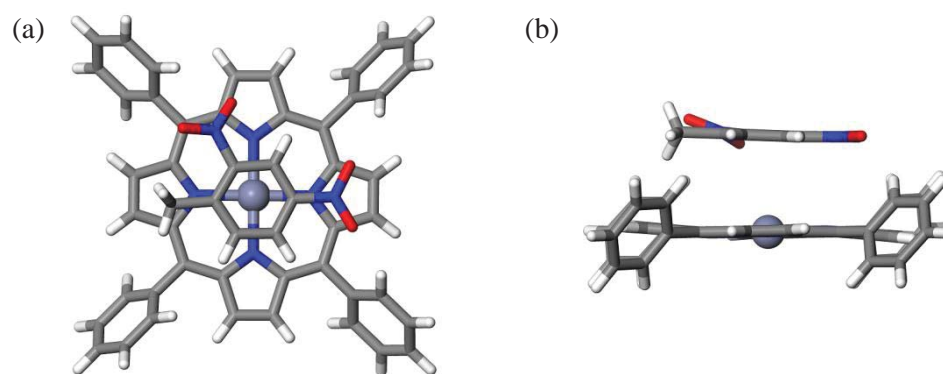


Figure 6.30. Crystal structure of ZnTPP and DNT co-crystal seen (a) top down and (b) from the side, showing main interaction between the porphyrin and nitro–aromatic compound.²⁶

Another important ability for these functional materials is to distinguish separate nitro–aromatic analytes. A more in depth study was performed to observe the difference in fluorescence spectra of PPF-23 before and after exposure to the vapors of NB, DNT, and TNT. The fluorescence emissions corresponding to the low energy Q–transitions of the porphyrin are both quenched. Large differences were observed in the relative quenching of PPF-23 by each analyte (Figures 6.31 and 6.32). The quenching percentage at the two fluorescent band maxima (610 nm and 660 nm) was used to separate the analyte signals by giving a two–dimensional separation of analytes (Figure 6.33). While we observed that this separation is nearly linear, meaning that differences in symmetry between analytes have little effect on the quenching of the different bands, there is a large difference in interaction between each analyte and PPF-23. Additional work is being performed to further separate these signals for better determination of the explosive vapors.

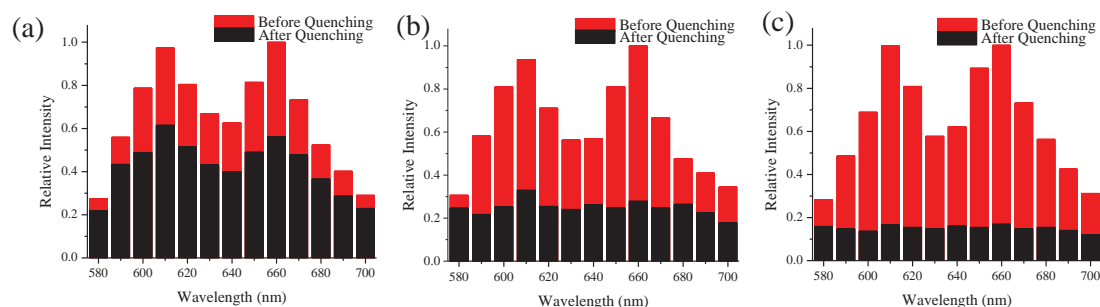


Figure 6.31. Fluorescence spectra of PPF-23 before and after quenching by (a) NB, (b) DNT, and (c) TNT.

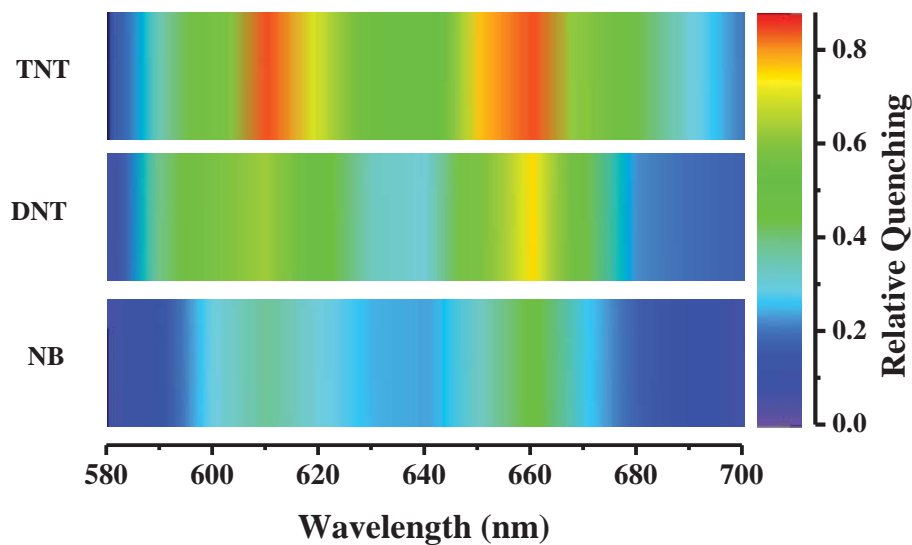


Figure 6.32. ‘False color’ plots showing the quenching spectra of PPF-23 when exposed to different nitro–aromatic compounds.

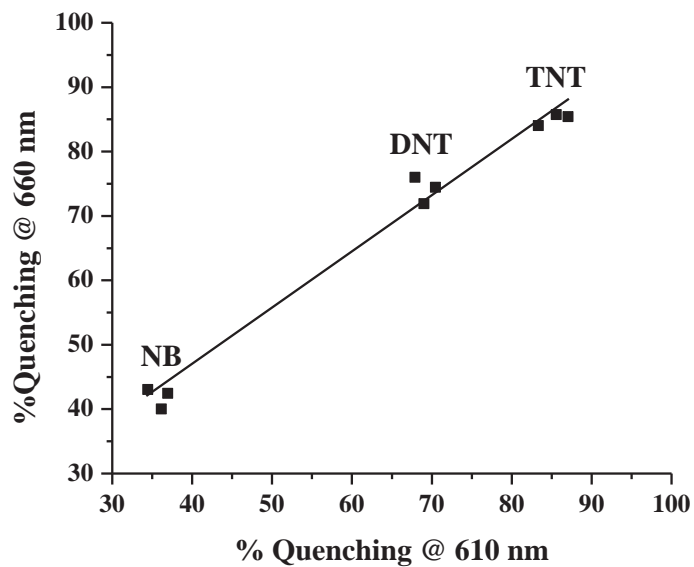


Figure 6.33. Graph showing the % quenching at 610 and 660 nm of PPF-23 from all three analytes.

6.4 Conclusions

In summary, we have synthesized two bilayer porphyrinic MOFs and used them for the fast and reversible detection of different nitro–aromatic explosives. By separating the fluorescent Zn–porphyrins apart within the MOF, self–quenching through porphyrin–porphyrin interaction is prohibited allowing for more efficient detection. By shrinking the intra–bilayer channel size, the mode of diffusion and interaction of the nitroaromatic analytes with the porphyrin can be predicted. The utilization of fluorescence microscopy is successful for visibly observing and quantifying the fluorescence quenching of our PPF crystals. Because of the strong interaction between porphyrins and nitro–aromatics and their quenching in the visible spectrum, we expect that additional porphyrinic MOFs will be developed in the future for highly sensitive and selective sensing applications.

6.5 References

- (1) Germain, M. E.; Knapp, M. J. *Chem. Soc. Rev.* **2009**, *38*, 2543.
- (2) Mullen, C.; Irwin, A.; Pond, B. V.; Huestis, D. L.; Coggiola, M. J.; Oser, H. *Anal. Chem.* **2006**, *78*, 3807.
- (3) (a) Petterson, A.; Wallin, S.; Östmark, H.; Ehlerding, A.; Johansson, I.; Nordberg, m.; Ellis, H.; Al–Khalili, A. *Proc. of SPIE* **2010**, *7664*, 76641K-1. (b) Eliasson, C.; Macleod, N. A.; Matousek, P. *Anal. Chem.* **2007**, *79*, 8185.
- (4) Lin, H.; Suslick, K. S. *J. Am. Chem. Soc.* **2010**, *132*, 15519.
- (5) Yang, J. –S.; Swager, T. M. *J. Am. Chem. Soc.* **1998**, *120*, 11864.
- (6) (a) Peng, Y.; Zhang, A. –J.; Dong, M.; Wang, Y. –W. *Chem. Commun.* **2011**, *47*, 4505. (b) Zyryanov, G. V.; Palacios, M. A.; Anzenbacher, P. *Org. Lett.* **2008**, *10*, 3681.
- (c) Shanmugaraju, S.; Joshi, S. A.; Sarathi Mukherjee, P. *J. Mater. Chem.* **2011**, *21*,

9130. (d) Vijayakumar, C.; Tobin, G.; Schmitt, W.; Kim, M. -J.; Takeuchi, M. *Chem. Commun.* **2010**, *46*, 874. (e) Zhang, K.; Zhou, H.; Mei, Q.; Wang, S.; Guan, G.; Liu, R.; Zhang, J.; Zhang, Z. *J. Am. Chem. Soc.* **2011**, *133*, 8424. (f) Nie, H.; Zhao, Y.; Zhang, M.; Ma, Y.; Baumgarten, M.; Müllen, K. *Chem. Commun.* **2011**, *47*, 1234.
- (7) Tao, S.; Yin, J.; Li, G. *J. Mater. Chem.* **2008**, *18*, 4872.
- (8) Tao, S.; Li, G.; Zhu, H. *J. Mater. Chem.* **2006**, *16*, 4521.
- (9) (a) Lan, A.; Li, K.; Wu, H.; Olson, D. H.; Emge, T. J.; Ki, W.; Hong, M.; Li, J. *Angew. Chem. Int. Ed.* **2009**, *48*, 2334. (b) Pramanik, S.; Zheng, C.; Zhang, X.; Emge, T. J.; Li, J. *J. Am. Chem. Soc.* **2011**, *133*, 4153. (c) Guo, M.; Sun, Z. -M. *J. Mater. Chem.* **2012**, *22*, 15939.
- (10) (a) Ding, S. -B.; Wang, W.; Qiu, L. -G.; Yuan, Y. -P.; Peng, F. -M.; Jiang, X.; Xie, A. -J.; Shen, Y. -H.; Zhu, J. -F. *Mater. Lett.* **2011**, *65*, 1385. (b) Gole, B.; Bar, A. K.; Mukherjee, P. S. *Chem. Commun.* **2011**, *47*, 12137.
- (11) Lauceri, R.; Campagna, T.; Raudino, A.; Purrello, R. *Inorg. Chim. Acta.* **2001**, *317*, 282.
- (12) (a) Tranchemontagne, D. J.; Mendoza-Cortés, J. L.; O'Keeffe, M.; Yaghi, O. M. *Chem. Soc. Rev.* **2009**, *38*, 1257. (b) Moulton, B.; Zaworotko, M. *Chem. Rev.* **2001**, *101*, 1629. (c) Murray, L. J.; Dincă, M.; Long, J. R. *Chem. Soc. Rev.* **2009**, *38*, 1294. (d) Farha, O. K.; Oezguer, Y. A.; Eryazici, I.; Malliakas, C. D.; Hauser, B. G.; Kanatzidis, M. G.; Nguyen, S. T.; Snurr, R. Z.; Hupp, J. T. *Nat. Chem.* **2010**, *2*, 944. (e) Ma, L.; Abney, C.; Lin, W. *Chem. Soc. Rev.* **2009**, *38*, 1248. (f) Lee, J.; Farha, O. K.; Roberts, J.; Scheidt, K. A.; Nguyen, S. T.; Hupp, J. T. *Chem. Soc. Rev.* **2009**, *38*, 1450. (g) Allendorf,

- M. D.; Bauer, D. A.; Bhakta, R. K.; Houk, R. J. T. *Chem. Soc. Rev.* **2009**, 38, 1330. (h) Odbadrakh, K.; Lewis, J. P.; Nicholson, D. M. *J. Phys. Chem. C* **2010**, 114, 7535.
- (13) (a) Frisch, M.; Cahill, C. L. *Dalton Trans.* **2006**, 4679. (b) Grunker, R.; Senkovska, I.; Biedermann, R.; Klein, N.; Klausch, A.; Baburin, I. A.; Mueller, U.; Kaskel, S. *Eur. J. Inorg. Chem.* **2010**, 3835. (c) Zou, R.; Abdel-Fattah, A. I.; Zu, H.; Burrell, A. K.; Larson, T. E.; McCleskey, T. M.; Wei, Q.; Janicke, M. T.; Hickmott, D. D.; Timofeeva, T. V.; Zhao, Y. *Cryst. Growth Des.* **2010**, 10, 1301. (d) Kent, C. A.; Liu, D.; Ma, L.; Papanikolas, J. M.; Meyer, T. J.; Lin, W. *J. Am. Chem. Soc.* **2011**, 133, 12940. (e) Xiao, Y.; Wang, L.; Cui, Y.; Chen, B.; Zapata, F.; Qian, G. *J. Alloy Compd.* **2009**, 484, 601. (f) Guo, Z.; Xu, H.; Su, S.; Cai, J.; Dang, S.; Xiang, S.; Qian, G.; Zhang, H.; O’Keeffe, M.; Chen, B. *Chem. Commun.* **2011**, 47, 5551. (g) Shustova, N. B.; Ong, T. –C.; Cozzolino, A. F.; Michaelis, V. K.; Griffin, R. G.; Dincă, M. *J. Am. Chem. Soc.* **2012**, 134, 15061. (h) Shustova, N. B.; McCarthy, B. D.; Dincă, M. *J. Am. Chem. Soc.* **2011**, 133, 20126. (i) Lee, C. Y.; Farha, O. K.; Hong, B. J.; Sarjeant, A. A.; Nguyen, S. T.; Hupp, J. T. *J. Am. Chem. Soc.* **2011**, 133, 15858. (j) Chen, B.; Yang, Y.; Zapata, F.; Lin, G.; Qian, G.; Lobkovsky, E. B. *Adv. Mater.* **2007**, 19, 1693. (k) Müller, Maike, Devaux, A.; Yang, C. –H.; De Cola, L.; Fischer, R. A. *Photochem. Photobiol. Sci.* **2010**, 9, 846. (l) Jiang, H. –L.; Tatsu, Y.; Lu, Z. –H.; Xu, Q. *J. Am. Chem. Soc.* **2010**, 132, 5586. (m) Zhang, X.; Ballem, M. A.; Hu, Z. –J.; Bergman, P.; Uvdal, K. *Angew. Chem.* **2011**, 123, 5847. (n) Zou, R.; Abdel-Fattah, A. I.; Xu, H.; Burrell, A. K.; Larson, T. E.; McCleskey, T. M.; Wei, Q.; Janicke M. T.; Hickmott, D. D.; Timofeeva, T. V.; Zhao, Y. *Cryst. Growth Des.* **2010**, 10, 1301. (o) Chandler, B. D.; Yu, J. O.; Cramb, D. T.; Shimizu, G. K. H. *Chem. Mater.* **2007**, 19, 4467. (p) Yang, E. –C.; Li, J.; Ding, B.; Liang, Q. –Q.; Wang, X. –G.; Zhao, X.

- J. *CrystEngComm* **2008**, *10*, 158. (q) Wang, C.; Lin, W. *J. Am. Chem. Soc.* **2011**, *133*, 4232. (r) Stylianou, K. C.; Heck, R.; Chong, S. Y.; Bacsá, J.; Jones, J. T. A.; Khimyak, Y. Z.; Bradshaw, D.; Rosseinsky, M. J. *J. Am. Chem. Soc.* **2010**, *132*, 4119.
- (14) Burnett, B. J.; Choe, W. *CrystEngComm*. **2012**, *14*, 6129.
- (15) Choi, E. –Y.; Wray, C. A.; Hu, C.; Choe, W. *CrystEngComm*. **2009**, *11*, 553.
- (16) SMART (version 6.532). *Program for Bruker CCD X-ray Diffractometer Control*, Bruker AXS Inc., Madison, WI, **2005**.
- (17) SAINT+ (version 6.45). *Program for Reduction of Data Collected on Bruker CCD Area Detector Diffractometer*, Bruker AXS Inc., Madison, WI, **2003**.
- (18) Sheldrick, G. M. SADABS, version 2.10, *Program for Empirical Absorption correction of Area Detector Data*, University of Göttingen, **2007**.
- (19) Sheldrick, G. M. SHELXTL, version 6.15, *Program Package for Structure Solution and Refinement*, Bruker Analytical X-ray Systems, Inc., Madison, WI, **2008**.
- (20) Speck, A. . *J. App. Cryst.* **2003**, *36*, 7.
- (21) <http://www.ccp14.ac.uk/ccp/web-mirrors/crush/astaff/holland/UnitCell.html>
- (22) Rsbweb.nih.gov/ij/
- (23) *Material Studio* (version 4.3): Program for Molecular Modeling and Analysis; Accelrys Software Inc.
- (24) (a) Lan, A.; Li, K.; Wu, H.; Olson, D. H.; Emge, T. J.; Ki, W.; Hong, M.; Li, J. *Angew. Chem. Int. Ed.* **2009**, *48*, 2334. (b) Pramanik, S.; Zheng, C.; Zhang, X.; Emge, T. J.; Li, J. *J. Am. Chem. Soc.* **2011**, *133*, 4153.
- (25) Chandrashekar, T. K.; Krishnan, V. *Inorg. Chem.* **1981**, *20*, 2782.

(26) Byrn, M. P.; Curtis, C. J.; Goldberg, I.; Hsiou, Y.; Khan, S. I.; Sawin, P. A.; Tendick, S. K.; Strouse, C. E. *J. Am. Chem. Soc.* **1991**, *113*, 6549.

CHAPTER 7

Drug Incorporation and Delivery in Porphyrin Paddlewheel Frameworks

7.1 Introduction

One emerging avenue for MOFs has been for biomedical applications.¹⁻⁵ MOFs have key advantages over other porous materials for such applications, including their ability to tune their composition by changing the metal and/or organic linker used in synthesis. MOFs additionally have large pores/cavities which could be filled with drug molecules, improving properties such as longer drug release, increased/reduced solubility, and targeted release.^{1,2}

Férey *et al.* reported the drug loading of ibuprofen into the pores of MIL-100 and MIL-101. MIL-100 and MIL-101 are isorecticular MOFs constructed from a Cr₃O SBU and 1,3,5-benzenetricarboxylate or 1,4-benzenedicarboxylate respectively.³ The assembly of these units creates a tetrahedral cage which is large enough to accommodate ibuprofen drugs inside. Indeed, upon immersion in an ibuprofen solution, 35 wt % and 140 wt % of ibuprofen were observed to load within the cavities of MIL-100 and MIL-101 respectively. Additionally it was observed that upon loading, the carboxylic acid group of the ibuprofen deprotonates and coordinates to an available axial site of the Cr₃O SBU. The delivery of the ibuprofen from MIL-100 and MIL-101 show that the kinetics of delivery depends on the location of the ibuprofen drug inside the pores. Guest molecules

of drug quickly diffused out, leaving only drug molecules which were either coordinated to the Cr₃O SBU or have strong $\pi - \pi$ interactions with the pore wall.

Coronas *et al.* reported the incorporation of caffeine molecules into the pores of ZIF-8 through two routes; a one-step synthetic route in which caffeine was added to the ZIF-8 reaction mixture and the MOF structure formed around the caffeine.⁴ Additionally, they were able to incorporate caffeine through a two-step method in which ZIF-8 is constructed and then caffeine diffuses into the pores. It was shown that the one-step method produced better loadings (ca. 28 wt % vs. 4.2 wt % in the two-step process) and a longer release time (27 days vs. 3 days in the two-step process). In the two-step process, caffeine is likely only able to access pores close to the edge of the crystal, whereas in the one-step process, all pores are accessible.

The use of porous solids for biomedical applications requires a biologically friendly composition, thus MOFs are perfect materials for such an application, due to the ability to choose biologically friendly components in the initial synthesis. For the metal composition, the most appropriate metals would be Ca, Mg, Zn, Fe, Ti, or Zr whose toxicity, estimated by their oral lethal dose 50 (LD₅₀), range from few $\mu\text{g}/\text{kg}$ up to more than 1 g/kg (calcium).¹ While these toxicity values will change due to factors like counteranion composition, oxidation state, etc. this estimation is robust enough to be useful for MOF construction. For the organic linker, there are two general possibilities of choice. One is an organic linker that is biomedically benign molecule, which is either not digested, or is benign upon digestion. A second possible choice of linker is that of endogenous organic molecules, that is, molecules that are constitutive part of body composition.⁶ Ideally, this would be the best case for the use of MOFs for bioapplications

since the linker might be reused once administered in the body, which would strongly decrease the risk of adverse effects.

While the most obvious use of a porous solid for bioapplications consists in encapsulating an active molecule in the pores and delivering it through host–guest/diffusion/degradation considerations, this process often has limited success in terms of loading, based on the size and the affinity of the molecule towards the pore.¹ Additionally, the release of the drug often happens through the degradation of the framework, releasing not only the intended drug molecule but also the metal ion and organic linker which could, if not chosen correctly, raise additional toxicity concerns. Using endogeneous linkers and bio friendly metal sources would potentially help with toxicity, but may not be porous or have a great affinity for the guest drug molecule. Thus a new method to create ‘bioactive MOFs’ has recently been investigated.⁷ The drug is coordinated to the metal SBU site as a structural component of the MOF which then can be released by framework degradation in physiological conditions (Figure 7.1).

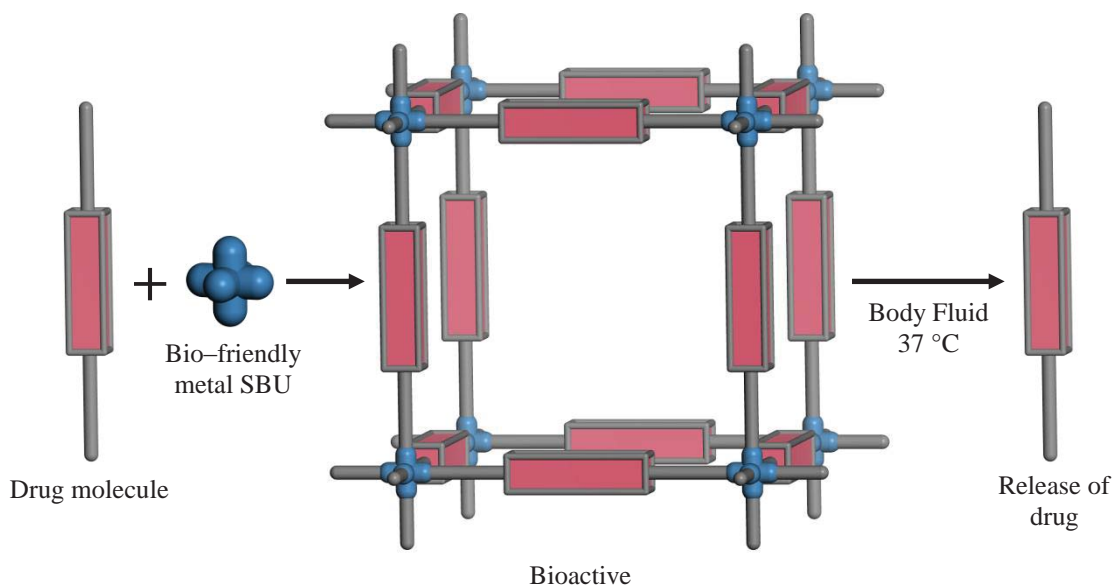


Figure 7.1. Schematic representation of the formation of a bioactive MOF built from a bioactive linker and a bio-friendly SBU.

Recently, Serre *et al.* reported the construction of a bioactive MOF which was constructed by coordinating a bioactive nicotinic acid to an iron based SBU creating BioMIL-1.⁷ BioMIL-1 contains very high drug content (71 wt %) and showed fast release through degradation of the MOF in phosphate buffer solution (PBS) at 37 °C. While this report is a great proof of concept of bioactive MOFs, the rapid release of the nicotinic acid is an issue for practical use and needs to be addressed. The stability of a given MOF varies as a function of its composition and topology. Thus, for a given bioactive linker, one could choose the right metal and structure for a suitable delivery.

In this chapter we describe the first example of incorporating porphyrins with a drug molecule to make a bioactive MOF for drug delivery applications. Porphyrins and their derivatives are a great example of endogenous organic molecules to be used for biomedical applications. Many porphyrins are found within the body, and the toxicity of most porphyrin derivatives is insignificant.⁸ Additionally, porphyrins and their analogues are known to be tumor targeting molecules.⁹ Thus incorporating an antitumor drug into a porphyrin paddlewheel framework (PPF) could potentially create a selective drug delivery system. Herein we report the synthesis of three bioactive-PPFs and the effect of interpenetration on the drug delivery kinetics.

7.2 Experimental Methods

PPF-101 A mixture of 5,10,15,20-tetrakis(4-carboxyphenyl)-2*H*,23*H*-porphyrin (TCPP) (7.9mg, 0.01 mmol), zinc nitrate hexahydrate (8.9 mg, 0.02 mmol), 4,4'-butamethylene bisacetamide (BMBA) (11.9 mg, 0.04 mmol), and 1M nitric acid in ethanol (45 μ L, 0.045 mmol) were added to a mixture of *N,N*-diethyl formamide (DEF) (1.5 mL) and ethanol (0.5 mL) in a capped pressure vessel and heated to 80 °C for 24 hrs, followed by slow cooling to room temperature over 9 hrs.

PPF-102 A mixture of TCPP (7.9 mg, 0.01 mmol), zinc nitrate hexahydrate (8.9 mg, 0.02 mmol), BMBA (8.9 mg, 0.03 mmol), and 1 M nitric acid in ethanol (50 μ L, 0.05 mmol) were added to a mixture of *N,N*-dimethyl formamide (DMF) (0.8 mL) and ethanol (1.2 mL) in a capped pressure vessel and heated to 80 °C for 24 hrs, followed by slow cooling to room temperature over 9 hrs.

PPF-103 A mixture of TCPP (7.9 mg, 0.01 mmol), zinc nitrate hexahydrate (8.9 mg, 0.03 mmol), 4,4'-hexamethylene bisacetamide (HMBA) (11.2 mg, 0.14 mmol), and 1M nitric acid in ethanol (50 μ L, 0.05 mmol) were added to a mixture of DEF (1.5 mL) and ethanol (0.5 mL) in a capped pressure vessel and heated to 80 °C for 24 hrs, followed by slow cooling to room temperature over 9 hrs.

PPF-4 from PPF-101 A mixture of filtered crystals of PPF-101 (14.7 mg, 0.01 mmol) and 4,4'-bipyridine (BPY) (3.2 mg, 0.02 mmol) were added to a mixture of DEF (1.5 mL) and ethanol (0.5 mL) in a capped vial, swirled by hand to mix, and left to react at room temperature for ~3 hrs. The purity of the resulting product was confirmed by PXRD.

Single crystal structure determination:

Crystals of PPF-101 (150 μm x 150 μm) and PPF-103 (110 μm x 230 μm) were sealed in a capillary for XRD measurement. Geometry and intensity data were obtained at room temperature with a Bruker SMARD Apex CCD area detector diffractometer. Preliminary lattice parameters and orientation matrices were obtained from three sets of frames. Data were collected using graphite-monochromated and MonoCap-collimated Mo- K_{α} radiation ($\lambda = 0.71073 \text{ \AA}$) with ω scan method.¹⁰ Data was processed with the SAINT+ program¹¹ for reduction and cell refinement. Multi-scan absorption corrections were applied to the data sets using the SADABS program for area detector.¹² The structure was solved by direct method and refined using SHELXTL.¹³ Disordered, independent solvent molecules inside the frameworks were eliminated in the refinement by PLATON/SQUEEZE.¹⁴ All atoms were refined with anisotropic displacement parameters.

A single crystal of PPF-102 was coated with paratone-*N* oil and the diffraction data measured at 100K with synchrotron radiation ($\lambda = 0.62998 \text{ \AA}$) on a ADSC Quantum-210 detector at 2D SMC with a silicon (111) double crystal monochromator (DCM) at the Pohang Accelerator Laboratory, Korea. The ADSC Q210 ADX program¹⁵ was used for data collection, and HKL3000sm (ver. 703r)¹⁶ was used for cell refinement, reduction and absorption correction. The crystal structure of PPF-102 was solved by the direct method and refined by full-matrix least-squares calculations using SHELXTL.¹³

X-ray powder diffraction (PXRD):

PXRD was collected on a Rigaku D/Max-B X-ray diffractometer with Bragg–Brentano parafocusing geometry, a diffracted beam monochromator, and a conventional copper target X-ray tube set to 35 KV and 25 mA.

Thermogravimetric analysis (TGA):

Performed on a Perkin Elmer STA 6000 thermogravimetric analyzer, heated from 25 °C to 800 °C at a rate of 10 °C/minute under N₂ atmosphere.

¹H NMR analysis:

Performed on a Bruker FT-NMR spectrometer (300 or 400 MHz).

Drug delivery setup:

TGA was used to estimate the molar mass of each bioactive–PPF system (see appendix A5.). ~4 mg samples of similarly sized (~50 μm in length) crystals of bioactive–PPFs were introduced to a 2 mL solution which simulates physiological conditions (phosphate buffered saline (PBS), pH = 7.4, 37 °C) and allowed to dissolve over time. At the designated time, 0.5 mL of the solution was separated from the remaining solution and crystals, and dried. The resulting solid was dissolved in 500 μL of DMSO-*d*₆ with an internal standard of 100 μL of dilute DCM (3 μL diluted with 500 μL of DMSO-*d*₆). ¹H NMR was obtained of the resulting solution. The peaks were integrated and compared to the internal DCM standard to obtain a concentration of Zn-TCPP and drug in solution. This data was used to calculate the % dissolved for each sample (See appendix A5. for raw data).

7.3 Results and Discussion

The drugs that we chose to create bioactive-PPFs were BMBA and HMBA, which belong to a class of antitumor drugs targeting human myeloma cells.¹⁷ These drugs are characterized by having two pyridyl groups at the end of a long di-amide chain (see Figure 7.2). Because of the two pyridyl groups, these molecules are attractive as pillaring agents to be incorporated in PPFs. Purple crystals of two new structures, PPF-101 and PPF-102, were each synthesized via a traditional one-pot solvothermal reaction of TCPP, zinc nitrate hexahydrate, and BMBA. The purity of the resulting crystals was confirmed by PXRD (Figures 7.3 and 7.4). Single crystal structures were obtained of both PPF-101 and PPF-102 (Table 7.1). PPF-101 is an AB stacked bilayer structure with $P4/nmm$ symmetry (Figure 7.5). PPF-102 is an AA stacked interpenetrated 3D structure with $P-1$ symmetry (Figure 7.5). PPF-101 and PPF-102 are framework isomers, in that they both contain a 1:1:1 stoichiometric ratio of porphyrin, paddlewheel, and BMBA, but differ in stacking arrangement. Because of this difference in stacking arrangement, the kinetics of drug delivery might be different.

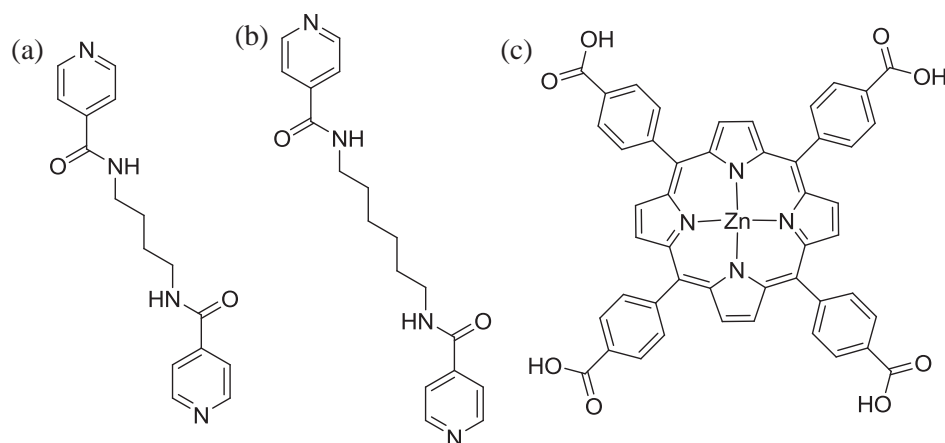


Figure 7.2. Target drug molecules (a) BMBA and (b) HMBA to be incorporated in MOFs with (c) TCPP to create bio-PPFs.

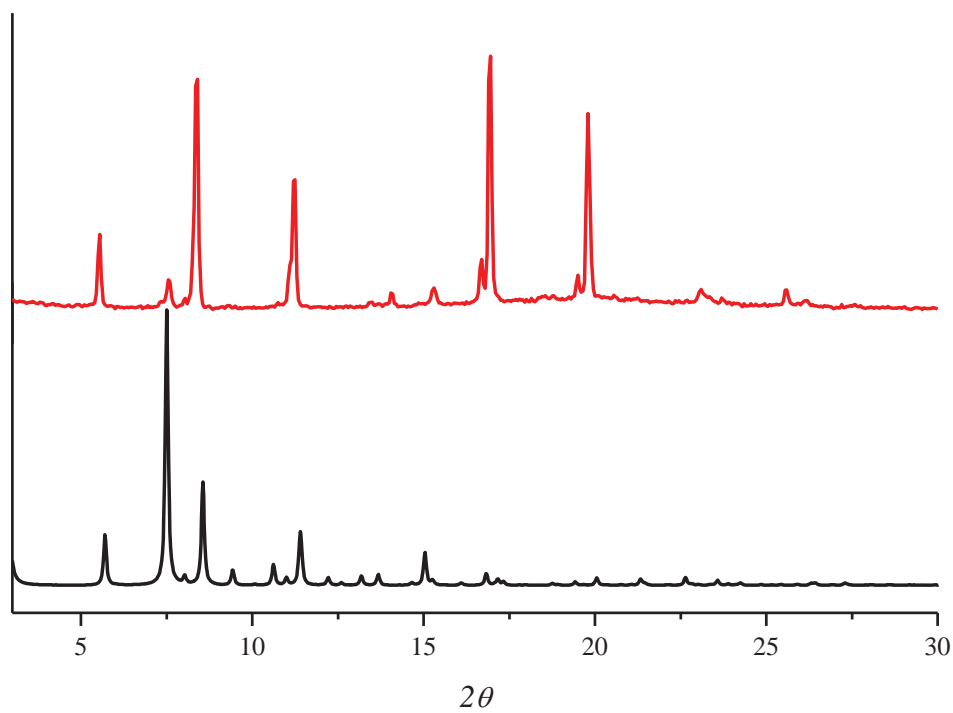


Figure 7.3. Theoretical (bottom) and experimental (top) PXR D patterns for PPF-101.

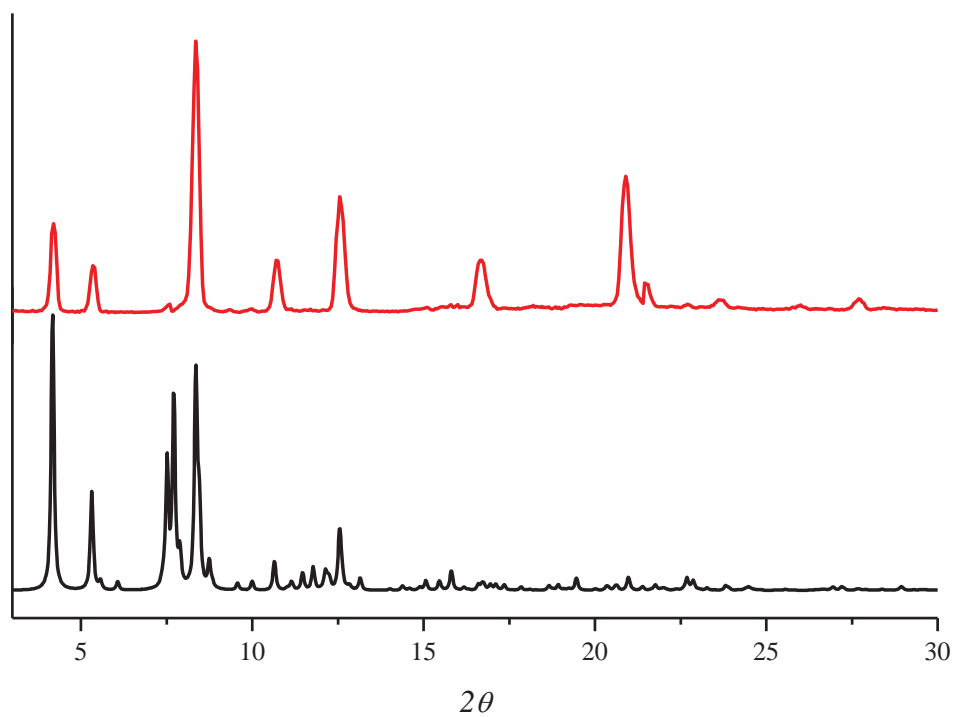


Figure 7.4. Theoretical (bottom) and experimental (top) PXR D patterns for PPF-102.

Complex	PPF-101	PPF-102	PPF-103
chemical formula*	$C_{64}H_{42}N_8O_{10}Zn_3$	$C_{64}H_{42}N_8O_{10}Zn_3$	$C_{66}H_{46}N_8O_{10}Zn_3$
formula weight*	1279.31	1279.31	1307.37
crystal system	tetragonal	triclinic	orthorhombic
space group	$P4/nmm$	$P-1$	$Pmma$
a (Å)	16.647(4)	16.346(3)	25.1139(12)
b (Å)	16.647(4)	16.942(3)	16.7870(8)
c (Å)	30.966(8)	22.231(4)	16.5996(8)
α (°)	90.00	78.84(3)	90.00
β (°)	90.00	76.13(3)	90.00
γ (°)	90.00	89.97(3)	90.00
V (Å ³)	8581(4)	5857(2)	6998.2(6)
Z	2	2	2
ρ_{calc} (g/cm ³)*	0.502	0.767	0.629
μ (mm ⁻¹)*	0.440	0.441	0.540
$R_1, I > 2\sigma(I)$	0.0634	0.1172	0.0683
$wR_2, I > 2\sigma(I)$	0.1567	0.3081	0.1798

*Based on the formula without uncoordinated solvent molecules.

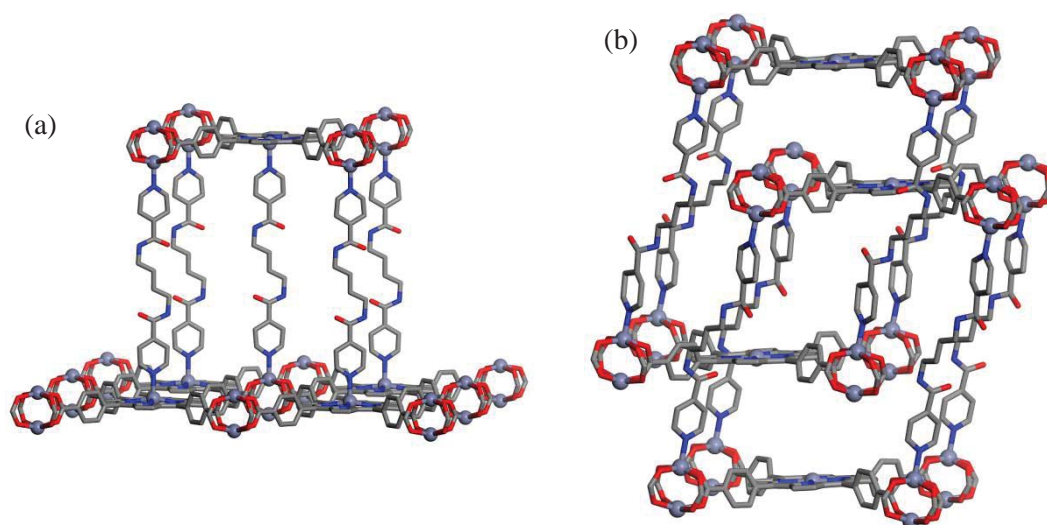


Figure 7.5. Schematic representation of single crystal structures of bio-PPFs (a) PPF-101 and (b) PPF-102.

To test the relative stability of the drug within the PPF structures, a linker replacement reaction was performed on both PPF-101 and PPF-102. The effect of interpenetration on the ability to replace structural linkers was discussed in chapter 3. PPF-19, an AA interpenetrated 3D structure like PPF-102, was shown to not be able to replace its dipyriddy linkers because the linker was effectively fixed within the alternate interpenetrated net. The non-interpenetrated isomer, PPF-18, readily replaced its dipyriddy linker, because of the availability of the introducing linker to diffuse in and replace the structural linker, which subsequently diffuses out of the crystal. Crystals of PPF-101 and PPF-102 were immersed in a solution containing BPY linker. Like the previous case of PPF-18 and PPF-19, the AB bilayer PPF-101 transformed to the BPY linked PPF-27 via the linker replacement as confirmed by PXRD (Figure 7.6). The AA interpenetrated PPF-102, however, did not transform, even after ~1 week of immersion in BPY solution as confirmed by PXRD (Figure 7.7). It can be assumed from this experiment that the BMBA drug within PPF-101 will diffuse out of the crystals faster than the BMBA within PPF-102.

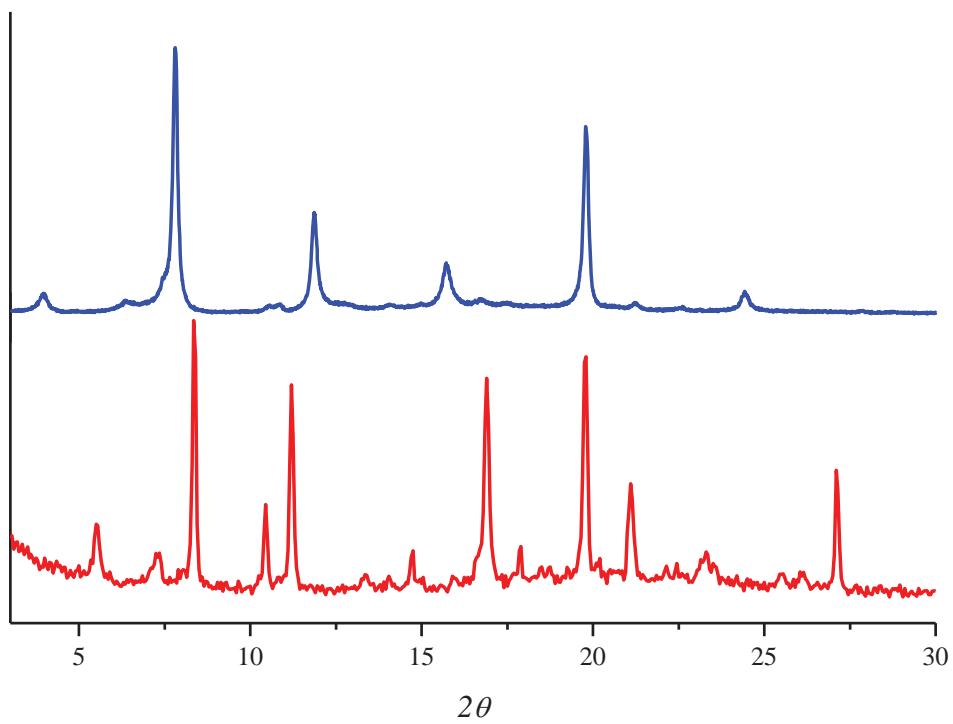


Figure 7.6. PXRD of PPF-101 before (below) and PPF-27 after (above) linker replacement transformation.

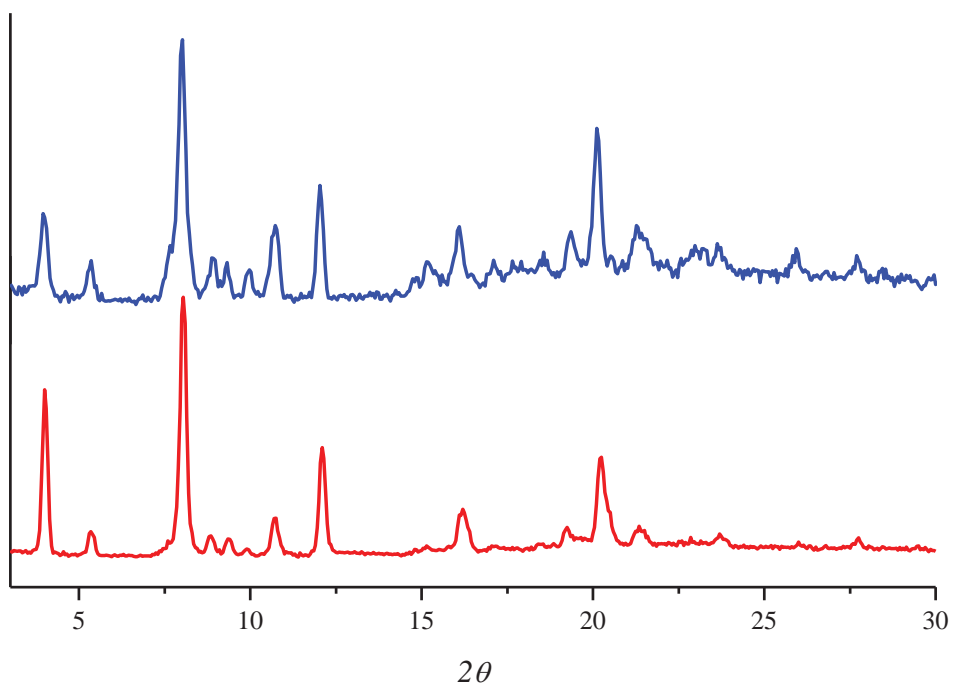


Figure 7.7. PXRD of PPF-102 before (below) and after (above) linker replacement transformation trial.

Crystals of PPF-101 were added to a PBS solution and heated at 37 °C to simulate biological conditions, and analyzed by ^1H NMR to find the % of drug and porphyrin dissolved from the crystals. It was found that after two hours, all of the BMBA had diffused out of PPF-101 and into solution (Figures 7.8 and 7.9). The % of porphyrin dissolved into solution within the same time range was much less indicating that the drugs were released from the 2D PPF layers at a faster rate than the full dissolution of the crystal. In contrast, PPF-102 took a significantly longer time to dissolve and release the drug into solution (Figures 7.10 and 7.11). Indeed, only after 2 days did all of the BMBA come into solution. Additionally, The percentage of porphyrin dissolved mirrors the percentage of BMBA released, indicating that the drug was released only upon framework destruction/dissolution.

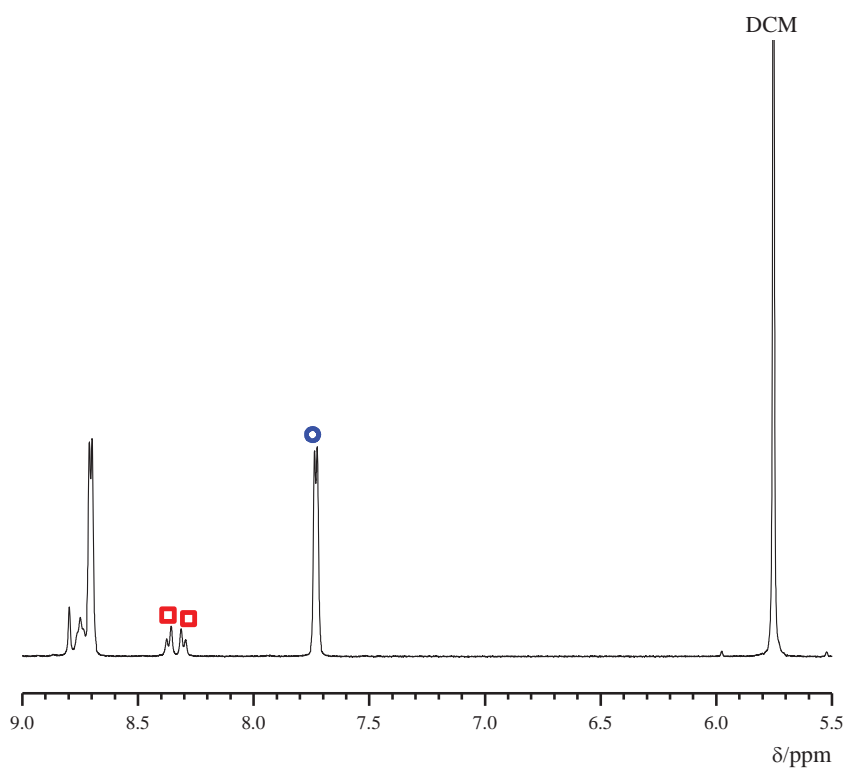


Figure 7.8. ^1H NMR spectra of dissolved PPF-101. Red squares and blue circles represent signals of ZnTCPP and BMBA respectively used in quantifying % dissolved.

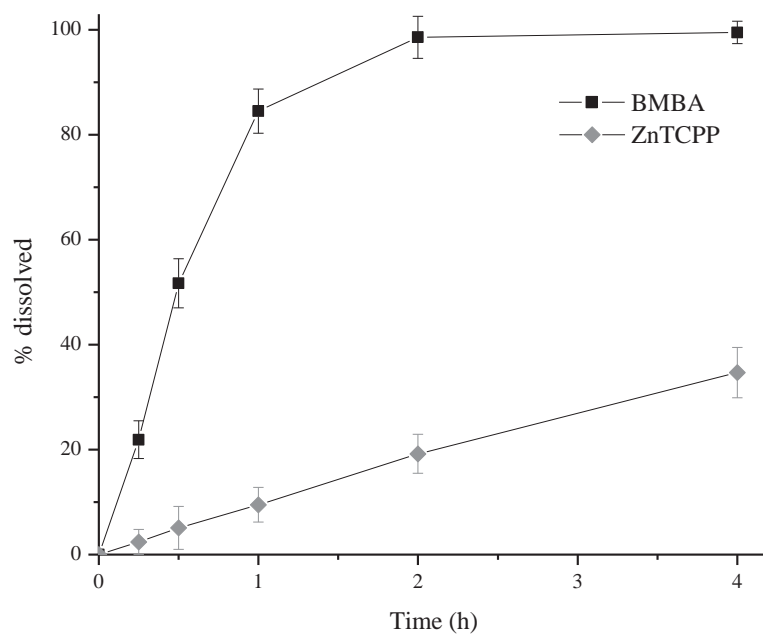


Figure 7.9. Time dependent dissolution of ZnTCPP and BMBA from PPF-101.

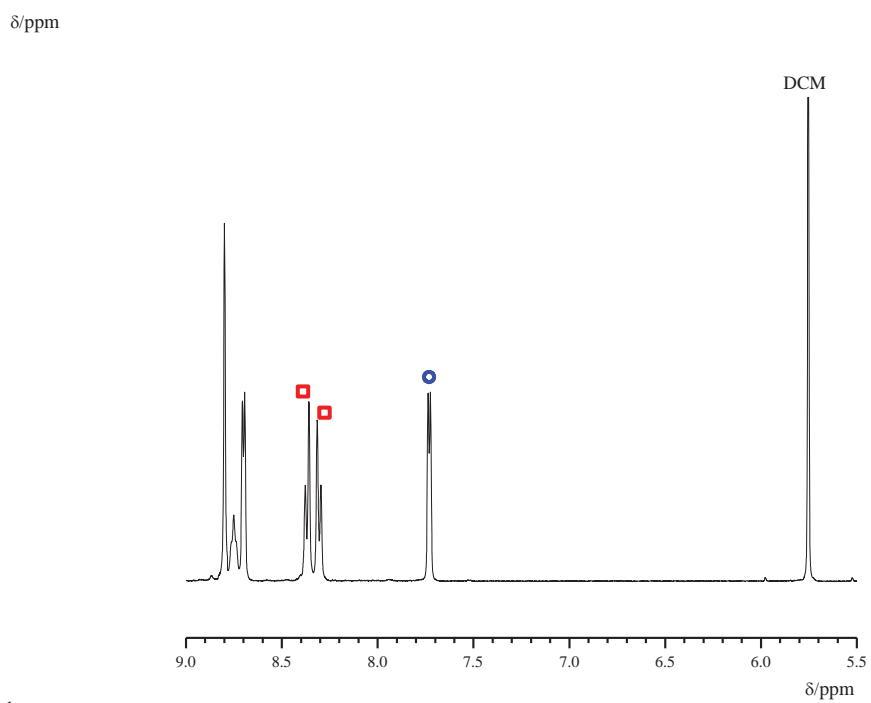


Figure 7.10. ^1H NMR spectra of dissolved PPF-102. Red squares and blue circles represent signals of ZnTCPP and BMBA respectively used in quantifying % dissolved.

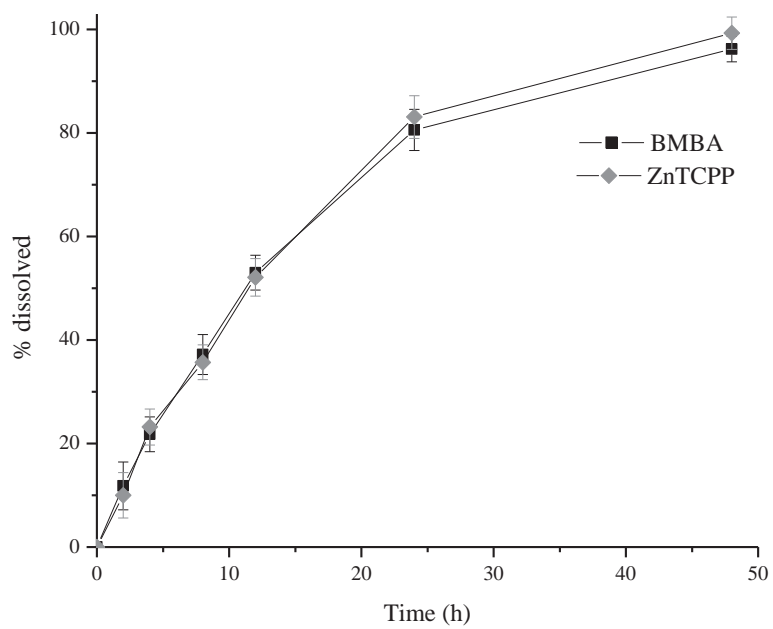


Figure 7.11. Time dependent dissolution of ZnTCPP and BMBA from PPF-102.

Because of the open nature of the AB bilayer structure of PPF-101, water could diffuse into the pores and disrupt the coordination bond between the BMBA and the axial site of the paddlewheel SBU. The BMBA then is unobstructed in its diffusion out of PPF-101, resulting in fast release of the drug. PPF-102, however, cannot fully release the BMBA after the disruption of the coordination bond to the axial site of the paddlewheel SBU. Since it is fixed within the cavity made by the alternate PPF net, it is only after that net is destroyed that the BMBA can come out into solution, resulting in a much slower release.

To further test the robustness of this hypothesis, another crystal system was synthesized with the longer drug HMBA, TCPP, and zinc nitrate via a traditional one-pot solvothermal reaction. The purity of the resulting crystals was confirmed by PXRD (Figure 7.12). A single crystal structure was obtained for the new phase, PPF-103 (See Table 7.1). PPF-103 is an AA interpenetrated 3D structure, similar to PPF-102, creating *Pmma* symmetry (Figure 7.13). The properties of PPF-103 are also similar to that of PPF-102. Upon immersion in BPY solution for ~1 week, the structure was retained as confirmed by PXRD, showing it to be immune to a linker replacement (Figure 7.14). The dissolution kinetics show a slow release of HMBA into the PBS solution, with 91 % of HMBA dissolved into solution after one day and fully dissolved by two days (Figures 7.15 and 7.16). Like PPF-102, the porphyrin % dissolution in PPF-103 mirrors the % dissolution of the drug indicating that it is upon framework destruction that the drug is released.

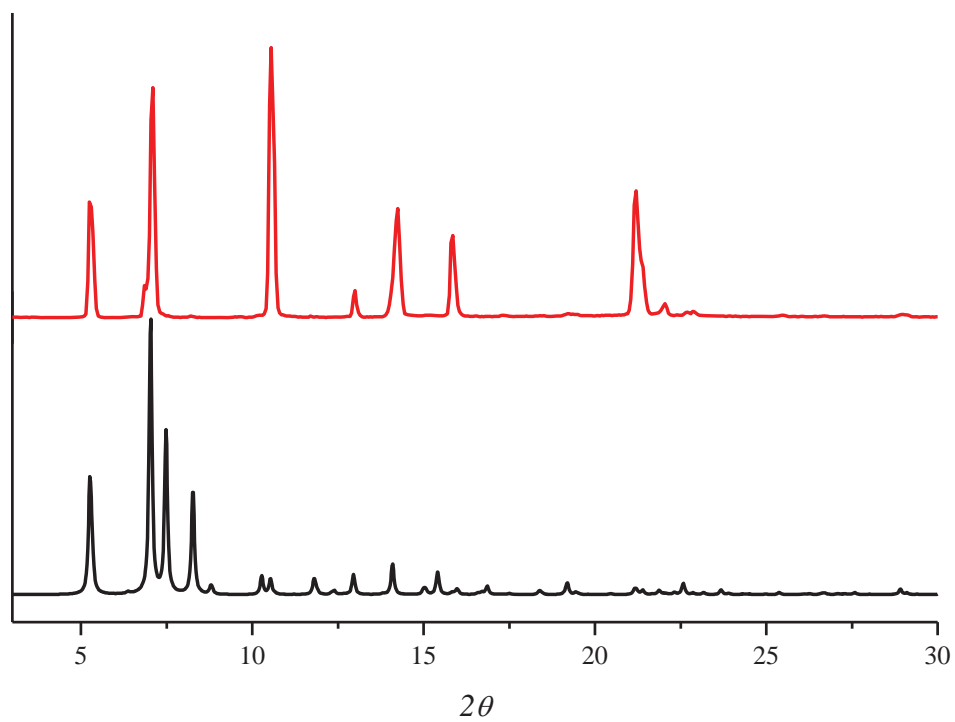


Figure 7.12. Theoretical (bottom) and experimental (top) PXRD patterns for PPF-103.

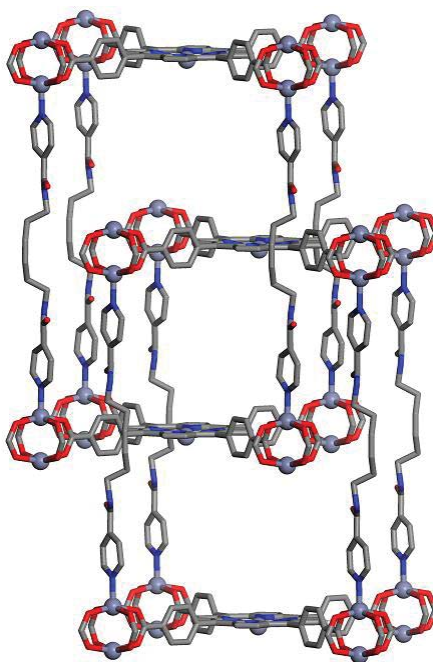


Figure 7.13. Schematic representation of single crystal structures of bio-PPF PPF-103.

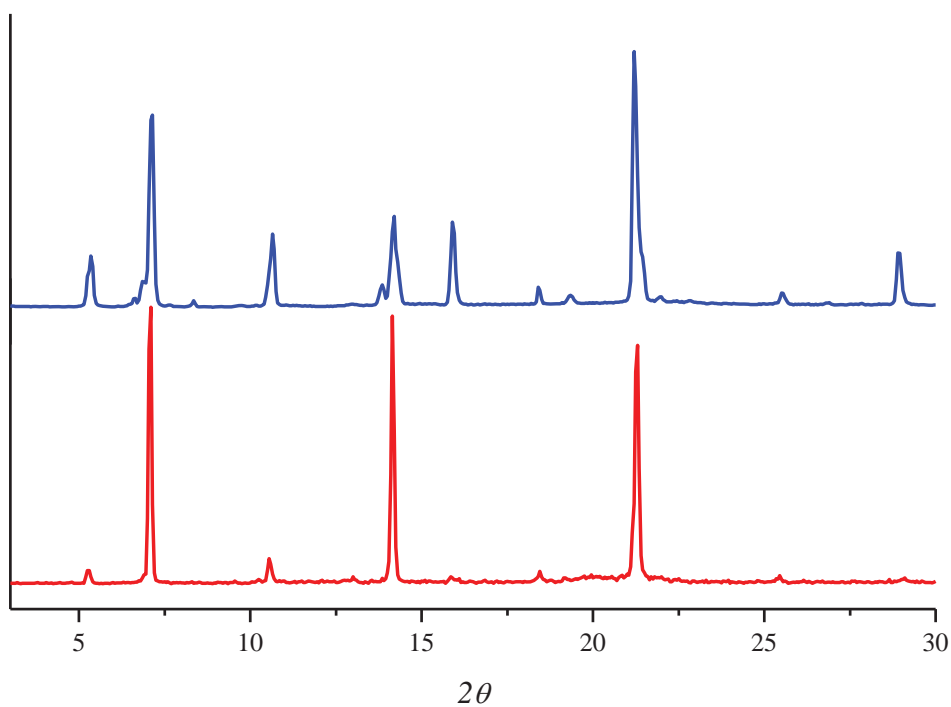


Figure 7.14. PXRD of PPF-103 before (below) and after (above) linker replacement transformation trial.

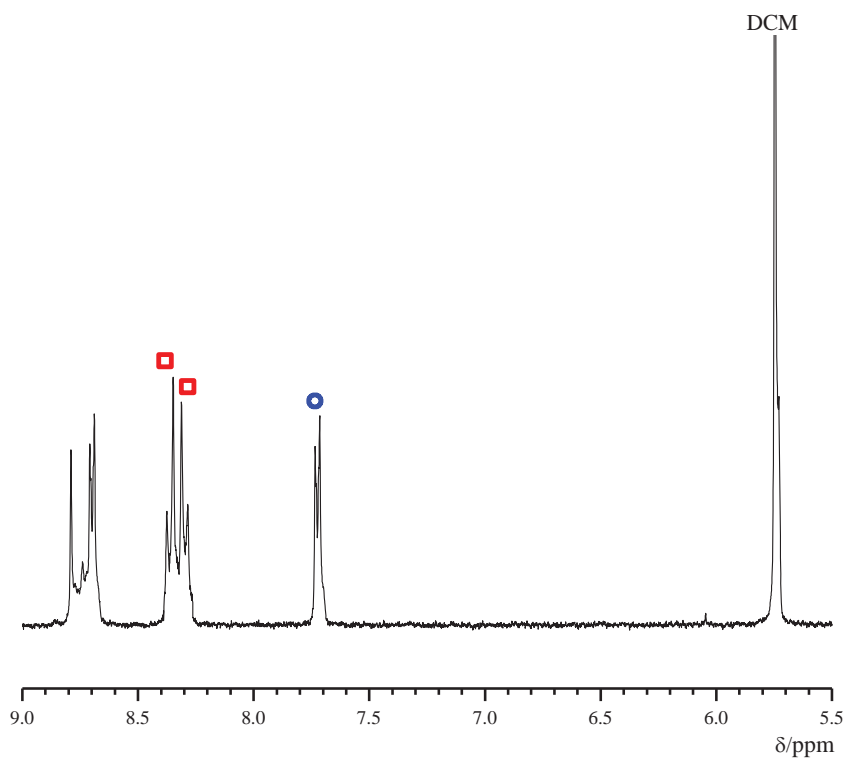


Figure 7.15. ^1H NMR spectra of dissolved PPF-103. Red squares and blue circles represent signals of ZnTCPP and BMBA respectively used in quantifying % dissolved.

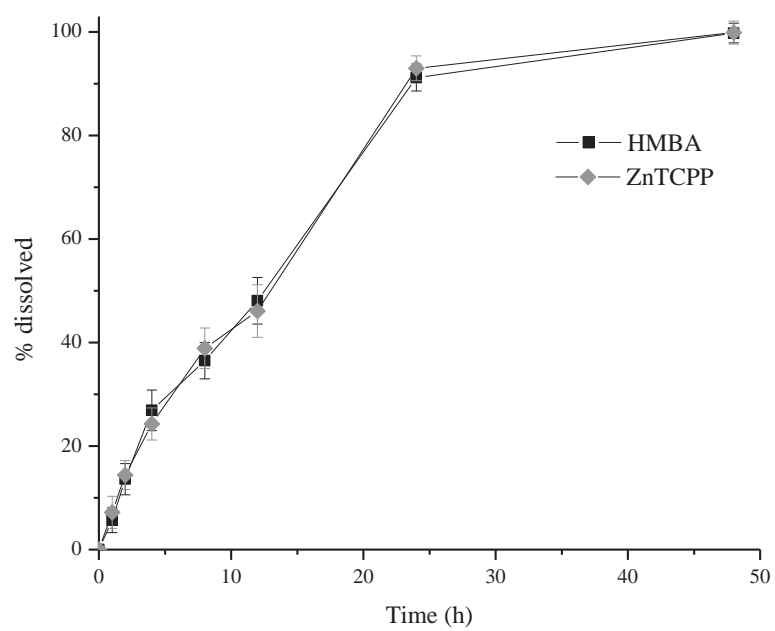


Figure 7.16. Time dependent dissolution of ZnTCPP and BMBA from PPF-103.

7.4 Conclusions

We constructed three new bio-PPFs which combines a bio-friendly zinc paddlewheel SBU with a possible tumor targeting porphyrin metalloligand and an anti-tumor drug to create a new drug delivery system. We have shown that the delivery of the drug within simulated biological solution is directly dependent on the packing of the MOF. The less restricted AB bilayer structure released the drug at a much faster rate than that of the more restricted AA interpenetrated 3D structure. This is the first time that the dependence of drug delivery kinetics on crystal packing in MOFs has been investigated. Additionally, this is the first case of creating framework isomers which have drastically different drug release kinetics, allowing for both a rapid release and a slow release with the same materials. It is our belief that porphyrin-based bio-MOFs could become a strong candidate for the next generation of drug delivery system.

7.5 References

- (1) Horcajada, P.; Gref, R.; Baati, T.; Allan, P. K.; Maurin, G.; Couvreur, P.; Férey, G.; Morris, R. E.; Serre, C. *Chem. Rev.* **2012**, *112*, 1232.
- (2) (a) Kitagawa, S.; Kataura, R.; Noro, S. –I. *Angew. Chem. Int. Ed.* **2004**, *43*, 2334. (b) Fere, G.; Serre, C. *Chem. Soc. Rev.* **2009**, *38*, 1380.
- (3) Horcajada, P.; Serre, C.; Vallet-Regí, M.; Sebban, M.; Taulelle, F.; Férey, G. *Angew. Chem. Int. Ed.* **2006**, *45*, 5974.
- (4) Liédana, N.; Galve, A.; Rubio, C.; Téllez, C.; Coronas, J. *Appl. Mater. Interfaces* **2012**, *4*, 5016.
- (5) (a) Vasconcelos, I. B.; da Silva, T. G.; Militão, G. C. G.; Soares, T. A.; Rodrigues, N. M.; Rodrigues, M. O.; da Costa, N. B.; Freire, R. O.; Junior, S. A. *RSC Adv* **2012**, *2*,

9437. (b) Wang, H. –N.; Meng, X.; Yang, G. –S.; Wang, X. –L.; Shao, K. –Z.; Su, Z. –M.; Wang, C. –G. *Chem. Commun.* **2011**, 47, 7128.
- (6) (a) Keskin, S.; Kizilel, S. *Ind. Eng. Chem. Res.* **2011**, 50, 1799. (b) Imaz, I.; Rubio–Martínez, M.; An, J.; Solé–Font, I.; Rosi, N. L.; Maspoch, D. *Chem. Commun.* **2011**, 47,7287. (c) Weber, R.; Bergerhoff, G. *Z. Kristallogr.* **1991**, 195, 878. (d) Serre, C.; Millange, F.; Surblé, S.; Férey, G. *Angew. Chem. Int. Ed.* **2004**, 43, 6286. (e) Serre, C.; Surblé, S.; Mellot–Draznieks, C.; Filinchuk, Y.; Férey, G. *Dalton Trans.* **2008**, 5462.
- (7) Miler, S. R.; Heurtaux, D.; Baati, T.; Horcajada, P.; Grenèche, J. –M.; Serre, C. *Chem. Commun.* **2010**, 46, 4526.
- (8) Chen, Z.; Zhou, S.; chen, J.; Deng, Y.; Luo, Z.; Chen, H.; Hamblin, M. R.; Huang, M. *ChemMedChem* **2010**, 5, 890.
- (9) Allen, C. m.; Sharman, W. M.; van Lier, J. E. *J. Porphyrins Phthalocyanines* **2001**, 5, 161.
- (10) SMART (version 6.532). *Program for Bruker CCD X–ray Diffractometer Control*, Bruker AXS Inc., Madison, WI, **2005**.
- (11) SAINT+ (version 6.45). *Program for Reduction of Data Collected on Bruker CCD Area Detector Diffractometer*, Bruker AXS Inc., Madison, WI, **2003**.
- (12) Sheldrick, G. M. SADABS, version 2.10, *Program for Empirical Absorption correction of Area Detector Data*, University of Göttingen, **2007**.
- (13) Sheldrick, G. M. SHELXTL, version 6.15, *Program Package for Structure Solution and Refinement*, Bruker Analytical X–ray Systems, Inc., Madison, WI, **2008**.
- (14) Speck, A. . *J. App. Cryst.* **2003**, 36, 7.

(15) Arvai, A. J.; Nielsen, C. ADSC Quantum-210 ADX Program, Area Detector System Corporation; Poway, CA, USA, 1983.

(16) Otwinowski, Z.; Minor, W.; in *Methods in Enzymology*, ed. Carter, Jr., C. W.; Sweet, R. M. Academic Press, New York, 1997, vol. 276, part A, pp. 307.

(17) (a) Siegel, D. A.; Zhang, X.; Feinman, R.; Teitz, T.; Zelenetz, A.; Richon, V. M.; Rifkind, R. A.; Marks, P. A.; Michaeli, J. *Proc. Natl. Acad. Sci. USA* **1998**, *95*, 162. (b) Aakeröy, C. B.; Forbes, S.; Desper, J. *J. Am. Chem. Soc.* **2009**, *131*, 17048.

CHAPTER 8

DEVELOPMENT OF ISORETICULAR Mn(III)– PORPHYRIN PADDLEWHEEL FRAMEWORK SERIES

8.1 Introduction

As discussed in Chapter 2, one of the many exciting possibilities of including porphyrin metalloligands into MOFs is the possibility of having coordinatively unsaturated metal centers on the pore surface of the MOF. These metal centers are very important for their ability to be used as sensing materials for small molecules, heterogeneous catalysis, and gas storage. Specifically for gas storage, metalloligands are important to increase the binding strength of the pore surface to gasses.¹ Currently, due to the weak dispersion interactions of H₂ with typical MOF materials, storing enough hydrogen to fuel a car is a formidable task, requiring high pressure and cryogenic temperatures.² Including coordinatively unsaturated metal centers on the pore surface is one way to improve the binding strength of H₂ to the pore surface to the required 15–20 kJ/mol.^{2,3}

Because of these great possibilities, our group has continually worked on the rational design of porphyrinic MOF material with coordinatively unsaturated metal centers. The self-assembly process of MOFs is intrinsically influenced by the preferred coordination geometry of the metal building units—both SBU and metalloligand metal center.⁴ This ordinarily is a desired effect—making it possible to predict the structures of the MOFs from their building units. It becomes a significant challenge, however, in the

construction of MOFs with coordinatively unsaturated metal centers. During the self-assembly process, the metal centers at the SBU and in the porphyrin core commonly become fully saturated with linkers, leaving no accessible metal centers in the MOF to perform chemistry on.

There have been a number of synthetic strategies reported to overcome this obstacle. Hupp *et al.* described a two-step synthesis to achieve a series of porphyrinic MOFs that contain coordinatively unsaturated metal sites.⁵ *meso*-tetra(4-carboxyphenyl)-porphyrin (TCPP) was statically heated with zinc nitrate hexahydrate in dimethyl formamide (DMF) to begin the assembly of a 2D grid similar to that assembled in PPF structures. Following this initial heating, a dipyriddy-substituted porphyrin was added to the reaction solution and further heated. The resulting crystal structure contains the dipyriddy-substituted porphyrin which acts as a pillar, coordinating to the paddlewheel SBUs of two adjacent layers, and leaving the TCPP in the 2D layers coordinatively unsaturated. Because of the relative bulky size of the porphyrin pillars, coordination was exclusively to the paddlewheel sites regardless of the metal ion in the TCPP. Indeed it was shown that these materials were porous by gas adsorption and one framework in the series containing Mn(III) porphyrin was found to have a catalytically active internal pore surface.

Previously, our group reported a bioinspired assembly of a new series of PPFs using a methylated pillar to distinguish between the paddlewheel and porphyrin metal centers based on steric hindrance.⁶ Four isostructural AA stacking frameworks were synthesized, all containing porphyrin accessible metal centers, via a traditional solvothermal synthesis of TCPP, zinc nitrate hexahydrate, and *meso*-2,2'-dimethyl-4,4'-

bipyridine (DMBPY) in DMF and ethanol. Because of steric hindrance between the methyl group on DMBPY and the porphyrin plane, it preferentially coordinated to the paddlewheel sites showing a site recognition commonly observed in biological systems.

In a continuing effort to achieve AA stacked PPF structures, our group has investigated a new synthetic strategy involving a stoichiometric limiting amount of pillar during the synthesis of PPFs.⁷ By limiting the amount of 4,4'-bipyridine (BPY) used in the synthesis of PPFs with Mn- and Fe-TCPP to 0.8 equivalents, coordination was observed selectively to the paddlewheel SBU, instead of at both the porphyrin and paddlewheel. The resulting crystals were single phase AA stacked PPF structures containing coordinatively unsaturated Mn(III)- or Fe(III)-TCPP. These structures became the newest members of the AA stacked PPF-5 series.

This chapter discusses the synthesis of single crystals of two new AA stacked Mn(III)-PPFs, PPF-31 and PPF-32, to be added with the previously mentioned PPF-5-Mn/Zn (in this nomenclature, the first metal indicates the ion within the porphyrin core, and the second metal indicates the ion in the paddlewheel SBU) creating a isorecticular series. Additionally the dichroic properties of PPF-5 and the gas sorption properties of PPF-31 will be detailed.

8.2 Experimental Methods

PPF-5-Mn/Zn A mixture of MnTCPPCl (8.8 mg, 0.01 mmol), zinc nitrate hexahydrate (5.9 mg, 0.02 mmol), 4,4'-bipyridine (BPY) (1.2 mg, 0.008 mmol), and 1.0 M nitric acid in methanol (40 μ L, 0.04 mmol) were added to a mixture of *N,N*-dimethyl formamide (DMF) (1.33 mL) and methanol (0.66 mL) in a capped vial and heated to 80 °C for 24 hrs, followed by slow cooling to room temperature over 9 hrs. Yield: 10.0 mg (79% based on porphyrin). Anal. Calcd. for $[\text{C}_{58}\text{H}_{32}\text{N}_7\text{O}_{11}\text{Zn}_2\text{Mn}] \cdot 4 \text{H}_2\text{O}$: C, 57.6; H, 3.4; N, 8.9%. Found: C, 57.3; H, 3.2; N, 8.9%.

PPF-31 A mixture of 5,10,15,20-tetrakis(4-carboxyphenyl)- Mn(III)- porphyrin chloride (MnTCPPCl) (8.8mg, 0.01 mmol), zinc nitrate hexahydrate (6.0 mg, 0.02 mmol), 1,4-diazabicyclo[2.2.2]octane (DABCO) (1.12 mg, 0.02 mmol) and 1.0 M nitric acid in methanol (45 μ L, 0.045 mmol) were added to a mixture of DMF (1.33 mL) and methanol (0.66 mL) in a capped pressure vessel and heated to 60 °C for 72hrs, followed by slow cooling to room temperature over 9hrs. Yield: 10.3 mg (82% based on porphyrin). Anal. Calcd. for $[\text{C}_{54}\text{H}_{36}\text{N}_7\text{O}_{11}\text{Zn}_2\text{Mn}] \cdot 2 \text{DMF} \cdot \text{methanol}$: C, 55.2; H, 3.8; N, 8.9%. Found: C, 55.1; H, 3.8; N, 9.1%

PPF-32 A mixture of MnTCPPCl (8.8 mg, 0.01 mmol), zinc nitrate hexahydrate (6.0 mg, 0.02 mmol), *trans*-1,2-Bis(4-pyridyl)-ethylene (BPYE) (1.8 mg, 0.01 mmol), 2-picoline (2.0 μ L, 0.02 mmol) and 1.0 M nitric acid in methanol (45 μ L, 0.045 mmol) were added to a mixture of DMF (1.33 mL) and methanol (0.66 mL) in a capped vial and heated to 80 °C for 24 hrs, followed by slow cooling to room temperature over 9 hrs. Yield: 9.5 mg (74% based on porphyrin). Anal. Calcd. for $[\text{C}_{60}\text{H}_{34}\text{N}_7\text{O}_{11}\text{Zn}_2\text{Mn}] \cdot 3 \text{H}_2\text{O}$: C, 59.1; H, 3.7; N, 8.8%. Found: C, 59.2; H, 3.0; N, 8.6%.

Single crystal structure determination:

Plate-shaped crystals of PPF-31 (300 μm x 300 μm) and PPF-32 (240 μm x 240 μm) were sealed in a capillary for XRD measurement. Geometry and intensity data were obtained at room temperature with a Bruker SMARD Apex CCD area detector diffractometer. Preliminary lattice parameters and orientation matrices were obtained from three sets of frames. Data were collected using graphite-monochromated and MonoCap-collimated Mo- K_{α} radiation ($\lambda = 0.71073 \text{ \AA}$) with ω scan method.⁸ Data was processed with the SAINT+ program⁹ for reduction and cell refinement. Multi-scan absorption corrections were applied to the data sets using the SADABS program for area detector.¹⁰ The structure was solved by direct method and refined using SHELXTL.¹¹ Disordered, independent solvent molecules inside the frameworks were eliminated in the refinement by PLATON/SQUEEZE.¹² All atoms were refined with anisotropic displacement parameters.

X-ray powder diffraction (PXRD):

Because the PPF crystals have platelet morphology, the PXRD spectra show significant preferred orientation when mounted onto a traditional flat stage. The relative intensities in the diffraction peaks thus deviate significantly to the simulated PXRD spectra which assume perfectly random orientations of the crystals. For PPF-31 and PPF-32, traditional flat stage PXRD was collected on a Rigaku D/Max-B X-ray diffractometer with Bragg-Brentano parafocusing geometry, a diffracted beam monochromator, and a conventional copper target X-ray tube set to 35 KV and 25 mA. For PPF-5-Mn/Zn, the deviations in intensity were overcome by following a method developed by Farha *et al.* in which crystals are mounted in a sealed capillary tube, and PXRD was performed while

the tube was spinning to remove the preferential orientation.⁵ Spinning capillary X-ray diffraction data were taken with a Bruker AXS DA X-ray diffractometer with a GADDS area detector and a conventional copper target X-ray tube set to 40 KV and 40 mA. Crystals were mounted in a 0.5 mm quartz capillary tube with a drop of mother liquor and sealed with epoxy. The PXRD data were collected with an area detector exposed for 10 minutes as rotation frames over 360° in ϕ , a χ angle of 54.74°, and at 2θ values of 21° and 25°. The resulting experimental PXRD patterns were treated for amorphous background scatter and collected into a single pattern, then compared to simulated patterns obtained from the single crystal structures using Mercury software.¹³

Reflectivity analysis:

Reflectivity spectra were taken on a microspectroreflectometer equipped with an arc lamp light source and light polarizer. Solution UV/Vis spectra Reflection intensity was measured on an aluminum mirror as a function of energy ($\times 10^3$ wavenumbers). A PPF-5-Mn/Zn crystal was then positioned on the mirror so that reflection intensity of the (001) face was measured as a function of energy ($\times 10^3$ wavenumbers) using light polarized along the porphyrin–paddlewheel plane. The crystal was then reoriented and positioned on the mirror so that reflection intensity of the (100) face was measured as a function of energy ($\times 10^3$ wavenumbers) using light polarized perpendicular to the porphyrin–paddlewheel plane. The quotient of crystal intensity over mirror intensity yields the reflectivity spectra for the (001) and (100) faces of PPF-5-Mn/Zn relative to that of the aluminum mirror.

UV/Vis analysis:

Data was recorded on a Shimadzu UV–2401PC spectrophotometer.

Thermogravimetric analysis:

Performed on a Perkin Elmer STA 6000 thermogravimetric analyzer, heated from 25 °C to 800 °C at a rate of 10 °C/minute under N₂ atmosphere.

8.3 Results and Discussion

Purple crystals of the two new structures, PPF-31 and PPF-32, were each synthesized via a traditional one-pot solvothermal reaction. The purity of the resulting crystals was confirmed by elemental analysis and PXRD (Figures 8.1 and 8.2). Single crystals suitable for single-crystal X-ray diffraction were obtained for PPF-31 and PPF-32 (Table 8.1). Both PPF-31 and PPF-32 are AA stacked 3D structures in which the 2D porphyrin paddlewheel layers are connected together by the dipyrrolyl pillars exclusively at the paddlewheel sites creating $P4/mmm$ symmetry (see Figure 8.3). The Mn site in the porphyrin core for both structures is coordinated axially by solvent molecules. While the counter ions were not solved by single crystal, valence bond sum calculations returned a value of 2.91 for the Mn ion in the porphyrin core of PPF-31 and 2.87 for the Mn ion in the porphyrin core of PPF-32 indicating that the manganese centers retain their +3 oxidation state upon crystallization.¹⁴

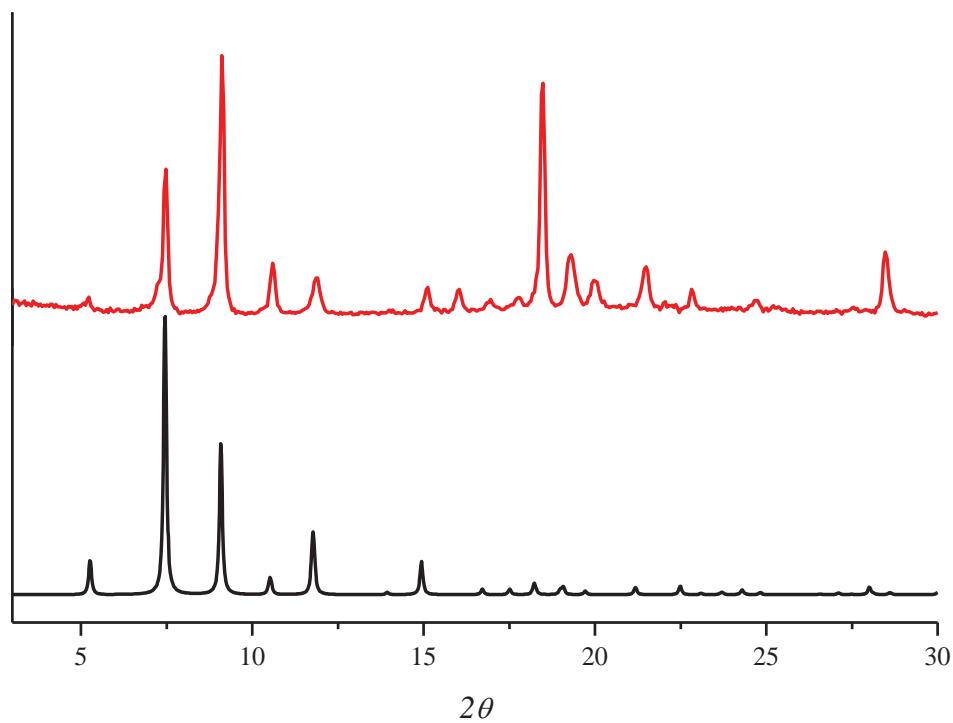


Figure 8.1. Theoretical (bottom) and experimental (top) PXRD patterns for PPF-31.

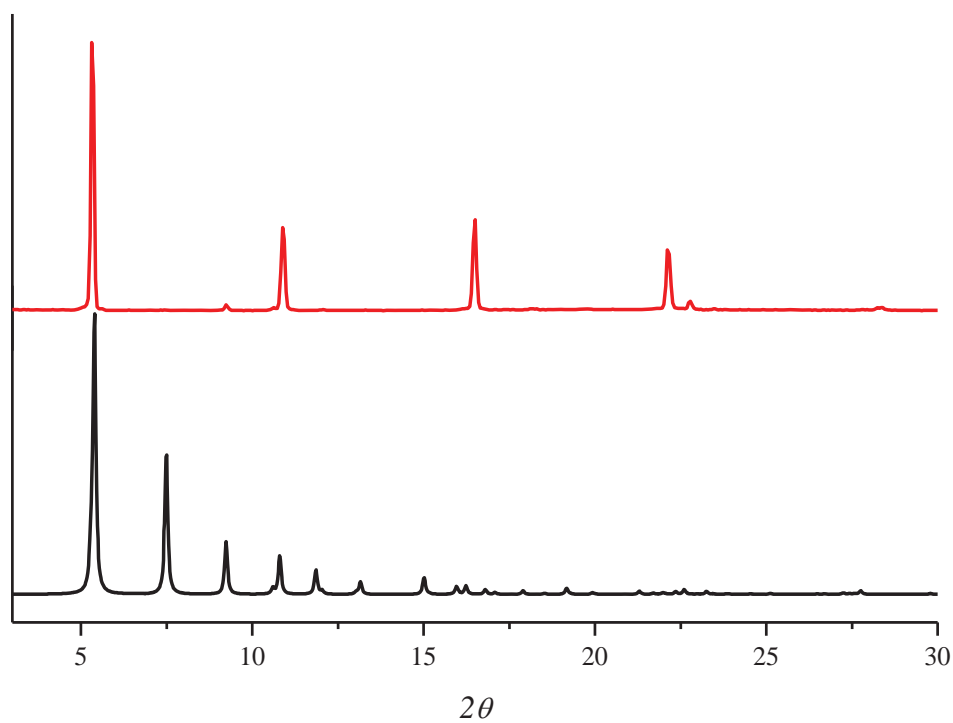


Figure 8.2. Theoretical (bottom) and experimental (top) PXRD patterns for PPF-32. The patterns match well when preferred orientation about the $(00l)$ is considered.

Table 8.1. Crystal data for PPF-31 and PPF-32

Complex	PPF-31	PPF-32
chemical formula*	C ₅₄ H ₃₆ N ₇ O ₁₁ Zn ₂ Mn	C ₆₀ H ₃₄ N ₇ O ₁₁ Zn ₂ Mn
formula weight*	1082.66	1152.71
crystal system	tetragonal	tetragonal
space group	<i>P4/mmm</i>	<i>P4/mmm</i>
<i>a</i> (Å)	16.76(2)	16.6762(12)
<i>b</i> (Å)	16.76(2)	16.6762(12)
<i>c</i> (Å)	9.726(13)	16.3649(12)
<i>V</i> (Å ³)	2731(6)	4551.0(6)
<i>Z</i>	1	1
ρ_{calc} (g/cm ³)*	0.680	0.427
μ (mm ⁻¹)*	0.579	0.349
<i>R</i> ₁ , <i>I</i> > 2 σ (<i>I</i>)	0.0708	0.0452
<i>wR</i> ₂ , <i>I</i> > 2 σ (<i>I</i>)	0.1733	0.1308

*Based on the formula without uncoordinated solvent molecules.

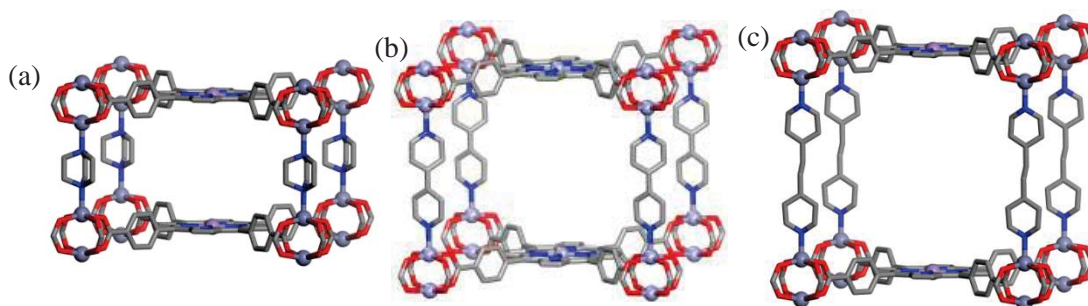


Figure 8.3. Schematic representation of single crystal structures of Mn(III) PPF series: (a) PPF-31, (b) PPF-5-Mn/Zn, and (c) PPF-32.

Analysis of the single crystal structure of PPF-31 shows the porphyrin paddlewheel layers connected together at the paddlewheel sites by disordered DABCO pillaring units. DABCO is the shortest pillaring linker used in any PPF structure, contracting the layer–layer distance within the structure to 9.7 Å. Analysis of the single crystal structure of PPF-32 reveals the Mn(III)TCPP stacked directly on top of each other despite the pyridyl groups in BPYE pillar being shifted laterally by 1.18 Å (see Figure 8.4). To achieve this stacking arrangement, BPYE is angled 8.48 ° away from normal to the porphyrin paddlewheel layers. The layer–layer distance within PPF-32 is 15.4 Å.

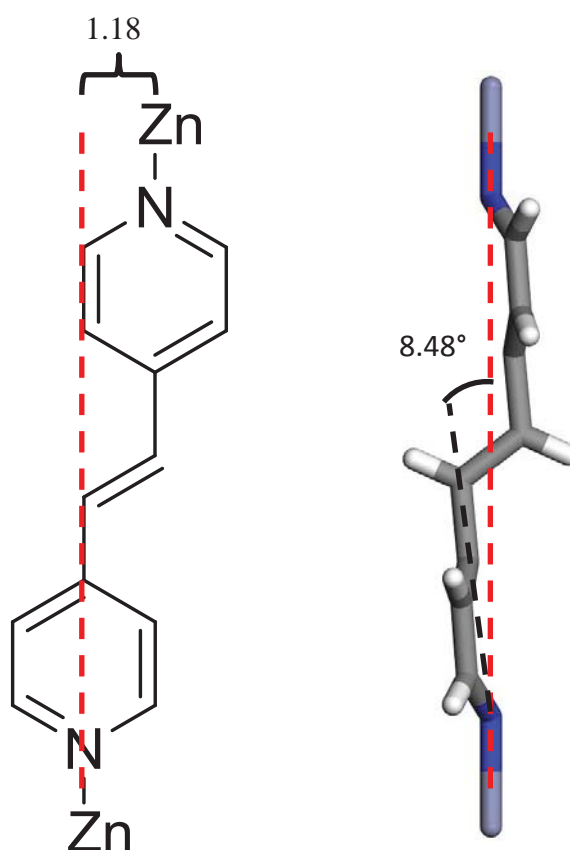


Figure 8.4. Molecular structure of BPYE pillar (a) as it would be in solution and (b) as it is found in PPF-32.

8.4 Dichroism of PPF-5-Mn/Zn

An important advantage of MOFs is that one can obtain highly predictable topology through coordination-driven self-assembly,¹⁵ and thereby the control of desired chemical or physical properties is feasible.¹⁶ To this end, synthesis and design of new optoelectronic materials, assembled from pigment molecules, might be one of the areas that might benefit greatly from such coordination-driven MOF approach; opto-electronic properties depend not only on intrinsic properties of the organic pigment, but also strongly on other collective factors such as their spatial arrangement and the intermolecular interactions with neighboring pigments.^{17,18} As seen in liquid crystal display, dye sensitized solar cell, and artificial light harvesting systems, the nature of a pigment as well as its arrangement in space are known to play crucial roles in optoelectronic applications.¹⁹⁻²¹ While the optical properties of the individual molecules can be well predicted, the same properties in the material is still not well understood. One major burden associated with this is that manipulating the arrangement of pigments still remains as an on-going challenge in materials chemistry.

Among the known strategies to create pigment organization, an important approach has been the use of solid-state or polymeric host materials.²² Layered materials such as clay minerals, hydrogen-bonded networks, and layered double hydroxides are extensively used for inclusion of pigments because these hosts offer two-dimensional expandable interlayer space for the inclusion of large pigment molecules such as porphyrins.²³⁻²⁸

Porphyrins (and chlorins) are unique pigments found in biological systems like photosynthetic purple bacterium *Rhodospseudomonas acidophila*,²⁹ and have been the

subject of intense investigation to be included in these layered materials. Such intensive research efforts are mainly due to the fact that porphyrin pigments absorb strongly in the visible spectrum and their photo–physical properties can be tuned by metallation, functionalization, and stacking of the porphyrin rings.³⁰ Intermolecular interaction and orientation of the porphyrins in the solid state often have significant effects on the optical properties, as exemplified by self–quenching of fluorescence if porphyrins are aggregated too close together within the clay, again demonstrating the importance of control of pigment organization.²⁴ When the synthetic strategy of incorporating porphyrins into host materials is used, an avoidable problem is the following. Even if the host materials are crystalline solids, the orientation and spatial arrangement of porphyrin pigments are extremely difficult to control, and therefore the structural information of pigments remain hard to obtain experimentally.^{27,28}

Incorporating porphyrins into MOFs provides precise control of both orientation and intermolecular separation of the porphyrin molecules.^{31,32} In this approach, unlike previous methods using host materials, the porphyrin pigment –the molecular building block– becomes a part of the “host” material and the “guest” pillar molecule regulates the arrangement (or stacking) of pigments.^{31,32} Herein the recent discovery of the highly anisotropic optical properties, demonstrated by a high–contrast dichroic effect exhibited by PPF-5-Mn/Zn is described.

Crystalline samples of PPF-5-Mn/Zn were synthesized through a traditional solvothermal method. The purity of these crystals were confirmed by PXRD (Figure 8.5). Crystals of PPF-5-Mn/Zn show two types of colored crystals under an optical microscope; one type is orange and transparent, and the other dark and reflective (Figure

8.6). However, the sample is single-phase, based on a careful analysis of the PXRD of the bulk phase. This puzzling situation was solved when one of the crystals was mounted inside a capillary tube. When the crystal was rotated, the color of the crystal changed from light transparent orange, to deep purple (and vice versa), thus exhibiting dichroism (Figure 8.7). Dichroism is an important property of liquid crystal diodes, wave optics, and light polarizers, and has been observed in solid state minerals since the 1950's.^{33,34} Many organic compounds and hybrid layered porphyrin materials have also exhibited this property.³⁵ However, there are surprisingly few known examples of dichroism in MOFs.³⁶

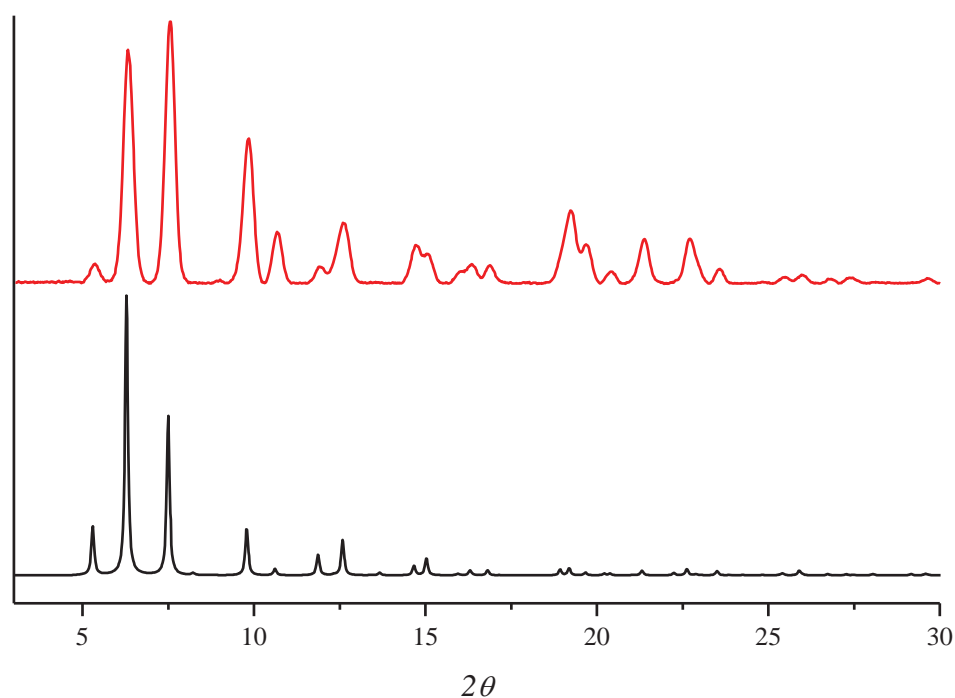


Figure 8.5. Theoretical (bottom) and experimental (top) PXRD patterns for PPF-5-Mn/Zn.

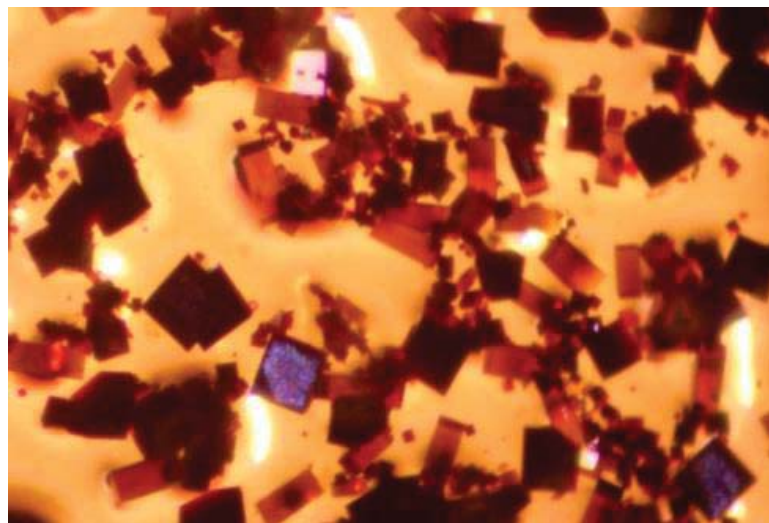


Figure 8.6. Optical microscope image of the bulk PPF-5-Mn/Zn showing the two different colored crystals. The dark purple square faces $\{001\}$ and the transparent orange rectangular faces $\{100\}$.

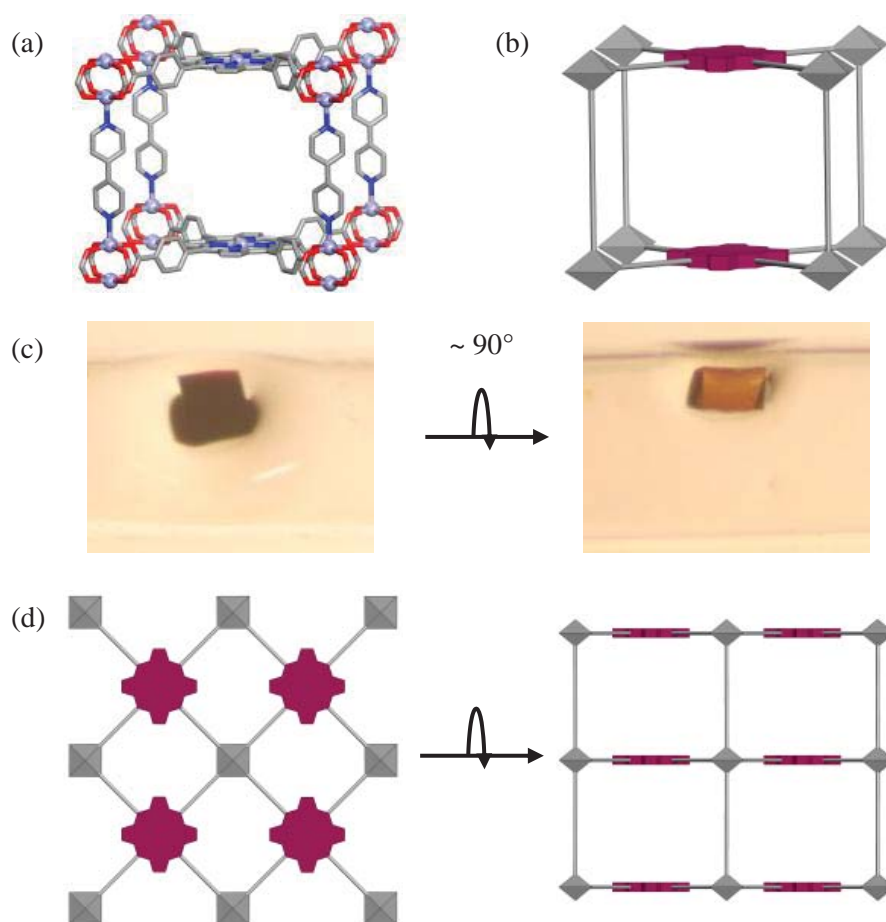


Figure 8.7. (a) Structure model of PPF-5-Mn/Zn. (b) Simplified representation of PPF-5-Mn/Zn highlighting the control of porphyrin aggregation and orientation. (c) Optical microscope image of PPF-5-Mn/Zn crystal showing the $\{001\}$ and $\{100\}$ faces. (d) Representation of the $\{001\}$ and $\{100\}$ faces.

The crystal faces were indexed (see Figure 8.8) showing that the deep purple face corresponds to the {001} face, while the light orange face corresponds to the {100} face (Figure 8.7). To quantify this dichroism, specular reflectivity spectra using polarized light of the {001} and {100} faces were obtained, then converted to absorptivity spectra through the Kramers–Kronig transform (Figure 8.9). The use of Kramers–Kronig transform is well documented elsewhere³⁷ and thus only a brief discussion is given here. A reflectivity spectrum is a product of the refractive index and absorptivity coefficient of a material. The Kramers–Kronig transform calculates an absorptivity spectrum by stripping out the refractive index component from the reflectivity spectrum. The calculation needs to be performed from absolute reflectivity. As such, the relative reflectivity spectrum obtained experimentally was multiplied by the absolute reflectance of the aluminum mirror wavelength by wavelength according to the following equation stated below:³⁷

$$AR_{cryst} = \frac{I_{cryst}}{I_0} = \frac{R_{cryst} \times I_{mirr}}{I_{mirr} / R_{mirr}} = R_{cryst} \times R_{mirr}$$

Where AR_{cryst} is the absolute reflectivity of the crystal, I_{cryst} is the reflection intensity of the crystal, I_0 is the intensity of incidence light, R_{cryst} is the reflectivity of the crystal, I_{mirr} is the reflection intensity of the mirror, and R_{mirr} is the reflectivity of the mirror. The Kramers–Kronig transform must be performed over the entire spectral range even though experimental values were obtained only from $13 \times 10^3 \text{ cm}^{-1}$ to $38 \times 10^3 \text{ cm}^{-1}$. Thus to transform the reflectivity values correctly, numerical values for reflectivity must be added to experimentally inaccessible regions of the spectrum ($0 - 13 \times 10^3 \text{ cm}^{-1}$ and $38 \times 10^3 \text{ cm}^{-1} - \infty$). Additionally, since most compounds strongly absorb in the vacuum UV region it is necessary to append an “effective absorption” to the high energy (\sim

$100 \times 10^3 \text{ cm}^{-1}$) end of the measured reflection spectrum.³⁷ The calculation is terminated when the calculated extinction coefficient approaches zero in regions where it is known from the solution spectrum that the molecule does not absorb. The refinement process thus involves varying the high and low wavelength reflectivity values and the “effective absorption” peak at low wavelength.

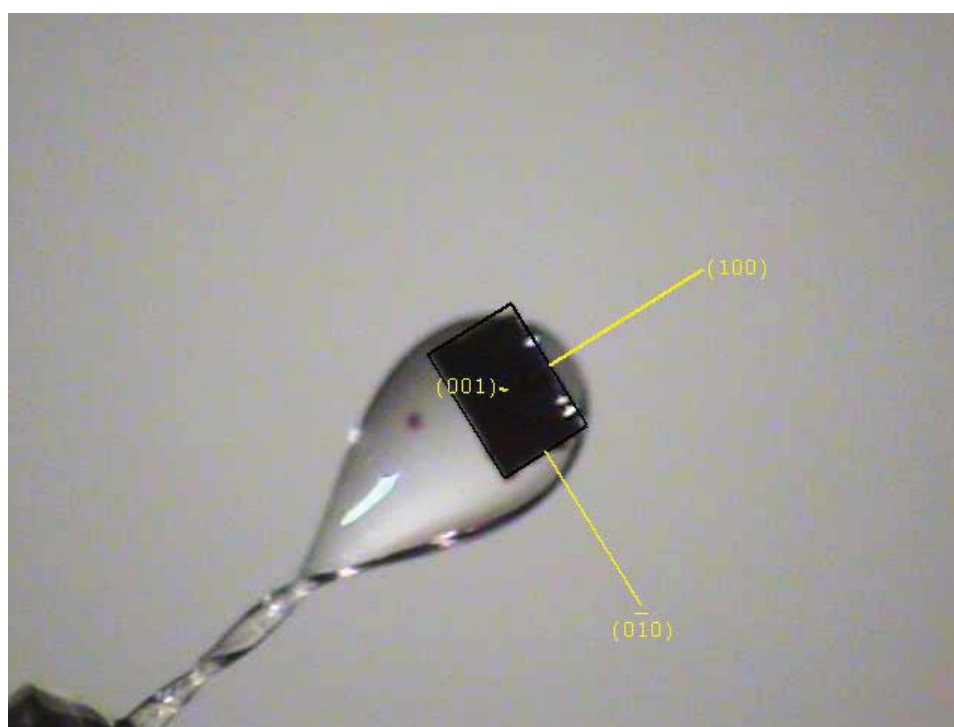


Figure 8.8. Face indexing performed on a crystal of PPF-5-Mn/Zn.

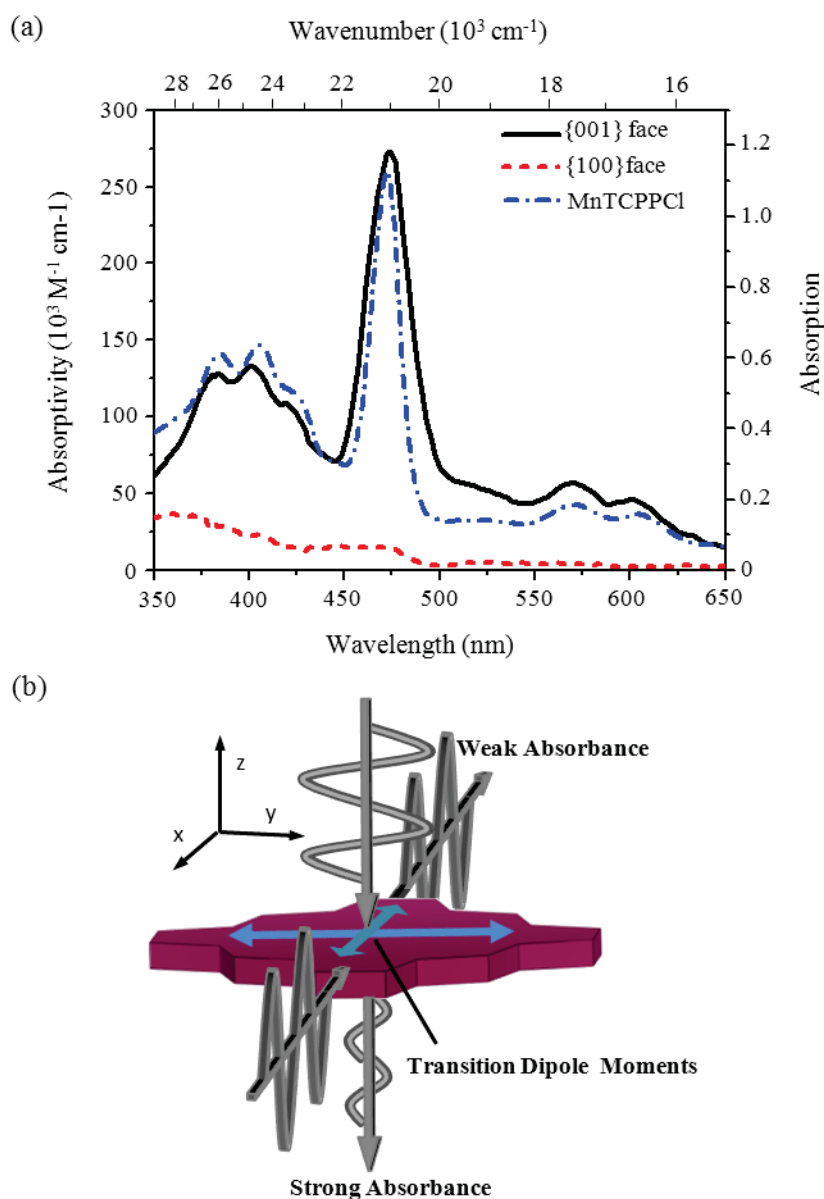


Figure 8.9. (a) Crystal absorptivity spectra of the {001} (black solid line), {100} (red dashed line) faces of PPF-5-Mn/Zn from the Kramers–Kronig transform of the reflectivity spectrum using y- and z- polarized light respectively, and the solution absorption spectra of dilute MnTCPPCl in methanol (blue dashed line). (b) Representation of the porphyrin pigment molecule within PPF-5-Mn/Zn with the main transition dipole moments along the xy plane of the porphyrin.

The absorptivity spectra of the {001} shows high intensity absorption in the energy range corresponding to transitions within the porphyrins, which corresponds well to the dark reflective {001} surface. The absorptivity spectra of the {100} face shows much less intensity absorption in the same energy range, which also corresponds well to the transparent light orange color observed under the microscope. The dichroic ratio between the {001} and {100} faces is defined as $A_{\{001\}}/A_{\{100\}}$ and was calculated at the Soret absorption to be 20.7.³⁸ This ratio is extremely large in comparison to other dichroic systems.^{33,34}

The spectra of the {001} face shows the largest absorptivity which is perpendicular to the porphyrin plane in the porphyrin paddlewheel 2D layer (Figure 8.9). The dark purple color is attributed to excitation of transitions whose transition dipole moment vectors are laid in the coordination plane. If we assume that the porphyrin retains D_{4h} symmetry in the PPF structure, the signal centered at 474 nm ($21.3 \cdot 10^3 \text{ cm}^{-1}$) fits the Soret absorption (b_{2u}, a'_{2u} to e_g transition) which is assigned as a porphyrin (π) to metal (d_{xz}, d_{yz}) charge transfer transition.³⁸ The absorption at 572 nm ($17.6 \cdot 10^3 \text{ cm}^{-1}$) is assigned to the a_{2u}, a_{1u} to e^*_g transition which is a π to π^* transition within the porphyrin ring.³⁸ The absorption at 603 nm ($16.6 \cdot 10^3 \text{ cm}^{-1}$) is assigned to the a_{2u} to a_{1g} transition which is a porphyrin (π) to metal (d_{z^2}) charge transfer transition.³⁸ The high energy transitions include an absorption at 402 nm ($24.9 \cdot 10^3 \text{ cm}^{-1}$) and is assigned to the a'_{2u} to a_{1g} transition which is a porphyrin (π) to (d_{z^2}) metal charge transfer transition.³⁸ The absorption at 378 nm ($26.5 \cdot 10^3 \text{ cm}^{-1}$) is assigned to the b_{2u}, a'_{2u} to e_g or the a_{2u}, a_{1u} to e_g transition, which are a porphyrin (π) to metal (d_{xz}, d_{yz}) charge transfer transition and a π to π^* transition within the porphyrin respectively.³⁸ Many of these transitions have a small

to no dependence to the out of plane direction, which explains the large dichroism created by using *z*-polarized light on the edge of the porphyrin as opposed to *x*- or *y*-polarized light on the plane of the porphyrin (Figure 8.9).

Because of the perfect AA stacking of the PPF-5-Mn/Zn structure, all of the porphyrins are in symmetrically identical positions. Thus, there is minimal aggregation-induced spectral shift to the absorptivity spectra (Figure 8.9). Traditionally when pigments aggregate, they fall within two categories: J aggregation and H aggregation based on the interaction between pigments in symmetrically different positions within the cell.³⁹ PPF-5-Mn/Zn assumes a *P4/mmm* symmetry, in which there is only one porphyrin per unit cell. As such the spectral features of the absorptivity spectra are almost identical to the solution absorbance spectra of MnTCPPCl creating a material which more resembles multiple single point pigment molecules. The small difference in the Soret absorption between MnTCPPCl and PPF-5-Mn/Zn of 5.6 nm can be attributed to small electronic contributions from the BPY pillar.⁴⁰

To summarize, these results demonstrate how the use of MOF approach can lead to a new type of pigment incorporated materials with greater control of pigment orientation. This design takes advantage of the symmetry of the porphyrin molecule to direct the formation of the crystals. In this manner, not only is the orientation of the porphyrin strictly controlled, but the spatial arrangement of the pigments is also controlled to exhibit extraordinary optical properties of the porphyrin like optical dichroism. Unlike pigment incorporated layered material, this approach makes use of the pigment molecule as a structure building unit (host), while the pillared “guest” controls the spatial arrangement of the pigments.

8.5 Gas Storage of PPF-31

As discussed in Chapter 1, MOFs have found great potential as highly porous material for applications in heterogeneous catalysis and gas storage/separation.^{1,2} Indeed, these materials have become a possible alternative to well-established porous materials such as zeolites for these applications. As purely inorganic materials, zeolites are extraordinarily robust and provide moderately high surface areas, which together facilitate catalytic activity. Nevertheless, their performance is limited by the stiffness of the framework, whose features, above all pore size and surface functionalization, are not readily modified using self-assembly approaches.⁴¹ In contrast, MOFs are very flexible in design, making it extremely easy to tune by judicious selections of inorganic and organic components, or *via* post-synthetic modification.^{16, 42} Depending upon the metal ions and organic linkers incorporated in the framework, key chemical and physical properties, such as pore size, surface area, guest binding capability, catalytic activity, can potentially be finely modulated. MOFs, however, suffer from a lack of thermal and chemical stability—key features needed to replace zeolites. Often the internal pores will collapse upon activation of the materials.

Stability during activation has been a significant challenge in PPFs. In the case of the 3D AA stacked structure PPF-11-Zn/Zn, the compound showed almost no accessible internal surface area (81 m²/g based on CO₂ adsorption) after activation, implying framework collapse.³² The lack of stability in PPFs is likely contributed by two major factors. First, because of the large porphyrin metalloligands used in our synthesis, the resulting large pores of our PPFs make these materials highly susceptible to pore collapse upon activation.⁴³ Secondly, the 2D PPF sheets are connected together axially by

dipyridyl pillaring linkers through a weak zinc–nitrogen bond. These bonds are significantly weaker than the in-plane zinc–oxygen bonds of the carboxylates in the paddlewheel units (150 kJ/mol and 360kJ/mol respectively).⁴⁴ This weak bond decreases the stability of the materials upon activation.

Because the large pore size is desirable for these materials, it is important to increase the stability by strengthening the pillaring connection between layers. As described in Chapter 3, the strength of Lewis acid–base derived connection between the SBU and linker is directly related to the basicity (pK_a) of the ligand.^{41,45–47} With this in mind, the DABCO pillared PPF-31 should be a very interesting PPF system to look into gas storage because of the strong pillar–paddlewheel interaction. Out of the three isorecticular Mn(III) PPFs, the DABCO in PPF-31 has the highest pK_a (see Table 8.2). This increase in basicity should strengthen the zinc–nitrogen at the paddlewheel SBU, creating a more stable material upon activation. Indeed PPF-31 is porous upon activation. Early studies of N_2 sorption data shows a Langmuir surface area of 1400 m^2/g (see Figure 8.10). While this is still low compared to other MOF material, PPF-31 shows the highest experimental surface area for any PPF structure.

Additionally, PPF-31 may possess very interesting sorption characteristics for CO_2 because of the small porphyrin to porphyrin distance in the internal pores. Connolly surface models of PPF-31 shows a Mn(III)–Mn(III) distance between neighboring porphyrins of ca. 5.1 Å which is only slightly larger than the length of CO_2 (ca. 4.5 Å). Because of this, it may be possible for the guest CO_2 molecule to exhibit increased heat of adsorption by interacting with two neighboring Mn(III) ions in the pore (Figure 8.11). Currently, CO_2 sorption experiments are being performed to confirm this possibility.

Table 8.2. Comparison of the pK_a values of pillaring linkers used in Mn(III) PPF series.

Pillar	pK _a	
	Literature	Calculated ^a
DABCO	8.60 ⁴⁸	8.49
BPY	4.82 ⁴⁹	4.93
BPYE	not available	4.50

^aCalculated values of pK_a was obtained using the ACD/I-Lab Web Service⁵⁰

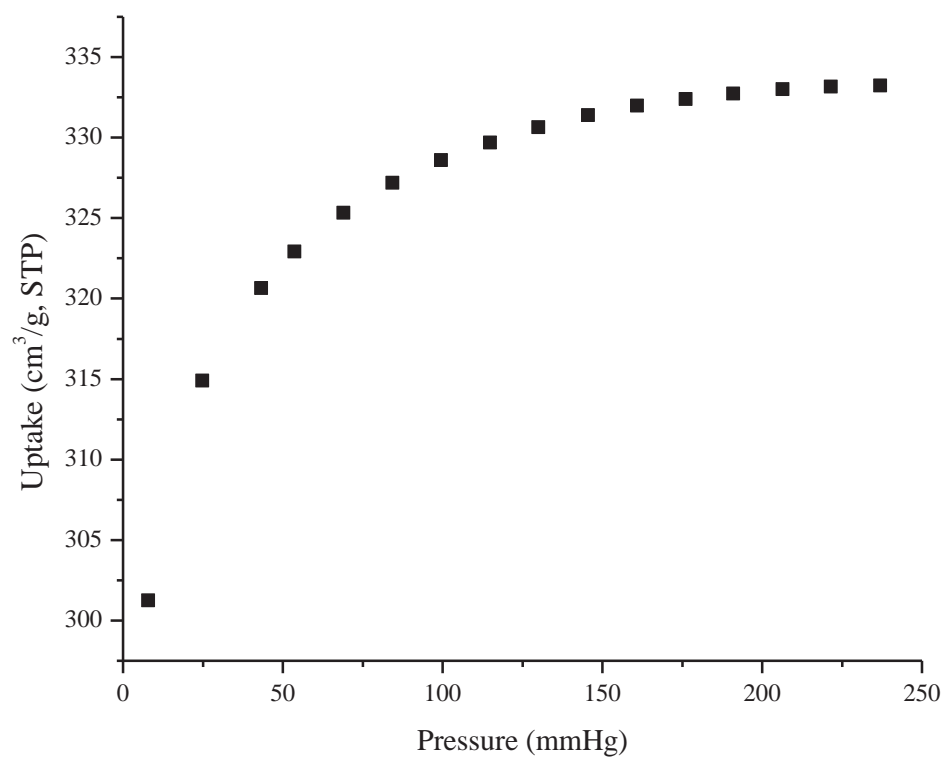


Figure 8.10. PPF-31 adsorption of N₂ at 77K.

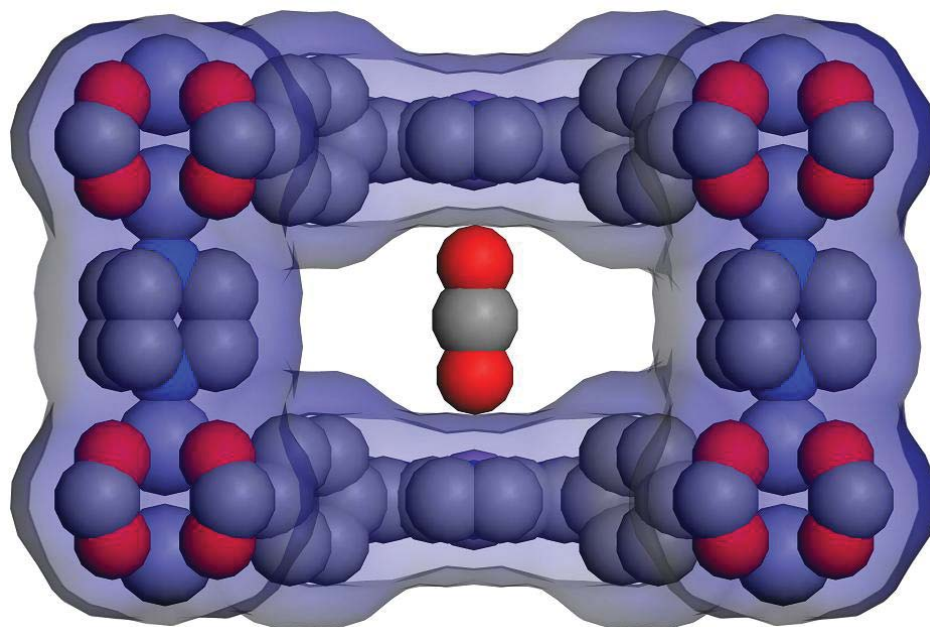


Figure 8.11. Connolly surface model of PPF-31 showing the theoretical close interaction between the Mn(III) sites of the porphyrin and a guest CO₂ molecule.⁵¹

8.6 Conclusions

Two new AA Mn(III) PPF structures, PPF-31 and PPF-32, were synthesized and their crystal structures were solved. PPF-31 and PPF-32 along with the previously reported PPF-5-Mn/Zn make up a new isorecticular MOF series with coordinatively unsaturated Mn(III) centers. PPF-31 was assembled with DABCO pillaring linker contracting the porphyrin paddlewheel layers relative to other PPFs. PPF-32 was assembled with BPYE pillaring linkers which, upon crystallization, distort their pyridyl groups in order to achieve ideal AA stacking. PPF-5-Mn/Zn shows incredible high-contrast dichroism because of the perfect control of porphyrin orientation and spacing. PPF-31, like the other structures in this series, contains accessible metal centers that are available for gas storage. In addition, the DABCO-paddlewheel coordination bond strength is stronger than other pyridyl-paddlewheel bonds because DABCO is a strong Lewis base. Because of the strength of the pillar-paddlewheel coordination bond, PPF-31 retained porosity upon activation as shown by gas sorption studies. Additional work on the dichroism of other PPFs and improved activation techniques are currently being investigated.

8.7 References

- (1) (a) Hu, Y. H.; Zhang, L. *Adv. Mater.* **2010**, *22*, 117. (b) Pavlishchuk, V. V.; Kolotilov, S. V. *Theor. Exp. Chem.* **2009**, *45*, 75. (c) Rowsell, J. L. C.; Spencer, E. C.; Eckert, J.; Howard, J. A. K.; Yaghi, O. M. *Science* **2005**, *309*, 1350.
- (2) Dincă, M.; Long, J. R. *Angew. Chem. Int. Ed.* **2008**, *47*, 6766.
- (3) (a) Chen, B.; Xiang, S.; Qian, G. *Acc. Chem. Res.* **2010**, *43*, 1115. (b) Kitagawa, S.; Noro, S. -I.; Nakamura, T. *Chem. Commun.* **2006**, *42*, 701. (c) Kitagawa, S.; Kitaura, R.;

- Noro, S. –I. *Angew. Chem. Int. Ed.* **2004**, *43*, 2334. (d) Kaye, S.; Long, J. R. *J. Am. Chem. Soc.* **2005**, *127*, 6506.
- (4) (a) Ockwig, N. W.; Delgado–Friedrichs, O.; O’Keeffe, M.; Yaghi, O. M. *Acc. Chem. Res.* **2005**, *38*, 176. (b) Delgado–Friedrichs, O.; O’Keeffe, M.; Yaghi, O. M. *Phys. Chem. Chem. Phys.* **2007**, *9*, 1034.
- (5) Farha, O. K.; Shultz, A. M.; Sarjeant, A. A.; Nguyen, S. T.; Hupp, J. T. *J. Am. Chem. Soc.* **2011**, *133*, 5652.
- (6) Barron, P. M.; Wray, C. A.; Hu, C.; Guo, Z.; Choe, W. *Inorg. Chem.* **2010**, *49*, 10217.
- (7) Barron, P. M. Design, Synthesis and Characterization of Porphyrin Paddlewheel Frameworks. Ph. D. Dissertation, University of Nebraska–Lincoln, State College, NE, May 2010.
- (8) SMART (version 6.532). *Program for Bruker CCD X–ray Diffractometer Control*, Bruker AXS Inc., Madison, WI, **2005**.
- (9) SAINT+ (version 6.45). *Program for Reduction of Data Collected on Bruker CCD Area Detector Diffractometer*, Bruker AXS Inc., Madison, WI, **2003**.
- (10) Sheldrick, G. M. SADABS, version 2.10, *Program for Empirical Absorption correction of Area Detector Data*, University of Göttingen, **2007**.
- (11) Sheldrick, G. M. SHELXTL, version 6.15, *Program Package for Structure Solution and Refinement*, Bruker Analytical X–ray Systems, Inc., Madison, WI, **2008**.
- (12) Speck, A. . *J. App. Cryst.* **2003**, *36*, 7.
- (13) <http://www.ccdc.am.ac.uk/products/mercury/>
- (14) (a) Brown, I. D.; Altermatt, D. *Acta Cryst.* **1985**, *41*, 244. (b) Thorp, H. H. *Inorg. Chem.* **1992**, *31*, 1585.

- (15) O’Keeffe, M.; Yaghi, O. M. *Chem. Rev.* **2012**, *112*, 675.
- (16) (a) Zaworotko, M. J. *Nature chem.* **2009**, *1*, 267. (b) Wang, Z.; Cohen S. M. *Chem. Soc. Rev.* **2009**, *38*, 1315. (c) Tanabe, k. K.; Cohen, S. M. *Chem. Soc. Rev.* **2011**, *40*, 498.
- (17) Electromagnetic wave propagated through a material is affected by these ordered molecules, exhibiting optical phenomena such as absorption, refraction, birefringence, retardation, and other optical effects. See ref. 18.
- (18) (a) Wuest, J. D. *Nature Chem.* **2012**, *4*, 74. (b) Jochum, T.; Reddy, C. M.; Eichhöfer, A.; Buth, G.; Szmytkowski, J.; Kalt, H.; Moss, D.; Balaban, T. S. *Proc. Nat. Acad. Sci. USA.* **2008**, *105*, 12736. (c) Matassa, R.; Sadun, C.; D’Ilario, L.; Marinelli, A.; Caminiti, R. *J. Phys, Chem. B* **2007**, *111*, 1994. (d) Evans, J. S.; Musselman, R. L. *Inorg. Chem.* **2004**, *43*, 5613.
- (19) (a) Tam–Chang, S. –W.; Mahinay, D.; Huang, L. *Adv. Mater.* **2008**, *47*, 165. (b) Tam–Chang, S. –W.; Seo, W.; Rove, K.; Casey, S. M. *Chem. Mater.* **2004**, *16*, 1832. (c) Piñol, R.; Lub, J.; García, M. P.; Peeters, E.; Serrano, J. L.; Broer, D.; Sierra, T. *Chem. Mater.* **2008**, *20*, 6076. (d) Zhang, X.; Gorohmaru, H.; Kadowaki, M.; Kobayashi, T.; Ishi–I, T.; Theiemann, T.; Mataka, S. *J. Mater. Chem.* **2004**, *14*, 1901.
- (20) (a) Han, H.; Liang, M.; Tang, K.; Cheng, X.; Zon, X.; Sun, Z.; Xue, S. *J. Photochem. Photobio. A: Chem.* **2011**, *225*, 8. (b) Liu, K. –Y.; Hsu, C. –L.; Ni, J. –S.; Ho, K. –C.; Lin, K. –F. *J. Colloid Interface Sci.* **2012**, *372*, 73. (c) Cheng, X.; Sun, S.; Liang, M.; Shi, Y.; Sun, Z. Xue, S. *Dyes Pigments* **2012**, *92*, 1292.
- (21) (a) Charvet, R.; Yamamoto, Y.; Sasaki, T.; Kim, J.; Kato, K.; Takata, M.; Saeki, A.; Seki, S.; Aida, T. *J. Am. Chem. Soc.* **2012**, *134*, 2524. (b) Tolkki, A.; Kaunisto, K.;

Efimov, A.; Kivistö, H.; Storbacka, L.; Savikoski, R.; Huttunen, K.; Lehtimäki, S.;

Lemmetyinen, H. *Phys. Chem. Chem. Phys.* **2012**, *14*, 3498.

(22) (a) Ogawa, M.; Kuroda, K.; *Chem. Rev.* **1995**, *95*, 339. (b) Soegiarto, A. C.; Ward, M. D. *Cryst. Growth Des.* **2009**, *9*, 3803. (c) Sugikawa, K.; Numata, M.; Kinoshita, D.; Kaneko, K.; Sada, K.; Asano, A.; Seki, S.; Shinkai, S. *Org. Biomol. Chem.* **2011**, *9*, 146.

(23) (a) Ishida, Y.; Shimada, T.; Masui, D.; Tachibana, H.; Inoue, H.; Takagi, S. *J. Am. Chem. Soc.* **2011**, *133*, 14280. (b) Rice, Z.; Bergkvist, M. *J. Colloid Interface Sci.* **2009**, *331*, 189.

(24) (a) Turro, N. J.; Kumar, C. V.; Grauer, Z.; Barton, J. K. *Langmuir* **1987**, *3*, 1056. (b) Kamat, P. V.; Gopidas, K. R.; Mukherjee, T.; Joshi, V.; Kokar, D.; Pathak, V. S.; Ghosh, P. K. *J. Phys. Chem.* **1991**, *95*, 10009.

(25) (a) Lipstman, S.; Muniappan, S.; Goldberg, I. *Acta Cryst.* **2007**, *63*, 371. (b) Goldberg, I.; Muniappan, S.; George, S.; Lipstman, S. *CrystEngComm* **2006**, *8*, 784. (c) Lei, S. B.; Wang, C.; Yin, S. X.; Wang, H. N.; Xi, F.; Liu, H. W.; Xu, B.; Wan, L. J.; Bai, C. L. *J. Phys. Chem. B* **2001**, *105*, 10838. (d) Dahal, S.; Goldberg, I. *J. Phys. Org. Chem.* **2000**, *13*, 382.

(26) (a) Jirickova, M.; Demel, J.; Kubat, P.; Hostomsky, J.; Kovanda, F.; Lang, K. *J. Phys. Chem. C* **2011**, *115*, 21700. (b) Taviot-Guého, C.; Halma, M.; Charradi, K.; Forano, C.; Mousty, C. *New J. Chem.* **2011**, *35*, 1898. (c) Chernia, Z.; Gill, D. *Langmuir* **1999**, *15*, 1625. (d) Bujdák, J.; Iyi, N. *Cent. Eur. J. Chem.* **2008**, *6*, 569.

(27) To address these design challenges, Takagi et. al. reported a “size-matching” strategy to orient the porphyrin molecules far enough away from each other that aggregation behavior was not observed. See: (a) Takagi, S.; Shimada, T.; Yui, T.; Inoue,

H. *Chem. Lett.* **2001**, *30*, 128. (b) Takagi, S.; Tryk, D. A.; Inoue, H. *J. Phys. Chem. B* **2002**, *106*, 5455. (c) Egawa, T.; Watanabe, H.; Fujimura, T.; Ishida, Y.; Yamato, M.; Masui, D.; Shimada, T.; Tachibana, H.; Yoshida, H.; Inoue, H.; Takagi, S. *Langmuir* **2011**, *27*, 10722.

(28) Takagi et. al. reported relative control of orientation of porphyrin on the clay surface by solvent polarity. See: Eguchi, M.; Takagi, S.; Inoue, H. *Chem. Lett.* **2006**, *35*, 14.

(29) Tubasum, S.; Cogdell, R. J.; Scheblykin, E. G.; Pullerits, T. *J. Phys. Chem. B* **2011**, *115*, 4963.

(30) (a) Yui, T.; Kobayashi, Y.; Yamada, Y.; Yano, K.; Fukushima, Y.; Torimoto, T.; Takagi, K. *ACS Appl. Mater. Interfaces* **2011**, *3*, 931. (b) Demel, J.; Kubát, P.; Jirka, I.; Kovář, P.; Pospíšil, M.; Lang, K. *J. Phys. Chem. C* **2010**, *114*, 16321. (c) Takagi, S.; Eguchi, M.; Tryk, D.; Inoue, H. *J. Photochem. Photobiol. C: Photochem. Rev.* **2006**, *7*, 104. (d) Takagi, S.; Aratake, Y.; Konno, S.; Masui, D.; Shimada, T.; Tachibana, H.; Inoue, H. *Micropor. Mesopor. Mat.* **2011**, *141*, 38.

(31) (a) Burnett, B. J.; Barron, P. M.; Choe, W. *CrystEngComm* **2012**, *14*, 3839. (b) Choi, E. -Y.; Wray, C. A.; Hu, C.; Choe, W. *CrystEngComm* **2009**, *11*, 553. (c) Choi, E. -Y.; Barron, P. M.; Novotny, R. W.; Son, H. -T.; Hu, C.; Choe, W. *Inorg. Chem.* **2009**, *48*, 426. (d) Barron, P. M.; Son, H. -T.; Hu, C.; Choe, W. *Cryst. Growth Des.* **2009**, *9*, 1960. (e) Chung, H.; Barron, P. M.; Novotny, R. W.; Son, H. -T.; Hu, C.; Choe, W. *Cryst. Growth. Des.* **2009**, *9*, 3327.

(32) Barron, P. M.; Wray, C. A.; Hu, C.; Guo, Z.; Choe, W. *Inorg. Chem.* **2010**, *49*, 10217.

- (33) (a) Tam–Chang, S. –W.; Huang, L. *Chem. Commun.* **2008**, *44*, 1957. (b) Chao, M. – H.; Kariuki, B. M.; Harris, K. D. M.; Collins, S. P.; Laundry, D. *Angew. Chem. Int. Ed.* **2003**, *42*, 2982. (c) Hara, S.; Houjou, H.; Yoshikawa, I.; Araki, K. *Cryst. Growth Des.* **2011**, *11*, 5113. (d) Houjou, H.; Kokubun, M.; Yoshikawa, I.; Araki, K. *Chem. Lett.* **2009**, *38*, 436. (e) Kahr, B.; Freudenthal, J.; Phillips, S.; Kaminsky, W. *Science* **2009**, *324*, *43*, 1407.
- (34) Yamada, S.; Tsuchida, R. *Bull. Chem. Soc. Jpn.* **1952**, *25*, 127.
- (35) (a) Eguchi, M.; Tahibana, H.; Takagi, S.; Tryk, D. A.; Inoue, H. *Bull. Chem. Soc. Jpn.* **2007**, *80*, 1350. (b) Iyi, N.; Sasai, R.; Fujita, T.; Deguchi, T.; Sota, T.; Arbeloa, F. L.; Kitamura, K. *Appl. Clay Sci.* **2002**, *22*, 125. (c) Subbiah, S.; Mokaya, R. *Chem. Commun.* **2003**, 860. (d) Yamamoto, T.; Maruyama, T.; Zhou, Z.; Ito, T.; Fukuda, T.; Yoneda, Y.; Begum, F.; Ikeda, T.; Sasaki, S.; Takezoe, H.; Fukuda, A.; Kubota, K. *J. Am. Chem. Soc.* **1994**, *116*, 4832. (e) Chithra, P.; Varghese, R.; Divya, K. P.; Ajayaghosh, A. *Chem. Asian J.* **2008**, *3*, 1365. (f) Huang, L.; Tam–Chang, S. –W.; Seo, W.; Rove, K. *Adv. Mater.* **2007**, *19*, 4149. (g) Huang, L.; Catalano, V. J.; Tam–Chang, S. –W. *Chem. Commun.* **2007**, 2016.
- (36) Harbuzaru, B. V.; Corma, A.; Rey, F.; Atienzar, P.; Jordá, J. L.; García, H.; Ananias, D.; Carlos, L. D.; Rocha, J. *Angew. Chem. Int. Ed.* **2008**, *47*, 1080.
- (37) (a) Anex, B. G.; Fratini, A. V. *J. Mol. Spectry.* **1964**, *14*, 1. (b) Lucarini, V.; Saarinen, j. j.; Peiponen, K. –E.; Vartiainen, E. M. *Kramers-Kronig Relations in Optical Materials Research*, 1st ed.; Springer–Verlag: Berlin, **2005**. (c) Weaver, J. H.; Krafka, C.; Lynch, D. W.; Koch, E. E. *Optical Properties of Metals*, 1st ed.; Fachinformationszentrum Energie: Germany, **1981**; pp.74-81.

- (38) (a) Boucher, L. J. *Coord. Chem. Rev.* **1972**, *7*, 289. (b) Fagadar–Cosma, E.; Mirica, M. C.; Balcu, I.; Bucovicean, C.; Credu, C.; Armeanu, I.; Fagadar–Cosma, G. *Molecules* **2009**, *14*, 1370.
- (39) (a) Bohn, P. W. *Annu. Rev. Phys. Chem.* **1993**, *44*, 37. (b) Andrade, S. M.; Costa, S. M. B. *Ann. N. Y. Acad. Sci.* **2008**, *1130*, 305.
- (40) Shustova, N. B.; Ong, T. –C.; Cozzolino, A. F.; Michaelis, V. k.; Griffin, R. G.; Dincă, M. *J. Am. Chem. Soc.* **2012**, *134*, 15061.
- (41) Colombo, V.; Galli, S.; Choi, H. J.; Han, G. D.; Maspero, A.; Palmisano, G.; Masciocchi, N.; Long, J. R. *Chem. Sci.* **2011**, *2*, 1311.
- (42) (a) Cohen, S. M. *Chem. Sci.* **2010**, *1*, 32. (b) Ahnfeldt, T.; Gunzelmann, D.; Loiseau, T.; Hirsemann, D.; Senker, J.; Férey, G.; Stock, N. *Inorg. Chem.* **2009**, *48*, 3057. (c) Hwang, Y. K.; Hong, D. –Y.; Chang, J. –S.; Jung, S. H.; Seo, Y. –K.; Kim, J.; Vimont, A.; Daturi, M.; Serre, C.; Férey, G. *Angew. Chem. Int. Ed.* **2008**, *47*, 4144. (d) Farha, O. K.; Mulfort, K. L.; Hupp, J. T. *Inorg. Chem.* **2008**, *47*, 10223. (e) Mulfort, K. L.; Farha, O. K.; Stern, C. L.; Sarjeant, A. A.; Hupp, J. T. *J. Am. Chem. Soc.* **2009**, *131*, 3866.
- (43) Abrahams, B. F.; Hoskins, B. F.; Michail, D. M.; Robson, R. *Nature* **1994**, *369*, 727.
- (44) Tranchemontagne, D. J.; Mendoza–Cortés, J. L.; O’Keeffe, m.; Yaghi, O. M. *Chem. Soc. Rev.* **2009**, *38*, 1257.
- (45) Choi, H. J.; Dincă, M.; Dailly, A.; Long, J. R. *Energy Environ. Sci.* **2010**, *3*, 117.
- (46) Low, j. J.; Benin, A. I.; Jakubczak, P.; Abrahamian, J. F.; Faheem, S. A.; Willis, R. *J. Am. Chem. Soc.* **2009**, *131*, 15834.
- (47) Jasuja, H.; Burch, N. C.; Huang, Y.; Cai, Y.; Walton, K. S. *Langmuir* **2013**, *29*, 633.
- (48) Satake, A.; Kobuke, Y. *Tetrahedron* **2005**, *61*, 13.

(49) Litke, S. V.; Mezentseva, T. V.; Lyalin, G. N.; Ershov, A. Y. *Opt. and Spectrosc.* **2003**, *95*, 917.

(50) Advanced Chemistry Development, Inc.: Toronto, Canada, 1996-2005.

<http://www.acdlabs.com>.

(51) Connolly Surface model was created using *Material Studio* (version 4.3): Program for Molecular Modeling and Analysis; Accelrys Software Inc.

CHAPTER 9

CATALYTICALLY ACTIVE PORPHYRIN PADDLEWHEEL FRAMEWORK FOR ALKENE EPOXIDATION

9.1 Introduction

For the past several decades, molecular metalloporphyrins have been intensively studied in biomimetic chemistry as artificial enzymes that mimic cytochrome P-450 enzymes, well known for catalyzing oxygen-transfer reactions in nature.¹ Especially, alkene epoxidation catalysis has been an important target reaction in academia and industry because epoxides are intermediates that can be easily transformed to valuable products via a ring opening reaction.² However, a major drawback of the homogeneous porphyrinic catalysts has been the formation of μ -oxo porphyrin dimers during the oxygen-transfer reaction.³ Therefore, it is highly desirable to develop a new porphyrin-based catalytic system to avoid this side reaction.

To overcome this synthetic challenge, several approaches have been identified including making heterogeneous catalysts by incorporating porphyrins into zeolites, aluminophosphates, clays, and scilicates,⁴ and attaching porphyrins on the surface of nanoparticles.^{5,6} While all of these approaches aid in preventing the μ -oxo dimer formation, they suffer from low porphyrin loading and leaching of the porphyrin into the solution during catalysis.^{4,5} An interesting new approach is to incorporate porphyrins into the synthesis of metal-organic frameworks (MOFs).⁷⁻¹⁵ Catalysis has been an important

target application for MOF chemists from the beginning of the field.¹⁶ By using porphyrin as a metal containing organic linker in the synthesis of MOFs, the porphyrin can accomplish two roles *i.e.* structural metal center and functional metal center.¹⁶ More importantly, in MOF synthesis, the porphyrin linkers become the “wall” of the frameworks and therefore the formation of μ -oxo porphyrin dimer can be prevented. We and others have used porphyrins in MOF synthesis,⁷⁻¹⁴ but it is rather striking that only few cases of porphyrinic MOFs have been used as heterogeneous catalysts.⁷⁻¹⁰ One of the major problems faced with porphyrinic MOF synthesis is that the metal ion within the porphyrin ring can be used as a structural joint, making it inaccessible for catalysis.^{7,11,12}

We have been working on a series of porphyrinic MOFs based on *meso*-tetrakis(4-carboxyphenyl)porphyrin (TCPP) metalloligand and $M_2(\text{COO})_4$ paddlewheel metal node. The combination of these two units results in a 2D square grid that can be further coordinated axially by dipyrindyl pillars to make 3D *porphyrin* paddlewheel frameworks, which we call PPFs.¹² Recently, Hupp and coworkers reported a catalytically-active porphyrinic MOF, ZnMn-RPM, based on the same 2D porphyrin-based square grid.⁷ The ZnMn-RPM compound showed catalytic activity toward epoxidation of styrene and the hydroxylation of cyclohexane.⁷ While the structure showed improved catalytic performance compared to the porphyrin monomer counterpart, upon recycling the compound for multiple catalysis sequences, the rate of catalysis was slowed by one-third, which could be due to a partial blockage of the pores by insoluble oxidant.^{7,8}

Because of these difficulties in retaining the integrity of the pores during catalysis, we have revisited an idea of catalyzing substrate on the external surface of the

MOFs instead of inside of the pores, analogous to metal nanoparticles commonly employed in heterogeneous catalysis.^{17,18} External surface catalysis is not common within MOFs, with only a few known examples.^{10,19} We hypothesize that applying this strategy makes possible for fast heterogeneous catalysis (eliminating the need for a substrate to diffuse into pores), along with no inherent vulnerability of pore collapse or blockage, which impact negatively on the desired catalytic reaction.

This chapter discusses a new 2D porphyrinic MOF, PPF-100, used as a heterogeneous catalyst for epoxidation of alkenes. PPF-100 is a nonporous structure decorated with catalytically active Mn sites fully exposed on the external surface (Figure 9.1). PPF-100 exhibits fast catalysis with excellent yields for the epoxidation of 12 different alkene substrates, and shows the yield of the styrene epoxidation exceeding other known homogeneous and heterogeneous Mn-based porphyrin catalysts.

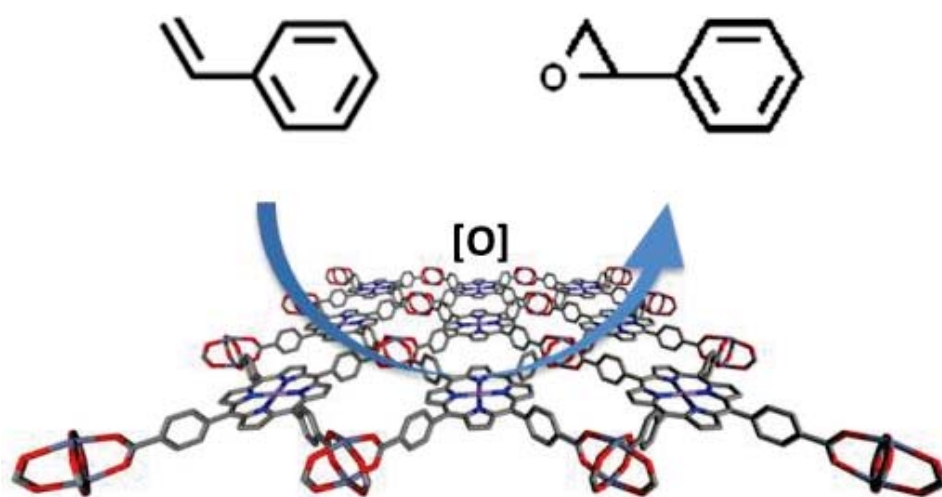


Figure 9.1. Schematic illustration of the surface catalyzed epoxidation reaction of styrene on PPF-100.

9.2 Experimental Methods

PPF-100 A mixture of 5,10,15,20-tetrakis(4-carboxyphenyl)-Mn(III)-porphyrin chloride (8.8 mg, 0.01 mmol), zinc nitrate hexahydrate (6.0 mg, 0.02), and 1.0 M nitric acid in ethanol (30 μ L, 0.03 mmol) were added to a mixture of *N,N*-dimethyl formamide (1.5 mL) and ethanol (0.5 mL) in a capped vial and heated to 60 °C for 72 hrs, followed by slow-cooling to room temperature over 9 hrs. Yield: 3.5 mg (29% based on porphyrin). Anal. Calcd. For $[\text{C}_{48}\text{H}_{24}\text{N}_4\text{O}_{12}\text{MnZn}_2 \cdot \text{NO}_3] 0.75 \text{ H}_2\text{O} \cdot 1.52 \text{ DMF}$: C, 51.7; H, 3.34; N, 7.48%. Found: C, 51.7; H, 2.98; N, 7.48%.

Single crystal structure determination:

Plate-shaped crystals of PPF-100 (90 x 90 μ m) were sealed in a capillary for XRD measurement. Geometry and intensity data were obtained at room temperature with a Bruker SMART Apex CCD area detector diffractometer. Preliminary lattice parameters and orientation matrices were obtained from three sets of frames. Data were collected using graphite-monochromated and MonoCap-collimated Mo- K_α radiation ($\lambda = 0.71073 \text{ \AA}$) with ω scan method.²⁰ Data was processed with the SAINT+ program²¹ for reduction and cell refinement. Multi-scan absorption corrections were applied to the data set using the SADABS program for area detector.²² The structure was solved by direct method and refined using SHELXTL.²³ Disordered, independent solvent molecules inside the frameworks were eliminated in the refinement by PLATON/SQUEEZE.²⁴ All atoms were refined with anisotropic displacement parameters.

X-ray powder diffraction (PXRD):

Data was collected on a Rigaku D/Max-B X-ray diffractometer with Bragg–Brentano parafocusing geometry, a diffracted beam monochromator, and a conventional copper target X-ray tube set to 35 KV and 25 mA.

Thermogravimetric analysis:

Performed on a Perkin Elmer STA 6000 thermogravimetric analyzer, heated from 25 °C to 800 °C at a rate of 10 °C/minute under N₂ atmosphere.

Elemental analysis:

Data was performed by MidwestMicro Labs LLC.

GC/MS:

All yields of products were measured on a Donam Systems 6200 gas chromatograph equipped with an FID and N₂ was used as carrier gas. Injector and column temperature kept at 230 °C and detector was at 250 °C. After the sample was injected and initial temperature kept at 50 °C for 3 min. The temperature was increased at a rate of 20 °/min until the temperature reached at 230 °C and then kept for 9 min.

Catalytic Alkene Epoxidation by PPF-100 or MnTCPPCl with PhIO:

To a mixture of substrate (0.25 mmol), PPF-100 or MnTCPPCl catalyst (0.001 mmol), dodecane (0.01 mmol), solvent (CH₂CL₂, 1 mL), and PhIO (0.05 mmol) was added. The mixture was stirred for 2 days at room temperature. Reaction was monitored by GC/Mass analysis of 20 μL aliquots withdrawn periodically from the reaction mixture. All reactions were run at least three times.

Stability of Catalyst during Epoxidation Reaction:

To a mixture of styrene (0.25 mmol), PPF-100 (0.001 mmol), dodecane (0.01 mmol), and solvent (CH_2Cl_2 , 5 mL), PhIO (0.05 mmol) was added. The mixture was stirred for 2 days at room temperature. When the reaction solution was completed, the supernatant was removed with a pipette. The remaining catalyst was washed three times with 5 mL of CH_2Cl_2 and then analyzed by PXRD.

Competitive Reactions of Styrene and *para*-substituted Styrenes for Hammett plot:

To a mixture of styrene (0.02 mmol) and *para* (X)-substituted styrene (0.02 mmol; X = OCH_3 , CH_3 , F, and CN), PPF-100 (0.003 mmol), and solvent (CH_2Cl_2 , 1 mL), PhIO (0.03 mmol) was added. The mixture was stirred for 7 hrs at room temperature. The amounts of styrenes before and after reactions were determined by GC/Mass. The relative reactivities were determined using the following equation: $k_x/k_y = \log(X_f/X_i)/\log(Y_f/Y_i)$ where X_i and X_f are the initial and final concentrations of substituted styrenes and Y_i and Y_f are the initial and final concentrations of styrene.²⁵

9.3 Results and Discussion

PPF-100 was synthesized via a solvothermal reaction of zinc nitrate hexahydrate, Mn(III) *meso*-tetra(4-carboxyphenyl)porphyrin chloride, *N,N*-dimethylformamide, and ethanol at 60 °C for 72 hrs. The purity of the resulting crystals was confirmed by elemental analysis and PXRD. A single crystal suitable for X-ray single crystal diffraction was selected and crystal data obtained (Table 9.1). Valence bond sum calculations returned a value of 3.03 for the Mn ion in the porphyrin core indicating that the manganese center retains its +3 oxidation state upon crystallization.²⁶ TCPP linker and Zn₂(COO)₄ paddlewheel metal node form a 2D grid pattern which is slightly puckered and shows a 'staircase' stacking pattern in which each layer is shifted by 5.8 Å laterally (Figure 9.2). Due to this unique stacking pattern, Conolly surface analysis of PPF-100 reveals only small pore sizes of 3.3 Å by 8.5 Å and a free space gap between layers of 2.3 Å (Figure 9.3). Such pore properties are confirmed by BET measurements. PPF-100 does not show any appreciable N₂ adsorption but only small amount of CO₂ adsorption (see Figures 9.4 and 9.5) in sharp contrast to our previously published 2D structure PPF-1.^{12a} The accessible space within PPF-100 is too small for many substrates and the corresponding products (Figure. 9.3 and Table 9.2). It is noteworthy that PPF-100 crystals grow in platelet morphology (see Figure 9.2e) in which the porphyrin 2D sheet lies on the high aspect 2D surface as evidenced by preferential orientation normal to [20-1] direction observed in PXRD pattern (Figures 9.6 and 9.7). These data support that PPF-100 contains numerous active metal centers exposed on the surface of the platelet crystals, unlike other MOFs where the active metal centers reside inside pores. Another key structural feature of PPF-100 is the topological constraints that prevent dimerization

of porphyrins. In PPF-100, adjacent porphyrins are physically separated, held together by paddlewheel metal nodes, and thus formation of μ -oxo dimer is strictly forbidden.

Furthermore, inter-particle dimer formation is highly unlikely due to steric hindrance and lattice mismatch, as can be seen in Figure 9.8.

Table 9.1. Crystal data for PPF-100

Complex	PPF-100
chemical formula*	$C_{48}H_{24}MnN_4O_{12}Zn_2$
formula weight*	1034.39
crystal system	monoclinic
space group	$C2/m$
a (Å)	20.971(3)
b (Å)	23.615(4)
c (Å)	9.7890(16)
β (°)	109.070(15)
V (Å ³)	4581.8(13)
Z	2
ρ_{calc} (g/cm ³)*	0.750
μ (mm ⁻¹)*	0.689
$R_1, I > 2\sigma(I)$	0.0462
$wR_2, I > 2\sigma(I)$	0.1246

*Based on the formula without uncoordinated solvent molecules.

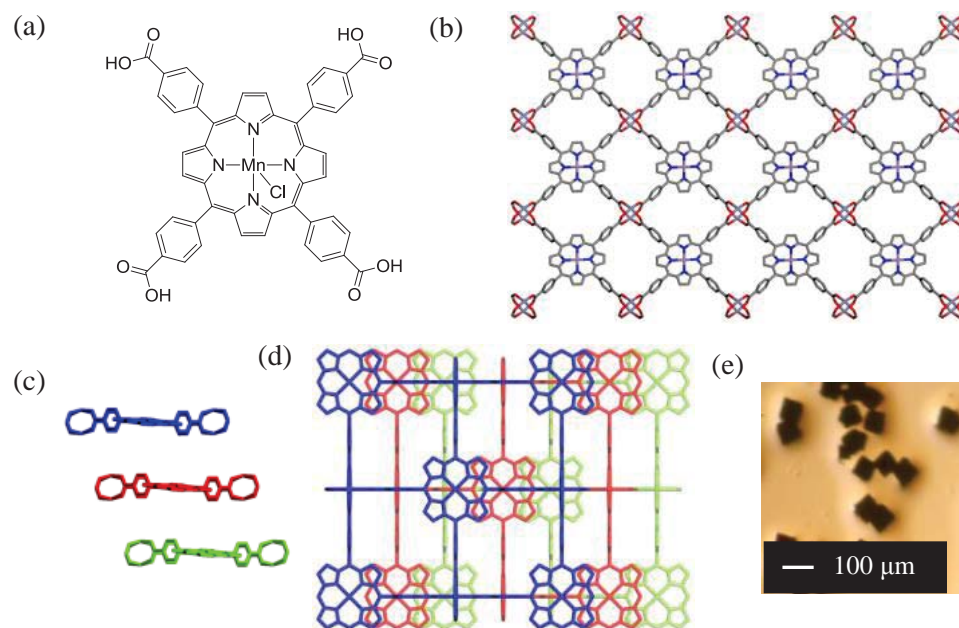


Figure 9.2. (a) A porphyrin linker, MnTCPPCl used in assembly of PPF-100. (b) 2D porphyrinic sheet coupled with the porphyrin linkers and $\text{Zn}(\text{COO})_4$ metal nodes. (c-d) Stacks of porphyrinic sheets viewed down the [221] and [20-1] directions, respectively. (e) Microscope photograph of PPF-100 showing platelet morphology of the crystals.

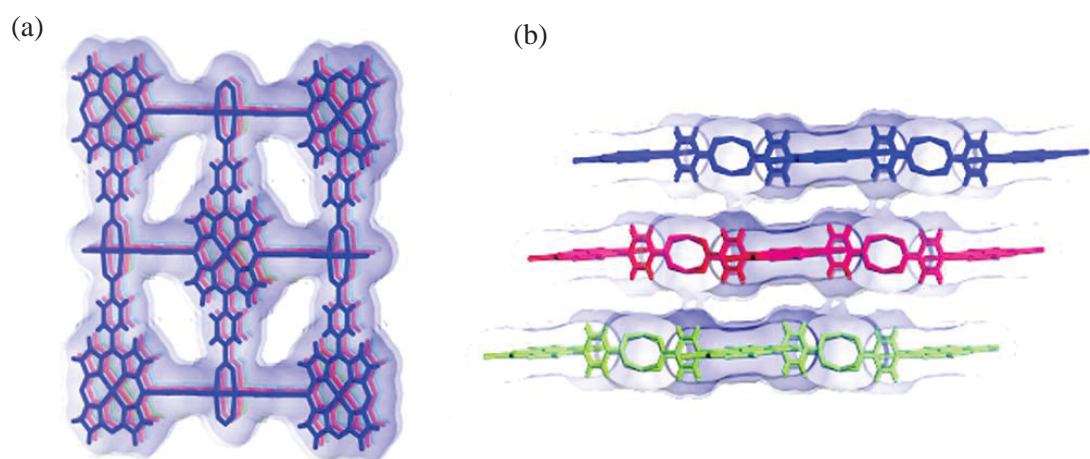


Figure 9.3. Conolly surface of PPF-100 (a) showing 1D channel ($8.5 \times 3.3 \text{ \AA}$) and (b) between layers (2.3 \AA) calculated with 1.4 \AA VDW scale factor using Material Studio.²⁷

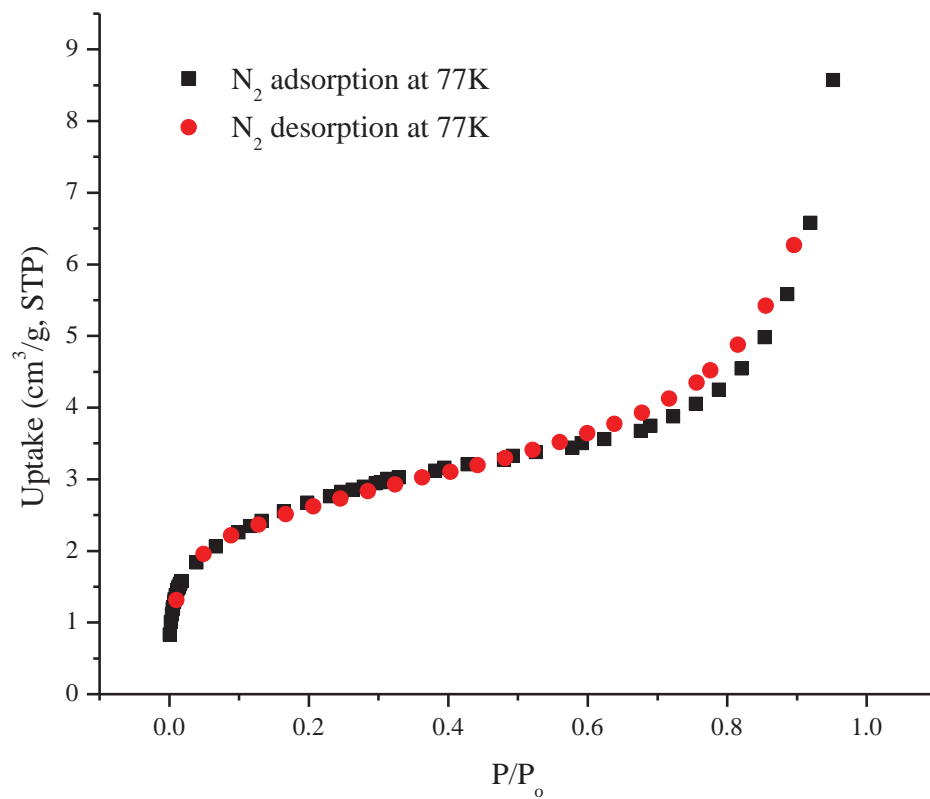


Figure 9.4. PPF-100 adsorption of N_2 at 77K.

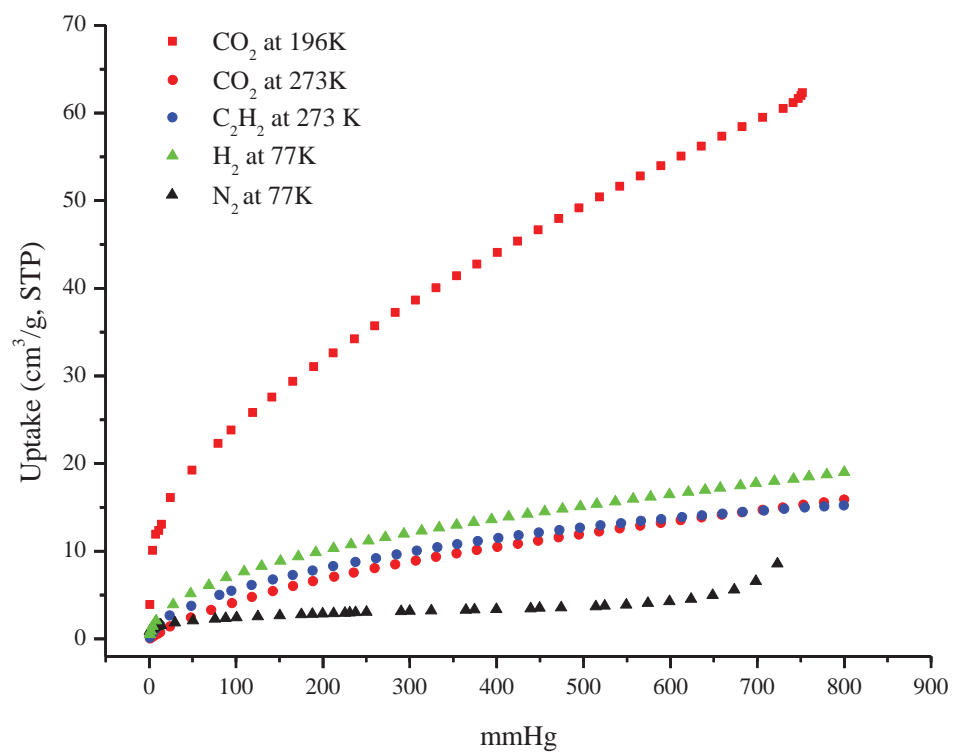


Figure 9.5. PPF-100 adsorption of N₂, H₂, CO₂, and C₂H₂.

Table 9.2. The smallest cross-section size of substrates

Substrate	The width and height of smallest cross section (\AA^2)	Substrate	The width and height of smallest cross section (\AA^2)
styrene	6.5×1.7	<i>cis</i> -2-hexene	5.1×5.1
cyclopentene	6.2×4.4	<i>trans</i> -2-hexene	5.0×5.0
cycloheptene	7.2×5.0	<i>cis</i> -2-octene	5.3×5.1
cyclooctene	7.3×5.4	<i>trans</i> -2-octene	5.2×5.2
cyclohexene	6.5×4.9	<i>cis</i> -stilbene	7.3×4.9
1-hexene	4.9×4.7	<i>trans</i> -stilbene	6.8×1.7

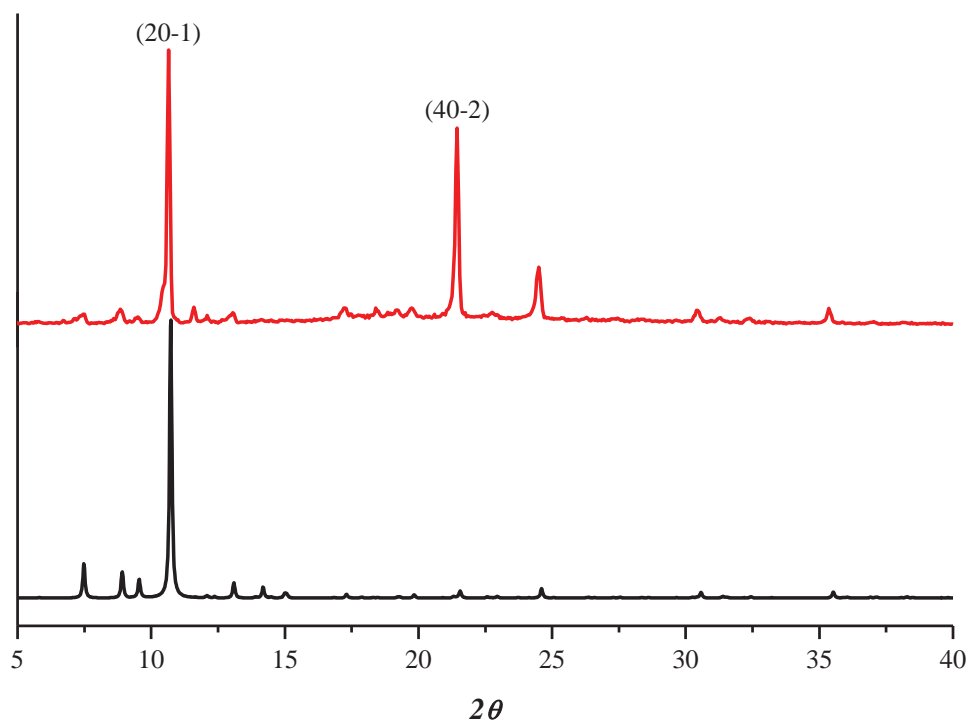


Figure 9.6. Theoretical (bottom) and experimental (top) PXRD patterns for PPF-100. The experimental pattern matches well with the theoretical pattern when preferred orientation about the (201) plane is considered. The theoretical powder pattern with preferred orientation was generated using Mercury.²⁸

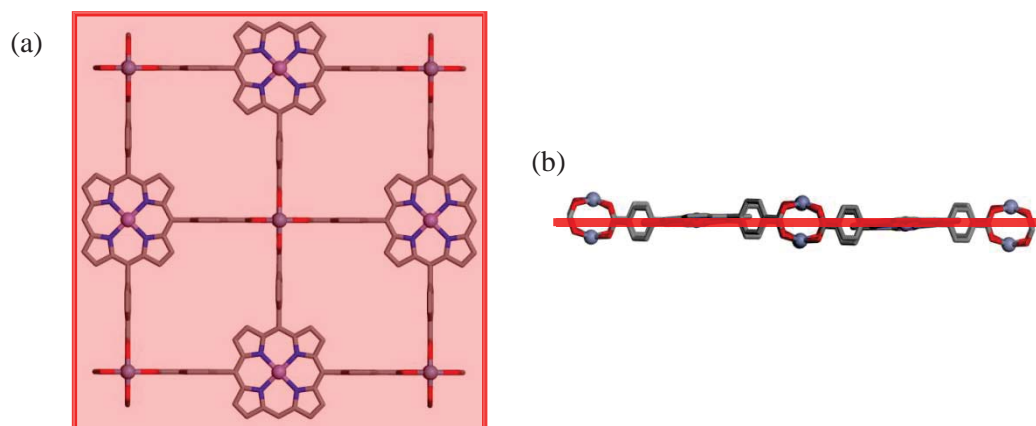


Figure 9.7. Illustration of the (20-1) plane bisecting the porphyrin paddlewheel 2D sheet viewed (a) perpendicular and (b) parallel to the sheet.

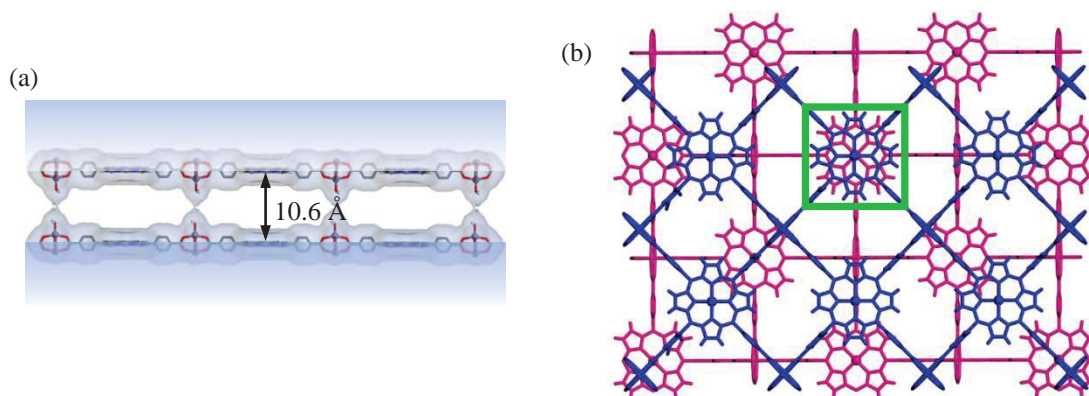
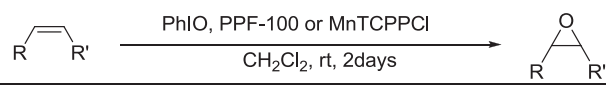
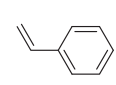
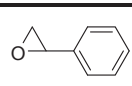
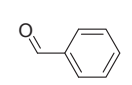
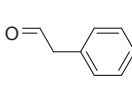
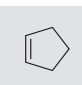
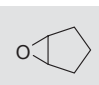
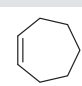
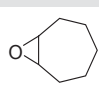
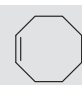
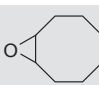
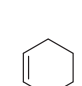
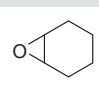
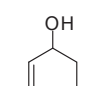
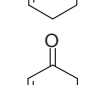
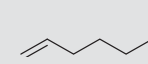
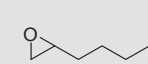
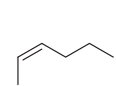
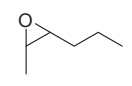
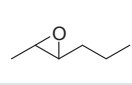
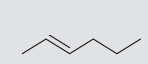
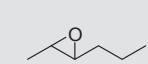
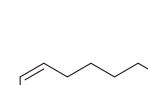
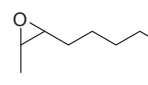
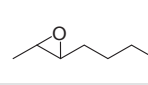
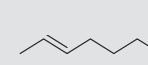
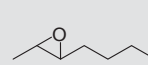
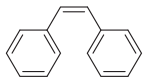
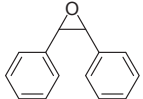
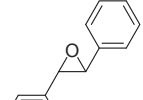
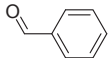
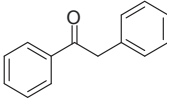
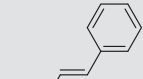
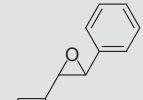
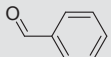
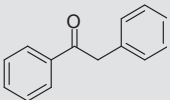


Figure 9.8. Illustration showing the inability of inter-particle μ -oxo dimer formation in PPF-100 system. (a) The porphyrin–porphyrin distance between two particles with matching lattices on the porphyrin paddlewheel surface is restricted to ≥ 10.6 Å due to steric hindrance created by the paddlewheel metal node. This distance is much longer than the 3.54 Å porphyrin–porphyrin distance observed in the μ -oxo dimer.²⁹ (b) The steric hindrance from the paddlewheel metal node can be overcome if one of the particle's porphyrin paddlewheel surface was rotated 45° from the adjacent surface. In this case the μ -oxo dimer is possible, but because of lattice mismatch, there is only a small percent of porphyrins lined up correctly to participate in dimer formation.

We performed epoxidation reactions for 12 different alkene substrates using PPF-100 as a heterogeneous catalyst. As shown in Table 9.3, PPF-100 was very effective for the epoxidation catalysis of these alkenes, affording 35–300% more products than monomeric MnTCPPCl. The reaction of cyclohexene (entry 5) produced the epoxidation product (32.7%), along with some amounts of cyclohexenone (35.4%) and cyclohexenol (37.4%), indicating that free radical oxidation reactions which include oxygen from the air were somewhat involved in the alkene epoxidation reactions.³⁰ The cyclohexenone and cyclohexanol are produced from this free radical oxidation reaction, and not through the same mechanism which creates the epoxide.³⁰ Surprisingly, terminal alkene 1-hexene, usually known as the least reactive alkene in metal-catalyzed epoxidations,^{30,31} was readily oxidized to the corresponding epoxides with high yield under these conditions (entry 6). *cis*-2-hexene was oxidized to *cis*-2-hexene oxide as the major product (73.8%) along with a small amount of *trans*-2-hexene oxide (16.0%), indicating that the catalytic epoxidation reaction occurs with 82% stereochemical retention (entry 7). As the alkene interacts with the Mn(V)=O center, the sp^2 carbons, which do not allow for free rotation, are changed to sp^3 carbon centers, allowing for free rotation around the carbon-carbon bond to create the *trans* product.³⁰ *trans*-2-hexene was oxidized exclusively to *trans*-2-hexene oxide (entry 8). Epoxidation reaction of *cis*- and *trans*-octene showed the similar results (entries 9 and 10). In the epoxidation of *cis*-2-octene, the stereochemical retention was observed to be 90%. This value is significantly larger than that observed with the monomeric Mn porphyrin system (43% retention).

Table 9.3. Alkene epoxidation by PPF-100.^a

				Yield of products (%) ^b		Retention time (min)	Column type ^c	
Entry	Substrate	Product	PPF-100		MnTCPPCl			
			PhIO	O ₂ (air)	PhIO			O ₂ (air)
1			69.0±0.4		23.4±2.6	10.09	H	
				19.5±4.0	16.1±0.1	9.36	H	
				53.6±2.1	17.4±1.0	10.28	H	
2			56.6±1.7		29.4±0.9	5.80	H	
3			55.7±5.9		29.4±0.6	9.44	H	
4			52.0±9.2		23.3±0.7	10.99	H	
5			32.7±2.9		24.8±2.1	5.76	H	
				37.4±1.3	34.9±6.1	8.70	H	
				35.4±1.9	30.0±3.8	8.86	H	
6			56.8±3.2		27.3±1.1	6.78	D	
7			73.8±5.6		27.1±1.4	6.39	D	
			16.0±0.3		16.3±0.6	5.97	D	
8			48.3±9.3		17.5±2.2	5.97	D	
9			50.9±2.3		25.0±2.2	9.36	D	
			5.7±0.2		17.8±3.8	9.01	D	
10			51.5±0.2		20.1±1.8	9.01	D	

11			41.7±1.5	17.6±5.1	15.35	H
			20.7±8.3	11.7±3.4	17.79	H
			7.3±0.5	6.2±1.4	9.36	H
			20.1±2.0	3.6±0.4	19.37	H
12			68.0±2.1	32.7±8.4	17.79	H
			22.6±0.3	35.3±0.8	9.36	H
			8.1±0.3	3.8±0.3	19.37	H

^a Reaction conditions: alkene (0.25 mmol), catalyst (1.0×10^{-3} mmol), oxidant (PhIO, 0.05 mmol), solvent (1 mL, CH_2Cl_2), reaction time (2 days). ^b Based on PhIO. ^c H : Agilent Tech., HP-FFAP, 30 m \times 0.32 mm \times 0.25 μm , D : Agilent Tech., DB-5, 30 m \times 0.32 mm \times 0.25 μm .

Product distribution of these aromatic alkenes indicates that either the peroxy radical or oxomanganese (IV) is partly involved as the epoxidizing agent since these species should oxidize the substrates to nonstereospecific or radical-induced rearranged products.³¹ However, we notice the formation of epoxide as the major products, some portion of free radical oxidation reactions, and a high degree of stereo specificity observed. These observations imply that two different oxidants, $\text{Mn}^{\text{V}}=\text{O}$ and $\text{Mn}^{\text{IV}}=\text{O}$, are produced in these catalytic reactions. Furthermore, the latter $\text{Mn}^{\text{IV}}=\text{O}$ complex is responsible for the nonstereoretentive portion of the epoxidation reaction.³¹

While high yields of the epoxides were observed in many cases, it is also noteworthy that the overall conversion for most of the substrates is near 100% (see Table 9.3). Analogous but lower yields were obtained for monomeric MnTCPPCl , suggesting that the assembly of MOF enhances its reactivity. Interestingly, PPF-100 is one of the most effective porphyrinic catalysts for alkene epoxidation reactions. The % yield of styrene epoxide catalyzed from PPF-100 was significantly higher than other manganese porphyrins in homogeneous and heterogeneous systems (Table 9.4). During catalysis, no induction period was observed because of the lack of pore size for diffusion into the interior of the crystals. Furthermore, because PPF-100 can be physically separated from the reaction solution, it can be recycled for multiple reactions. When recycling experiments were performed in the epoxidation of cyclooctene, PPF-100 continued to be catalytically active after 4 catalytic cycles, yielding comparable amount of products as from the first cycle (Table 9.5). Additionally, after the oxidation reaction, the supernatant was analysed by UV-vis spectroscopy, and no traces of porphyrin were observed, showing that there was no leaching of the active porphyrin during the catalysis. Loss of

crystallinity was observed by powder X-ray diffraction of PPF-100 after catalysis, but structural peaks were still observable (Figure 9.9).

Table 9.4. Epoxidation of styrene (Sub) by porphyrin as homogeneous or heterogeneous catalysis (Cat) at room temperature.^a

Compound ^b	Yield of styrene epoxide (%)	Molar ratio Cat. : Sub. : PhIO	Reaction time	Reference
MnTCPPCl	23 ^c	1:250:50	24 h	This work
PPF-100	69 ^c	1:250:50	24 h	This work
MnTSPCl	64 ^d	1:1000:100	1 h	4b
AU:SC12	38 ^c	1:5000:1000	7 h	5b
ZnMn-RPM	45 ^d	1:5000:1000	13h	7

^a All reaction condition : solvent (CH₂Cl₂), room temperature. ^b TSP : Threitol-Strapped Porphyrin, see the compound **3b** in ref. 4b for structure, AU:SC12 : Porphyrin with gold cluster, ZnMn-RPM: Zn/Mn Robust Porphyrinic Materials, calculated from data in ref 7. ^c Based on PhIO. ^d Based on consumption PhIO.

Table 9.5. Recycle Experiments of epoxidation of cyclooctene.^a

Run	Yield of products (%) ^b
1	52.0 ± 9.2
2	55.1 ± 5.8
3	50.8 ± 1.8
4	50.3 ± 1.0

^a Reaction conditions: alkene (0,25 mmol), catalyst (1.0 × 10⁻³ mmol porphyrin), oxidant (PhIO, 0.05 mmol), solvent (1 mL, CH₂Cl₂), reaction time (2 days).

^b Yields based on PhIO.

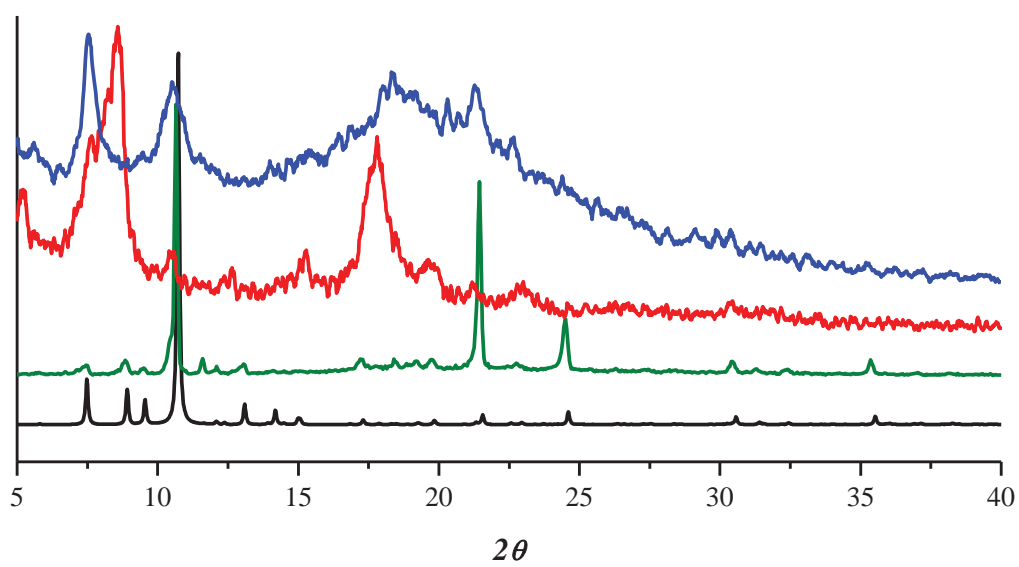


Figure 9.9. Simulated (black), as synthesized (green), after catalysis (red) and re-immersed in DMF (blue) PXRD patterns of PPF-100.

To obtain further information about the nature of the reactive intermediates, competition experiments were carried out between styrene and equivalent amounts of *p*-substituted styrene derivatives. The relative binding constant K_{rel} was plotted against the substituent constant σ .³² A significant electronic effect on the reaction rates was observed, showing that the more electron-rich alkenes react faster than electron-deficient substrates. The rate data gave a good linear Hammett plot with ρ values of -1.3 for PPF-100 (Figure 9.10), confirming the expected electrophilic character of the oxidant. The value is higher than that reported for the epoxidation of styrenes using Mn^{III} tetraphenylporphyrin ($\rho = -0.41$).³²

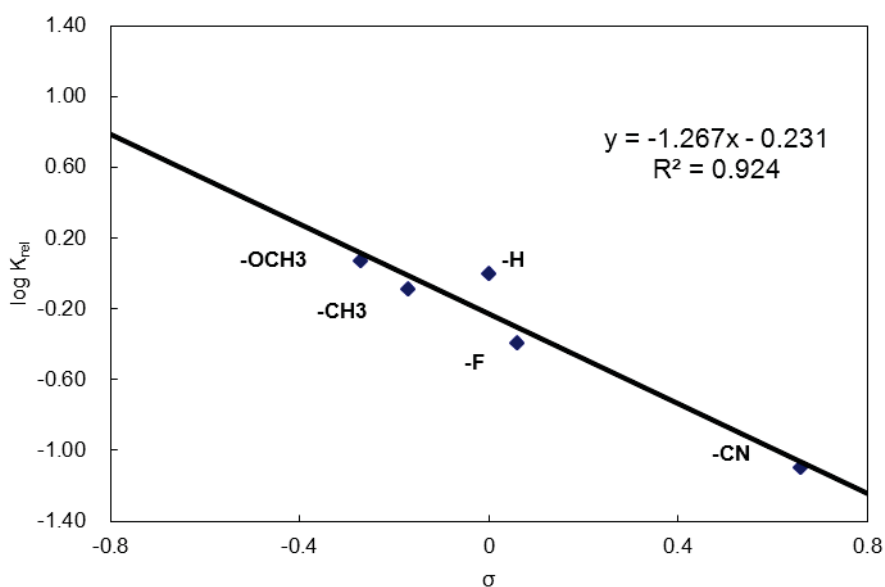


Figure 9.10. Hammett plot for the relative reactivity of styrene to *para*-substituted styrenes with PPF-100.

9.4 Conclusion

In summary, a biomimetic porphyrinic MOF, PPF-100, was synthesized and its catalytic properties were studied, showing the successful alkene epoxidation. Because the pores are very small within PPF-100, all of the catalytic reactions occur on the surface. Having catalytically active metal centers readily available on the surface rather than inside of the pores of the structure allows fast catalysis and recyclable catalysts in which pore collapse or blockage is not an issue. PPF-100 shows high yields for the epoxidation of 12 alkenes. External surface catalysis on MOFs has not been extensively explored, which could produce recyclable, self-supported catalysts in numerous other catalytic reactions.

9.5 References

- (1) Collman, J. P.; Boulatov, R.; Sunderland, C. J.; Fu, I. *Chem. Rev.* **2004**, *104*, 561. (b) Hupp, J. T.; *Nat. Chem.* **2010**, *2*, 432.
- (2) Finney, N. S.; Pospisil, P. J.; Ghang, S.; Palucki, M.; Kosler, R. G.; Hansen, K. B.; Jacobson, E. N. *Angew. Chem. Int. Ed.* **1997**, *36*, 1720.
- (3) Merlau, M. L.; Cho, S. -H.; Sun S. -S.; Nguyen, S. T.; Hupp, J. T. *Inorg. Chem.* **2005**, *44*, 5523.
- (4) (a) Bedioui, F. *Coord. Chem. Rev.* **1995**, *144*, 39. (b) Collman, J. P.; Lee, V. J.; Kellen-Yuen, C. J.; Zhang, X.; Ibers, J. A.; Braumna, J. I. *J. Am. Chem. Soc.* **1995**, *117*, 692.
- (5) (a) Zhang, J. -L.; Liu, Y. -L.; Che, C. -M. *Chem. Commun.* **2002**, *38*, 2906. (b) Murakami, Y.; Konishi, K. *J. Am. Chem. Soc.* **2007**, *129*, 14401.

- (6) Another approach for homogeneous catalysts include building “picket-fence” porphyrins. See: Xia, Q. -H.; Ge, H. -Q.; Ye, C. -P.; Liu, Z. -M.; Su, K. -X. *Chem. Rev.* **2005**, *105*, 1603.
- (7) Farha, O. K.; Shultz, A. M.; sarjeant, A. A.; Nguyen, S. T.; Hupp, J. T. *J. Am. Chem. Soc.* **2011**, *133*, 5652.
- (8) More recently, Zaworotko and coworkers were successful in synthesizing a MOF which contains porphyrins in many pores that is capable of retaining catalytic performance for alkene epoxidation after six cycles. See: Zhang, Z.; Zhang, L.; Wojtas, L.; Nugent, P.; Eddaoudi, M.; Zaworotko, M. J. *J. Am. Chem. Soc.* **2012**, *134*, 924.
- (9) (a) Xie, M. -H.; Yang, X. -L.; Wu, C. -D. *Chem. Commun.* **2011**, *47*, 5521. (b) Zou, C.; Zhang, Z.; Xu, X.; Gong, Q.; Li, J.; Wu, C. -D. *J. Am. Chem. Soc.* **2012**, *134*, 87. (c) Yang, X. -L.; Xie, M. -H.; Zou, C.; He, Y.; Chen, B.; O’Keeffe, M.; Wu, C. -D. *J. Am. Chem. Soc.* **2012**, *134*, 10638. (d) Fateeva, A.; Chater, P. A.; Ireland, C. P.; Tahir, A. A.; Khimyak, Y. Z.; Wiper, P. V.; Darewnt, J. R.; Rosseinsky, M. J. *Angew. Chem. Int. Ed.* **2012**, *51*, 1. (e) Feng, D.; Gu, Z. -Y.; Li, J. -R.; Jiang, H. -L.; Wei, Z.; Zhou, H. -C. *Angew. Chem. Int. Ed.* **2012**, *51*, 10307.
- (10) Suslick, K. S.; Bhyrappa, P.; Chou, J. H.; Kosal, M. E.; Nakagaki, S.; Smithenry, D. W.; Wilson, S. R. *Acc. Chem. Res.* **2005**, *38*, 283.
- (11) Choi, E. -Y.; DeVries, L. D.; Novotny, R. W.; Hu, C.; Choe, W. *Cryst. Growth Des.* **2010**, *10*, 171. (b) Danilovic, D.; Lin, C. L.; Yuen, T.; Pan, L.; Li, J. *Appl. Phys.* **2007**, *101*, 103.
- (12) (a) Choi, E. -Y.; Barron, P. M.; Novotny, R. N.; Hu, C.; Kwon, Y. -U.; Choe, W. *CrystEngComm* **2008**, *10*, 824. (b) Choi, E. -Y.; Barron, P. M.; Novotny, R. W.; Son, H.

–T.; Hu, C.; Choe, W. *Inorg. Chem.* **2009**, *48*, 426. (c) Barron, P. M.; Son, H. –T.; Hu, C.; Choe, W. *Cryst. Growth Des.* **2009**, *9*, 1960. (d) Barron, P. M.; Wray, C. A.; Hu, C.; Guo, Z.; Choe, W. *Inorg. Chem.* **2010**, *49*, 10217.

(13) The importance of porphyrin building blocks in MOF–based catalysis was first addressed by Robson and coworkers. See: Abrahams, B. F.; Hoskins, B. F.; Michail, D. M.; Robson, R. *Nature* **1994**, *369*, 727.

(14) (a) Goldberg, I. *CrystEngComm* **2008**, *10*, 637. (b) Wang, X. –S.; Meng, L.; Cheng, Z.; Kim, C.; Wojtas, L.; Chrzanowski, M.; Chen, Y. –X.; Zhang, X. P.; Ma, S. *J. Am. Chem. Soc.* **2011**, *133*, 16322.

(15) For general reviews on MOFs see chapter 1 and (a) Yaghi, O. M.; O’Keeffe, M.; Ockwig, N. W.; Chae, H. K.; Eddaoudi, M.; Kim, J. *Nature* **2003**, *423*, 705. (b) Eddaoudi, M.; Kim, J.; Rosi, N.; vodak, D.; Wachter, J.; O’Keeffe, M.; Yaghi, O. M. *Science* **2002**, *295*, 469. (c) O’Keeffe, M.; Yaghi, O. M. *Chem. Rev.* **2012**, *112*, 675.

(16) Wang, Z.; Chen, G.; Ding, K. *Chem. Rev.* **2009**, *109*, 322.

(17) Bawaked, S.; Dummer, N. F.; Dimitratos, N.; Bethell, D.; He, Q.; Kiely, C. j.; Hutchings, G. J. *Green Chem.* **2009**, *11*, 1037.

(18) (a) Zhang, W.; Deng, W.; Wang, Y. *Chem. Commun.* **2011**, 9275. (b) Rodriguez, J. A.; Stacchiola, D. *Phys. Chem. Chem. Phys.* **2010**, *12*, 9557.

(19) (a) Corma, A.; Garcia, h.; Llabrés, I.; Xamena, F. X. *Chem. Rev.* **2010**, *110*, 4606.

(b) Gomez–Lor, b.; Gutierrez–Puebla, E.; Iglesias, M.; Monge, M. A.; Ruiz–Valero, C.; Snejko, N. *Inorg. Chem.* **2002**, *41*, 2429.

(20) SMART (version 6.532). *Program for Bruker CCD X–ray Diffractometer Control*, Bruker AXS Inc., Madison, WI, **2005**.

- (21) SAINT+ (version 6.45). *Program for Reduction of Data Collected on Bruker CCD Area Detector Diffractometer*, Bruker AXS Inc., Madison, WI, **2003**.
- (22) Sheldrick, G. M. SADABS, version 2.10, *Program for Empirical Absorption correction of Area Detector Data*, University of Göttingen, **2007**.
- (23) Sheldrick, G. M. SHELXTL, version 6.15, *Program Package for Structure Solution and Refinement*, Bruker Analytical X-ray Systems, Inc., Madison, WI, **2008**.
- (24) Speck, A. . *J. App. Cryst.* **2003**, 36, 7.
- (25) Han, J. H.; Yoo, S. -K.; Seo, J. S.; Hong, S. J.; Kim S. K.; Kim, C. *Dalton Tans.* **2005**, 36, 402.
- (26) (a) Brown, I. D.; Altermatt, D. *Acta Cryst.* **1985**, 244. (b) Thorp, H. H. *Inorg. Chem.* **1992**, 31, 1585.
- (27) *Material Studio* (version 4.3): *Program for Molecular Modeling and Analysis*; Accelrys Software Inc.
- (28) <http://www.ccdc.am.ac.uk/products/mercury/>
- (29) (a) Schardt, B. C.; Hollander, F. J.; Hill, C. L. *J. Am. Chem. Soc.* **1982**, 104, 3964. (b) Schardt, B. C.; Hollander, F. J.; Hill, C. L. *Chem. Commun.* **1981**, 17, 765.
- (30) (a) Sheldon, R. A.; Kochi, J. k. *Metal-Catalyzed Oxidants of Organic Compounds* Academic Press, New York, **1981**, Chapter 2. (b) Shing, T. K. M.; Yeung, Y. Y.; Su, P. L. *Org. Lett.* **2006**, 8, 3149. (c) Lee, S. H.; Xu, L.; Park, B. K.; Mironov, Y. V.; Kim, S. H.; Song, Y. J.; kim C.; Kim Y.; Kim, S. -J. *Chem. Eur. J.* **2010**, 16, 4678. (d) Song, Y. J.; Lee, S. H.; Park, H. M.; Kim, S. H.; Goo, H. G.; Eom, G. H.; Lee, J. H.; Lah, S.; Kim, Y.; Kim, S. -J.; Lee, J. E.; Lee, H. -I.; Kim, C. *Chem. Eur. J.* **2011**, 17, 7336.

(31) (a) Groves, J. T.; Stern, M. K. *J. Am. Chem. Soc.* **1988**, *110*, 8628. (b) Groves, J. T.; Stern, M. K. *J. Am. Chem. Soc.* **1987**, *109*, 3812.

(32) Bortolini, O.; Meunier, B. *Perkin Trans.* **1984**, *2*, 1967.

CHAPTER 10

PORPHYRIN PADDLEWHEEL FRAMEWORK NANOSHEETS THROUGH EXFOLIATION

10.1 Introduction

Bulk crystals of MOFs have seen great success for storage, separations, sensors, size- and shape-selective catalysis and molecular recognition.¹⁻⁴ However, sensors, catalytic devices and other related nanotechnological devices and applications using porous materials depend critically on the availability of thin films and their integration with other components such as electrodes. This is still a major challenge and not yet well studied. In addition, understanding the roles played by the nanoscale size and by the interfacial conditions in integrated systems in defining the properties of such porous solids can lead to optimization of their potential functionalities.⁵⁻⁷

In the rational design of thin film MOF materials, one large concern is to avoid the tendency of molecules to closely aggregate in order to stabilize their intermolecular assembly. This is observed in self-assembled monolayers.^{5,8} This would destroy the sought after porous properties of the material and possibly impede on the functionality of the materials used as well. There are a number of ways to successfully implement thin films on substrates. Recently there have been a number of bottom-up approaches which have seen success.^{5,9-11}

Among these approaches is electrochemical deposition. Dincă and coworkers have successfully synthesized thin films of MOF-5 crystals on conductive surfaces

through a cathodic electrodeposition technique commonly used in metal oxide and hydroxide films.⁹ This technique requires the electrochemical generation of hydroxide anions by the reduction of water or oxoanions such as NO_3^- and ClO_4^- . Cathodic generation of HO^- creates a pH gradient near the electrodes surface needed for the deprotonation of the carboxylic acid functional groups needed to begin nucleation of MOF-5. The growth of MOF-5, thus, happens directly on the electrode surface. While it is indeed successful in growing MOF-5 on a fluorine-doped tin oxide working electrode, the orientation of the crystal growth is not well controlled. Additionally, the films created are on the magnitude of 10 μm —too thick for many nanotechnology applications. Finally it suffers from contamination by plating of zinc from the zinc nitrate source intended to be used to create the Zn_4O secondary building unit (SBU) in MOF-5.

Hupp *et al.* developed a thin film of the chemically robust and thermally stable zeolitic imidazolic framework, ZIF-8, through a simple immersion technique in which a glass or silicon substrate was immersed into a solution containing the building units.¹⁰ It was shown that thin film is finished growing around 30 minutes and around 50 nm. Thicker films could also be obtained by repeating the process with fresh solutions. These films were successful in small molecule sensing by changes in the refractive index of the material when introduced to different chemical species. While this technique is very successful, it also suffers from lack of control of the orientation of crystal growth which would impede many electronic applications.

Kitagawa *et al.* has been highly successful in creating ultrathin (≤ 20 nm) MOF films using a modified Langmuir–Blodgett/layer-by-layer method.⁵ For this they use tetra-(carboxy-phenyl) substituted porphyrins along with the paddlewheel SBUs and

pyrazine to create 2 dimensional porphyrin paddlewheel layers (similar to those made in PPF structures) on a monolayer by monolayer basis on silicon substrates. The axial positions of the paddlewheel units and also the metalloporphyrins of each monolayer are capped by pyrazine ligands. As more monolayers are introduced, the pyrazine ligands act as a directing agent, ordering the layers due to π - π stacking interactions between other pyrazine ligands. This method is very successful in creating highly oriented, ultrathin films for use in sensing and nanoelectronics. Control over layer stacking, however, is impeded because pillaring linkers cannot be used in this method which would impede on the monolayer by monolayer growth. The layer stacking then is only controlled by weak π - π and can only obtain a staircase arrangement. Having the ability to include pillars in order to obtain different stacking arrangements could enhance porosity for sensing or catalytic applications.

As a continuing effort to produce thin film MOF material for nanodevices, we have explored a “top-down” method of exfoliating PPF-crystals through sonication for the creation of 2D PPF nanosheets with very high aspect ratios (Figure 10.1). This method is very popular for other 2D materials such as graphene. Graphene layers within graphite can be intercalated with potassium metal to separate the layers and disrupt inter-layer interactions and then exfoliated in ethanol to form a dispersion of carbon sheets.¹² Additional sonication of these materials can even afford carbon nanoscrolls. These sheets of graphene are very thin, often monolayers, and can have very large aspect ratios ($> 1\mu\text{m}$). Indeed other layered material such as layered double hydroxide (LDH) material can be successfully exfoliated by soaking in water creating ultrathin (2–5 nm) sheets with in-plane dimensions of 200-500 nm.¹³

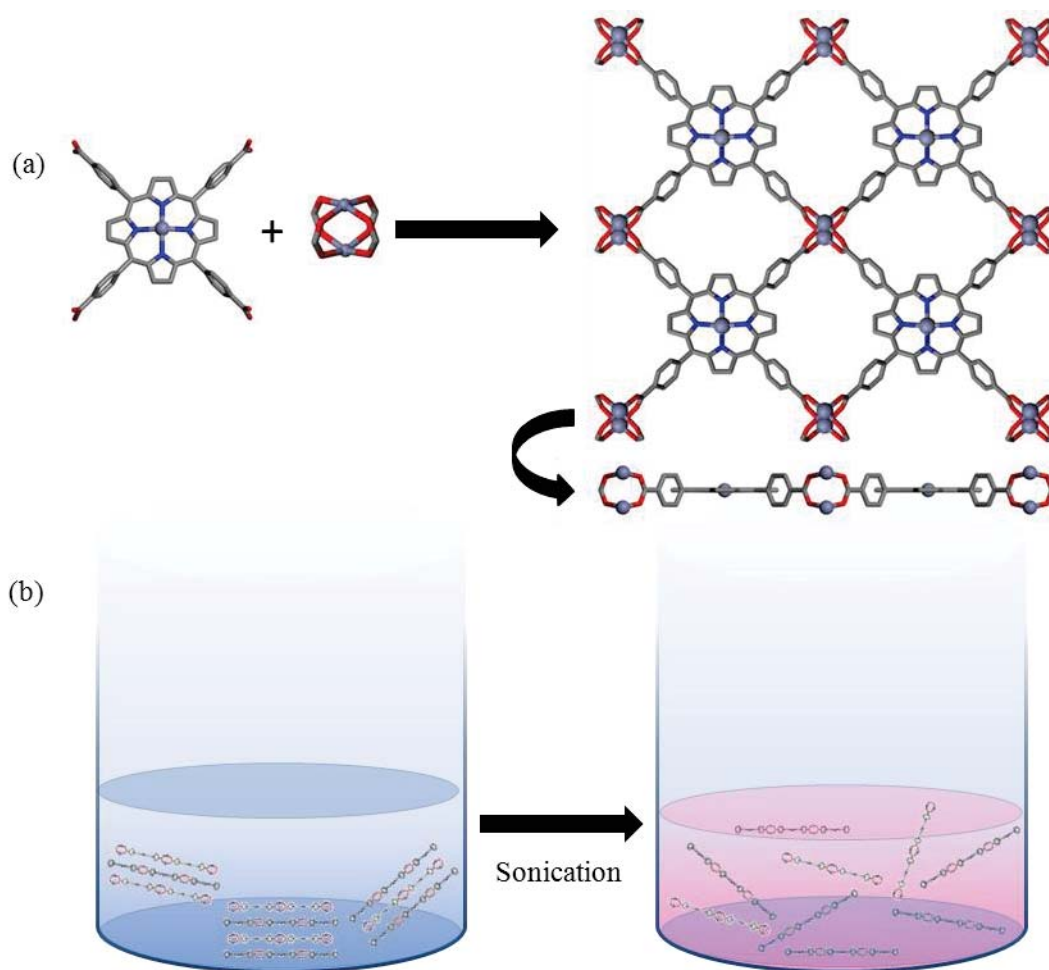


Figure 10.1. (a) The combination of porphyrin and paddlewheel SBUs creates the 2D PPF layers. (b) Synthetic strategy to create nanosheets through a top down exfoliation process by sonicating 2D layered PPF crystals.

10.2 Experimental Methods

PPF-1 A mixture of 5,10,15,20-tetrakis(4-carboxyphenyl)porphyrin (TCPP) (7.9 mg, 0.01 mmol), zinc nitrate hexahydrate (8.9 mg, 0.03), and pyrazine (1.6 mg, 0.02 mmol) were added to a mixture of *N,N*-diethyl formamide (DEF) (1.5 mL) and ethanol (0.5 mL) in a capped vial and heated to 80 °C for 24 hrs, followed by slow-cooling to room temperature over 9 hrs. Purity of the resulting PPF-1 phase was confirmed by powder X-ray diffraction.

PPF-100 A mixture of 5,10,15,20-tetrakis(4-carboxyphenyl)-Mn(III)-porphyrin chloride (Mn-TCPPCl)(8.8 mg, 0.01 mmol), zinc nitrate hexahydrate (6.0 mg, 0.02), and 1.0 M nitric acid in ethanol (30 μ L, 0.03 mmol) were added to a mixture of *N,N*-dimethyl formamide (DMF) (1.5 mL) and ethanol (0.5 mL) in a capped vial and heated to 60 °C for 72 hrs, followed by slow-cooling to room temperature over 9 hrs. Purity of the resulting PPF-100 phase was confirmed by powder X-ray diffraction.

PPF-27 A mixture of filtered crystals of PPF-1 (14.7 mg, 0.01 mmol) and 4,4'-bipyridine (BPY) (3.2 mg, 0.02 mmol) were added to a mixture of DEF (1.5 mL) and ethanol (0.5 mL) in a capped vial, swirled by hand to mix, and left to react at room temperature typically for ~ 2hrs. Purity of the resulting PPF-27 phase was confirmed by powder X-ray diffraction.

X-ray powder diffraction (PXRD):

Data was collected on a Rigaku D/Max-B X-ray diffractometer with Bragg-Brentano parafocusing geometry, a diffracted beam monochromator, and a conventional copper target X-ray tube set to 35 KV and 25 mA. The PXRD patterns of the suspended nanosheets was performed by depositing a drop of MOF/mother liquor onto the X-ray

stage and heating gently on a hot plate to remove the solvent. The process was repeated until there was a thick film on the stage for investigation. The resulting experimental PXRD patterns were compared to simulated patterns obtained from the single crystal structures using Mercury software.¹⁴

Scanning Electron Microscopy (SEM):

Data was collected on a Hitachi S4700 Field-Emission SEM set at 15 kV. Samples were chrome coated for better imaging using a Cressington 108 auto sputter coater.

Atomic Force Microscopy (AFM):

Data was collected on a Dimension 3100 SPM system in contact mode ($\sigma = 1.05$ nm). A droplet of MOF/mother liquor was deposited on a clean (sonicated in acetone and ethanol each for 10 min., then washed with DI water and air dried) Si wafer, then let air dry for investigation.

Exfoliation Process:

Filtered crystal samples of PPF-1, PPF-100, or PPF-27 were added to 5 mL of DEF in a capped vial and sonicated typically ~3 hrs. The resulting suspension was then centrifuged to sediment the larger particles, and decanted. The nanosheet suspension was further diluted with additional DEF for microscopy.

10.3 Results and Discussion

In this investigation into creating PPF nanosheets by exfoliation, three 2D layered structures were chosen: PPF-1, PPF-100, and PPF-27. PPF-1 and PPF-100 were assembled through a traditional solvothermal synthesis.¹⁵ PPF-27 was assembled through a sequential self-assembly approach (see Chapter 4).¹⁶ The purity of all samples was confirmed by PXRD (Figures 10.2, 10.3, and 10.4). PPF-1 is a 2D layered structure assembled from Zn-TCPP and $\text{Zn}(\text{COO})_4$ paddlewheel SBU. PPF-1 is AB stacked in which the zinc ion within the porphyrin core of one layer lies directly above the zinc ion in the paddlewheel of the next layer (Figure 10.2). The layers are separated by solvent molecules at a distance of 8.5 Å. PPF-100 is assembled from Mn-TCPPCl and $\text{Zn}(\text{COO})_4$ paddlewheel SBU to form a 2D grid pattern which is slightly puckered and shows a ‘staircase’ stacking pattern in which each layer is shifted by 5.8 Å laterally (Figure 10.3). The interlayer spacing in PPF-100 is 5.9 Å – much smaller than that of PPF-1. PPF-27 is an AB stacked 2D bilayer structure in which two neighboring layers are connected by BPY pillars. The inter-bilayer distance in PPF-27 is 8.4 Å and held apart by solvent guest molecules (Figure 10.4).

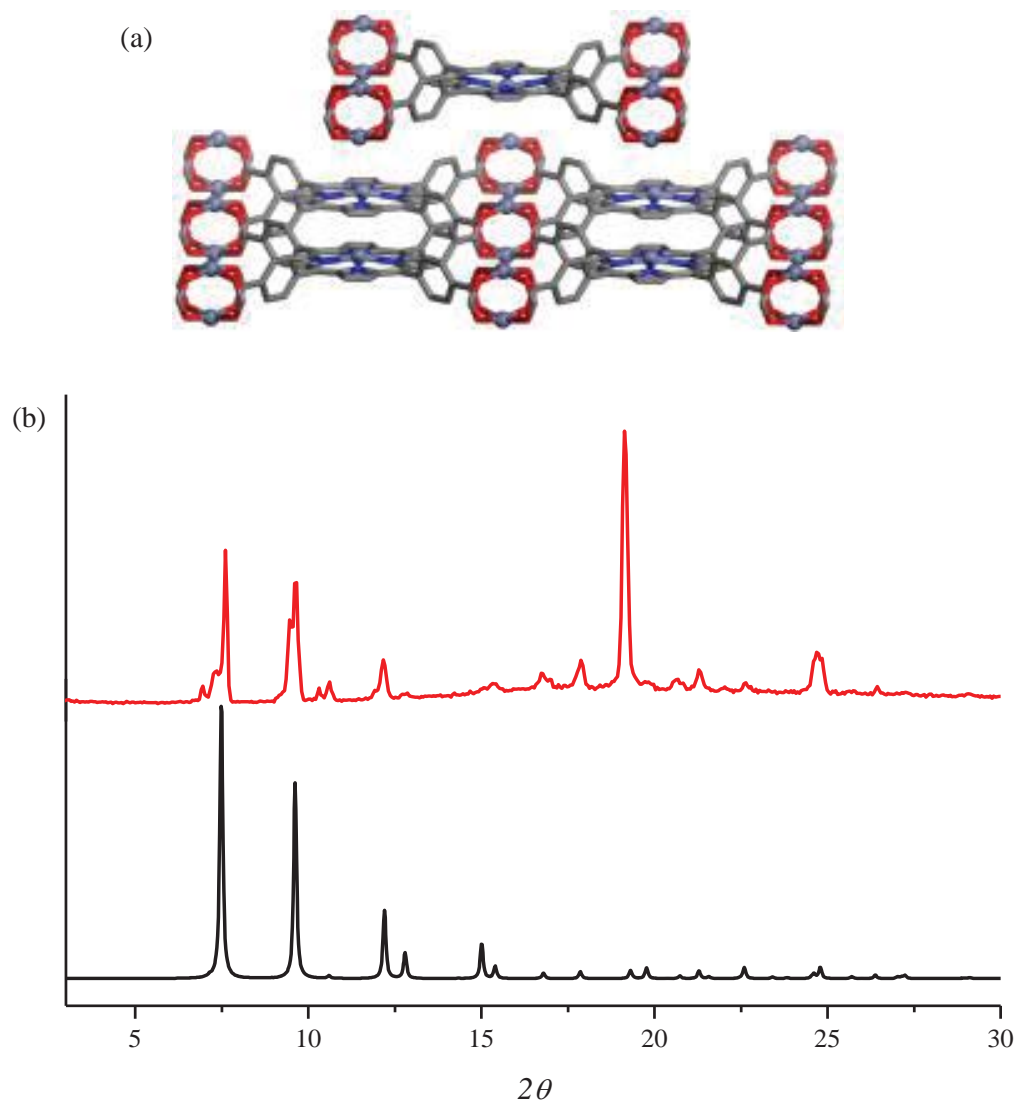


Figure 10.2. (a) Representation of single crystal structure of PPF-1. (b) Simulated (bottom) and experimental (top) PXRD patterns for PPF-1.

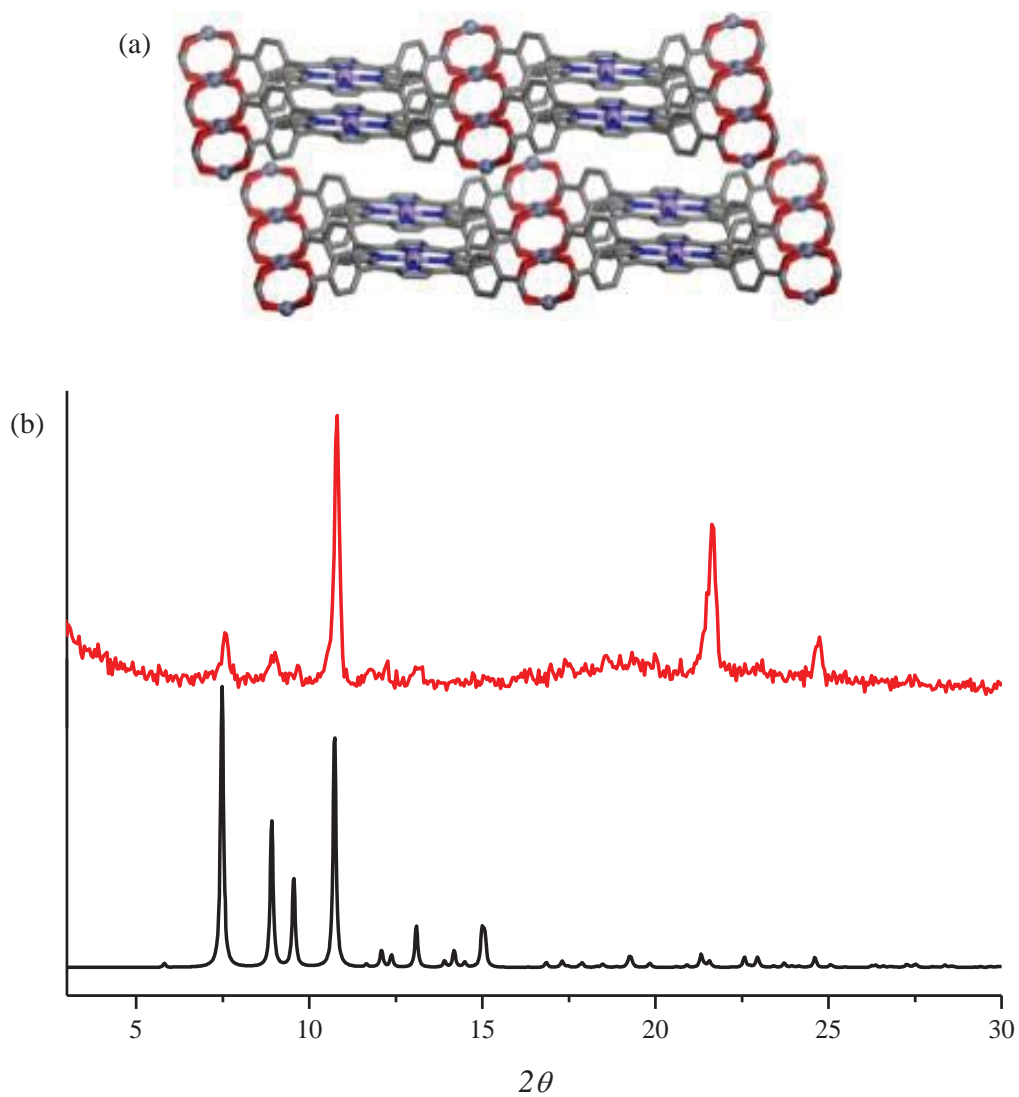


Figure 10.3. (a) Representation of single crystal structure of PPF-100. (b) Simulated (bottom) and experimental (top) PXRD patterns for PPF-100.

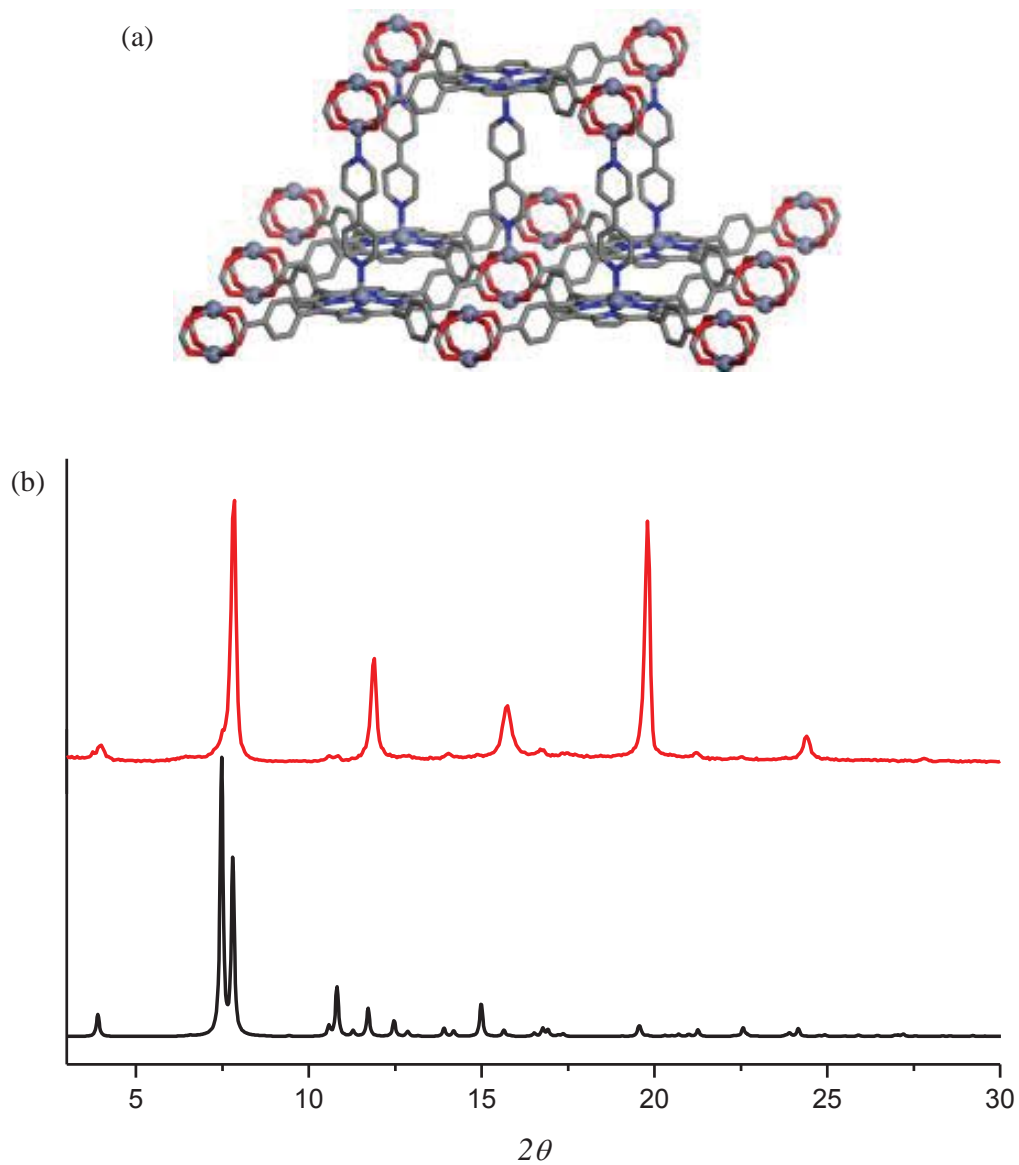


Figure 10.4. (a) Representation of single crystal structure of PPF-27. (b) Simulated (bottom) and experimental (top) PXRD patterns for PPF-27.

Samples of PPF-1, PPF-100, and PPF-27 were introduced to a vial containing DEF solvent. Qualitative tests were performed with PPF-1 to choose the appropriate solvent for exfoliation (see appendix A1.8 for details). To aid in the exfoliation process, the samples were sonicated for ~3 hrs. The resulting suspensions for all samples appeared pink and nontransparent. Indeed, all samples exhibit the Tyndall effect. It should be noted that this process does not produce uniform particles. Upon letting the samples sit, many larger particles began to sink to the bottom of the vial. In order to separate the larger particles, the samples were centrifuged and the nanosheet suspension was decanted off. The samples were then investigated by PXRD, SEM, and AFM.

The exfoliation of PPF-1 produced sub-micron particles comprised of many layers. SEM images show irregularly shaped, stepped particles with an average length and width between 0.6 and 1.5 μm (Figure 10.5). The different layers shown in the images indicate that the layers aren't completely exfoliated to monolayers, and that through the exfoliation process, the 2D PPF square grid sheets are also broken. PXRD of PPF-1 shows that the particles are still highly crystalline after exfoliation (Figure 10.6). The 2θ peaks are slightly shifted after exfoliation indicating a decrease in interlayer spacing from 8.8 \AA to 6.9 \AA . AFM images also show stepped particles with a thickness of 3–4 nm corresponding to ~6 PPF-1 layers in each sheet/step, and in-plane dimensions of 1–1.5 μm (Figure 10.5). A typical height profile of a nanosheet with an aspect ratio of ~250 is shown in Figure 10.5. Additionally, the AFM image shows one sheet in the beginning stages of curling around onto itself creating a nanoscroll. This feature is also observed in graphene nanosheets through a sonication assisted exfoliation process.¹²

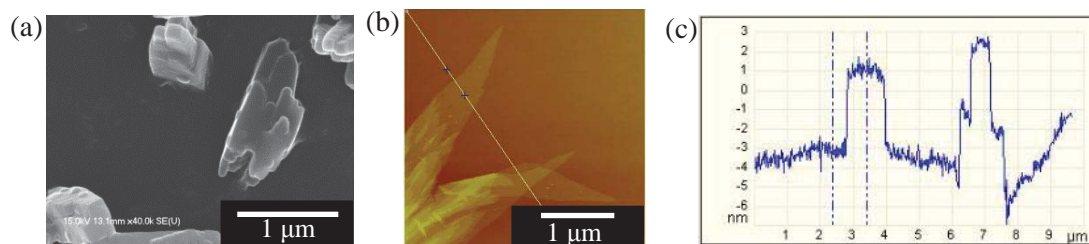


Figure 10.5. (a) SEM image of exfoliated PPF-1 particles. (b) AFM image of exfoliated PPF-1 particles. (c) The height profile corresponding to the particle marked in (b).

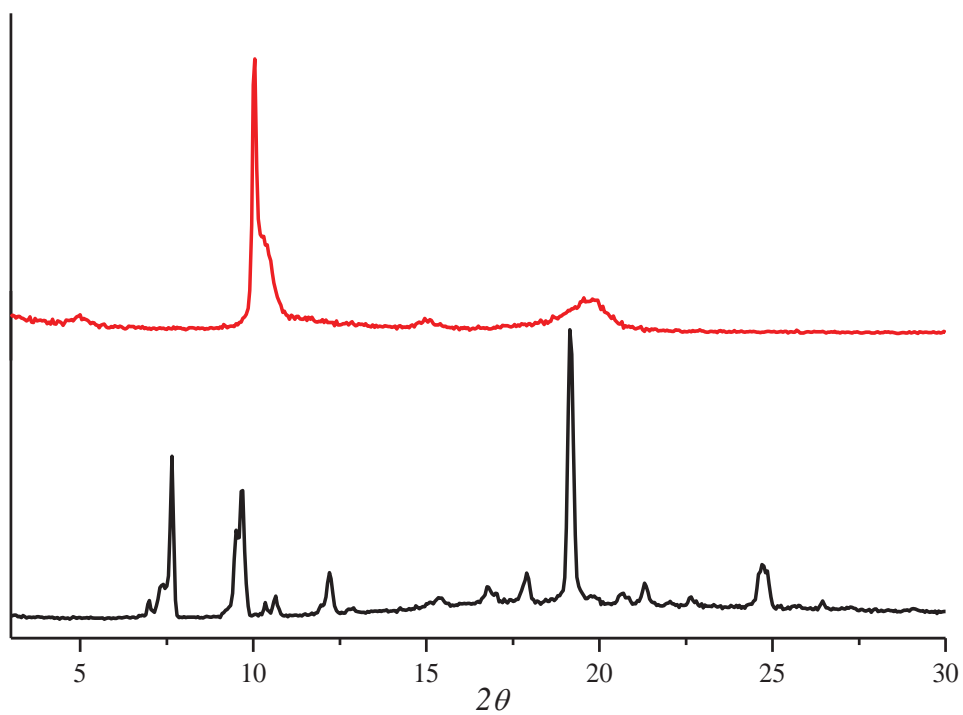


Figure 10.6. Powder X-ray diffraction of PPF-1 before (below) and after (above) sonication.

Investigation of the exfoliated products of PPF-100 show small very small particles. SEM images show particles the size of 200 nm wide and thick (Figure 10.7). Upon further investigation, individual layers within these particles can be observed, showing evidence that upon sonication, the individual layers were not fully exfoliated. Additionally the particles are much smaller than that of PPF-1. This may be due to the smaller interlayer distance observed in PPF-100 over PPF-1. An increase in the amount of solvent molecules between layers of the material disrupts any intermolecular attraction between layers, making it easier to exfoliate. Often with graphene, potassium ions are intercalated between the layers and then reacted with ethanol to separate the graphene layers.¹² In the PPFs, solvent can be thought of as an intercalate to separate the individual layers for better exfoliation. Indeed, analysis of the PXRD of PPF-100 particles show the interlayer distance is still very small (6.6 Å) (Figure 10.8). AFM images also show particles having in-plane dimensions of 200 nm and a thickness of 4.8 nm corresponding to 7 layers of PPF-100 in each nanosheet (Figure 10.7). A typical height profile of a nanosheet with an aspect ratio of ~ 40 is shown in Figure 10.7.

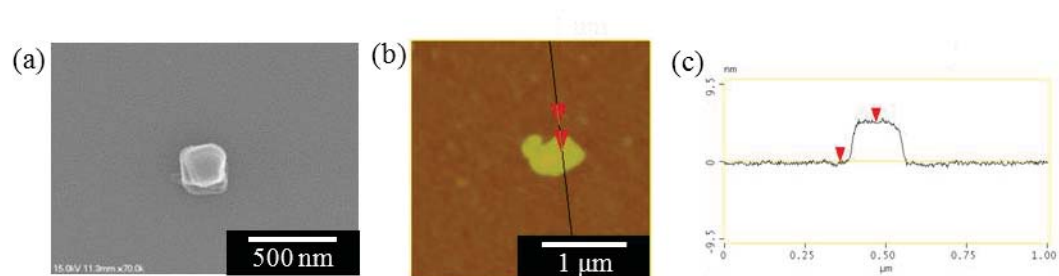


Figure 10.7. (a) SEM image of exfoliated PPF-100 particles. (b) AFM image of exfoliated PPF-100 particles. (c) The height profile corresponding to the particle marked in (b).

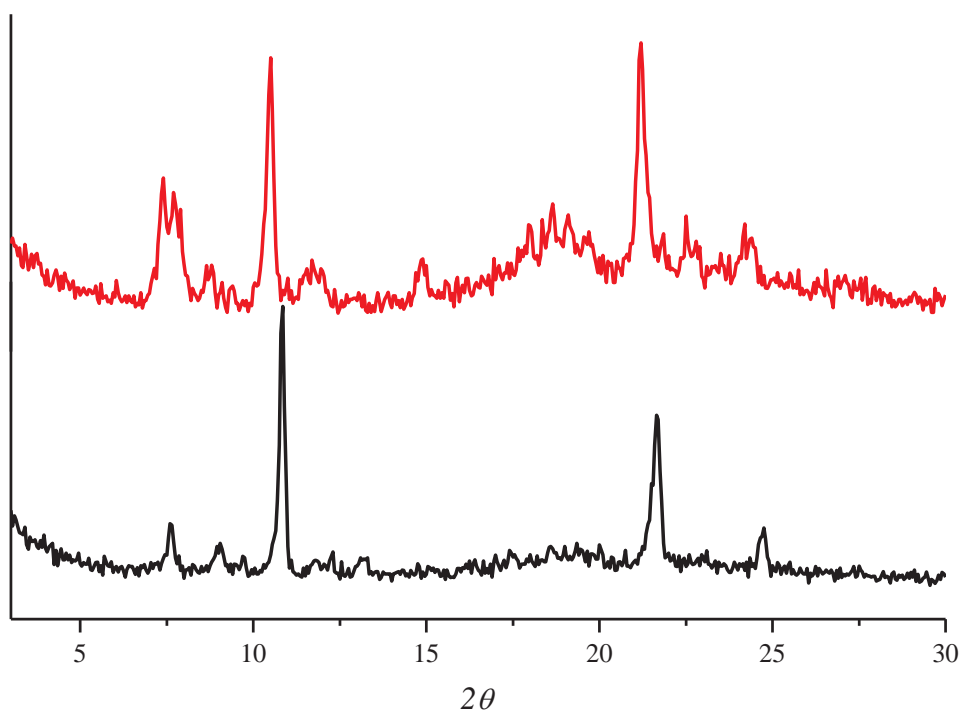


Figure 10.8. Powder X-ray diffraction of PPF-100 before (below) and after (above) sonication.

SEM images of the exfoliation product of PPF-27 shows square platelet particles with a length of ~ 300 nm (Figure 10.9). While the overall crystal morphology is retained for this system, the particle size is significantly reduced and the product particles have rounded corners indicating that there is still significant destruction of the 2D square grid PPF layers upon sonication. PXRD shows that the crystallinity is very well maintained and that the inter bilayer spacing only changes by a small amount (from 8.4 \AA to 9.1 \AA) (Figure 10.10). Investigating the exfoliation product of PPF-27 also shows square platelet particles. Figure 10.9 shows a slightly destroyed square particle that has an in-plane length of 1.7 \mu m and a depth of 6.2 nm which corresponds to only 3 layers of PPF-27 per nanosheet particle (data summarized in Table 10.1). The aspect ratio of such a particle is ~ 270 —the largest of all three samples. Additionally, exfoliation to only 3 layers was achieved for the PPF-27 system with the morphology well retained. By covalently attaching two subsequent layers together by BPY pillars to make a bilayer has increased the mechanical strength of the 2D sheets, allowing for such a high aspect ratio and small amount of layers present in the particles.

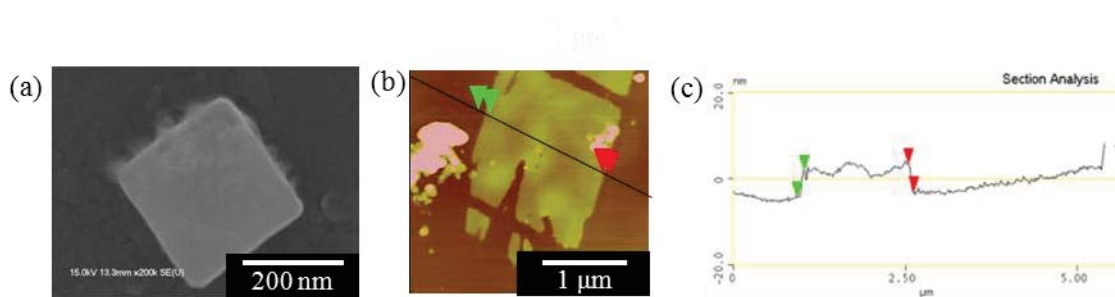


Figure 10.9. (a) SEM image of exfoliated PPF-27 particles. (b) AFM image of exfoliated PPF-27 particles. (c) The height profile corresponding to the particle marked in (b).

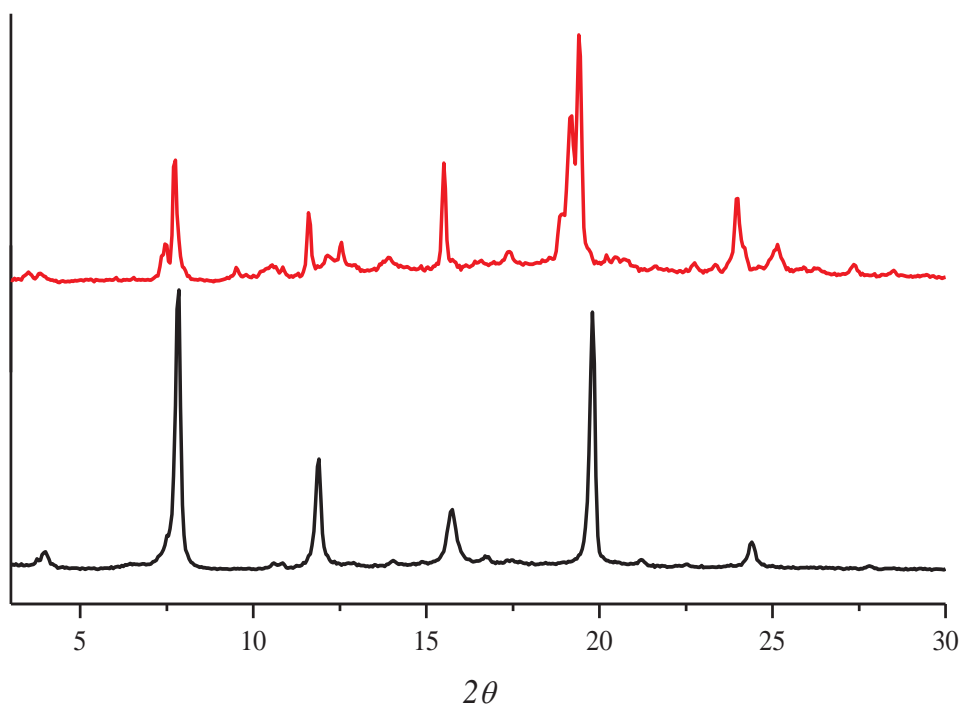


Figure 10.10. Powder X-ray diffraction of PPF-27 before (below) and after (above) sonication.

Table 10.1. Comparison of # of PPF layers in the nanosheets of PPF-1, PPF-100, and PPF-27.

Structure	Thickness of nanosheet (nm)^a	Thickness of each PPF layer (nm)	# of PPF layers in nanosheet
PPF-1	4.0	0.72	6
PPF-100	4.8	0.69	7
PPF-27	6.2	2.07	3

^aData obtained from height profile of corresponding AFM images.

10.4 Conclusions

We have demonstrated a new top–down method to obtain high aspect ratio nanosheets of porphyrinic MOF material through an exfoliation process by solution sonication. This technique has been well established for other 2D materials such as graphene, LDHs, and aluminophosphates, but has not been studied in MOF material. Along with making nanosheets of PPFs, there is preliminary evidence that this technique could also be adapted to create nanoscrolls of these materials. The ability to effectively exfoliate layers without disrupting the 2D layers is a function of the initial interlayer spacing as evidenced by the difference in exfoliation of PPF-1 and PPF-100. The best system for this technique, however, is the bilayer structure PPF-27, wherein there is a relative strengthening effect by connecting two layers together to achieve high aspect ratio nanosheets. While this work is still in its infancy, this demonstrates that a top–down method can be an effective route to achieve thin film MOF materials for nanodevices.

10.5 References

- (1) Férey, G. *Chem. Soc. Rev.* **2008**, *37*, 191.
- (2) Seo, J. S.; Whang, D.; Lee, H.; Jun, S. I.; Oh, J.; Jin, Y.; Kim, K. *Nature* **2000**, *404*, 982.
- (3) Kitagawa, S.; Kitaura, R.; Noro, S. *Angew. Chem. Int. Ed.* **2004**, *43*, 2334.
- (4) Li, Q.; Zhang, W.; Miljanić, O. Š.; Sue, C. –H.; Zhao, Y. –L.; Liu, L.; Knobler, C. B.; Stoddart, J. F.; Yaghi, O. M. *Science* **2009**, *325*, 855.
- (5) (a) Makiura, R.; Motoyama, S.; Umemura, Y.; Yamanaka, H.; Sakata, O.; Kitagawa, H. *Nature Mater.* **2010**, *9*, 565. (b) Makiura, R.; Kitagawa, H. *Eur. J. Inorg. Chem.* **2010**, *2010*, 3715. (c) Motoyama, S.; Makiura, R.; Sakata, O.; Kitagawa, H. *J. Am. Chem. Soc.*

- 2011**, *133*, 5640. (d) Xu, G.; Yamada, T.; Otsubo, K.; Sakaida, S.; Kitagawa, H. *J. Am. Chem. Soc.* **2012**, *134*, 16524.
- (6) Zachner, D.; Shekhah, O.; Wöll, D.; Fischer, R. A. *Chem. Soc. Rev.* **2009**, *38*, 1418.
- (7) Choi, M.; Na, K.; Kim, J.; Sakamoto, Y.; Terasaki, O.; Ryoo, R. *Nature* **2009**, *461*, 246.
- (8) Kind, M.; Wöll, C. *Prog. Surf. Sci.* **2009**, *84*, 230.
- (9) Li, M.; Dincă, M. *J. Am. Chem. Soc.* **2011**, *133*, 12926.
- (10) (a) Lu, G.; Hupp, J. T. *J. Am. Chem. Soc.* **2010**, *132*, 7832. (b) Lu, G.; Farha, O. K.; Zhang, W.; Huo, F.; Hupp, J. T. *Adv. Mater.* **2012**, *24*, 3970.
- (11) Shekhah, O.; Fu, L.; Sougrat, R.; Belmabkhout, Y.; Cairns, A. J.; Giannelis, E. P.; Eddaoudi, M. *Chem. Commun.* **2012**, *48*, 11434.
- (12) Viculis, L. M.; Mack J. J.; Kaner, R. B. *Science* **2003**, *299*, 1361.
- (13) Manohara, G. V.; Kamath, P. V.; Milius, W. *J. Solid State Chem.* **2012**, *196*, 356.
- (14) <http://www.ccdc.cam.ac.uk/products/mercury>
- (15) Choi, E. -Y.; Wray, C. A.; Hu, D.; Choe, W. *CrystEngComm* **2009**, *11*, 553.
- (16) Burnett, B. J.; Barron, P. M.; Hu, C.; Choe, W. *J. Am. Chem. Soc.* **2011**, *133*, 9984.

CHAPTER 11

FINAL THOUGHTS AND FUTURE DIRECTIONS

11.1 Quaternary Structures

Traditionally, MOFs are considered ‘simple’ structures because they are constructed from a small number of building units: a metal ion SBU, and one or two organic ligands. It is important to design more complex MOFs using multiple building units with complementary functionalities to create more functional materials. This is a daunting task, however, because attempts to increase the number of building units in MOFs generally lead to mixed phase materials, instead of single phase of mixed units with very few examples to the contrary. Yaghi *et al.* were successful in creating a single phase MOF-5–type structure with up to eight different benzene dicarboxylate derivatives.¹ This lone example shows the possibility of incorporating multiple ligands into the same phase, however there was no control as to the where the linkers were actually in the crystal. The functional groups were randomly distributed within the solid, limiting the functionality of the material as a whole. A better way would be to have absolute control over each of the building units, thus complementary functionalities could be systematically constructed close to each other. SSA could be a great avenue for doing this. In Chapters 3 and 4, we discussed the ability to exchange or insert organic linkers into PPFs, creating ternary (having three components: porphyrin metalloligand, paddlewheel SBU, and dipyriddy pillar) structures. We envision two design routes to obtain PPFs with quaternary structures. For the first design, targeted linker replacement

would be employed (Figure 11.1). As shown in chapter 3, the ABBA stacked PPF-18 readily exchanges its lengthy DPNI pillars with BPY to create PPF-4 showing a large contraction in the crystallographic c dimension. The ABBA stacked PPF-18 was characterized by having two separate stacking connections: an AB porphyrin-to-paddlewheel connection, and an AA paddlewheel-to-paddlewheel connection. This creates two different bonding environments. In Chapter 2, we discussed that in a previously published work, if a methylated bipyridine pillar was used in PPF synthesis, only AA paddlewheel-to-paddlewheel connection was observed because of the steric hindrance of the methyl group to the porphyrin plane.² If a methylated bipyridine pillar was used as the exchanging pillar for PPF-18, it would potentially only target the AA paddlewheel-to-paddlewheel connection, leaving the AB porphyrin-to-paddlewheel layer alone. This would create a new quaternary phase that had alternating pillaring, with precise control of the position of all building units in the material.

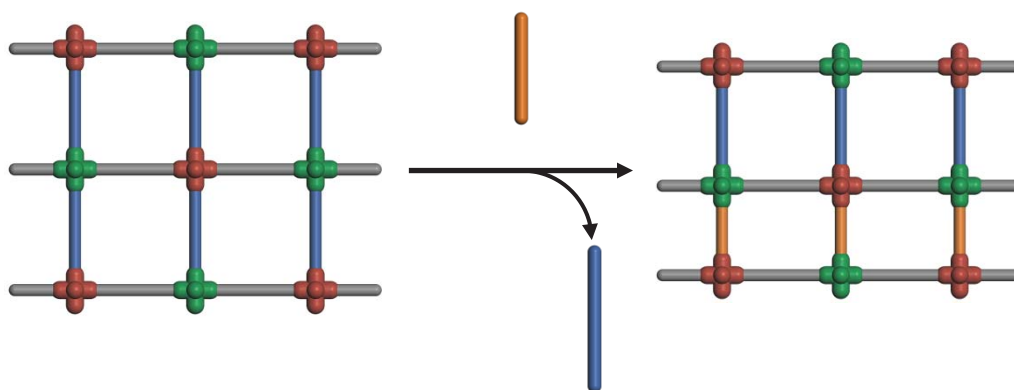


Figure 11.1. Schematic representation of selective linker replacement to obtain a quaternary structure.

The second route would employ the linker insertion reaction (Figure 11.2). In Chapter 4, the AB stacked 2D bilayer structure PPF-27 was constructed by inserting BPY pillars in between every other layer of the 2D layered structure PPF-1. If crystals of PPF-27 were immersed again in a BPY solution, further coordination was observed to create the fully pillared 3D framework PPF-4. This showed the stepwise manner in which we could insert pillars into PPF structures. If crystals of PPF-27 were immersed in a different dipyrridyl solution, it is possible to have that pillar insert into the remaining layers creating a new quaternary structure that had alternating pillaring, again with precise control of the position of all building units. We have tried this with the longer DPT and DPNI linkers, but did not observe any new phase (see chapter 4). This does not prove that this transformation cannot happen; however it suggests that there may be a need for special synthetic conditions to successfully insert the second pillaring unit.

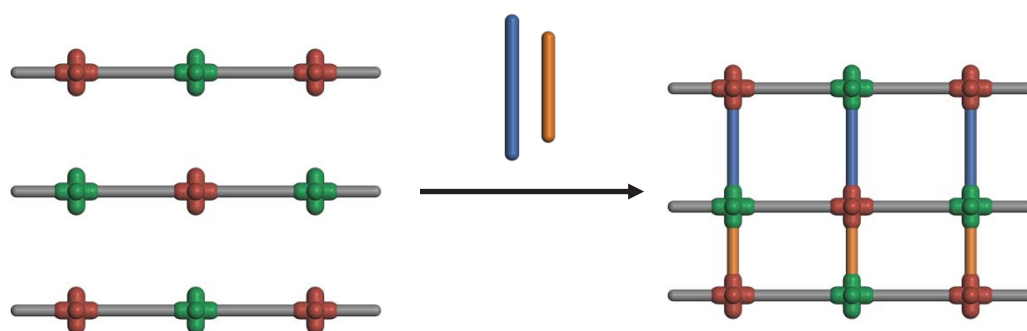


Figure 11.2. Schematic representation of linker insertion reaction to obtain a quaternary structure.

11.2 Multi-fluorophore PPFs

The use of MOF material as an explosive vapor sensor via a fluorescence quenching mechanism was discussed in Chapter 6. An important property for these materials is to identify which explosive vapor is being detected. Suslick *et al.* has developed a colorimetric sensor array which can successfully identify a wide range of toxic gasses and vapors.³ This array methodology is successful because it employs many different sensors which interact with the analyte in a unique way, effectively creating a distinct sensing pattern for each analyte. A new way to accomplish identification of different analytes would be to incorporate multiple fluorophores into a single MOF structure creating array-type sensing within one material. Hupp *et al.* created a porphyrin-based MOF which contains two fluorescent organic ligands.⁴ While this system indeed includes two different fluorescent molecules, the fluorescence of one ligand, bodipy, is quenched by transferring energy to Zn-porphyrin. Thus, only the fluorescence of Zn-porphyrin is observable, making this system non-ideal for identification of explosives. A new possible structure could be constructed with an anthracene-based pillar and Zn-porphyrin. As discussed in Chapter 6, Zn-porphyrins will quench in the presence of nitroaromatic compounds. Anthracene-based pillars also quench in the presence of these compounds.⁵ Thus, incorporating both ligands into the same MOF could be used for the identification of explosive analytes.

We synthesized crystals of a new PPF structure which contains 9,10-bis(pyridine-4-ylethynyl)anthracene (DPEA) and Zn-TCPP via a traditional solvothermal method (Figure 11.3). This new structure, PPF-35, is indeed fluorescent, and shows fluorescence characteristic to both DPEA and Zn-TCPP indicating that both

ligands act independently of each other (Figure 11.4). Crystals of PPF-35 were used to detect different nitroaromatics, but did not quench. This is believed to be from lack of sufficient activation of the pores. Further work is needed to optimize PPF-35 for nitroaromatic explosive detection and identification.

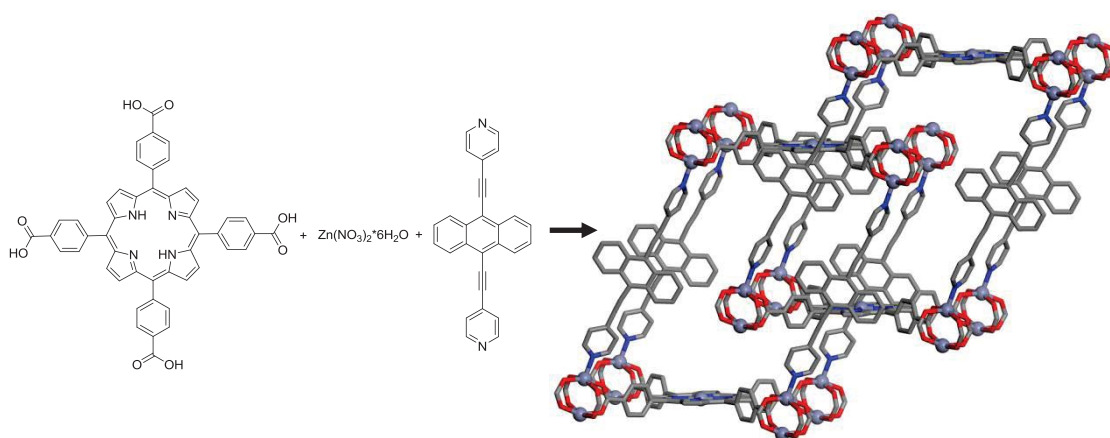


Figure 11.3. Synthesis of PPF-35 from DPEA, TCPP, and $\text{Zn}(\text{NO}_3)_2 \cdot 6\text{H}_2\text{O}$.

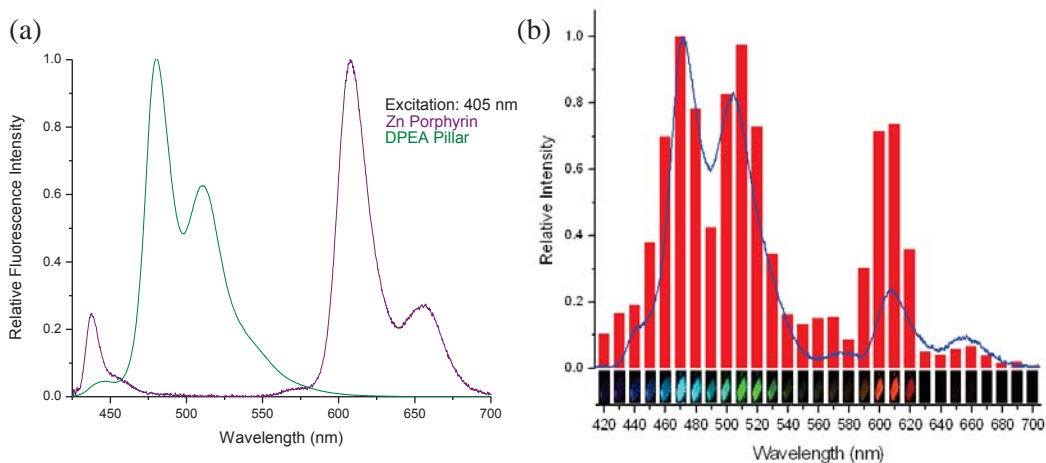


Figure 11.4. (a) Fluorescence spectra of DPEA (green) and Zn-TCPP (purple). (b) Bottom: Fluorescence microscope images of PPF-35 crystals (150 μm in length) above their corresponding emission wavelength. Top: Relative fluorescence emission intensity of each fluorescence image (red columns). Fluorescence emission from suspension (blue line) is added for comparison purposes.

11.3 ABBA Stacked Fe PPFs through Core–Shell Growth

As discussed in Chapter 2, one of the reasons to use metalloligands in MOFs is to increase the interaction between the pore walls and guest molecules. One model from nature that could be adopted for MOFs is that of myoglobin. Oxygen is bound to the ferrous heme iron in myoglobin with greater affinity than hemoglobin because of the coordination geometry of the heme iron.⁶ The heme iron is coordinated from a single axial histidine which increases the binding association on the other axial position tenfold.⁷ In order to achieve this biomimetic structure, iron porphyrin needs to be arranged in an ABBA stacking pattern. This arrangement, however, is extremely hard to achieve in PPFs. As discussed in chapter 2, the stacking pattern in PPFs is mainly dictated by the preferred coordination geometry of the porphyrin. Iron porphyrin will coordinate twice axially creating an AB pattern if there are excess amounts of BPY pillar in the synthesis. In chapter 8, we discussed that the AA stacking pattern can be achieved with metals like manganese and iron if there is a limiting amount of BPY pillar used in the synthesis, discouraging the further coordinated AB stacking pattern. The ABBA stacking pattern, however, has still not been seen with iron porphyrin. A new technique to create ABBA stacked iron porphyrin frameworks would be to create a core structure of PPF-4 (an ABBA stacked zinc porphyrin framework) and subsequently growing iron porphyrin framework shell structure on it. The stacking of the core PPF-4 will act as a template for the stacking of the iron porphyrin shell structure, creating an ABBA stacked framework.

I synthesized core PPF-4 crystals through a solvothermal synthesis of TCPP, zinc nitrate hexahydrate, BPY pillar, and excess benzaldehyde. The benzaldehyde was

included in the synthesis to compete with TCPP for the coordination to the zinc ions which make the paddlewheel complex. Traditionally, crystals of PPF-4 have large a and b axes corresponding to the 2D square grid PPF layers. By including benzaldehyde in the synthesis, the resulting crystals have an elongated c axis (Figure 11.5). This is important for the growing of iron porphyrin shell. Ideal shell growth would happen on the crystallographic a and b axes, where the stacking arrangement is controlled. Growth along the crystallographic c axis could still yield either an AB or AA stacking arrangement. By heating a solution containing the core PPF-4 crystals and the building units for shell growth (iron porphyrin, zinc nitrate, and BPY pillar) at slightly lower temperatures than normal solvothermal growth, shell growth is favored over nucleation of a new phase.⁸ We tried initial shell growth experiments, which didn't work, indicating that much more research is needed in this area.

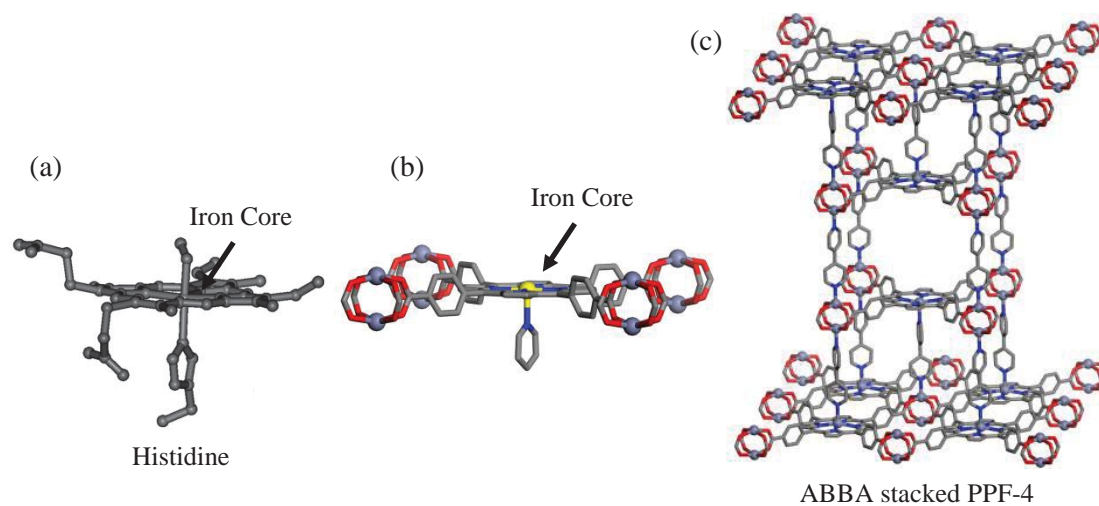


Figure 11.5. (a) Structure of heme within myoglobin.⁶ (b) Structure of five coordinate iron porphyrin. (c) ABBA stacking pattern in PPF-4 to obtain five coordinate iron porphyrin.

11.4 Enzymatic Cascade through Oriented Attachment Growth

As we discussed in Chapters 1 and 2, MOFs have been studied for use in catalysis for the development of cleaner and more efficient chemical processes. These materials are highly effective for having large internal surface area with multiple internal functional centers for catalysis. The next generation of MOF catalysts will mimic biological enzymatic systems. One important improvement for these materials would be to design multiple catalytic centers in a sequential manner within the same crystals to be able to perform enzymatic-like cascade reactions. Enzymatic cascade reactions combine several enzymatic transformations in concurrent one-pot processes.⁹ These types of reactions offer considerable advantages over step-by-step catalysis reactions such as a reduced demand of time, cost and chemicals for product recovery. Additionally, reactions in which the intermediates are unstable or toxic become possible since these intermediates do not accumulate but are transformed further into the final product. One requirement for this type of reaction is for the multiple catalytic centers to be close together, to fully transform the reactants to products without the intermediates traveling a long distance.

Building this type of catalysis in MOFs is possible through an oriented attachment growth mechanism. First a pillared paddlewheel MOF will be constructed using a dicarboxylate ligand, $Zn_2(COO)_4$ paddlewheel SBU, and a functional dipyriddy ligand which corresponds to one step within the cascade reaction. Second, this MOF will be immersed in a solution containing the same dicarboxylate ligand, zinc source, and a different functional ligand corresponding to the second step within the cascade reaction. Heating this solution will result in the growth of the new MOF on a specific face of the initial MOF because of the lattice matching of both MOFs due to the same dicarboxylate

ligand (Figure 11.6).⁸ Thus, the two catalytic centers will be incorporated into the same crystal, making it a great candidate for enzymatic-like cascade reactions.

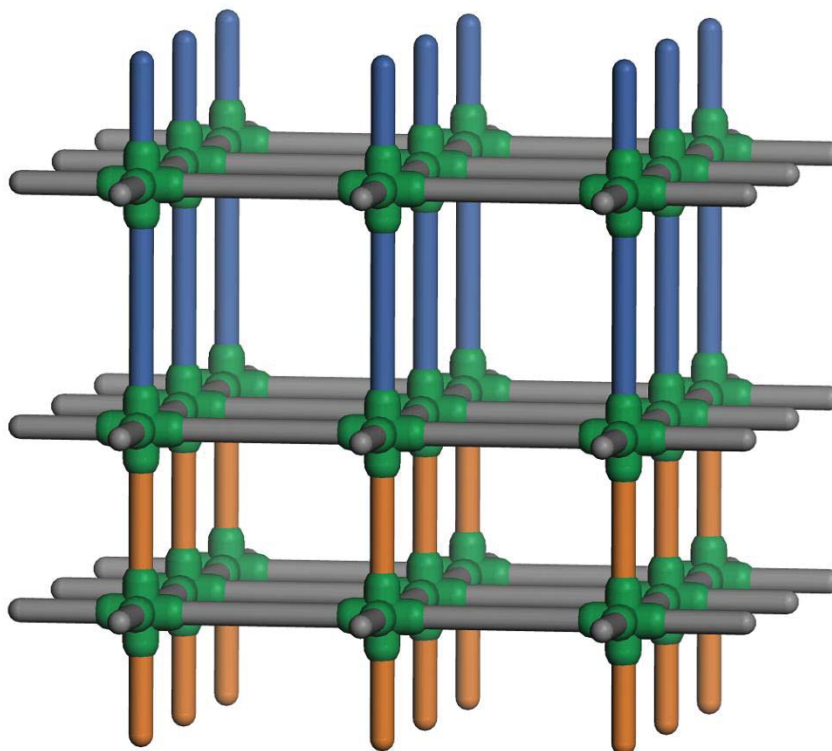


Figure 11.6. Schematic illustration of MOF constructed with two distinct functional pillars (depicted as blue and orange rods) created by oriented attachment growth for enzymatic-like cascade reactions.

11.5 References

- (1) Deng, H.; Doonan, C. J.; Furukawa, H.; Ferreira, R. B.; Towne, J.; Knobler, C. B.; Wang, B.; Yaghi, O. M. *Science* **2010**, *327*, 846.
- (2) Barron, P. M.; Wray, C. A.; Hu, C.; Guo, Z.; Choe, W. *Inorg. Chem.* **2010**, *49*, 10217.
- (3) (a) Janzen, M. C.; Ponder, J. B.; Bailey, D. P.; Ingison, C. K.; Suslick, K. S. *Anal. Chem.* **2006**, *78*, 3591. (b) Lim, S. h.; Feng, L.; Kemling, J. W.; Musto, C. J.; Suslick, K. S. *Nature Chem.* **2009**, *1*, 562. (c) Feng, L.; Musto, C. J.; Kemling, J. W.; Lim, S. H.; Suslick, K. S. *J. Am. Chem. Soc.* **2010**, *132*, 4046.
- (4) Lee, C. Y.; Farha, O. K.; Hong, B. J.; Sarjeant, A. A.; Nguye, S. T.; Hupp, J. T. *J. Am. Chem. Soc.* **2011**, *133*, 15858.
- (5) Zyryanov, G. V.; Palacios, M. A.; Anzenbacher, P. *Org. Lett.* **2008**, *10*, 3681.
- (6) Brunori, M.; Bourgeois, D.; Vallone, B. *J. Struct. Bio.* **2004**, *147*, 223.
- (7) Antonini, E.; Brunori, M. *Hemoglobin and Myoglobin in their Reactions with Ligands*, 1st ed.; North Holland Publishing Co: Amsterdam, 1971.
- (8) Furukawa, S.; Hirai, K.; Takashima, Y.; Nakagawa, K.; Kondo, M.; Tsuruoka, T.; Sakata, O.; Kitagawa, S. *Chem. Commun.* **2009**, *45*, 5097.
- (9) Ricca, E.; Brucher, B. Schrittwieser, J. H. *Adv. Synth. Catal.* **2011**, *353*, 2239.

APPENDIX

A1. Chapter 2 Data

Table A1.1. Summary of Porphyrinic Metal–Organic Framework Compounds

	Compound Formula ^b	Common Name	Dimensionality	Reference
1	[(CdNO ₃) ₂ (PdTPyP)]·(H ₂ O)		3D	1
2	[(ZnTPyP)]·(CH ₃ OH)·(H ₂ O)		3D	2
3	[(ZnTPyP)]·(H ₂ O)		3D	2
4	[Cu(CuTPyP)]·(BF ₄)		3D	3
5	[Cu(CuTCyP)]·(BF ₄)		3D	3
6	[PbI ₂ (H ₂ TPyP)]		2D	4
7	[PbI ₂ (Ni _{0.3} TPyP)]		2D	4
8	[PbI ₂ (Zn _{0.5} TPyP)]		2D	4
9	[CdI ₂ (H ₂ TPyP)]		2D	4
10	[CdI ₂ (Zn _{0.2} TPyP)]		2D	4
11	[CdI ₂ (Cu _{0.1} TPyP)]		2D	4
12	[(MnTPyP)]·10(H ₂ O)	SMTP-1(Mn)	3D	5
13	[(CoTPyP)]·2(CH ₃ COOH)·2(H ₂ O)	SMTP-1(Co)	3D	5
14	[(MnTPyP)]·2(C ₂ H ₅ OH)·4(H ₂ O)	SMTP-1(Mn)	3D	5
15	[Cu(TPyP)]·(Cu ₂ Mo ₃ O ₁₁)		3D	6
16	[Fe(TPyP)]·2(Mo ₆ O ₁₉)·38(H ₂ O)		3D	6
17	[(NaC ₇ H ₅ O ₂)(H ₂ TCPP)]·3(C ₉ H ₁₀ O ₂)		2D	7
18	[Zn(ZnTCPP)]		2D	7
19	[Zn(TPyP)]·5(C ₆ H ₅ NO ₂)		2D	8
20	[Pb(NO ₃) ₂ (H ₂ TPyP)]·C ₆₀ ·1.5(C ₂ H ₂ Cl ₄)		2D	9
21	[Pb(NO ₃) ₂ (H ₂ TPyP)]·C ₇₀		2D	9
22	[(Cu ₂ (CH ₃ COO) ₄) ₂ (CuTIOPP)]		2D	10
23	[(Co ₃)(CoTCPP)]	PIZA-1	3D	11
24	[(FeTPyP)]		2D	12
25	[(FeTPyP)]		2D	12
26	[Ag ₄ (H ₂ TPyP) ₃]·(NO ₃) ₄		2D	13
27	[Ag ₂ (H ₂ TPyP)(NO ₃)](NO ₃)		3D	13
28	[Ag ₈ (ZnTPyP) ₇ (H ₂ O) ₂](NO ₃) ₈		3D	13
29	[Zn ₄ O(<i>trans</i> -ZnDCPP) ₃]	PIZA-4	3D	14
30	[(MnTCPP)]·(C ₃ H ₇ NO)·2.55(H ₂ O)		2D	15
31	[(Zn(H ₂ O) ₂) ₂ (PtTCPP)]		2D	16
32	[(Zn(H ₂ O) ₂) ₂ (PdTCPP)]		2D	16
33	[(Cu ₂ V ₂ O ₂ (O ₃ PC ₆ H ₅) ₄)(CuTPyP)]·2(H ₂ O)		3D	17
34	[(V ₄ O ₄ (O ₃ PC ₆ H ₅) ₄)(NiTPyP)]·2(H ₂ O)		3D	17
35	[AgSO ₃ CF ₃] ₂ (H ₂ TPyP)]		2D	18
36	[(Ag(C ₆ H ₆ ClN) ₂)(H ₂ TPyP)]·2(C ₇ H ₇ SO ₃)		2D	18
37	[(Ag ₂ C ₆ H ₆ ClN)(ZnTPyP) ₂]·2(SO ₃ CF ₃)		2D	18
38	[(AgC ₇ H ₇ SO ₃) ₂ (ZnTPyP)]·(C ₄ H ₉ NO)		2D	18
39	[(<i>trans</i> -ZnDPyP) ₃]·(C ₂ H ₅ OH)		3D	19
40	[Ni ₃ O ₈ (NiTCPP)]		3D	20
41	[HgI ₂ (3-H ₂ TPyP)]·C ₆₀		2D	21
42	[Co ₃ (CoTCPP) ₂]	PIZA-2	3D	22
43	[Mn ₃ (MnTCPP) ₂]·(C ₃ H ₇ NO)	PIZA-3	3D	22
44	[Pr ₂ (C ₂ O ₄)(H ₂ TCPP)]		3D	23
45	[Dy ₄ (H ₂ TCPP) ₃]·2(C ₃ H ₇ NO)·4(H ₂ O)		3D	23
46	[Nd ₄ (H ₂ TCPP) ₃]·2(C ₃ H ₇ NO)·4(H ₂ O)		3D	23
47	[Cu ₂ (C ₂ H ₃ O ₂)(CuTPyP)]		2D	24
48	[Cd(H ₂ TPyP)(SH) ₂]		3D	25
49	[CdI ₂ (CdTPyP)]		3D	25

50	[Cd(CdTPyP) ₂ (SC ₂ H ₅ O) ₂] · 2(C ₃ H ₇ NO)		2D	25
51	[<i>trans</i> -ZnDPyDIPP]		2D	26
52	[(<i>trans</i> -ZnDPyDCyP) ₃] · 2(H ₂ O)		3D	27
53	[(<i>trans</i> -ZnDPyDMPP) ₃]		3D	27
54	[(<i>trans</i> -ZnDPyDTFMPP) ₃]		3D	27
55	[Tm(3-H ₂ TCPP)]		2D	28
56	[Ce ₃ (H ₂ TCPP) ₂](NO ₃)		3D	28
57	[Co ₂ (<i>cis</i> -ZnDCPP)(C ₁₀ H ₈ N ₂)] · (H ₂ O) · 4(C ₃ H ₇ NO)	PPF-6- Zn/Co	2D	29
58	[Zn ₂ (<i>cis</i> -ZnDCPP)(C ₁₀ H ₈ N ₂)]	PPF-6-Zn/Zn	2D	29
59	[MnCl ₂ (H ₂ TPyP)] · 6(C ₂ H ₂ Cl ₄)		2D	30
60	[Zn ₂ (ZnTCPP)]	PPF-1-Zn/Zn	2D	31
61	[Co ₂ (CoTCPP)]	PPF-1-Co/Co	2D	31
62	[Co ₂ (CoTCPP)(C ₁₀ H ₈ N ₂) ₂]	PPF-3-Co/Co	3D	32
63	[Zn ₂ (ZnTCPP)(C ₁₀ H ₈ N ₂) _{1.5}]	PPF-4	3D	32
64	[Co ₂ (PdTCPP)(C ₁₀ H ₈ N ₂)]	PPF-5-Pd/Co	3D	32
65	[Zn ₂ (MnTCPP)(C ₁₀ H ₈ N ₂) ₂](NO ₃)	PPF-3-Mn/Zn	3D	33
66	[Co ₂ (MnTCPP)(C ₁₀ H ₈ N ₂) ₂](NO ₃)	PPF-3-Mn/Co	3D	33
67	[Zn ₂ (FeTCPP)(C ₁₀ H ₈ N ₂) ₂](NO ₃)	PPF-3-Fe/Zn	3D	33
68	[Co ₂ (FeTCPP)(C ₁₀ H ₈ N ₂) ₂](NO ₃)	PPF-3-Fe/Co	3D	33
69	[Co ₂ (PtTCPP)(C ₁₀ H ₈ N ₂)]	PPF-5-Pt/Co	3D	33
70	[Zn ₂ (NiTCPP)(C ₁₀ H ₈ N ₂)]	PPF-5-Ni/Zn	3D	33
71	[Zn ₂ (VTCPP)(O)(C ₁₀ H ₈ N ₂)]	PPF-5-V=O/Zn	3D	33
72	[Zn ₂ (ZnTCPP)(C ₁₂ H ₈ N ₆)]	PPF-18	2D	34
73	[Zn ₂ (ZnTCPP)(C ₁₂ H ₈ N ₆)]	PPF-19	3D	34
74	[Zn ₂ (ZnTCPP)(C ₁₂ H ₈ N ₆) _{1.5}]	PPF-20	3D	34
75	[Zn ₂ (ZnTCPP)(C ₂₄ H ₁₂ N ₄ O ₄)]	PPF-21	2D	34
76	[Zn ₂ (ZnTCPP)(C ₂₄ H ₁₂ N ₄ O ₄) _{1.5}]	PPF-22	3D	34
77	[Zn ₂ (<i>trans</i> -ZnDCPP)(C ₁₀ H ₈ N ₂)]	PPF-25	3D	35
78	[ZnTPEP]		2D	36
79	[Zn ₂ (C ₃₄ H ₁₈ O ₈)(DPyDFPP)]	ZnPO-MOF	3D	37
80	[(3-ZnTPyP) ₂] · 2(C ₃ H ₇ NO)	MPF-3	2D	38
81	[(ZnTPyP)]		2D	39
82	[(Cu(C ₅ HO ₂ F ₆) ₂)(CuTPyP)]		2D	40
83	[ZnCl ₂ (ZnTPyP)] · 3(C ₂ H ₂ Cl ₄)		2D	41
84	[ZnBr ₂ (ZnTPyP)] · 3(C ₂ H ₂ Cl ₄)		2D	41
85	[Zn ₂ (ZnTCPP)(C ₁₂ H ₁₂ N ₂)]	PPF-11-Zn/Zn	3D	42
86	[Co ₂ (CoTCPP)(C ₁₂ H ₁₂ N ₂)]	PPF-11-Co/Co	3D	42
87	[Zn ₂ (MnTCPP)(C ₁₂ H ₁₂ N ₂)]	PPF-11-Mn/Zn	3D	42
88	[Zn ₂ (FeTCPP)(C ₁₂ H ₁₂ N ₂)]	PPF-11-Fe/Zn	3D	42
89	[Zn ₂ (ZnTCMOPP)] · 5(C ₃ H ₇ NO)		2D	43
90	[(3-CoTPyP) ₂]		2D	44
91	[(3-CoTPyP) ₂] · 2(C ₃ H ₇ NO)		2D	44
92	[(CdCl ₂) ₂ (3-H ₂ TPyP) ₂]		3D	44
93	[(CdCl ₂) ₄ (3-CdTPyP) ₄]		3D	44
94	[(Cu ₂) ₂ (3-CuTPyP)]		3D	44
95	[CuCl ₄ (3-CuTPyP)]		3D	45
96	[CuI ₄ (3-CuTPyP)]		3D	45
97	[MnCl ₃ (3-MnTPyP) ₂]		3D	45
98	[Zn ₂ (ZnTCPP)(C ₁₀ H ₈ N ₂)]	PPF-27	2D	46
99	[CdI ₂ (H ₂ TPyP)]	HMOF-1	3D	47
100	[Cu ₂ (CuBPDCP) ₂]	MMPF-1	3D	48
101	[Cd _{1.25} (PdTCPP)] · (H ₂ O) · 2(DMF)		3D	49
102	[Zn(HCOO) ₂ (SnTPyP)] · 4(NO ₃) · (C ₃ H ₇ NO) · 4(H ₂ O)		3D	50
103	[Zn ₂ (ZnTCPP)(<i>trans</i> -ZnDPyDFPP)]	ZnZn-RPM	3D	51
104	[Zn ₂ (ZnTCPP)(<i>trans</i> -MnDPyPFPP)]	ZnMn-PRM	3D	51
105	[Zn ₂ (AlTCPP)(<i>trans</i> -ZnDPyPFPP)]	AlZn-RPM	3D	51
106	[Zn ₂ (PdTCPP)(<i>trans</i> -MnDPyPFPP)]	PdMn-RPM	3D	51
107	[Zn ₂ (FeTCPP)(<i>trans</i> -ZnDPyPFPP)]	FeZn-RPM	3D	51
108	[Zn ₂ (FeTCPP)(<i>trans</i> -MnDPyPFPP)]	FeMn-RPM	3D	51
109	[Zn ₂ (ZnTCPP)(C ₂₉ H ₂₅ N ₄ BF ₂)]	BOP MOF	3D	52
110	[Fe(NiTCPP)](Li)	MIL-141(Li)	3D	53
111	[Fe(NiTCPP)](Na)	MIL-141(Na)	3D	53

112	[Fe(NiTCPP)](K)	MIL-141(K)	3D	53
113	[Fe(NiTCPP)](Rb)	MIL-141(Rb)	3D	53
114	[Fe(NiTCPP)](Cs)	MIL-141(Cs)	3D	53
115	[Zn ₄ (OH) ₂ (H ₂ O) ₂ (ZnTCPEP) ₂ (C ₆ H ₆ N ₂) ₂] · 2(C ₃ H ₇ NO) · 10.5(H ₂ O)		3D	54
116	[HSm(VTPPS)(O)]		3D	55
117	[(FeTCPP)]		2D	56
118	[Cd(MnTPyP)(C ₂ H ₇ NO) ₄ (PW ₁₂ O ₄₀)] · 2(C ₂ H ₇ NO) · 5(H ₂ O)		2D	57
119	[Cd(H ₂ O)(C ₄ H ₁₂ N)(H ₂ TCPP)] · 4(C ₅ H ₁₁ NO) · H ₂ O		2D	58
120	[Cd(H ₂ O)(C ₄ H ₁₂ N)(FeTCPP)] · 2(C ₅ H ₁₁ NO) · H ₂ O		2D	58
121	[Cd(H ₂ O)(C ₄ H ₁₂ N)(CoTCPP)] · 4(C ₅ H ₁₁ NO) · H ₂ O		2D	58
122	[Cd(H ₂ O)(C ₄ H ₁₂ N)(NiTCPP)] · 2(C ₅ H ₁₁ NO) · H ₂ O		2D	58
123	[Cd(H ₂ O)(C ₄ H ₁₂ N)(CuTCPP)] · 2(C ₅ H ₁₁ NO) · H ₂ O		2D	58
124	[Cd(H ₂ O)(C ₄ H ₁₂ N)(ZnTCPP)] · 2(C ₅ H ₁₁ NO) · H ₂ O		2D	58
125	[Cd(H ₂ O)(C ₄ H ₁₂ N)(PcTCPP)] · 2(C ₅ H ₁₁ NO) · H ₂ O		2D	58
126	[Cd ₂ (C ₄ H ₁₂ N) ₂ (FeTCPP) ₂ (O)]		3D	58
127	[Pb ₂ (H ₂ TCPP)] · 4(C ₃ H ₇ NO) · H ₂ O		3D	59
128	[Pb ₂ (CoTCPP)(H ₂ O)(C ₃ H ₇ NO)] · 1.5(C ₃ H ₇ NO)		3D	59
129	[Pb ₂ (NiTCPP)(C ₃ H ₇ NO)(H ₂ O)] · 1.5(C ₃ H ₇ NO) · 2(H ₂ O)		3D	59
130	[Pb ₂ (CuTCPP)(C ₃ H ₇ NO)(H ₂ O)] · 1.5(C ₃ H ₇ NO) · 2(H ₂ O)		3D	59
131	[Pb ₂ (VTCPP)(O)(H ₂ O) ₂] · 4(C ₃ H ₇ NO)		3D	59
132	[(Co ₃ (OH)(H ₂ O)) ₄ (CoTDCPP) ₃] · 20(H ₂ O) · 22(CH ₃ OH) · 25(C ₄ H ₉ NO)	MMPF-2	3D	60
133	[(Zr ₆ (OH) ₄ (O) ₄ (H ₂ TCPP) ₃]	MOF-525	3D	61
134	[(Zr ₆ (OH) ₄ (O) ₄ (FeTCPPCl) ₃]	MOF-525-Fe	3D	61
135	[(Zr ₆ (OH) ₄ (O) ₄ (CuTCPP) ₃]	MOF-525-Cu	3D	61
136	[(Zr ₆ O ₈ (H ₂ TCPP) ₂] · 8(H ₂ O)	MOF-545	3D	61
137	[(Zr ₆ O ₈ (FeTCPPCl) ₂] · 8(H ₂ O)	MOF-545-Fe	3D	61
138	[(Zr ₆ O ₈ (CuTCPP) ₂] · 8(H ₂ O)	MOF-545-Cu	3D	61
139	[(Mn ₅ Cl ₂)(MnTDCPP)(Cl)(C ₃ H ₇ NO) ₄ (H ₂ O) ₄] · 2(C ₃ H ₇ NO) · 8(CH ₃ COOH) · 14(H ₂ O)	ZJU-18	3D	62
140	[(Mn ₅ Cl ₂)(NiTDCPP)(H ₂ O) ₈] · 7(C ₃ H ₇ NO) · 6(CH ₃ COOH) · 11(H ₂ O)	ZJU-19	3D	62
141	[(Cd ₅ Cl ₂)(MnTDCPP)(Cl)(H ₂ O) ₆] · 13(C ₃ H ₇ NO) · 2(CH ₃ COOH) · 9(H ₂ O)	ZJU-20	3D	62
142	[(AlOH) ₂ (H ₂ TCPP)] · 3(C ₃ H ₇ NO) · 2(H ₂ O)	Al-PMOF	3D	63
143	[(AlOH) ₂ (ZnTCPP)]		3D	63
144	[Zr(OH) ₈ (H ₂ TCPP)]	PCN-222	3D	64
145	[Zr(OH) ₈ (ZnTCPP)]	PCN-222(Zn)	3D	64
146	[Zr(OH) ₈ (CuTCPP)]	PCN-222(Cu)	3D	64
147	[Zr(OH) ₈ (NiTCPP)]	PCN-222(Ni)	3D	64
148	[Zr(OH) ₈ (CoTCPP)]	PCN-222(Co)	3D	64
149	[Zr(OH) ₈ (MnTCPP)]	PCN-222(Mn)	3D	64
150	[Zr(OH) ₈ (FeTCPP)]	PCN-222(Fe)	3D	64
151	[(Zn ₂) ₈ (ZnTDCPP) ₆ (NO ₃) ₈] · 6(C ₂ H ₆ SO) · 25(H ₂ O)	MMPF-4	3D	65
152	[(Cd ₂) ₅ (CdTDCPP) ₆ (H ₃ O) ₈] · 36(C ₂ H ₆ SO) · 11(H ₂ O)	MMPF-5	3D	65
153	[Cu ₂ (<i>trans</i> -ZnBPDCP)] · 6.5(C ₃ H ₇ NO) · 3.5(H ₂ O)		3D	66
154	[Cu ₂ (<i>trans</i> -NiBPDCP)] · 4.5(C ₃ H ₇ NO) · 4.5(H ₂ O)		3D	66
155	[Cu ₂ (<i>trans</i> -PdBPDCP)] · 3.5(C ₃ H ₇ NO) · 6.5(H ₂ O)		3D	66
156	[Cu ₂ (<i>trans</i> -MnBPDCP)(NO ₃)] · 3.5(C ₃ H ₇ NO) · 5(H ₂ O)		3D	66
157	[Cu ₂ (<i>trans</i> -RuBPDCP)(CO)] · 5(C ₃ H ₇ NO) · 5(H ₂ O)		3D	66
158	[Co ₂ (<i>trans</i> -CoDCDBP)(H ₂ O) ₅] · 6(H ₂ O) · 12(C ₂ H ₅ OH) · 12(C ₃ H ₇ NO)	MMPF-3	3D	67
159	[Zn ₂ (H ₂ O) ₂ (ZnTBCPPP)(H ₂ O) ₂] · (C ₃ H ₇ NO) · 6(H ₂ O)	UNLPPF-1	3D	68

^asorted by year of publication. ^bsee list of abbreviations.

List of Abbreviations for Table A1.1:

TPP = 5,10,15,20-tetraphenylporphyrin

TPyP = 5,10,15,20-tetra(4-pyridyl)porphyrin

3-TPyP = 5,10,15,20-tetra(3-pyridyl)porphyrin

TCyP = 5,10,15,20-tetra(4-cyanophenyl)porphyrin

TIOPP = 5,10,15,20-tetra(3-isonicotinoyl)porphyrin

TCPP = 5,10,15,20-tetra(4-carboxyphenyl)porphyrin

3-TCPP = 5,10,15,20-tetra(3-carboxyphenyl)porphyrin

trans-DCPP = 5,15-di(4-carboxyphenyl)-10,20-diphenylporphyrin

trans-DPyP = 5,15-di(4-pyridyl)-10,20-diphenylporphyrin

cis-DCPP = 5,10-di(4-carboxyphenyl)-15,20-diphenylporphyrin

trans-DPyDIPP = 5,10-di(4-pyridyl)-10,20-di(4-iodophenyl)porphyrin

trans-DPyDCyP = 5,10-di(4-pyridyl)-10,20-di(4-cyanophenyl)porphyrin

trans-DPyDMPP = 5,10-di(4-pyridyl)-10,20-di(4-methoxyphenyl)porphyrin

trans-DPyDHPP = 5,10-di(4-pyridyl)-10,20-di(4-hydroxyphenyl)porphyrin

trans-DPyDTFMPP = 5,10-di(4-pyridyl)-10,20-di(4-trifluoromethylphenyl)porphyrin

TPEP = 5,10,15,20-tetra(4-phenylester)porphyrin

trans-DPyDFPP = 5,15-dipyridyl-10,20-di(pentafluorophenyl)porphyrin

trans-BPDCP = 5,15-Bis(3,5-dicarboxyphenyl)porphyrin

TCMOPP = 5,10,15,20-tetra(4-carboxymethyleneoxyphenyl)porphyrin

TCPEP = 5,10,15,20-tetra(4-carboxyphenylethynyl)porphyrin

TPPS = 5,10,15,20-tetra(4-sulfonatophenyl)porphyrin

TDCPP = 5,10,15,20-tetra(3,5-dicarboxyphenyl)porphyrin

Trans-DCDBP = 5,15-bis(3,5-dicarboxyphenyl)-10,20-bis(2,6-dibromophenyl)porphyrin

TBCPPP = 3,5-bi[(4-carboxyphenyl)phenyl]porphyrin

A2. Chapter 3 Data

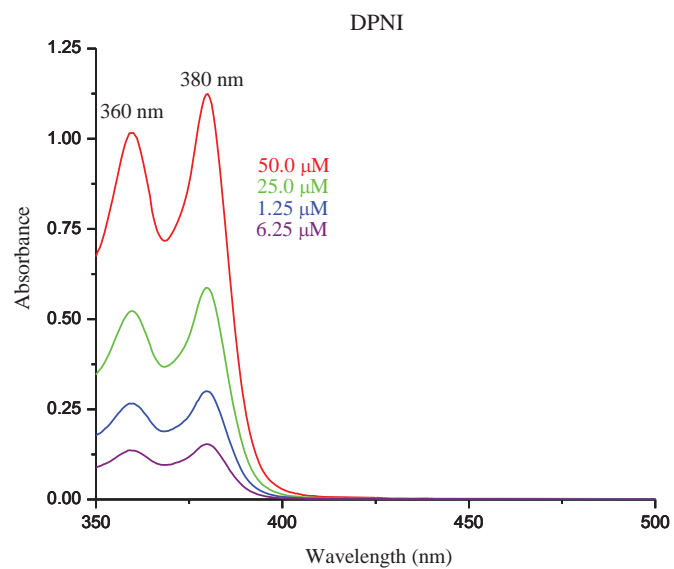


Figure A2.1. UV/vis absorption spectra of DPNI (standard solution). The two peaks centered at 360 nm and 380 nm are consistent with π to π^* transitions observed in all naphthalene diimides.

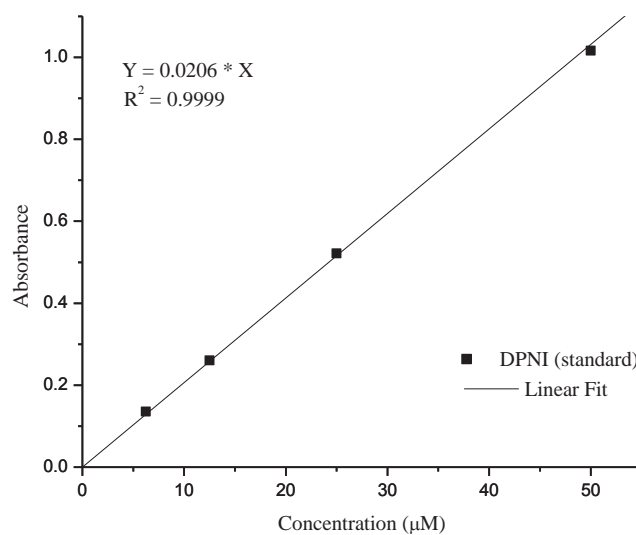


Figure A2.2. Calibration curve for UV/vis absorption at 360 nm for DPNI.

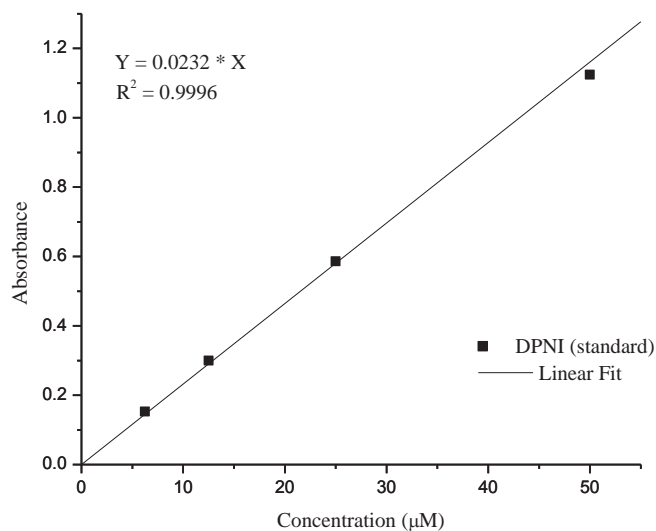


Figure A2.3. Calibration curve of UV/Vis absorption at 380 nm for DPNI.

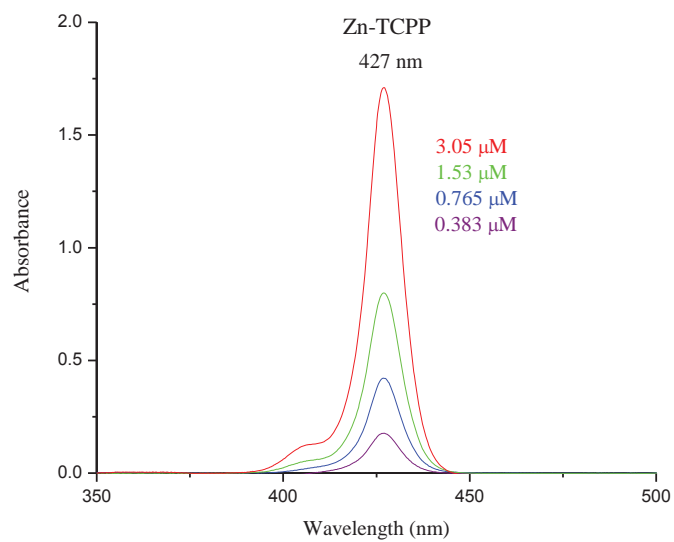


Figure A2.4. UV/vis absorption spectra of ZnTCPP (standard solution). The main absorption centered at 427 nm corresponds to the Soret band of ZnTCPP.

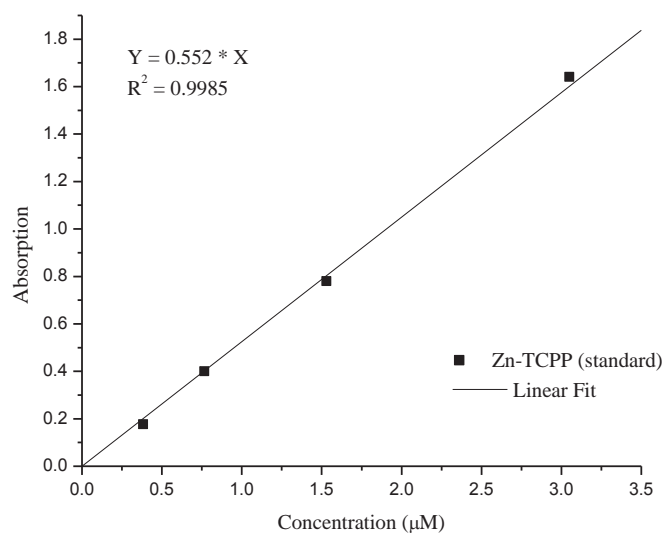


Figure 2.5. Calibration curve for UV/vis absorption at 427 nm for ZnTCPP.

A3. Chapter 4 Data

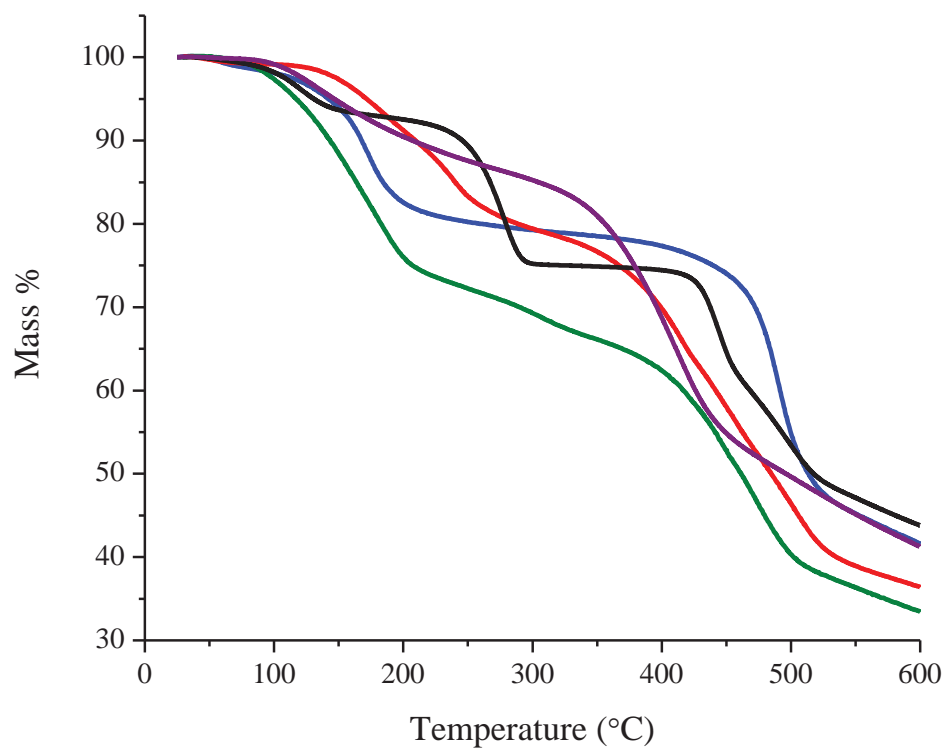


Figure A3.1. TGA data for PPF-1 (black), PPF-27 (red), PPF-18 (blue), PPF-21 (green), and PPF-4 (purple).

A4. Chapter 5 Data

Table A4.1. ICP–OES results for SUMOF-4 copper metal metathesis

Reaction Time (min)	Average Zn Conc. (ppm)	Average Cu Conc. (ppm)	% Composition Zn	% Composition Cu
15	803.8	9.6	98.8	1.2
30	904.9	19.0	97.9	2.1
60	809.7	37.2	95.6	4.4
120	741.5	31.3	95.9	4.1
240	800.8	51.2	94.0	6.0
360	754.2	65.9	91.9	8.1
480	774.5	85.1	90.1	9.9
720	822.8	106.8	88.5	11.5
1080	662.3	137.5	82.8	17.2
1440	690.1	181.6	79.1	20.9
2160	637.6	212.4	75.0	25.0
2880	628.4	207.7	75.2	24.8
4320	643.7	216.2	74.9	25.1
Standard ^a	832.3	0.0	100	0.0

^aSample of SUMOF-4 was immersed in DMF with no copper nitrate for 3 days.

Table A4.2. ICP–OES results for PPF-5-Fe/Zn copper metal metathesis

Reaction Time (hr)	Average Zn Conc. (ppm)	Average Cu Conc. (ppm)	% Composition Zn	% Composition Cu	Average Fe Conc. (ppm)
18	559.9	23.9	95.9	4.1	286.9
168	11.6	603.4	1.8	98.2	313.7
Standard ^a	562.1	0.0	100	0.0	274.4

^aSample of PPF-5-Fe/Zn was immersed in DMF with no copper nitrate for 7 days.

A5. Chapter 7 Data

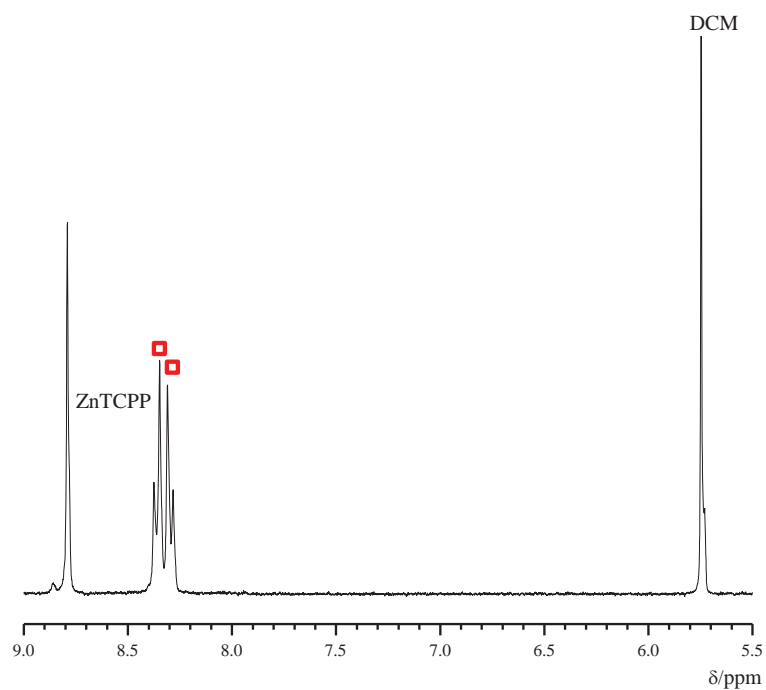


Figure A5.1. ^1H NMR spectra of ZnTCPP solution with DCM internal standard. Red squares represent ZnTCPP signal used for quantitative analysis of concentration.

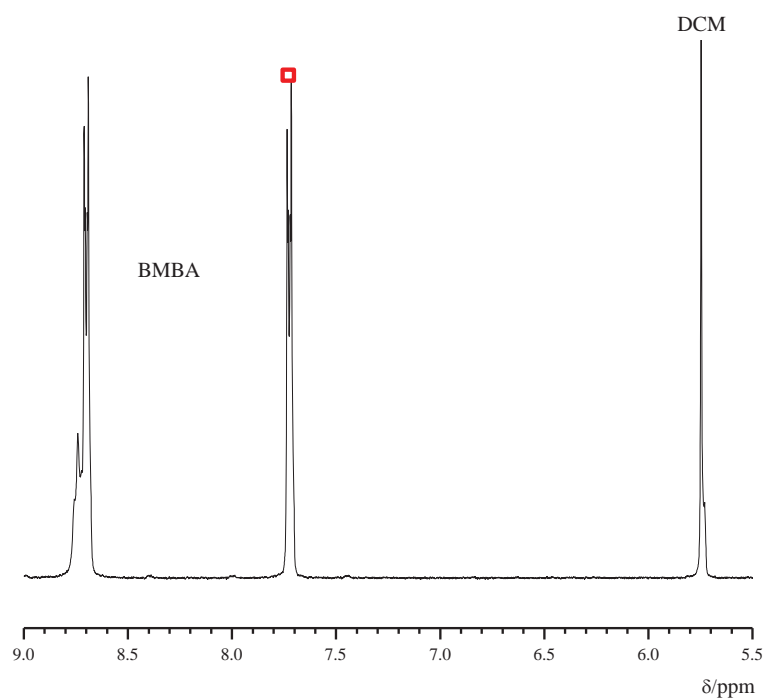


Figure A5.2. ^1H NMR spectra of BMBA solution with DCM internal standard. Red squares represent BMBA signal used for quantitative analysis of concentration.

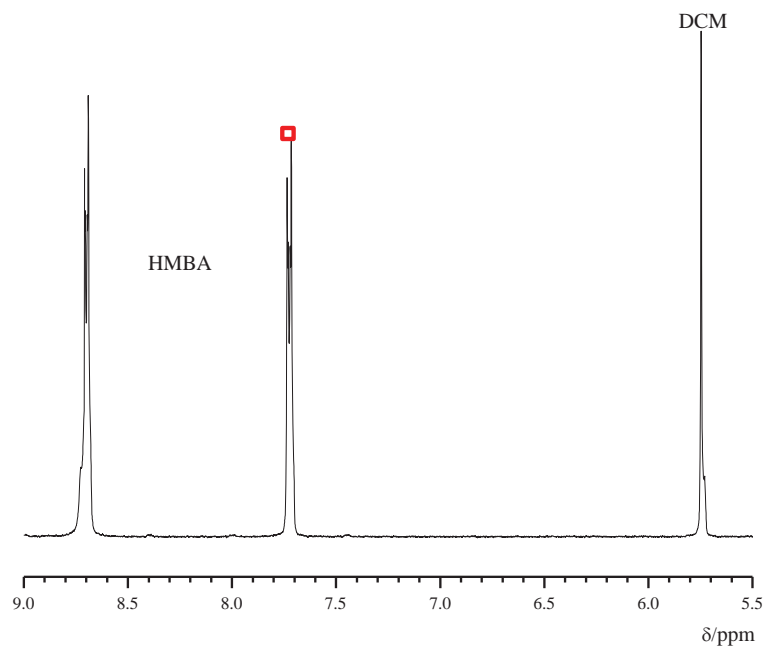


Figure A5.3. ¹H NMR spectra of HMBA solution with DCM internal standard. Red squares represent HMBA signal used for quantitative analysis of concentration.

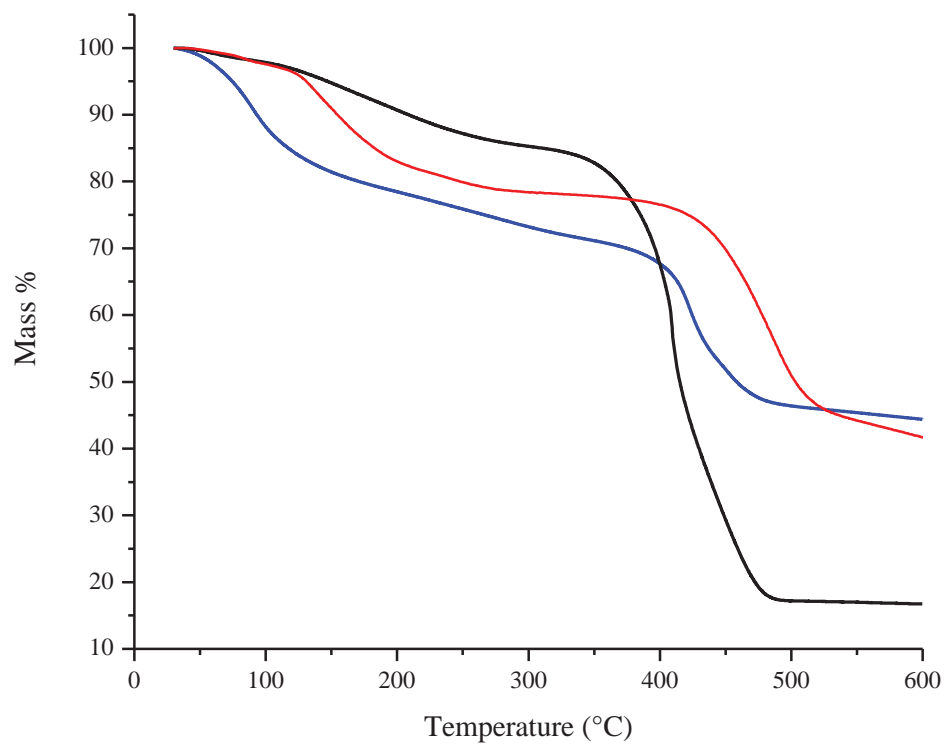


Figure A5.4 . TGA data for PPF-101 (black), PPF-102 (red), and PPF-103 (blue).

Table 5.1. Raw ¹H NMR data for drug delivery of PPF-101.

Time (hr)	Sample Mass (mg)	Sample Amt. (mmol)	Theoretical Conc. (M)	Integration at 8.2-8.4 ^a	# H's	Integration at 7.72-7.74 ^b	# H's	ZnTCPP (M) ^c	BMBA (M) ^d	% ZnTCPP dissolved	% BMBA dissolved
0.25	4.0	2.7 X 10 ⁻³	1.4 X 10 ⁻³	0.00	16	0.53	4	0.0	2.5 X 10 ⁻⁴	0.0	18.2
				0.56		6.6 X 10 ⁻⁵		3.5 X 10 ⁻⁴	4.8	25.5	
0.5	4.1	2.8 X 10 ⁻³	1.4 X 10 ⁻³	0.12	16	1.40	4	1.4 X 10 ⁻⁵	6.6 X 10 ⁻⁴	1.0	47.0
				1.09		1.3 X 10 ⁻⁴		7.9 X 10 ⁻⁴	9.2	56.4	
1.0	4.1	2.8 X 10 ⁻³	1.4 X 10 ⁻³	0.73	16	2.39	4	8.5 X 10 ⁻⁵	1.1 X 10 ⁻³	6.1	80.3
				1.52		2.64		1.8 X 10 ⁻⁴	1.2 X 10 ⁻³	12.8	88.7
2.0	4.0	2.7 X 10 ⁻³	1.4 X 10 ⁻³	1.80	16	2.75	4	2.1 X 10 ⁻⁴	1.3 X 10 ⁻³	15.5	94.7
				2.67		2.98		3.1 X 10 ⁻⁴	1.4 X 10 ⁻³	23.0	102.6
4.0	4.2	2.9 X 10 ⁻³	1.4 X 10 ⁻³	3.64	16	2.97	4	4.3 X 10 ⁻⁴	1.4 X 10 ⁻³	29.8	97.4
				4.83		3.10		5.7 X 10 ⁻⁴	1.5 X 10 ⁻³	39.6	101.6

^aSignal at 8.2–8.4 corresponds to phenyl H's of ZnTCPP. ^bSignal at 7.72-7.74 corresponds to the pyridyl H's of BMBA. ^cCalculated by comparing the integration per hydrogen of ZnTCPP to the integration per hydrogen of DCM of known concentration. ^dCalculated by comparing the integration per hydrogen of BMBA to the integration per hydrogen of DCM of known concentration.

Table 5.2. Raw ^1H NMR data for drug delivery of PPF-102.

Time (hr)	Sample Mass (mg)	Sample Amt. (mmol)	Theoretical Conc. (M)	Integration at 8.2-8.4 ^a	# H's	Integration at 7.72-7.74 ^b	# H's	ZnTCPP (M) ^c	BMBA (M) ^d	% ZnTCPP dissolved	% BMBA dissolved
2	3.9	2.4×10^{-3}	1.2×10^{-3}	0.72	16	0.22	4	8.4×10^{-5}	1.0×10^{-4}	0.0	18.2
				1.36		0.39		1.6×10^{-4}	1.8×10^{-4}	4.8	25.5
4	3.8	2.4×10^{-3}	1.2×10^{-3}	2.11	16	0.49	4	2.5×10^{-4}	2.3×10^{-4}	1.0	47.0
				2.60		0.61		3.0×10^{-4}	2.9×10^{-4}	9.2	56.4
8	4.1	2.6×10^{-3}	1.3×10^{-3}	3.64	16	0.94	4	4.3×10^{-4}	4.4×10^{-4}	6.1	80.3
				4.16		1.09		4.9×10^{-4}	5.1×10^{-4}	12.8	88.7
12	4.1	2.6×10^{-3}	1.3×10^{-3}	5.40	16	1.38	4	6.3×10^{-4}	6.5×10^{-4}	15.5	94.7
				5.96		1.51		7.0×10^{-4}	7.1×10^{-4}	23.0	102.6
24	4.0	2.5×10^{-3}	1.2×10^{-3}	8.53	16	2.07	4	1.0×10^{-3}	9.7×10^{-4}	29.8	97.4
				9.16		2.22		1.1×10^{-3}	1.0×10^{-3}	39.6	101.6
48	3.9	2.4×10^{-3}	1.2×10^{-3}	10.08	16	2.45	4	1.2×10^{-3}	1.1×10^{-3}	97.1	94.4
				10.55		2.54		1.2×10^{-3}	1.2×10^{-3}	101.7	97.9

^aSignal at 8.2–8.4 corresponds to phenyl H's of ZnTCPP. ^bSignal at 7.72-7.74 corresponds to the pyridyl H's of BMBA. ^cCalculated by comparing the integration per hydrogen of ZnTCPP to the integration per hydrogen of DCM of known concentration. ^dCalculated by comparing the integration per hydrogen of BMBA to the integration per hydrogen of DCM of known concentration.

Table 5.3. Raw ^1H NMR data for drug delivery of PPF-103.

Time (hr)	Sample Mass (mg)	Sample Amt. (mmol)	Theoretical Conc. (M)	Integration at 8.2-8.4 ^a	# H's	Integration at 7.72-7.74 ^b	# H's	ZnTCPP (M) ^c	HMBA (M) ^d	% ZnTCPP dissolved	% HMBA dissolved
1	4.2	2.3×10^{-3}	1.2×10^{-3}	0.42	16	0.08	4	4.7×10^{-5}	3.7×10^{-5}	4.0	3.2
				1.02		0.20		1.2×10^{-4}	9.4×10^{-5}	10.3	8.1
2	4.0	2.2×10^{-3}	1.1×10^{-3}	1.10	16	0.25	4	1.3×10^{-4}	1.2×10^{-4}	11.7	10.6
				1.62		0.39		1.9×10^{-4}	1.8×10^{-4}	17.2	16.6
4	4.0	2.2×10^{-3}	1.1×10^{-3}	2.00	16	0.54	4	2.3×10^{-4}	2.5×10^{-4}	21.2	22.9
				2.58		0.73		3.0×10^{-4}	3.4×10^{-4}	27.4	30.8
8	4.2	2.3×10^{-3}	1.2×10^{-3}	3.46	16	0.82	4	4.0×10^{-4}	3.8×10^{-4}	35.0	33.0
				4.24		0.99		5.0×10^{-4}	4.6×10^{-4}	42.9	40.0
12	4.1	2.3×10^{-3}	1.1×10^{-3}	3.96	16	1.05	4	4.6×10^{-3}	4.9×10^{-4}	41.0	43.5
				4.94		1.27		5.8×10^{-3}	5.9×10^{-4}	51.2	52.6
24	4.2	2.3×10^{-3}	1.2×10^{-3}	8.96	16	2.19	4	1.0×10^{-3}	1.0×10^{-3}	90.6	88.6
				9.44		2.32		1.1×10^{-3}	1.1×10^{-3}	95.4	93.8
48	4.0	2.2×10^{-3}	1.1×10^{-3}	9.20	16	2.31	4	1.1×10^{-3}	1.1×10^{-3}	97.7	98.1
				9.62		2.40		1.1×10^{-3}	1.1×10^{-3}	102.1	101.9

^aSignal at 8.2–8.4 corresponds to phenyl H's of ZnTCPP. ^bSignal at 7.72-7.74 corresponds to the pyridyl H's of HMBA. ^cCalculated by comparing the integration per hydrogen of ZnTCPP to the integration per hydrogen of DCM of known concentration. ^dCalculated by comparing the integration per hydrogen of HMBA to the integration per hydrogen of DCM of known concentration.

References

- (1) Abrahams, B. F.; Hoskins, B. F.; Robson, R. *J. Am. Chem. Soc.* **1991**, *113*, 3606.
- (2) Krupitsky, H.; Stein, Z.; Goldberg, I.; Strouse, C. E. *J. Incl. Phenom.* **1994**, *18*, 177.
- (3) Abrahams, B. F.; Hoskins, B. F.; Michail, D. M.; Robson, R. *Nature* **1994**, *369*, 727.
- (4) Sharma, C. V. K.; Broker, G. A.; Huddleston, J. G.; Baldwin, J. W.; Metzger, R. M.; Rogers, R. D. *J. Am. Chem. Soc.* **1999**, *121*, 1137.
- (5) Lin, K. –J. *Angew. Chem. Int. Ed.* **1999**, *38*, 2730.
- (6) Hagrman, D.; Hagrman, P. J.; Zubieta, J. *Angew. Chem. Int. Ed.* **1999**, *38*, 3165.
- (7) Diskin–Posner, Y.; Dahal, S.; Goldberg, I. *Chem. Commun.* **2000**, 585.
- (8) Diskin–Posner, Y.; Patra, G. K.; Goldberg, I. *Dalton* **2001**, 2775.
- (9) Sun, D.; Tham, F. S.; Reed, C. A.; Boyd, P. D. W. *Proc. Natl. Acad. Sci. USA* **2002**, *99*, 5088.
- (10) Zimmer, B.; Bulach, V.; Hosseini, M. W.; De Cian, A.; Kyritsakas, N. *Eur. J. Inorg. Chem.* **2002**, 3079.
- (11) Kosal, M. E.; Chou, J. H.; Wilson, S. R.; Suslick, K. S. *Nat. Mater.* **2002**, *1*, 118.
- (12) Pan, L.; Kelly, S.; Huang, X. Y.; Li, J. *Chem. Commun.* **2002**, 2334.
- (13) Carlucci, L.; Ciani, G.; Proserpio, D. M.; Porta, F. *Angew. Chem. Int. Ed.* **2003**, *42*, 317.
- (14) Smithenry, D. W.; Wilson, S. R.; Suslick, K. S. *Inorg. Chem.* **2003**, *42*, 7719.
- (15) Shmilovits, M.; Vinodu, M.; Goldberg, I. *New. J. Chem.* **2004**, *28*, 223.
- (16) Shmilovits, M.; Vinodu, M.; Goldberg, I. *Cryst. Growth Des.* **2004**, *4*, 633.
- (17) Yucesan, g.; Golub, V.; O’Conner, C. J.; Zubieta, J. *CrystEngComm* **2004**, *6*, 323.
- (18) Carlucci, L.; Ciani, G.; Proserpio, D. M.; Porta, F. *CrystEngComm* **2005**, *7*, 78.
- (19) Deiters, E.; Bulach, V.; Hosseini, M. W. *Chem. Commun.* **2005**, *41*, 3906.
- (20) Kempe, R. *Z. Anorg. Allg. Chem.* **2005**, *631*, 1038.
- (21) Taylor, S. K.; Jameson, G. B.; Boyd, P. D. W. *Supromol. Chem.* **2005**, *17*, 543.
- (22) Suslick, K. S.; Bhyrappa, P.; Chou, J. –H.; Kosal, M. E.; Nakagaki, S.; Smithenry, D. W.; Wilson, S. R. *Acc. Chem. Res.* **2005**, *38*, 283.
- (23) George, S.; Lipstman, S.; Goldberg, I. *Cryst. Growth Des.* **2006**, *6*, 2651.
- (24) Ohmura, T.; Usuki, A.; Fukumori, K.; Ohta, T.; Ito, M.; Tatsumi, K.; *Inorg. Chem.* **2006**, *45*, 7988.
- (25) Zheng, N.; Zhang, J.; Bu, X.; Feng, P. *Cryst. Growth Des.* **2007**, *7*, 2576.
- (26) Lipstman, S.; Muniappan, S.; Goldberg, I. *Cryst. Growth Des.* **2008**, *8*, 1682.
- (27) Kühn, E.; Bulach, V.; Hosseini, M. W. *Chem. Commun.* **2008**, 5104.
- (28) Lipstman, S.; Goldberg, I. *J. Mol. Struct.* **2008**, *890*, 101.
- (29) Choi, E. –Y.; Barron, P. M.; Novotney, R. W.; Hu, C.; Kwon, Y. –U.; Choe, W. *CrystEngComm* **2008**, *10*, 824.

- (30) Seidel, R. W.; Oppel, I. M. *Struct. Chem.* **2009**, *20*, 121.
- (31) Choi, E. -Y.; Wray, C. A.; Hu, C.; Choe, W. *CrystEngComm* **2009**, *11*, 553.
- (32) Choi, E. -Y.; Barron, P. M.; Novotny, R. W.; Son, H. -T.; Hu, C.; Choe, W. *Inorg. Chem.* **2009**, *48*, 426.
- (33) Barron, P. M.; Son, H. -T.; Hu, C.; Choe, W. *Cryst. Growth Des.* **2009**, *9*, 1960.
- (34) Chung, H.; Barron, P. M.; Novotny, R. W.; Son, H. -T.; Hu, C.; Choe, W. *Cryst. Growth Des.* **2009**, *9*, 3327.
- (35) Verduzco, J. M.; Chung, H.; Hu, C.; Choe, W. *Inorg. Chem.* **2009**, *48*, 9060.
- (36) Chen, W.; Fukuzumi, S. *Eur. J. Inorg. Chem.* **2009**, 5494.
- (37) Shultz, A. M.; Farha, O. K.; Hupp, J. T.; Nguyen, S. T. *J. Am. Chem. Soc.* **2009**, *131*, 4204.
- (38) Choi, E. -Y.; DeVries, L. D.; Novotny, R. W.; Hu, C.; Choe, W. *Cryst. Growth Des.* **2010**, *10*, 171.
- (39) Lipstman, S.; Goldberg, I. *CrystEngComm* **2010**, *12*, 52.
- (40) Seidel, R. W.; Oppel, I. M. *CrystEngComm* **2010**, *12*, 1051.
- (41) Seidel, R. W.; Oppel, I. M. *Annorg. Allg. Chem.* **2010**, 636, 446.
- (42) Barron, P. M.; Wray, C. A.; Hu, C.; Guo, Z.; Choe, W. *Inorg. Chem.* **2010**, *49*, 10217.
- (43) Karmakar, A.; Goldberg, I. *CrystEngComm* **2010**, *12*, 4095.
- (44) Lipstman, S.; Goldberg, I. *Cryst. Growth Des.* **2010**, *10*, 5001.
- (45) Lipstman, S.; Goldberg, I. *Cryst. Growth Des.* **2010**, *10*, 4596.
- (46) Burnett, B. J.; Barron, P. M.; Hu, C.; Choe, W. *J. Am. Chem. Soc.* **2011**, *133*, 9984.
- (47) DeVries, L. D.; Barron, P. M.; Hurley, E. P.; Hu, C.; Choe, W. *J. Am. Chem. Soc.* **2011**, *133*, 14848.
- (48) Wang, S. -X.; Meng, L.; Cheng, Q.; Kim, C.; Wojtas, L.; Chrzanowski, M.; Chen, Y. -S.; Zhang, X. P.; Ma, S. *J. Am. Chem. Soc.* **2011**, *133*, 16322.
- (49) Xie, M. -H.; Yang, X. -L.; Wu, C. -D. *Chem. Commun.* **2011**, *47*, 5521.
- (50) Xie, M. -H.; Yang, X. -L.; Zhou, C.; Wu, C. -D. *Inorg. Chem.* **2011**, *50*, 5318.
- (51) Farha, O. K.; Sultz, A. M.; Sarjeant, A. A.; Nguyen, S. T.; Hupp, J. T. *J. Am. Chem. Soc.* **2011**, *133*, 5652.
- (52) Lee, C. Y.; Farha, O. K.; Hong B. J.; Sarjeant, A. A.; Nguyen, S. T.; Hupp, J. T. *J. Am. Chem. Soc.* **2011**, *133*, 15858.
- (53) Fateeva, A.; Devautour-Vinot, S.; Heymans, N.; Devic, T.; Grenèche, J. -M.; Wuttke, S.; Miller, S.; Lago, A.; Serre, C.; De Weireld, G.; Maurin, G.; Vimont, A.; Férey, G. *Chem. Mater.* **2011**, *23*, 4641.
- (54) Matsunaga, S.; Endo, N.; Mori, W. *Eur. J. Inorg. Chem.* **2011**, 4550.
- (55) Chen, W. -T.; Yamada, Y.; Liu, G. -N.; Kubota, A.; Ichikawa, T.; Kojima, Y.; Guo, G. -C.; Fukuzumi, S.; *Dalton Trans.* **2011**, *40*, 12826.

- (56) Fidalgo–Marijuan, A.; Barandika, G.; Bazán, B.; Urtiaga, M. –K.; Arriortua, M. –I. *Polyhedron* **2011**, *30*, 2711.
- (57) Zou, C.; Zhang, Z.; Xu, X.; Gong, Q.; Li, J.; Wu, C. –D. *J. Am. Chem. Soc.* **2012**, *134*, 87.
- (58) Smythe, N. C.; Butler, D. P.; Moore, C. E.; McGowan, W. R.; Rheingold, A. L.; Beauvais, L. G. *Dalton Trans.* **2012**, *41*, 7855.
- (59) Zou, C.; Xie, M. –H.; Kong, G. –Q.; Wu, C. –D. *CrystEngComm* **2012**, *14*, 4850.
- (60) Wang, X. –S.; Chrzanowski, M.; Kim, C.; Gao, W. –Y.; Wojtas, L.; Chen, Y. –S.; Zhang, X. P.; Ma, S. *Chem. Commun.* **2012**, *48*, 7173.
- (61) Morris, W.; Voloskiy, B.; Demirt, S.; Gándarat, F.; McGrier, P. L.; Furukawa, H.; Cascio, D.; Stoddard, J. F.; Yaghi, O. M. *Inorg. Chem.* **2012**, *51*, 6443.
- (62) Yang, X. –L.; Xie, M. –H.; Zou, C.; He, Y.; Chen, B.; O’Keeffe, M.; Wu, C. –D. *J. Am. Chem. Soc.* **2012**, *134*, 10638.
- (63) Fateeva, A.; Cater, P. A.; Ireland, C. P.; Tahir, A. A.; Khimyak, Y. Z.; Wiper, P. V.; Darewnt, J. R.; Rosseinsky, M. J. *Angew. Chem. Int. Ed.* **2012**, *51*, 7440.
- (64) Feng, D.; Gu, Z. –Y.; Li, J. –R.; Jiang, H. –L.; Wei, Z.; Zhou, H. –C. *Angew. Chem. Int. Ed.* **2012**, *51*, 10307.
- (65) Wang, X. –S.; Chrzanowski, M.; Gao, W. –Y.; Wojtas, L.; Chen, Y. –S.; Zaworotko, M. J.; Ma, S. *Chem. Sci.* **2012**, *3*, 2823.
- (66) Matsunaga, S.; Endo, N.; Mori, W. *Eur. J. Inorg. Chem.* **2012**, 4885.
- (67) Meng, L.; Cheng, Q.; Kim, C.; Gau, W. –Y.; Wojtas, L.; Chen, Y. –S.; Zaworotko, M. J.; Zhang, X. P.; Ma, S. *Angew. Chem. Int. Ed.* **2012**, *51*, 10082.
- (68) Johnson, J. A.; Lin, Q.; Wu, L. –C.; Obaidi, N.; Olson, Z. L.; Reeson, T. C.; Chen, Y. –S.; Zhang, J. *Chem. Commun.* **2013**, *49*, 2828.